

# Study of the $B \rightarrow S$ Gamma at BaBar Using the Sum of Exclusive Modes<sup>\*</sup>

Teela Maria Pulliam

Stanford Linear Accelerator Center  
Stanford University  
Stanford, CA 94309

SLAC-Report-670  
September 2002

Prepared for the Department of Energy  
under contract number DE-AC03-76SF00515

Printed in the United States of America. Available from the National Technical Information Service, U.S. Department of Commerce, 5285 Port Royal Road, Springfield, VA 22161.

---

• Ph.D. thesis, UC Santa Cruz, Santa Cruz, Ca, 95064

UNIVERSITY of CALIFORNIA  
SANTA CRUZ

**STUDY OF  $b \rightarrow s\gamma$  AT *BaBar* USING THE SUM OF EXCLUSIVE  
MODES.**

A dissertation submitted in partial satisfaction of the  
requirements for the degree of  
DOCTOR OF PHILOSOPHY

in

PHYSICS

by

**Teela Marie Pulliam**

September 2002

The Dissertation of Teela Marie Pulliam is  
approved:

---

Professor Bruce Schumm, Chair

---

Professor Hartmut Sadrozinski

---

Professor Robert Johnson

---

Professor Michael Dine

---

Frank Talamantes  
Vice Provost and Dean of Graduate Studies

# Table of Contents

List of Figures	viii
List of Tables	xii
Abstract	xviii
Dedication	xix
Acknowledgements	xx
<b>1 Introduction</b>	<b>1</b>
1.1 The Standard Model . . . . .	1
1.2 $\text{BF}(b \rightarrow s\gamma)$ . . . . .	3
1.3 $b \rightarrow s\gamma$ Spectrum . . . . .	5
1.4 Measuring $b \rightarrow s\gamma$ at <i>BABAR</i> . . . . .	5
1.4.1 Backgrounds . . . . .	5
1.4.2 Methods . . . . .	6
1.5 Other Measurements . . . . .	8
1.6 Outline . . . . .	9
<b>2 Signal Model</b>	<b>11</b>
2.1 Resonant contributions . . . . .	11
2.2 Non-resonant contribution to $b \rightarrow s\gamma$ . . . . .	12
2.3 Signal Shape . . . . .	14
2.4 $X_S$ final states . . . . .	15
2.5 Final State Category Fractions $f_j$ . . . . .	19
<b>3 The <i>BABAR</i> Experiment</b>	<b>26</b>
3.1 The PEP-II Asymmetric $e^+e^-$ $B$ Factory . . . . .	26
3.2 The <i>BABAR</i> Detector . . . . .	27

3.2.1	Silicon Vertex Tracker (SVT)	28
3.2.2	Drift Chamber (DCH)	29
3.2.3	Charged Particle Tracking	29
3.2.4	Detector of Internally Reflected Cherenkov Light (DIRC)	30
3.2.5	Particle Identification System	32
3.2.6	Electromagnetic Calorimeter (EMC)	32
3.2.7	Instrumented Flux Return (IFR)	34
<b>4</b>	<b>Analysis Method Summary</b>	<b>37</b>
<b>5</b>	<b>Data and Monte Carlo Samples</b>	<b>44</b>
<b>6</b>	<b>Selection</b>	<b>47</b>
6.1	Filter	48
6.2	Exclusive final states reconstruction	48
6.3	Quality cuts	51
6.3.1	High Energy Gamma Selection	51
6.3.2	Charged pions and kaon selection	54
6.3.3	$K_S$ selection	55
6.3.4	Neutral Pion Identification	56
6.4	Fisher Discriminant	56
6.4.1	Input variables for the Fisher Discriminant	57
6.4.2	Description of the Fisher Discriminant	58
6.4.3	Optimization of the cut	59
6.5	$\Delta E^*$ Window Selection	59
6.6	Multiple Candidates	59
6.7	Final Sample	61
<b>7</b>	<b>Background Composition</b>	<b>68</b>
7.1	Composition of continuum and $B\bar{B}$ backgrounds	68
7.2	Cross-Feed Background	76
7.2.1	Cross-feed background definition	76
7.2.2	Hadronic mass resolution	79
7.2.3	Cross-feed Sources Study	83
<b>8</b>	<b>Signal Efficiency</b>	<b>90</b>
<b>9</b>	<b>Background Subtraction</b>	<b>94</b>
9.1	Method	94
9.2	Toy-MC studies	97

9.2.1	Toy-MC Samples . . . . .	98
9.2.2	Non-peaking Background Subtraction . . . . .	100
9.2.3	Peaking background subtraction. . . . .	102
<b>10</b>	<b>Monte Carlo and Data Fit Results</b>	<b>108</b>
10.1	Fits to Monte Carlo . . . . .	108
10.1.1	Signal Monte Carlo . . . . .	108
10.1.2	Background Monte Carlo . . . . .	113
10.2	Fits to data . . . . .	117
10.3	Comparison of Final State Category Yields . . . . .	119
<b>11</b>	<b>Determination of Partial Branching Fractions using the MC Ex-</b>	
	<b>pectations</b>	<b>131</b>
11.1	Partial Branching Fraction Definition . . . . .	131
11.2	Partial Branching Fraction results . . . . .	132
11.3	Interpretation of the PBF results . . . . .	133
11.3.1	$K_S$ production . . . . .	134
11.3.2	$\pi^0$ production . . . . .	135
11.3.3	Hadronic multiplicity . . . . .	138
<b>12</b>	<b>Systematic Errors</b>	<b>142</b>
12.1	Photon systematics . . . . .	143
12.2	B-counting systematics . . . . .	144
12.3	Errors associated with the selection variables . . . . .	144
12.4	Fit Systematics . . . . .	145
12.4.1	Crystal Ball Width . . . . .	146
12.4.2	Crystal Ball $\alpha$ and tail . . . . .	148
12.4.3	Monte Carlo Crystal Ball Peak . . . . .	149
12.4.4	Data Crystal Ball Peak . . . . .	150
12.4.5	Cross-Feed Argus Shape . . . . .	151
12.4.6	Background Argus Shape . . . . .	152
12.4.7	Summary of Fit Systematics . . . . .	153
12.5	Signal Definition Systematic . . . . .	155
12.6	$B\bar{B}$ Peaking Yield . . . . .	157
12.7	Efficiency Systematics . . . . .	158
12.7.1	Difference between data and MC detection efficiencies . . .	159
12.7.2	Systematic errors on difference between data and MC ef- ficiencies . . . . .	160
12.8	Transition between resonant and non-resonant Monte Carlo. . . .	163

12.9	Generator error due to model dependence . . . . .	164
12.10	Summary of the systematic errors . . . . .	165
12.11	Partial BFs with systematic errors . . . . .	166
<b>13</b>	<b>Weighted Partial Branching Fractions</b>	<b>170</b>
13.1	Weighting procedure . . . . .	170
13.2	$\pi^0$ weights . . . . .	172
13.3	$\pi^0$ and 2-body weights . . . . .	173
13.4	$\pi^0$ , 2-body and $\pi^0$ (second iteration) weights . . . . .	173
13.5	Weighted Partial Branching Fraction Results . . . . .	174
13.6	Systematics due to the weights . . . . .	180
<b>14</b>	<b>Inclusive Branching Fractions</b>	<b>189</b>
14.1	Branching Fraction Formula . . . . .	189
14.2	Final State Fractions . . . . .	191
14.3	Inclusive Branching Fraction Results . . . . .	194
14.4	Comparison . . . . .	195
<b>15</b>	<b>Conclusions</b>	<b>199</b>
<b>Appendix A: The PDFs used in the fits</b>		<b>201</b>
A.1	Argus Background Distribution . . . . .	201
A.2	Crystal Ball Lineshape Distribution . . . . .	201
<b>Appendix B: Isospin Correction for <math>K_S \rightarrow \pi^0\pi^0</math> in <math>K^*\gamma</math></b>		<b>202</b>
B.1	Four Resonant Modes . . . . .	203
B.2	Correction for the <i>all</i> final state category . . . . .	204
B.3	Correction for the $\pi$ final state category . . . . .	204
B.4	Correction for the $\pi^0$ final state category . . . . .	205
B.5	Correction for the $K_S$ final state category . . . . .	205
<b>Appendix C: Plots for the toy–MC studies</b>		<b>207</b>
<b>Appendix D: Plots for all the fits</b>		<b>211</b>
D.1	Signal Monte Carlo Fits . . . . .	211
D.2	Cross–Feed Monte Carlo Fits . . . . .	221
D.3	$B\bar{B}$ + Continuum Monte Carlo Fits . . . . .	231
D.4	$B\bar{B}$ Monte Carlo Fits . . . . .	241
D.5	Data Fits . . . . .	245



# List of Figures

1.1	The “penguin” diagram for the process $b \rightarrow s\gamma$ . $V_{qb}$ and $V_{qs}^*$ are the CKM matrix elements which give the order of the quark coupling, where $q = u, c, t$ .	3
2.1	Hadronic mass and photon energy spectra.	23
2.2	Hadronic mass and photon energy spectra for three Kagan and Neubert models.	24
2.3	Hadronic mass spectra at the generator level.	25
2.4	The final state fractions for the <i>all</i> category as a function of $M_{Had}$ .	25
3.1	The <i>BABAR</i> detector.	27
3.2	Measurement of $dE/dx$ in the DCH as a function of track momenta.	30
3.3	Track reconstruction efficiency in the DCH as a function of a) transverse momentum, b) polar angle.	31
3.4	Kaon identification efficiency for the Tight PID selection.	33
3.5	The EMC energy resolution.	34
3.6	The EMC angular resolution.	35
3.7	The IRF muon detection efficiency.	36
6.1	Photon selection variables.	52
6.2	$\pi^0$ and $\eta$ vetoes.	53
6.3	Bump distance distribution.	54
6.4	$K_S$ selection variables.	56
6.5	Event Shapes	57
6.6	Variables used in the Fisher Discriminant.	64
6.7	Fisher Discriminant distributions.	65
6.8	Optimization plots for the Fisher Discriminant made using just true B for the signal.	65
6.9	$\Delta E^*$ resolution.	66

6.10	Plot of the number of candidates per event for the $X_s\gamma$ Monte Carlo sample. The histogram is normalized to an area of 1. . . . .	66
6.11	Plot of $\Delta E^*$ for the candidate with the smallest and the next to smallest $\Delta E^*$ . . . . .	67
7.1	Background levels after the selection. . . . .	69
7.2	Dependence of $B\bar{B}$ and continuum background on hadronic mass. . . . .	71
7.3	Fit of the Continuum background Monte Carlo ( <b>uds</b> and <b>ccb</b> ) to an Argus shape. . . . .	72
7.4	Fit of the $B\bar{B}$ background to an Argus plus Crystal Ball function. . . . .	73
7.5	Momentum and $\cos\theta$ distributions for the other daughter of a $\pi^0$ or $\eta$ decay in $B\bar{B}$ background. . . . .	75
7.6	True minus reconstructed $M_{Had}$ . . . . .	78
7.7	Sample signal and cross-feed distributions for $M_{Had}$ 1.0-2.4 GeV/ $c^2$ . . . . .	78
7.8	Fits to the cross-feed $m_{ES}$ distribution with either a Argus or Argus plus Crystal Ball function. . . . .	79
7.9	$M_{Had}$ resolution for events with true = reco mode and $m_{ES}$ in the peaking region, fit with Gaussian plus linear function. . . . .	84
8.1	Signal efficiency as a function of $M_{Had}$ for the <i>all</i> final state category. . . . .	93
9.1	Example fits for the signal, cross-feed, continuum plus $B\bar{B}$ $B^+B^-$ and data samples. . . . .	106
9.2	Diagram of the fitting procedure. . . . .	107
10.1	Free fit to MC signal sample in bin $M_{Had} = 0.6-1.0$ GeV to obtain a value for the Crystal Ball peak. . . . .	109
10.2	MC signal fit over the wide $M_{Had}$ bin, 0.6-1.0 GeV/ $c^2$ . . . . .	125
10.3	MC signal fit over the wide $M_{Had}$ bin, 1.0-2.4 GeV. . . . .	126
10.4	Sample MC signal fits. . . . .	127
10.5	Sample MC cross-feed fits. . . . .	127
10.6	Sample MC background (continuum plus $B\bar{B}$ ) fits. . . . .	127
10.7	Sample MC $B\bar{B}$ background fit. . . . .	128
10.8	$B\bar{B}$ fit for the <i>all</i> category in $M_{Had}$ 1.6-1.8 GeV/ $c^2$ . . . . .	128
10.9	Fits to obtain the data Crystal Ball peak parameter. . . . .	129
10.10	Sample data fits. . . . .	129
10.11	The data, cross-feed, $B\bar{B}$ and signal yields as a function of $M_{Had}$ . . . . .	130

11.1	Signal yield and PBF for the different final state categories. . . .	140
11.2	Truncated hadronic multiplicity in signal MC and data. . . . .	141
12.1	Fisher discriminant and $\cos \theta_{T^*}$ distribution for off-resonance data (dots) and continuum MC after all the selection cuts are applied.	145
13.1	Data over MC ratios. No weights are yet applied. . . . .	173
13.2	Data over MC ratios with the y-axis magnified. No weights are yet applied. . . . .	174
13.3	Data over MC ratios. The $\pi^0$ weight is applied. . . . .	177
13.4	Data over MC ratios. The $\pi^0$ and 2 body weights are applied. . .	180
13.5	Data over MC ratios. The $\pi^0$ (two iterations) and 2 body weights are applied. . . . .	181
13.6	Data over MC ratios, where the y-axis is expanded. The $\pi^0$ (two iterations) and 2 body weights are applied. . . . .	182
13.7	Signal yield and WPBF for the all the categories with $\pi^0$ (2 it- erations) and 2 body weight. When the error is shown is just a statistical error. . . . .	185
13.8	Truncated hadronic multiplicity in signal MC and data after weight- ing. . . . .	187
14.1	Upper plot: Inclusive branching fraction as a function of the hadronic mass. Lower plot: Inclusive branching fraction as a func- tion of $E_\gamma^B$ . . . . .	198
15.1	PBF $M_{Had}$ Spectrum. . . . .	200
C.1	Toy-background (toy-bb plus toy-cont) fits with a fixed CB and an Argus function. Free parameters: the normalization, the ratio among the CB and the Argus function and the Argus function shape. . . . .	208
C.2	Toy-data fits with a fixed CB and an Argus function. Free param- eters: the normalization, the ratio among the CB and the Argus function and the Argus function shape. . . . .	209
C.3	Toy-data fits with a fixed CB and two Argus functions. Free parameters: the normalization, the ratio among functions and the Argus function shapes. . . . .	210
D.1	MC signal fits for $M_{Had} = 0.6-0.8$ GeV/ $c^2$ . . . . .	212
D.2	MC signal fits for $M_{Had} = 0.8-1.0$ GeV/ $c^2$ . . . . .	213
D.3	MC signal fits for $M_{Had} = 1.0-1.2$ GeV/ $c^2$ . . . . .	214

D.4	MC signal fits for $M_{Had} = 1.2-1.4$ GeV/ $c^2$ .	215
D.5	MC signal fits for $M_{Had} = 1.4-1.6$ GeV/ $c^2$ .	216
D.6	MC signal fits for $M_{Had} = 1.6-1.8$ GeV/ $c^2$ .	217
D.7	MC signal fits for $M_{Had} = 1.8-2.0$ GeV/ $c^2$ .	218
D.8	MC signal fits for $M_{Had} = 2.0-2.2$ GeV/ $c^2$ .	219
D.9	MC signal fits for $M_{Had} = 2.2-2.4$ GeV/ $c^2$ .	220
D.10	MC cross-feed fits for $M_{Had} = 0.6-0.8$ GeV/ $c^2$ .	222
D.11	MC cross-feed fits for $M_{Had} = 0.8-1.0$ GeV/ $c^2$ .	223
D.12	MC cross-feed fits for $M_{Had} = 1.0-1.2$ GeV/ $c^2$ .	224
D.13	MC cross-feed fits for $M_{Had} = 1.2-1.4$ GeV/ $c^2$ .	225
D.14	MC cross-feed fits for $M_{Had} = 1.4-1.6$ GeV/ $c^2$ .	226
D.15	MC cross-feed fits for $M_{Had} = 1.6-1.8$ GeV/ $c^2$ .	227
D.16	MC cross-feed fits for $M_{Had} = 1.8-2.0$ GeV/ $c^2$ .	228
D.17	MC cross-feed fits for $M_{Had} = 2.0-2.2$ GeV/ $c^2$ .	229
D.18	MC cross-feed fits for $M_{Had} = 2.2-2.4$ GeV/ $c^2$ .	230
D.19	$B\bar{B}+$ continuum fits for $M_{Had} = 0.6-0.8$ GeV/ $c^2$ .	232
D.20	$B\bar{B}+$ continuum fits for $M_{Had} = 0.8-1.0$ GeV/ $c^2$ .	233
D.21	$B\bar{B}+$ continuum fits for $M_{Had} = 1.0-1.2$ GeV/ $c^2$ .	234
D.22	$B\bar{B}+$ continuum fits for $M_{Had} = 1.2-1.4$ GeV/ $c^2$ .	235
D.23	$B\bar{B}+$ continuum fits for $M_{Had} = 1.4-1.6$ GeV/ $c^2$ .	236
D.24	$B\bar{B}+$ continuum fits for $M_{Had} = 1.6-1.8$ GeV/ $c^2$ .	237
D.25	$B\bar{B}+$ continuum fits for $M_{Had} = 1.8-2.0$ GeV/ $c^2$ .	238
D.26	$B\bar{B}+$ continuum fits for $M_{Had} = 2.0-2.2$ GeV/ $c^2$ .	239
D.27	$B\bar{B}+$ continuum fits for $M_{Had} = 2.2-2.4$ GeV/ $c^2$ .	240
D.28	$B\bar{B}$ fits for $M_{Had} = 1.8-2.0$ GeV/ $c^2$ .	242
D.29	$B\bar{B}$ fits for $M_{Had} = 2.0-2.2$ GeV/ $c^2$ .	243
D.30	$B\bar{B}$ fits for $M_{Had} = 2.0-2.2$ GeV/ $c^2$ .	244
D.31	Data fits for $M_{Had} = 0.6-0.8$ GeV/ $c^2$ .	246
D.32	Data fits for $M_{Had} = 0.8-1.0$ GeV/ $c^2$ .	247
D.33	Data fits for $M_{Had} = 1.0-1.2$ GeV/ $c^2$ .	248
D.34	Data fits for $M_{Had} = 1.2-1.4$ GeV/ $c^2$ .	249
D.35	Data fits for $M_{Had} = 1.4-1.6$ GeV/ $c^2$ .	250
D.36	Data fits for $M_{Had} = 1.6-1.8$ GeV/ $c^2$ .	251
D.37	Data fits for $M_{Had} = 1.8-2.0$ GeV/ $c^2$ .	252
D.38	Data fits for $M_{Had} = 2.0-2.2$ GeV/ $c^2$ .	253
D.39	Data fits for $M_{Had} = 2.2-2.4$ GeV/ $c^2$ .	254

# List of Tables

1.1	Elementary particles and gauge bosons. . . . .	2
1.2	Published measurements of the inclusive rate $b \rightarrow s\gamma$ . . . . .	9
2.1	Predicted contributions from exclusive modes to the $b \rightarrow s\gamma$ final states. . . . .	12
2.2	List of some final states of the $b \rightarrow s\gamma$ process. . . . .	17
2.3	Some of the $X_S$ final states and their rates. . . . .	19
2.4	Distribution of events in the $X_S$ Monte Carlo, KN465 and KN480, at the generator level. . . . .	20
2.5	Percent of $X_S\gamma$ events at the generator level, per each final state category. . . . .	21
2.6	Fraction of $K^*\gamma$ events, at the generator level, per each final state category. . . . .	22
3.1	Overview of detector performance. . . . .	28
4.1	List of twelve final states used in the analysis. . . . .	38
6.1	Quality cuts applied for the good track selection. . . . .	48
6.2	. . . . .	49
6.3	Efficiencies obtained from MC signal and background events after the filter and requiring at least one reconstructed $B$ . . . . .	50
6.4	Signal efficiencies for each of the cuts on the photons. . . . .	54
6.5	Signal efficiencies for each of the cuts on the $K_S$ . . . . .	55
6.6	Number of events with a true B among the candidates for each mode. . . . .	61
6.7	The fraction of reconstructed final candidates for each true mode for events where one of the multiple candidates is truth matched. . . . .	62
6.8	The fraction of reconstructed final candidates for each true mode after the best candidate selection. . . . .	63

7.1	Number of background events from $B\bar{B}$ and continuum Monte Carlo for each final state. . . . .	70
7.2	Breakdown of $B\bar{B}$ background event according to the mother of the high energy photon. . . . .	74
7.3	The number of events, with (true = reco) mode and $m_{\text{ES}}$ in the peaking region (5.27 to 5.29 GeV/ $c^2$ ), passing the full selection in bins of true and reconstructed $M_{\text{Had}}$ . . . . .	81
7.4	The number of events in the peaking $m_{\text{ES}}$ range (5.27 to 5.29 GeV/ $c^2$ ), with (true != reco) mode, passing the full selection in bins of true and reconstructed $M_{\text{Had}}$ . . . . .	82
7.5	$M_{\text{Had}}$ resolution. . . . .	83
7.6	Number of events in the final selection split into signal and cross-feed, then into truth mode categories, then into reconstructed mode categories and finally presented in two bins of low $M_{\text{Had}}$ . . .	87
7.7	Number of events in the final selection split into signal and cross-feed, then into truth mode categories, then into reconstructed mode categories and finally presented in two bins of high $M_{\text{Had}}$ . .	88
7.8	The number of cross-feed events in the peaking $m_{\text{ES}}$ region. . . .	89
8.1	The signal efficiencies. . . . .	92
9.1	Values of the fit function parameters extracted from the fits to the different MC samples. . . . .	99
9.2	Fractions of signal, cross-feed, continuum, and $B\bar{B}$ events, in the toy-data sample over the full $m_{\text{ES}}$ range. . . . .	100
9.3	The Argus shape parameters from a fit to the full MC $B\bar{B}$ and full MC continuum events. . . . .	101
9.4	The Argus shape parameters from a fit to the toy-bb plus toy-continuum events. . . . .	102
9.5	$\chi^2$ values for fits to the $m_{\text{ES}}$ toy-data distribution using either one or two Argus functions. . . . .	103
9.6	Measured fraction of events in the Crystal Ball in the toy-data fits.	104
9.7	Measured and generated signal events in the toy-data. . . . .	105
10.1	The Crystal Ball tail and $\alpha$ parameters. . . . .	110
10.2	The width of the Crystal Ball function in MeV/ $c^2$ . . . . .	111
10.3	The cross-feed Argus shape parameters. . . . .	112
10.4	The cross-feed yield. . . . .	113
10.5	The ( $B\bar{B}$ + continuum) background Argus shape parameters. . .	115
10.6	The $B\bar{B}$ peaking yield. . . . .	116

10.7	$B\bar{B}$ yield from fits to the $B\bar{B}$ or $B\bar{B}$ plus continuum samples. . .	117
10.8	The data yield. . . . .	119
10.9	The yield from the various samples for the <i>all</i> final state category. . . . .	120
10.10	The yield from the various samples for the <i>2-body</i> , <i>3-body</i> and <i>4-body</i> final state categories. . . . .	121
10.11	The yield from the various samples for $\pi$ and $\pi^0$ final state categories. . . . .	122
10.12	The yield from the various samples for $K$ and $K_S$ final state categories. . . . .	123
10.13	The difference in the yields between the sum of <i>2-</i> , <i>3-</i> , <i>4-body</i> , or $\pi$ , $\pi^0$ , or $K$ , $K_s$ final state categories and the <i>all</i> final state category in nine $M_{Had}$ bins. . . . .	124
11.1	The partial branching fraction ( $10^{-6}$ ) for all the different final state categories as a function of $M_{Had}$ . . . . .	133
11.2	The ratios for the $K_S$ and $K$ final state categories as a function of $M_{Had}$ . . . . .	135
11.3	The ratios for the $\pi^0$ and $\pi$ final state categories as a function of $M_{Had}$ . . . . .	136
11.4	Predicted <i>4-body</i> final states for different resonant substructures. . . . .	137
11.5	Parameterization of truncated hadronic multiplicity in signal MC and data. . . . .	139
11.6	Ratios of 2/3-body for $M_{Had}$ above 1.0 GeV/ $c^2$ for data and Monte Carlo. . . . .	139
11.7	Ratio of 4/3-body for $M_{Had}$ above 1.0 GeV/ $c^2$ for data and Monte Carlo. . . . .	139
12.1	Photon systematics . . . . .	143
12.2	Average percent change in data, cross-feed, $B\bar{B}$ yield and systematic error, when changing the fixed Crystal Ball width. . . . .	147
12.3	Average percent change in data, cross-feed, $B\bar{B}$ yield and systematic error, when changing the fixed Crystal Ball width and adjusting the Argus shape parameters. . . . .	148
12.4	Crystal Ball width obtained from fits to Signal Monte Carlo and from fits to cross-feed Monte Carlo. . . . .	149
12.5	Average percent change in data, cross-feed, $B\bar{B}$ yield and systematic error, when changing the fixed Crystal Ball $\alpha$ and tail parameters. . . . .	150
12.6	Percent change in cross-feed and $B\bar{B}$ yield and percent systematic error when changing the fixed Monte Carlo Crystal Ball peak. . . . .	151

12.7	Percent change in data yield and percent systematic error when changing the fixed Crystal Ball peak in the data fits . . . . .	152
12.8	Percent change in data and cross-feed yield and percent systematic error when changing the fixed cross-feed Argus shape. . . . .	153
12.9	Percent change in data yield and percent systematic error when changing the fixed background Argus shape. . . . .	154
12.10	Percent systematic errors from the fitting procedure for the <i>all</i> final state category. . . . .	154
12.11	Percent changes in the yields, efficiency and PBF from varying the $\Delta M_{Had}$ cut in the signal sample definition. . . . .	156
12.12	Comparison of the generated and fit Crystal Ball fraction from a toy-MC sample of $B\bar{B}$ plus continuum. . . . .	157
12.13	The change in the PBF when applying a 20% systematic error to the $B\bar{B}$ yield, after the 10% shift has been applied. . . . .	158
12.14	The corrected signal efficiencies after the data-MC corrections are applied. . . . .	161
12.15	Systematic errors on difference between data and MC efficiencies from data control samples. . . . .	162
12.16	Detection efficiency systematics for each final state using Table 12.15.	162
12.17	The total systematic error in % per each mass bin and for the <i>all</i> final state category due to the smearing and killing factors. . . . .	163
12.18	Signal Efficiency estimated using the $X_s\gamma$ contribution or $K^*\gamma$ . . . . .	164
12.19	Cross-feed yield estimated using the $K^*\gamma$ contribution and $X_s\gamma$ . . . . .	164
12.20	Efficiency difference between the $X_S\gamma$ models KN495 and KN465. . . . .	165
12.21	Percent systematic errors from all the systematic contributions, except the signal modeling, for the <i>all</i> final state category. . . . .	166
12.22	The partial branching fraction ( $10^{-6}$ ) for the different final state categories as a function of $M_{Had}$ using the shifted efficiencies. . . . .	167
12.23	Parameterization of truncated hadronic multiplicity in signal MC and data. . . . .	168
12.24	Ratios of 2/3-body for $M_{Had}$ above 1.0 GeV/ $c^2$ for data and Monte Carlo after systematic corrections. . . . .	168
12.25	Ratios of 4/3-body for $M_{Had}$ above 1.0 GeV/ $c^2$ for data and Monte Carlo after systematic corrections. . . . .	168
12.26	The ratios for the $K_S$ and $K$ final state categories as a function of $M_{Had}$ . . . . .	169
12.27	The ratios for the $\pi^0$ and $\pi$ final state categories as a function of $M_{Had}$ . . . . .	169

12.28	The partial branching fraction ( $10^{-6}$ ) for the <i>all</i> final state category as a function of $M_{Had}$ using the shifted efficiencies and showing the statistical and systematic errors. . . . .	169
13.1	Ratio of the $\pi^0$ weighted efficiency and the original efficiency in %.	175
13.2	Ratio of the $\pi^0$ and 2 body weighted efficiency and the original efficiency in %.	176
13.3	Ratio of the $\pi^0$ (two iterations) and 2 body weighted efficiency and the original efficiency in %.	178
13.4	The width of the CB function for the signal events after the weights are applied, in $\text{MeV}/c^2$ .	179
13.5	The x-feed Argus shape parameters after the weights are applied.	181
13.6	The weighted signal efficiencies (%).	183
13.7	WPBR (in $10^{-6}$ ) results after the weights are applied.	184
13.8	Parameterization of truncated hadronic multiplicity in signal MC and data after the weights are applied.	184
13.9	Ratios of 2/3-body for $M_{Had}$ above $1.0 \text{ GeV}/c^2$ for data and Monte Carlo after weights are applied.	186
13.10	Ratios of 4/3-body for $M_{Had}$ above $1.0 \text{ GeV}/c^2$ for data and Monte Carlo after weights are applied.	186
13.11	The ratios for the $K$ and $K_S$ final state categories as a function of $M_{Had}$ . The $\pi^0$ (two iterations) and 2 body weight is applied.	186
13.12	The ratios for the $\pi^0$ and $\pi$ final state categories as a function of $M_{Had}$ . The $\pi^0$ (two iterations) and 2 body weight is applied.	187
13.13	The weights used along with their statistical errors, listed according to category and in the order applied.	187
13.14	The percent change of the signal efficiencies obtained with the weights changed by plus or minus 1 sigma.	188
13.15	The weighted partial branching fractions with statistical and systematic errors for the <i>all</i> final state category.	188
14.1	Table showing the conversion between recoil hadronic mass and $E_\gamma^B$ , the photon energy in the B rest frame. The units are GeV.	190
14.2	Cross-feed efficiencies (in %) for the <i>all</i> final state category, in $200 \text{ MeV}/c^2$ bins of the hadronic mass.	191
14.3	The $f_i$ s in percent, at the generator level, for the <i>all</i> final state category, in $200 \text{ MeV}/c^2$ bins of the hadronic mass.	192
14.4	Percent generator missing fractions.	193
14.5	Inclusive Branching Fraction . . . . .	195

14.6 Cumulative Inclusive Branching Fraction in $10^{-6}$ . . . . .	196
14.7 Published measurements of the inclusive rate $b \rightarrow s\gamma$ . . . . .	196

## Abstract

Study of  $b \rightarrow s\gamma$  at *BABAR* using the sum of exclusive modes.

by

Teela Marie Pulliam

The electromagnetic penguin process  $b \rightarrow s\gamma$  is very interesting to theorists because it can be used to constrain contributions from new physics that could enter at the one loop level. The high statistics of  $B\bar{B}$  events collected at the *BABAR* experiment make a measurement of this rare decay possible. The branching fraction of a sum of exclusive  $b \rightarrow s\gamma$  decay modes is measured as a function of the strange hadronic mass. This is a large step toward the measurement of the  $b \rightarrow s\gamma$  rate.

For Tom and Carol.

## Acknowledgements

It's late. I started late in the day and will (hopefully) finish early tomorrow. All this is possible only because my mother taught me that it never is too late in the day to start something. And gosh it has been a long journey. Somehow my whole academic career started with someone asking me every night at the dinner table, "Did you do your homework?" I thought I would strangle him if he didn't stop asking me that, but somehow he has survived.

Then there were many stops along the way. Jason inspired me to work hard during the week and then I might manage to take the weekend off. That didn't always work for me (but did for him). Maybe some day I will be able to manage my time better. (Not working on the weekends sounds like a good thing to practice as a post-doc.)

And Hartmut jumped up and down and up and down as many times as there were plots to show him, although usually it ended with "Thats all wrong... do it again," but, it did not matter, because he would jump again the next time.

Bill and Alec, wow, they used to heat up the lab with their political discussions. It was a welcome distraction to debugging some test stand or beeping a board (but it was Tim who was the king of beepers). Everything changes. No more fights. Now they agree probably too well and can both retire, although not stay idle. Bill has promised to some day figure out that consciousness thing.

Then there was Sumita and Risa and many days and nights full of homework. Three heads were certainly better than one. It was a time of new friends and new loves. And lots of beer and glasses for our cupboard, thanks to Riko. Riko, who not only could answer any Paw questions I had, but also held mandatory relaxation sessions at the clinic known as 99. Somehow it turned from beer and bagel nights into movies and knitting nights, but two good friends stayed the same or even got better (timandsumita).

And then comes BaBar and commuting (or was it computing?) and Max. If Kim hadn't expected him home every night at a reasonable hour I think we might still be sitting in that tiny office in 280 with only one computer. From Max I learned how efficient I should be, and that a good nights rest should come very high on the list of things to accomplish.

And the journey would not have ended (or at least not as nicely) without Francesca, after whom I seem to be always following.

Where did I learn some physics along the way? Why, from Bruce, who was always supportive and from Steve who's many many ideas got us through the rough times.

And thanks to Jürg and David, who banished me from the office until this monster was written, and always had good advice (and cookies from Suzanne

and little Tania's to cuddle). And there was Michael with a smile and a fresh-mozzarella sandwich.

And thanks Melissa for the special card and for making me feel... good.

And this year, besides being one for finishing, was one of new beginnings thanks to Troy and Briana, Merle Lynne and Moana.

Und wer noch? Thanks to Wilko who was always understanding and took care of most everything (including me) when needed.

And where will things go now? Who can say, but this, at least, is done.

# Chapter 1

## Introduction

A child is naturally driven to explore the world around them and to ask questions of everyone. The ever present “Why?” that can drive parents to distraction is a fundamental tool a child uses to learn and to assert themselves in their small universe of experience. As scientists we are driven to continue to ask fundamental questions about our universe. It is our privilege and responsibility to play the child and with every answer found turn right back around and ask another question.

### 1.1 The Standard Model

Particle physics addresses the question: “What is matter made of?” The Standard Model represents the current status of the answer. It describes the fundamental particles and their interactions. By fundamental particles we mean the basic building blocks of matter, structureless point-like particles. There are two classes of fundamental particles, quarks and leptons, and three forces through which they interact <sup>1</sup>: strong, weak and electromagnetic (EM). Table 1.1 lists the elementary particles along with the gauge bosons that mediate their interactions. For each quark and lepton listed in the table there exists a corresponding anti-particle which has the same mass and spin, but opposite charge. There are three “generations”, or pairs, of quarks and leptons.

The first generation, up and down quarks and electrons, are the stable particles which make up the immediate world around us. Up and down quarks are bound together by the strong force to make protons (uud) and neutrons (udd).

---

<sup>1</sup>Gravity is not (yet) incorporated into the Standard Model and is assumed to be too weak to significantly effect the interaction of particles.

Protons and neutrons are subsequently bound together by the same strong force, forming nuclei. The electromagnetic force binds nuclei and electrons together to make atoms, which are what we, and everything we see, are made of. The weak force is responsible for processes such as the conversion of a neutron to a proton, known as  $\beta$  decay. Combinations of quarks, in twos (mesons) or threes (baryons), make up a zoo of particles called hadrons. These heavy hadrons are unstable and therefore, even when created in a collider experiment, decay very quickly.

	spin	charge
Quarks		
u (up)	1/2	+2/3
d (down)	1/2	-1/3
c (charm)	1/2	+2/3
s (strange)	1/2	-1/3
t (top)	1/2	+2/3
b (bottom)	1/2	-1/3
Leptons		
e (electron)	1/2	-1
$\nu_e$ (neutrino)	1/2	0
$\mu$ (muon)	1/2	-1
$\nu_\mu$ (neutrino)	1/2	0
$\tau$ (tau)	1/2	-1
$\nu_\tau$ (neutrino)	1/2	0
Gauge Bosons		
$\gamma$ (photon) [EM]	1	0
$W^\pm, Z$ [weak]	1	$\pm 1, 0$
$g$ (gluon) [strong]	1	0

Table 1.1: Elementary particles and gauge bosons. For each quark and lepton there exists an anti-particle which has the same mass and spin, but opposite charge.

The Standard Model can be used to predict experimentally measurable quantities, such as particle decay rates. Many experiments have been carried out to test its predictions, and so far none have found any large discrepancies. Therefore, it is considered a well accepted model, but it does not explain all the observed phenomena. For example, it can not explain the baryon asymmetry of the universe [1]. In the early universe we believe there was an equal amount

of matter and anti-matter. As the universe expanded and cooled something happened that caused an imbalance. CP violation is an essential part of the mechanism that can cause this. CP violation is the breaking of the combined charge (C) and parity (P) symmetries, and allows for different decay rates between particles and their anti-particles. Only a small amount of CP violation is allowed in the standard model, and the baryon asymmetry produced is too small by many orders of magnitude to have caused a matter dominated universe. There are many models which provide extensions to the standard model to address issues such as this. Often these extensions introduce new particles which can change the rate of rare processes, such as  $b \rightarrow s\gamma$ .

## 1.2 BF( $b \rightarrow s\gamma$ )

The  $b \rightarrow s\gamma$  transition proceeds through the electroweak penguin diagram shown in Figure 1.1. The photon can be radiated from the internal quark line as well as from the  $W$  loop as shown in the figure. In the Standard Model there is no direct coupling between the bottom and strange quark and therefore this transition can happen, at lowest order, only through one-loop diagrams. The  $b$  quark radiates a  $W$  boson and changes flavor. The  $W$  boson is then re-absorbed and the quark changes flavor again. A top quark in the loop gives the largest contribution to the amplitude since it has the strongest coupling to the bottom quark. The Cabbibo-Kobayashi-Maskawa (CKM) matrix elements give the order of the coupling;  $V_{tb}$ , is of order 1, while  $V_{cb}$  and  $V_{ub}$  are very small. Within the Standard Model the  $b \rightarrow s\gamma$  transition has a relatively large rate compared to other loop processes due to the massive top quark in the loop.

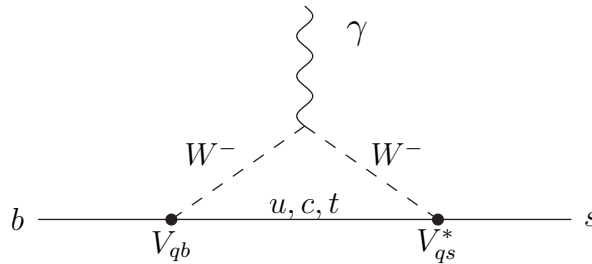


Figure 1.1: The “penguin” diagram for the process  $b \rightarrow s\gamma$ .  $V_{qb}$  and  $V_{qs}^*$  are the CKM matrix elements which give the order of the quark coupling, where  $q = u, c, t$ .

There has been a lot of interest in the possibility that the amplitude may be modified by non-Standard Model physics, e.g. super-symmetry, left-right sym-

metric models, two Higgs doublets, or extra generations [2]. These introduce additional particles which can replace the  $W$  and/or  $t$  in the loop, and therefore generate additional diagrams which change the decay amplitude. The  $b \rightarrow s\gamma$  rate is especially sensitive to this effect since its first order diagram is at loop level and therefore any new diagrams are likely to have contributions on the same order.

The Standard Model rate has been calculated to next-to-leading order by Chetyrkin, Misiak and Münz [3],  $BF(b \rightarrow s\gamma) = (3.28 \pm 0.33) \times 10^{-4}$ . The most recent calculation (2001) by Gambino and Misiak [4] is:

$$BF(b \rightarrow s\gamma) = (3.60 \pm 0.30) \times 10^{-4}.$$

This calculation includes a different treatment of the charm-loop contributions, although there is some disagreement over the value of the effective charm mass used.

The general framework for the calculation of the  $b \rightarrow s\gamma$  branching fraction is provided by heavy-quark effective theory (HQET). The theoretical analysis of  $B \rightarrow X_s\gamma$  also relies on the assumption of quark-hadron duality, which says that the inclusive  $B$  meson decay into hadrons and the photon is well approximated, at the 10% level, by the corresponding partonic decay rate. The energy released into the final state by the decay of the heavy b-quark is large compared to the QCD scale and therefore the final states are not necessarily dominated by sharp resonances, but rather can be described by a non-resonant spectrum. There then can be a factorization between the short-distance part of the decay (the disappearance of the b-quark) and the long-distance part (the hadronization of the decay products). For inclusive quantities it is enough to consider the short-distance part of the decay.

The  $B \rightarrow X_s\gamma$  rate is usually normalized to that for the semileptonic rate, which eliminates a strong dependence on the b-quark mass:

$$BF(B \rightarrow X_s\gamma) \equiv \frac{\Gamma(B \rightarrow X_s\gamma)}{\Gamma(B \rightarrow X_c e \bar{\nu}_e)} \cong \frac{\Gamma(b \rightarrow s\gamma)}{\Gamma(b \rightarrow c e \bar{\nu}_e)} BF(B \rightarrow X_c e \bar{\nu}_e), \quad (1.1)$$

The parton level widths are calculated in the spectator model including corrections for short-distance QCD effects. The perturbative QCD corrections are important and introduce large logarithms which are resummed and enhance the rate by a factor of 2-3.

### 1.3 $b \rightarrow s\gamma$ Spectrum

In the  $B$  meson decay system  $B \rightarrow X_s\gamma$  is a two body decay. The photon energy spectrum in this system is given by the kinematic equation:

$$E_\gamma^B = \frac{M_B^2 - M_{Had}^2}{2M_B}, \quad (1.2)$$

where  $E_\gamma^B$  is the photon energy,  $M_{Had}$  the hadronic mass of the  $X_s$ , and  $M_B$  the  $B$ -meson mass.

Experimentally, the full spectrum is not accessible. As discussed further in the next section, the low energy portion of the photon spectrum is populated by large backgrounds and is therefore hard to measure. A good theoretical understanding of the spectral shape is needed since experimentally only a portion of the spectrum is measured. The theory must give a prediction in order to extend the measured spectrum over the full phase space.

The spectral shape is determined by the ‘‘Fermi motion’’ of the  $b$  quark inside the  $B$  meson which can be consistently described by taking a convolution of the parton model predictions for the spectrum with a universal shape function [5],[6]. This is done within the framework of HQET, and the spectral shape is a function of the HQET parameters  $m_b$  and  $\lambda_1$ . The shape of the photon spectrum is determined by QCD dynamics and will not be affected by new physics contributions beyond the standard model. Our modeling of the spectral shape is discussed in detail in next chapter.

In addition, a fit to the experimental  $b \rightarrow s\gamma$  spectrum can provide a measurement of the HQET parameters, which can then be used in the extraction of  $V_{ub}$  from the experimental measurements of  $b \rightarrow ul\nu$  decays [7].

Note that because of the two body nature of the  $b \rightarrow s\gamma$  decay, the spectrum can be equivalently described in terms of  $E_\gamma$  or the hadronic mass of the  $X_s$ ,  $M_{Had}$ . The equation above gives the kinematic formula relating the two.

## 1.4 Measuring $b \rightarrow s\gamma$ at *BABAR*

### 1.4.1 Backgrounds

The photons from the  $B \rightarrow X_s\gamma$  decays are quite high energy which provides a clean experimental handle to single out this mode in generic  $B$  meson decays. The photon energy spectrum has a peak around 2.4 GeV and a tail which extends below 1.8 GeV. Backgrounds which produce photons in this energy range are

mostly from initial state radiation (ISR) or continuum events where a  $\pi^0$  or  $\eta$  decay very asymmetrically into two photons. These backgrounds can be reduced using event shape variables and  $\pi^0$  or  $\eta$  vetoes, or by subtracting expectations from data taken below the  $B$  meson production threshold.

Another category of backgrounds comes from generic  $B\bar{B}$  decays where, again, the high energy photon comes from an asymmetric  $\pi^0$  or  $\eta$  decay. These backgrounds are harder to handle and limit our ability to measure the full  $b \rightarrow s\gamma$  spectrum. They are found to have a large contribution, on the same order as the signal, at the low end of the photon energy spectrum.

## 1.4.2 Methods

There are two approaches to measuring the  $b \rightarrow s\gamma$  branching fraction and spectrum. The first is a fully inclusive approach where only the photon is selected and the  $X_s$  system is not at all reconstructed. The other is a semi-inclusive approach, where the photon is selected but then a number of  $X_s$  exclusive modes are fully reconstructed. These two approaches are complementary and can eventually be combined to make best use of the data. For the moment, in *BABAR*, they are investigated separately. The semi-exclusive approach is what is described in this document. Both methods are described briefly below.

### Fully Inclusive Method

The simplest approach to measuring the  $B \rightarrow X_s\gamma$  branching fraction and spectrum is a fully inclusive approach. The high energy photon is selected, but the hadronic system, the  $X_s$  is not reconstructed. Event shape variables are used to suppress the continuum backgrounds. One idea to improve the continuum background subtraction is to use a lepton tag. This means to require a high a high energy lepton, presumably from the other  $B$ , in the event. This signature is more characteristic of  $B\bar{B}$  decays than continuum events and therefore will help to suppress continuum backgrounds. The disadvantage of the method is that it is not very efficient and will greatly reduce the statistics in the signal but also get rid of almost all of the continuum background. There is no equivalent trick to use to suppress the  $B\bar{B}$  backgrounds which dominate at low  $E_\gamma$ . Usually simply a cut is applied on the  $E_\gamma$  spectrum to exclude the region where the background dominates.

The  $E_\gamma$  spectrum can be measured by counting signal events in bins of  $E_\gamma$ . The branching fraction can then calculated in each bin, correcting for the signal efficiency obtained from signal MC. The spectrum can be fit to obtain a mea-

surement of the theoretical model parameters and to allow for an extrapolation to  $E_\gamma$  below what is measured.

One limitation of this method is the experimental resolution of the photon energy. *BABAR* is an asymmetric B-factory, which means that the  $B$  mesons are not created at rest in the  $\Upsilon(4S)$  rest frame and therefore there is an experimental smearing of the photon energy spectrum on the order of 150 MeV.

This approach is elegant, but statistics limited. The  $E_\gamma$  spectrum is model dependent, while the branching fraction, which is the integral over the spectrum, is not. In an ideal fully inclusive analysis, the full spectrum is measured and the selection has a uniform efficiency over the full  $E_\gamma$  range. Therefore, a model independent measurement of the branching fraction is obtained. In practice, a cut on  $E_\gamma$  introduces model dependence when the measured spectrum is extrapolated over the full phase space. With high statistics and more understanding of the  $B\bar{B}$  backgrounds the cut on  $E_\gamma$  can be reduced to include more of the spectrum, and to reduce the model dependence.

### Semi-inclusive Method

A semi-inclusive analysis includes the same photon selection as the fully inclusive method, but then reconstructs a number of exclusive final states of the  $X_s$ . This is effectively a tighter selection and therefore there is less background to contend with.

Event shape variables can be used to suppress the continuum backgrounds.  $B\bar{B}$  backgrounds usually have to be estimated from the Monte Carlo and subtracted. Events are required to be reconstructed in one of the exclusive modes. Quality cuts on the daughter candidates also reduce backgrounds, although an additional background contribution comes from wrongly reconstructed signal events.

As described above, the  $B \rightarrow X_s \gamma$  decays are distributed over a spectrum which can be described in terms of the photon energy or  $X_s$  hadronic mass,  $M_{Had}$ . Since this is a two-body decay process, the photon energy spectrum and the recoil hadronic mass spectrum give equivalent information. In a semi-inclusive analysis we can measure the recoil hadronic mass spectrum instead of the photon energy spectrum. We can convert this to an equivalent photon energy spectrum using the kinematic equation 1.2. The hadronic mass resolution can be an order of magnitude better than the smeared photon energy spectrum resolution discussed in the previous section. This allows for a better measurement of the spectrum shape.

The hadronic mass spectrum can be measured in bins of  $M_{Had}$ . Due to sta-

tistical and background subtraction limitations the measured spectrum must be restricted. The background subtracted data yield in each bin must be corrected for the signal efficiency, estimated from signal Monte Carlo, to obtain the partial branching fraction. These are not the inclusive branching fractions since they are measured with respect to the reconstructed final states only. Therefore the spectrum must first be corrected for the fraction of the total  $X_s$  final states that the measured final states represent. The corrected spectrum then can be fit to extract the theoretical model parameters and extrapolated over the full spectrum to provide a measurement of the inclusive  $b \rightarrow s\gamma$  branching fraction.

This approach is more model dependent than the fully inclusive one. There is a large uncertainty in the correction of the partial branching fractions due to limited understanding of the distribution of the  $X_s$  final states. There is little experimental knowledge of the higher resonance or non-resonant contributions at high hadronic mass and therefore the Monte Carlo is not necessarily a good model of the data there.

In this document we will present results up to the partial branching fractions. This is the experimentally measurable quantity. The correction to this spectrum, to extract the inclusive branching fraction and model parameters, will be discussed and some preliminary results will be presented. The treatment of the model dependent errors will not be dealt with here. A complete treatment is under discussion within the *BABAR* experiment.

## 1.5 Other Measurements

The original measurement of the branching fraction by CLEO [8] has been replaced by newer results based on the full CLEO II data sample of  $9.2 \text{ fb}^{-1}$  of on-resonance and  $4.6 \text{ fb}^{-1}$  of off-resonance data [9].

Confirmation of the CLEO result came from an analysis by ALEPH in 1998 [10], and BELLE has recently published their initial result based on  $6 \text{ fb}^{-1}$  [11] using a semi-exclusive method which is very similar to the method presented in this document.

All these results are summarized in Table 1.2, where the first error is the statistical error, and the second (and third) errors give the systematic uncertainties, including model dependence where this is quoted separately. So far, there is no discrepancy seen between the measured branching fraction and the standard model prediction listed above.

The CLEO analysis is quite advanced and uses a combination of both the fully inclusive and semi-inclusive methods. CLEO is also the only experiment to

Experiment	$\text{Br}(b \rightarrow s\gamma) \times 10^{-4}$
CLEO 2001 [9]	$3.21 \pm 0.43 \pm 0.27^{+0.18}_{-0.10}$
ALEPH 1998 [10]	$3.11 \pm 0.80 \pm 0.72$
BELLE 2001 [11]	$3.36 \pm 0.53 \pm 0.42 \pm 0.52$
Unofficial World Average	$3.24 \pm 0.34 \pm 0.35$

Table 1.2: Published measurements of the inclusive rate  $b \rightarrow s\gamma$ .

determine information about the spectral shape so far [9]. They use an inclusive analysis of the gamma energy spectrum to measure the HQET parameters.

The *BABAR* results presented in this document are made on a  $21fb^{-1}$  sample from the first year of data taking. We expect results with statistical and systematic errors comparable to BELLE. Our background subtraction is not as efficient as BELLE's and therefore we do not gain much from our higher statistics.

A more detailed comparison between CLEO, BELLE and *BABAR* results is presented in Section 14.4.

## 1.6 Outline

This document is organized as follows. In Chapter 2 we describe in more detail the theoretical model behind our measurement. In Chapter 3 we give a brief description of the BaBar experiment and highlight the components of the detector most relevant for this analysis. In Chapter 4 we present a short summary of the analysis method, outlining the important issues and methods. In Chapter 5 we list the data and Monte Carlo samples used in the analysis. In Chapter 6 we describe the event selection used to pick out our signal events and reduce backgrounds. In Chapter 7 we examine the three background sources, continuum,  $B\bar{B}$  and cross-feed events. In Chapter 8 we present the results for the Monte Carlo signal efficiency after the event selection. In Chapter 9 we present the background subtraction method and in Chapter 10 we list the results of the fits to data and Monte Carlo. In Chapter 11 we combine the signal yield and efficiency to obtain results for the partial branching fraction, meaning the branching fraction with respect to the twelve exclusive final states which are reconstructed, as a function of hadronic mass. In Chapter 12 we discuss the systematic errors on the partial branching fractions. In examining the partial branching fraction results we find that there are significant differences between the data and Monte Carlo fragmentation. In Chapter 13 we describe a method

for weighting the Monte Carlo events to force the fragmentation to better match that of the data. This adjusts the partial branching fractions results. The weighted partial branching fraction spectrum is the experimental result which we present.

We then discuss a method to convert this to inclusive branching fractions by weighting the partial branching fractions by a factor to account for the rest of the  $b \rightarrow s\gamma$  final states which are not reconstructed. We sum this spectra over our measured hadronic mass range, and then extrapolate it to the full spectrum, to produce a result for the inclusive branching fraction for  $b \rightarrow s\gamma$ . We present these preliminary results in Chapter 14, as well as a comparison with previous results. In Chapter 15 we give our final conclusions.

# Chapter 2

## Signal Model

The signal for  $b \rightarrow s\gamma$  is modeled as the sum of resonant and non-resonant contributions. In the simplest version, which we use in this analysis, only the  $K^*(892)$  resonance is considered as a separate contribution, with higher resonances being taken as part of the non-resonant model.

### 2.1 Resonant contributions

The decay  $B \rightarrow K^*(892)\gamma$  has been measured by CLEO [12], BELLE [13] and BABAR [14], to have an average branching fraction of  $(4.2 \pm 0.7 \pm 0.3) \times 10^{-5}$  (which is the average of  $(4.6 \pm 0.6 \pm 0.3) \times 10^{-5}$  and  $(3.8 \pm 0.8 \pm 0.3) \times 10^{-5}$ , the branching fractions for the neutral and charged mode respectively) which corresponds to 13% of the inclusive rate, taking the ratio of the measured exclusive and inclusive branching fractions, as listed in Table 1.2. We note that the exclusive branching fraction is not well predicted by theory because it requires the difficult calculations of hadronic form factors. In fact recent calculations give values of  $\approx 7 \times 10^{-5}$  which are large compared to the experimental measurement [15].

There are also preliminary results from CLEO and BELLE for the decay  $B \rightarrow K_2^*(1430)\gamma$  [12, 16]. There are many more higher resonances which have not been measured, although the rates have been predicted by theory. For example, the predictions of Veseli and Olsson [17] can be seen in Table 2.1 listed in percent of the inclusive rate. The two measured rates are also shown. Note that the theoretical predictions for the resonant contributions do not account for the full inclusive rate. This is because a large fraction of the rate for hadronic masses above 1 GeV/ $c^2$  is expected to be non-resonant.

Exclusive mode	Veseli & Olsson	Experiment
$K^*(892)$	$(16.8 \pm 6.4)\%$	$(13 \pm 4)\%$
$K_1(1270)$	$(4.3 \pm 1.6)\%$	
$K_1(1400)$	$(2.1 \pm 0.9)\%$	
$K^*(1410)$	$(4.1 \pm 0.6)\%$	
$K_2^*(1430)$	$(6.2 \pm 2.9)\%$	$(5 \pm 3)\%$
$K_2(1580)$	$(1.7 \pm 0.4)\%$	
$K_1(1650)$	$(1.7 \pm 0.6)\%$	
$K^*(1680)$	$(0.5 \pm 0.2)\%$	
Total	$(37.3 \pm 13.6)\%$	–

Table 2.1: Predicted contributions from exclusive modes to the  $b \rightarrow s\gamma$  final states.

## 2.2 Non-resonant contribution to $b \rightarrow s\gamma$

The general framework for the  $B \rightarrow X_S\gamma$  decay calculations is provided by the Heavy-Quark Effective Theory (HQET). In HQET the hadron is considered as composed of a heavy quark,  $b$ , and “light-degrees of freedom” consisting of quarks anti-quarks and gluons. The Lagrangian is written as an expansion in terms of  $1/m_b$  taking the limit  $m_b \rightarrow \infty$ . The leading order corresponds to an expansion up to  $1/m_b$  terms, and the first corrections appear at the  $O(1/m_b^2)$ .

The full next-to-leading order calculation of the  $B \rightarrow X_S\gamma$  branching fraction in the Standard Model was only completed in 1997, bringing down the theoretical uncertainty from 30% to about 10%. In 1998, Kagan and Neubert [5] provided a study of “Fermi motion” effects in a full next-to-leading order calculation. The Fermi motion of the  $b$ -quark inside the  $B$ -meson determines the characteristic shape of the photon spectrum. It can be described by the convolution of the parton model prediction for the spectrum with a universal shape function which determines the light-cone momentum,  $k_+$ , distribution of the  $b$ -quark in the  $B$ -meson,  $F(k_+)$ . This convolution transforms the phase-space boundaries defined by parton kinematics into the proper physical boundaries defined by hadron kinematics. The “Fermi-motion” fills the gap between the parton model spectrum endpoint of  $m_b/2$  to the physical endpoint at  $m_B/2$ .

The shape function is a universal, i.e. process independent, characteristic of the  $B$ -meson since it is derived assuming an inclusive decay spectra in processes with mass-less partons in the final state, such as  $B \rightarrow X_s\gamma$  and  $B \rightarrow X_u\gamma$ , where the  $s$ - and  $u$ -quark can be considered massless. Given the poor knowledge

of the gamma spectrum moments, Kagan and Neubert adopt an exponential distribution which depends on just the first and second moments of the spectrum, i.e. the mean and width of the distribution, although other parameterizations have been suggested in the literature. The formula is:

$$F(k_+) = (1 - x)^a e^{(1+a)x}; \quad x = \frac{k_+}{\bar{\Lambda}} \leq 1, \quad (2.1)$$

where  $\bar{\Lambda} = m_B - m_b$  is the energy contributed by the light-degrees of freedom. The two free parameters are preferably taken as the effective b-quark mass,  $m_b$ , sensitive to the mean gamma energy (or first moment), and a parameter,  $\lambda_1 = -\mu_\pi^2$ , where  $\mu_\pi^2$  is related to the kinetic energy of the b-quark inside the  $B$  meson. Therefore,  $\lambda_1$  is directly proportional to width of the gamma energy spectrum (the second moment). The parameters  $\lambda_1$  and  $m_b$  are not totally independent, naively it might be expected that  $\lambda_1$  increases as  $m_b$  decreases. Reasonable ranges for the two parameters are: 4.55 to 4.95 GeV for  $m_b$  and -0.5 to -0.2 GeV<sup>2</sup> for  $\lambda_1$ .

The spectrum can be described equivalently in terms of the photon energy or the hadronic mass of the  $X_s$  system. The relation between the two spectra can be derived from kinematics:

$$E_\gamma^B = \frac{M_B^2 - M_{Had}^2}{2M_B}, \quad (2.2)$$

where  $E_\gamma^B$  is the photon energy,  $M_{Had}$  the hadronic mass and  $M_B$ , the  $B$ -meson mass. In the following we will concentrate our discussion on the hadronic mass spectrum, since that is what we will directly measure.

It's important to note that the spectrum does not show a strong dependence on the choice of the shape function, as we can see from the hadronic mass and energy photon spectrum for three different shape functions in Figure 2.1. However, the spectrum does depend strongly on  $m_b$  and  $\lambda_1$ . Figure 2.2 shows the hadronic mass and photon energy spectrum for three different values of  $m_b$  and  $\lambda_1$ .

It is necessary to recall that the theoretical predictions for the photon energy and hadronic mass spectra must be understood in terms of quark-hadron duality. This is possible since the decay of the heavy b-quark releases enough energy into the system such that the resulting final states are not necessarily dominated by sharp resonant structures. This allows for a factorization between the short-distance contributions coming from the decay of the b-quark and the long-distance contributions coming from the hadronization of the decay products.

This factorization implies that for inclusive quantities it is enough to consider only the short-distance part.

The true hadronic mass spectrum in the low-mass region may have resonance structures, and therefore may look quite different than the predicted spectrum. To account for this two regions are considered, as discussed in the next section, one consisting of the  $K^*\gamma$  resonance and the other including the higher resonances and the non-resonant contributions.

## 2.3 Signal Shape

Both the resonant and non-resonant descriptions contribute to the  $b \rightarrow s\gamma$  spectrum. The  $K^*\gamma$  peak is quite narrow and at a low hadronic mass (high photon energy) where it can be cleanly measured. Therefore, it is the one resonance that we will consider separately.

According to Kagan and Neubert [5], the hadronic mass spectrum for  $b \rightarrow s\gamma$  can be described by a Breit–Wigner for  $K^*(892)$  and a continuum for the higher resonances and the non-resonant contributions. The higher resonances have widths exceeding the level spacing among them, and hence are overlapping, and therefore can be included in the non-resonant continuum. A sharp cut-off mass is defined where a transition is made between the  $K^*$  resonance and the non-resonant model. The ratio of  $K^*(892)\gamma$  to the non-resonant  $b \rightarrow s\gamma$ , as well as the cut-off mass, depend on the input parameters,  $m_b$  and  $\lambda_1$ . This transition region will be examined as part of the Monte Carlo model systematic studies.

In this analysis we use one non-resonant ( $X_s\gamma$ ) Monte Carlo signal sample generated using the Kagan and Neubert recipe with an exponential shape,  $m_b = 4.65$  GeV,  $\lambda_1 = -0.3$  GeV<sup>2</sup>, and a cut-off mass of 1.0 GeV/ $c^2$ . This gives a ratio between  $K^*(892)$  and  $X_s\gamma$  of about 13%. This one sample is used throughout the analysis to calculate the signal efficiencies and subtract combinatoric backgrounds. We are able to use only one sample in our measurement of the hadronic mass spectrum since most of the quantities derived from the signal Monte Carlo are not dependent on the values of the model parameters when looking in hadronic mass bins.

The shape of the spectrum varies with varying model parameters, and therefore so does the magnitude of the signal in individual bins of hadronic mass. However, this does not affect the signal efficiency per bin since it is normalized to the number of generated events in each bin. The fragmentation (as seen in the next section) also does not depend on the model parameters. We assume, therefore, that our measured spectrum is not model dependent, although we do quote

a systematic on the overall efficiency comparing two sets of model parameters.

Figure 2.3 shows the hadronic mass spectrum generated by the above Kagan and Neubert recipe.

## 2.4 $X_S$ final states

Depending on the charge of the  $B$  meson, the non-resonant part of the inclusive final state,  $B \rightarrow X_S \gamma$ , is made up of  $(s, \bar{d})$  or  $(s, \bar{u})$  quarks plus the photon.

Table 2.2 shows some of the final states of the  $X_S$  resulting from hadronization by JetSet [18]. The twelve channels used in our analysis are listed, for  $B^0$  and  $B^+$  separately. The final states are also labeled by category. The final state categories, which will be used later in the analysis, are defined as follows:

- *all*: Includes 12 final states with one kaon and one, two or three pions, where only one of the pions is allowed to be neutral and the kaon is a k-short or charged. These are the 12 final states used to reconstruct candidates in this analysis.
  - the *all* category can be split in terms of hadronic multiplicity:
    - \* *2-body*: Includes 4 final states with one kaon and one pion.
    - \* *3-body*: Includes 4 final states with one kaon and two pions, where only one pion can be neutral.
    - \* *4-body*: Includes 4 final states with one kaon and three pions, where only one pion can be neutral.
  - or in terms of states with only charged or charged and neutral pions:
    - \*  $\pi$  : Includes 6 final states with one kaon and one, two or three charged pions.
    - \*  $\pi^0$ : Includes 6 final states with one kaon and one, two or three pions, where one pion is neutral.
  - or in terms of states with charged kaons or k-shorts:
    - \*  $K$ : Includes 6 final states with a charged kaon and one, two or three pions, where only one pion can be neutral.
    - \*  $K_S$ : Includes 6 final states with a k-short and one, two or three pions, where only one pion can be neutral.
- *5-body*: Includes 4 final states with one kaon and four pions, where only one pion can be neutral.

- *6-body*: Includes 4 final states with one kaon and five pions, where only one pion can be neutral.
- $2\pi^0$ s: Includes 8 final states with one kaon and two to five pions where two of the n-pions are neutral.
- *sss*: Includes 4 final states with three kaons.
- *other*: Includes everything not listed above, e.g. states with k-longs, higher than 6-body multiplicity or more than two  $\pi^0$ s.

Note that the sum of the *2,3,4-body* categories is the same as the *all* category. The same is true for the sum of the  $\pi$  and  $\pi^0$  or the sum of the  $K$  and  $K_S$  categories. We do not consider final states with  $K_L$ s.

The fragmentation of the quarks for the non-resonant part is made using the standard version of JetSet. We wish to emphasize the following points:

- The fragmentation of a hadronic system with a particular mass is independent of the modeling of the hadronic mass spectrum. Specifically it does not depend on  $m_b$  and  $\lambda_1$ , as seen in Table 2.4 and discussed below.
- Differences between the fractions of final states contributing to the total inclusive rate depend both on the fragmentation and on the hadronic mass spectrum. At masses of  $1 \text{ GeV}/c^2$ , the 2-body channels dominate, but as the hadronic mass increases the fraction of higher multiplicity events increase. This can be seen in Table 2.4 and is discussed below.
- There is a significant difference in reconstruction efficiency as a function of the number of pions in the final state. There are also effects due to the differences in detection efficiency between  $K_s : K^+$  and  $\pi^0 : \pi^+$ . These efficiency differences lead to a significant decrease of the experimental efficiency with increasing hadronic mass. This is discussed in the end of Chapter 8.
- We do not know if the fragmentation is correctly modeled by JetSet. This is something that we check using data. We find that there are significant differences between data and Monte Carlo, and correct the Monte Carlo to account for them. This is discussed in the end of Chapter 11 and the Monte Carlo weighting procedure is detailed in Chapter 13.

$B^0\bar{B}^0$		$B^+B^-$	
Mode	categories	Mode	comment
$K\pi$	<i>2-body</i> , $\pi$ , $K$	$K\pi^0$	<i>2-body</i> , $\pi^0$ , $K$
$K_S\pi^0$	<i>2-body</i> , $\pi^0$ , $K_S$	$K_S\pi$	<i>2-body</i> , $\pi$ , $K_S$
$K\pi\pi^0$	<i>3-body</i> , $\pi^0$ , $K$	$K_S\pi\pi^0$	<i>3-body</i> , $\pi^0$ , $K$
$K_S\pi\pi$	<i>3-body</i> , $\pi$ , $K_S$	$K\pi\pi$	<i>3-body</i> , $\pi$ , $K$
$K_S\pi^0\pi\pi$	<i>4-body</i> , $\pi^0$ , $K_S$	$K_S\pi\pi\pi$	<i>4-body</i> , $\pi$ , $K_S$
$K\pi\pi\pi$	<i>4-body</i> , $\pi$ , $K$	$K\pi^0\pi\pi$	<i>4-body</i> , $\pi^0$ , $K$
$K\pi\pi\pi\pi^0$	<i>5-body</i>	$K_S\pi\pi\pi\pi^0$	<i>5-body</i>
$K_S\pi\pi\pi\pi$	<i>5-body</i>	$K\pi\pi\pi\pi$	<i>5-body</i>
$K\pi\pi\pi\pi\pi$	<i>6-body</i>	$K_S\pi\pi\pi\pi\pi$	<i>6-body</i>
$K_S\pi\pi^0\pi\pi\pi$	<i>6-body</i>	$K\pi\pi^0\pi\pi\pi$	<i>6-body</i>
$K_S\pi^0\pi^0$	$2\pi^0$	$K\pi^0\pi^0$	$2\pi^0$
$K\pi\pi^0\pi^0$	$2\pi^0$	$K_S\pi\pi^0\pi^0$	$2\pi^0$
$K_S\pi\pi^0\pi^0\pi$	$2\pi^0$	$K\pi\pi^0\pi^0\pi$	$2\pi^0$
$K\pi\pi^0\pi^0\pi\pi$	$2\pi^0$	$K_S\pi\pi^0\pi^0\pi\pi$	$2\pi^0$
$KKK_S$	<i>sss</i>	$KKK$	<i>sss</i>
$K_SK_SK_S$	<i>sss</i>	$KK_SK_S$	<i>sss</i>

Table 2.2: List of some final states of the  $b \rightarrow s\gamma$  process. The twelve (six from  $B^0\bar{B}^0$ , and six from  $B^+B^-$ ) channels used in this analysis are listed first. The relevant final state categories are also listed.

Table 2.3 lists the fraction of generated events (in percent) for the  $X_s\gamma$  sample generated with two different  $m_b$  parameters broken down by final state. The  $B^0 \rightarrow \gamma X_S$  and  $B^\pm \rightarrow \gamma X_S$  samples are shown separately in the  $M_{Had}$  range 1.0 – 2.4 GeV/ $c^2$ . This table presents only generator level numbers, no reconstruction or selection is applied on the events. The fractions are with respect to the full Monte Carlo sample (over all hadronic mass). For example, the first cell in the table says that 7.59% of the  $B^0 \rightarrow \gamma X_S$  Monte Carlo sample is generated with the final state  $K^+\pi^-$  in the  $M_{Had}$  range 1.0–2.4 GeV/ $c^2$ .

The sum of all the final states (vertically) for each neutral and charged  $B$  sample does not add to 100% since the hadronic mass range is restricted. For example, the total for the  $B^0 \rightarrow \gamma X_S$ , with  $m_b = 4.65$  GeV/ $c^2$ , sample is 75%, which means that 75% of all the generated events have a hadronic mass in the range 1.0–2.4 GeV/ $c^2$ .

Table 2.4 shows how the  $X_s$  events are distributed in each  $M_{Had}$  bin at the generator level for the two samples. The fractions are averaged over  $B^0 \rightarrow \gamma X_S$  and  $B^\pm \rightarrow \gamma X_S$  and normalized to each hadronic mass bin. Therefore, summing across a row gives 100%. For example, the first entry says that 32.9% of the generated events in the  $M_{Had}$  bin 1.0-1.2 GeV/ $c^2$  are 2-body events (where the *2-body* category is defined in Table 2.2 and in the itemized list above). The row labeled “average” lists the average over the  $M_{Had}$  bins.

From Table 2.4 one can see how the amount of *2-* and *3-body* events decrease with increasing  $M_{Had}$  while the *4-*, *5-* and *6-body* events have the opposite behavior. The percent of  $2\pi^0$  events also increases slightly with hadronic mass. The sss events are always a small contribution, while the contribution from the *other* category is always large and increasing with hadronic mass.

Comparing the two samples ( $m_b = 4.65$  or  $4.80$  GeV/ $c^2$ ) in Table 2.3 we see that when summed over a restricted  $M_{Had}$  range (0.6-2.4 GeV/ $c^2$ ) the fractions are slightly model dependent. This is because the two models have different  $M_{Had}$  distributions and so more or less of a certain mode will fit with in the range, see Figure 2.2. On the other hand, if we look in bins of hadronic mass, as in Table 2.4 we do not see any model dependence in the fractions for the different final state categories. This shows that the fragmentation does not depend on the model parameters.

Modes	$m_b$ GeV/ $c^2$		Modes	$m_b$ GeV/ $c^2$	
	4.65	4.80		4.65	4.80
$B^0 \rightarrow \gamma X_S, X_S \rightarrow$	Fraction (%)		$B^\pm \rightarrow \gamma X_S, X_S \rightarrow$	Fraction (%)	
$K^+\pi^-$	7.59	9.28	$K^+\pi^0$	4.12	4.98
$K_S\pi^0$	2.03	2.48	$K_S\pi^+$	3.76	4.62
$K^+\pi^-\pi^0$	11.9	13.8	$K_S\pi^+\pi^0$	5.92	6.83
$K_S\pi^+\pi^-$	4.91	5.71	$K^+\pi^+\pi^-$	9.76	11.4
$K_S\pi^0\pi^+\pi^-$	4.22	4.26	$K_S\pi^+\pi^+\pi^-$	1.43	1.41
$K^+\pi^-\pi^+\pi^-$	2.97	2.88	$K^+\pi^0\pi^+\pi^-$	8.59	8.73
Subtotal	33.65	38.46	Subtotal	33.59	37.95
<i>5-body</i>	4.58	4.14	<i>5-body</i>	2.88	2.61
<i>6-body</i>	0.867	0.717	<i>6-body</i>	1.48	1.23
$2\pi^0$	6.47	6.17	$2\pi^0$	6.77	6.73
<i>sss</i>	0.311	0.30	<i>sss</i>	0.621	0.603
<i>other</i>	29.2	29.2	<i>other</i>	29.7	29.9
Total	75.08	78.99	Total	75.06	79.04

Table 2.3: Some of the  $X_S$  final states and their rates (in percent) according to two different Kagan and Neubert signal models. The slight model dependence of the fractions is a result of the different predictions for the hadronic mass spectrum.

## 2.5 Final State Category Fractions $f_j$

In this analysis we reconstruct events in twelve final states (the first twelve states listed in Table 2.2). In each hadronic mass bin we calculate the partial branching fraction using all twelve final states together (the *all* category) or for some sub-set of the twelve final states (the *2-body*, *3-body*, *4-body* categories or the  $\pi$ ,  $\pi^0$  categories, or the  $K$ ,  $K_S$  categories). The partial branching fraction is calculated with respect to the category used.

In order to compute the inclusive branching fraction we need to correct the partial branching fraction by the fraction of the total possible final states that each category represents,  $f_j$ .

Table 2.5 shows the fraction of  $X_S$  events for two samples, KN465 and KN480, at the generator level, per  $M_{Had}$  bin, per each final state category. In the table we list only the nine final state categories that include all or a sub-set of the twelve final states used to reconstruct events in this analysis. These are the categories which will be used to measure partial branching fractions. (For the

KN465								
$M_{Had}$	<i>2-body</i>	<i>3-body</i>	<i>4-body</i>	<i>5-body</i>	<i>6-body</i>	$2\pi^0$	<i>sss</i>	<i>other</i>
1.0–1.2	32.9	32.0	1.41	0.002	0	2.63	0	29.6
1.2–1.4	20.6	36.7	7.52	0.285	0.007	3.79	0	30.3
1.4–1.6	12.5	28.9	13.7	2.96	0.254	6.64	0.688	34
1.6–1.8	8.15	20.3	16.2	6.13	0.982	9.55	1.19	37.5
1.8–2.0	5.65	14.6	14.8	8.41	2.41	11.9	0.878	41.5
2.0–2.2	4.23	11.0	11.9	8.38	3.49	12.3	0.674	48.3
2.2–2.4	3.33	8.53	9.61	7.61	4.08	12.0	0.55	54.9
average	12.5	21.7	10.7	4.82	1.6	8.42	0.568	39.4
KN480								
$M_{Had}$	<i>2-body</i>	<i>3-body</i>	<i>4-body</i>	<i>5-body</i>	<i>6-body</i>	$2\pi^0$	<i>sss</i>	<i>other</i>
1.0–1.2	33.0	32.0	1.44	0	0	2.65	0	29.5
1.2–1.4	20.4	37.0	7.49	0.274	0.007	3.78	0	30.2
1.4–1.6	12.6	28.9	13.8	2.97	0.232	6.6	0.659	33.9
1.6–1.8	8.19	20.6	16.2	5.91	0.984	9.54	1.19	37.3
1.8–2.0	5.72	14.7	14.5	8.44	2.39	11.9	0.899	41.5
2.0–2.2	4.12	11.2	11.8	8.33	3.51	12.3	0.675	48.2
2.2–2.4	3.23	8.71	9.57	7.44	4.04	11.9	0.582	55
average	12.5	21.9	10.7	4.76	1.6	8.37	0.571	39.4

Table 2.4: Distribution of events in the  $X_s$  Monte Carlo, KN465 and KN480, at the generator level, per final state category, in 200 MeV/ $c^2$  bins of the hadronic mass. The fractions (listed in percent) are normalized in each  $M_{Had}$  bin. The  $B^0 \rightarrow \gamma X_S$  and  $B^\pm \rightarrow \gamma X_S$  samples are averaged over.

*2-, 3-, 4-body* categories these are the same numbers as shown in Table 2.4.)

The *all* column lists the percent of the total final states that the twelve final states represent. For example, the first entry says that in the  $M_{Had}$  bin 1.0-1.2 GeV/ $c^2$  we are using 66.4% of the possible final states for the  $X_s$  KN465 decay. In the highest  $M_{Had}$  bin, 2.2-2.4 GeV/ $c^2$  this decreases to 21.5%, and averaging over the  $M_{Had}$  range 1.0-2.4 GeV/ $c^2$ , it is 45%.

The tables show the fractions for the final state categories in bins of hadronic mass. Comparing the two different samples, KN465 and KN480, we see that these fractions, and therefore the fragmentation, are not model dependent. We therefore will only consider one  $X_s\gamma$  signal model, KN465, from now on.

We also need to consider the final state fractions for the  $K^*\gamma$  resonance which

KN465								
$M_{Had}$	<i>all</i>	<i>2-body</i>	<i>3-body</i>	<i>4-body</i>	$\pi$	$\pi^0$	$K$	$K_S$
1.0–1.2	66.4	32.9	32.0	1.41	36.5	29.8	44.1	22.2
1.2–1.4	64.8	20.6	36.7	7.52	31.1	33.7	43.4	21.4
1.4–1.6	55.1	12.5	28.9	13.7	24.1	31.0	36.8	18.3
1.6–1.8	44.7	8.15	20.3	16.2	18.7	26.0	29.9	14.8
1.8–2.0	35.0	5.65	14.6	14.8	14.4	20.7	23.5	11.5
2.0–2.2	27.2	4.23	11.0	11.9	11.1	16.0	18.1	9.05
2.2–2.4	21.5	3.33	8.53	9.61	8.84	12.6	14.4	7.05
average	44.9	12.5	21.7	10.7	20.7	24.3	30.0	14.9
KN480								
$M_{Had}$	<i>all</i>	<i>2-body</i>	<i>3-body</i>	<i>4-body</i>	$\pi$	$\pi^0$	$K$	$K_S$
1.0–1.2	66.5	33.0	32.0	1.44	36.8	29.7	44.3	22.1
1.2–1.4	64.9	20.4	37.0	7.49	31.2	33.7	43.4	21.5
1.4–1.6	55.3	12.6	28.9	13.8	24.1	31.2	37	18.3
1.6–1.8	45.0	8.19	20.6	16.2	18.8	26.1	30.1	14.9
1.8–2.0	35.0	5.72	14.7	14.5	14.4	20.5	23.5	11.5
2.0–2.2	27.2	4.12	11.2	11.8	11.2	16	18.1	9.05
2.2–2.4	21.5	3.23	8.71	9.57	8.85	12.7	14.4	7.14
average	45.0	12.5	21.9	10.7	20.8	24.3	30.1	14.9

Table 2.5: Percent of  $X_s\gamma$ , KN465 and KN480, events, at the generator level, per each final state category, in 200 MeV/ $c^2$  bins of the hadronic mass.

makes up our signal model below  $M_{Had}=1.0\text{ GeV}/c^2$ .

The decay  $B \rightarrow K^*\gamma$  has a limited number of final states which include the four 2-body final states listed in Table 2.2. According to isospin factors the four final states are distributed as follows B,

$$\begin{aligned}
B^0 &\rightarrow K^{*0}\gamma, K^{*0} \rightarrow K^+\pi^- \text{ (2/3) or } K_S\pi^0 \text{ (1/6)} \\
B^+ &\rightarrow K^{*+}\gamma, K^{*+} \rightarrow K^+\pi^0 \text{ (1/3) or } K_S\pi^+ \text{ (1/3)}
\end{aligned}$$

Summed and averaged over neutral and charged  $B$ s these four modes represent 3/4 of the total final states. Modes with  $K_L$  make up the balance. This fraction does not depend on hadronic mass since the composition of the final states does not change. This is different than the  $X_s$  fractions which do depend on hadronic mass since there are different amounts of *2,3,4-body* events in different  $M_{Had}$  ranges.

Table 2.6 shows the final state category fractions for the  $K^*\gamma$  resonance. Figure 2.4 shows the final state fractions over our full range of  $M_{Had}$ , 0.6–2.4 GeV/ $c^2$ .

$M_{Had}$	<i>all</i>	<i>2-body</i>	<i>3-body</i>	<i>4-body</i>	$\pi$	$\pi^0$	$K$	$K_S$
0.6–1.0	75	75	0	0	50	25	50	25

Table 2.6: Fraction of  $K^*\gamma$  events, at the generator level, per each final state category.

# Generator Output

$mb=4.8, \lambda_1=-0.3$

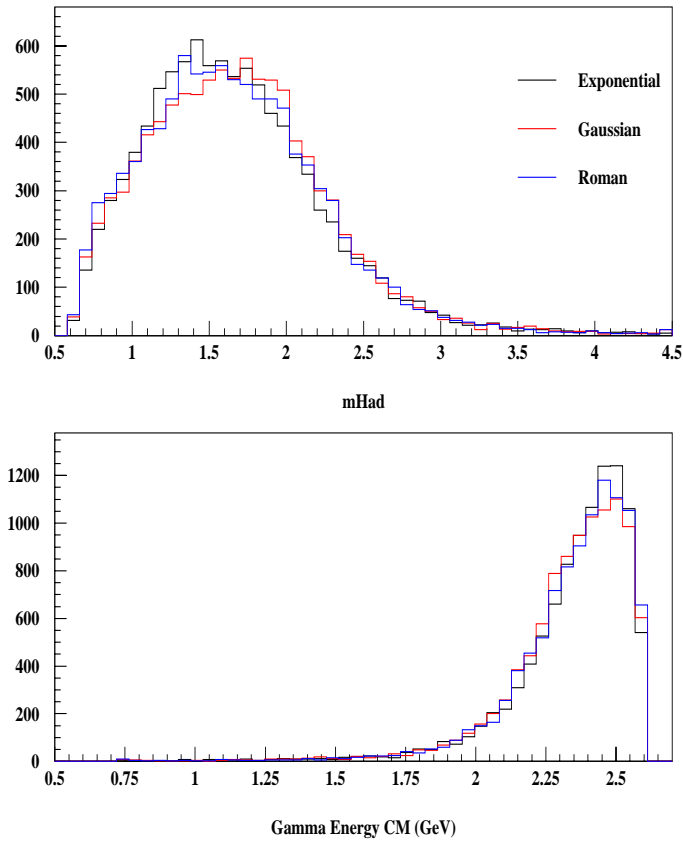


Figure 2.1: Hadronic mass spectra (upper plot) and corresponding photon spectra (lower plot) for three different shape functions according to the non-resonant spectrum Kagan and Neubert [5]. Arbitrary normalization.

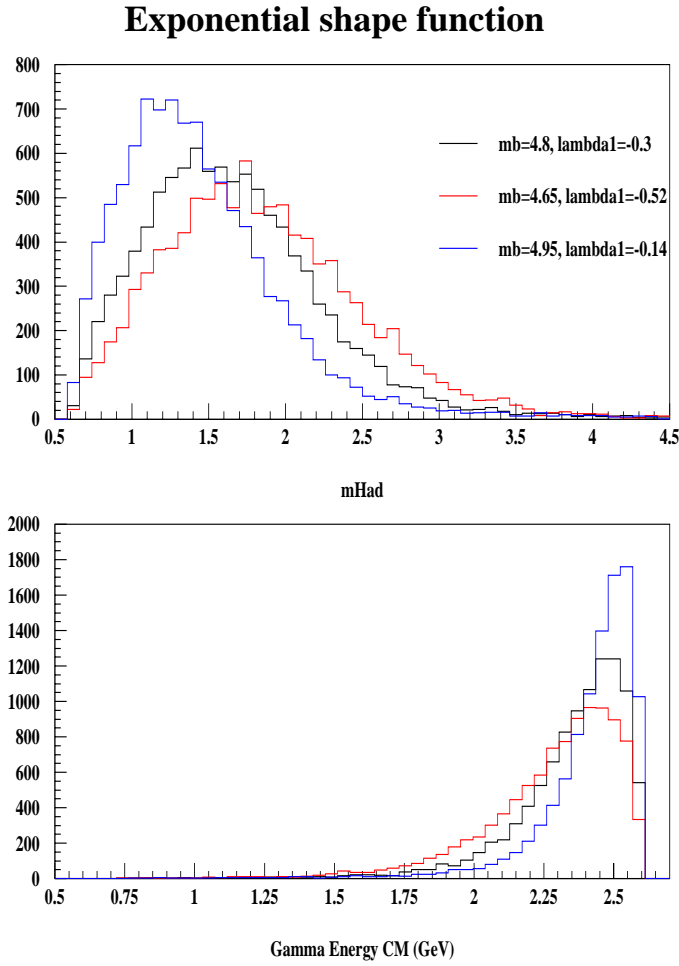


Figure 2.2: Hadronic mass spectra (upper plot) and corresponding photon spectra (lower plot) for the exponential shape function for three values of  $m_b$  and  $\lambda_1$ , according to the Kagan and Neubert [5] model. Arbitrary normalization.

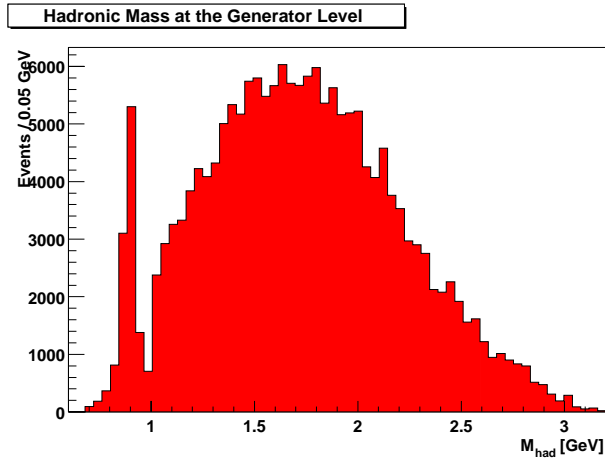


Figure 2.3: Hadronic mass spectra at the generator level. This plot is made using the Kagan and Neubert recipe to use the resonant  $K^*\gamma$  contribution up to  $1.0 \text{ GeV}/c^2$  and then use the non-resonant  $X_S\gamma$  contribution above. An exponential shape function is used with  $m_b = 4.65 \text{ GeV}/c^2$  and  $\lambda_1 = -0.3 \text{ GeV}^2$  as input parameters for the non-resonant model.

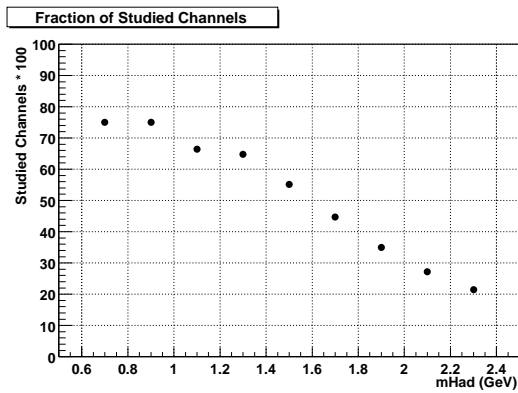


Figure 2.4: The final state fractions for the *all* category as a function of  $M_{Had}$ .

# Chapter 3

## The BABAR Experiment

The *BABAR* experiment gets its name from the millions of pairs of  $B$  mesons that it detects every year. It is located at the PEP-II asymmetric  $e^+e^- B$  Factory, where  $B\bar{B}$  pairs,  $B$  mesons and their anti-particles,  $B$ -bar mesons, are produced in record numbers. This allows for new studies of  $CP$ -violation in  $B$  meson decays, and other high precision measurements of decays of bottom and charm mesons and of  $\tau$  leptons.

### 3.1 The PEP-II Asymmetric $e^+e^- B$ Factory

The PEP-II Asymmetric  $e^+e^- B$  Factory is located at the Stanford Linear Accelerator Center (SLAC) in northern California. PEP-II is an  $e^+e^-$  collider operating at a center-of-mass energy of 10.58 GeV, which is exactly the  $\Upsilon(4S)$  resonance. The  $\Upsilon(4S)$  resonance decays exclusively to  $B^0\bar{B}^0$  or  $B^+B^-$  pairs.

PEP-II consists of two separate storage rings. The high-energy ring stores a 9-GeV electron beam, and the low-energy ring stores a 3.1-GeV positron beam. The electrons and positrons are created and accelerated in the three kilometer long Linac which also provides beams for other fixed target experiments at SLAC. The two beams are brought together at one interaction point around which the *BABAR* detector is built. PEP-II is an asymmetric collider since the energies of the two beams are not the same. Therefore, the  $\Upsilon(4S)$  which is created when an electron and positron collide, has some momentum in the lab frame, equivalent to a Lorentz boost of  $\beta\gamma = 0.56$ . This boost causes the two  $B$  mesons to separate by on average  $300\ \mu\text{m}$  before they decay allowing for reconstruction of the two separate decay vertices's and a measurement of their relative decay times. This is a design feature which is essential for the  $CP$ -violation measurement, where the time dependence of the  $B^0$  and  $\bar{B}^0$  mesons are compared.

The PEP-II design luminosity is  $3 \times 10^{33} \text{ cm}^{-2} \text{ s}^{-1}$ , which it reached in the first year of running (2000). The peak luminosity reached by May 2002 is  $4.6 \times 10^{33} \text{ cm}^{-2} \text{ s}^{-1}$ .

## 3.2 The *BABAR* Detector

A cross-section of the *BABAR* detector is shown in Figure 3.1<sup>1</sup>. It is comprised of a charged particle tracking system made up of a silicon vertex tracker (SVT) and a drift chamber (DCH), a particle identification device, the detector of internally reflected Cherenkov light (DIRC), an electromagnetic calorimeter (EMC), and a superconducting solenoid designed for a field of 1.5T, which has an instrumented flux return (IFR) for muon and neutral hadron detection.

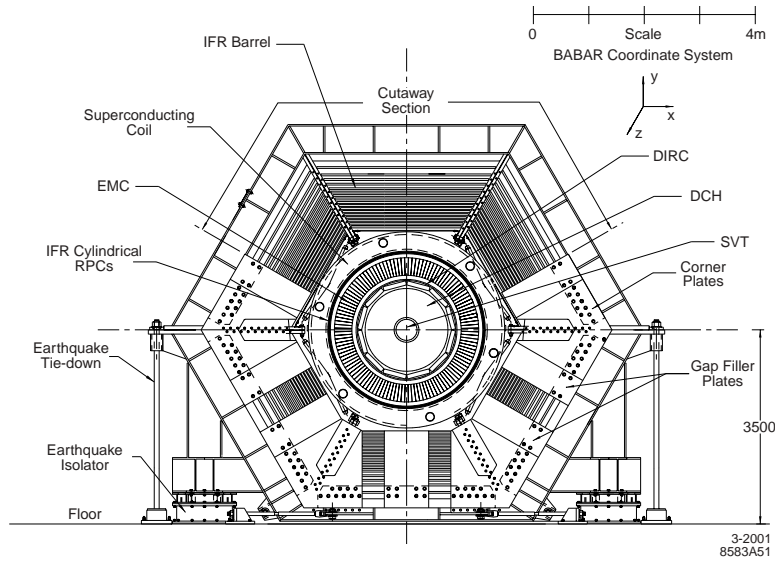


Figure 3.1: A cross-section of the *BABAR* detector. The five detector components are labeled, SVT, DCH, DIRC, EMC and IFR, listed from the inside out.

In this analysis the important components are the tracking system, to efficiently reconstruct the charged pions and kaons, the particle identification system for the charged kaon, and the calorimeter for efficiency and clear detection

<sup>1</sup>All figures, tables and numbers in this chapter, except where noted otherwise, are taken from a publication in the Nuclear Instruments and Methods (NIM) journal about the *BABAR* detector [19].

of the high energy photon. In the following these important components will be described along with their performance. Table 3.1 summarizes the detector systems, coverage and performance. A detailed description of all aspects of the *BABAR* detector can be found published here [19].

system	$\theta_1, \theta_2$	channels	layers	performance
SVT	20.1°, -29.8°	150K	5	$\sigma_{d_0} = 55 \mu\text{m}$ $\sigma_{z_0} = 65 \mu\text{m}$ $\sigma_\phi = 1 \text{ mrad}$
DCH	17.2°, -27.4°	7,104	40	$\sigma_{\tan\lambda} = 0.001$ $\sigma_{p_t}/p_t = 0.47\%$ $\sigma_{dE/dx} = 7.5\%$
DIRC	25.5°, -38.6°	10,752	1	$\sigma_{\theta_C} = 2.5 \text{ mrad}/\text{track}$
EMC(C)	27.1°, -39.2°	2 x 5760	1	$\sigma_E/E = 3.0\%$ $\sigma_\phi = 3.9 \text{ mrad}$
EMC(F)	15.8°, 27.1°	2 x 820	1	$\sigma_\theta = 3.9 \text{ mrad}$
IFR(C)	47°, -57°	22K+2K	19+2	90% $\mu^\pm$ eff.
IFR(F)	20°, 47°	14.5K	18	6 – 8% $\pi^\pm$ mis-id
IFR(B)	-57°, -26°	14.5K	18	(loose sel., 1.5-3 GeV/c)

Table 3.1: Overview of coverage and performance of the *BABAR* detector systems. The notation (C), (F) and (B) refer to the central barrel, forward and backward components of the system, respectively. The detector coverage in the laboratory frame is specified in terms of the polar angles  $\theta_1$  (forward) and  $\theta_2$  (backward). The number of readout channels is listed. Performance numbers are quoted for 1 GeV/c particles, except where noted. The performances for the SVT and DCH are quoted for a combined fit to the track.

### 3.2.1 Silicon Vertex Tracker (SVT)

The SVT has a five layer cylindrical geometry made from double-sided silicon strip detectors. The first three layers provide position and angle information for the measurement of the vertex position. They are mounted very close to the beam-pipe (4mm, 12mm, and 26mm away) in order to minimize the effect of the distortion of track trajectories due to multiple scattering in the water-cooled beryllium beam-pipe. The outer two layers (about 100mm and 140mm away from the beam pipe) provide the angular measurements needed to match SVT and DCH tracks.

The strips on either side of the silicon sensors are oriented perpendicular to each other to provide two dimensional tracking. When assembled, one set of strips,  $\phi$  strips run parallel to the beam while the other set,  $z$  strips run perpendicular to the beam direction. The active silicon area is  $0.96m^2$ , about 150,000 readout channels, and the geometrical acceptance is 90% in the center-of-mass system.

The read-out electronics for the SVT not only provide binary hit information, but also provide information about the pulse height of the signal generated by a charged track interacting with a strip. This is done by recording the time that the pulse height from a strip is above a threshold which distinguishes signal from noise: time-over-threshold (ToT). The ToT value is calibrated and from it the pulse height can be inferred which is a measurement of the ionization loss in the SVT sensor:  $dE/dx$ . The double-sided sensors can provide up to 10 measurements of  $dE/dx$  per track. This provides a  $2\sigma$  separation between kaons and pions for particles with a momentum up to  $500\text{ MeV}/c^2$ .

### 3.2.2 Drift Chamber (DCH)

The DCH is designed for efficient detection of charged particles, and precision measurements of their momentum and angles. The DCH consists of 40 layers of small hexagonal cells. To provide two dimensional position measurements 24 of the 40 cells are strung at small angles to the  $z$ -axis. The helium based gas mixture (80:20, helium:isobutane) along with low mass aluminum field wires provides a  $dE/dx$  resolution of 7%.

For low momentum particles (below  $700\text{ MeV}/c$ ) the DCH can provide particle identification by measuring ionization loss,  $dE/dx$ , in the chamber. Figure 3.2 shows the  $dE/dx$  measurement as a function of track momenta.

### 3.2.3 Charged Particle Tracking

The SVT and the DCH make up the charged particle tracking system. Tracks are reconstructed in the DCH and then an attempt is made to extend the tracks back into the SVT. A stand-alone tracking algorithm is then applied on any hits in the SVT not matched to a DCH track. Finally, a track matching algorithm is applied to try to match up any stand-alone tracks in both of the detectors. The tracking system covers 92% of the solid angle in the center of mass system. Figure 3.3 shows the track reconstruction efficiency in the DCH as a function of transverse momentum or polar angle. The two slightly different curves are for two different operating voltages in the DCH. The efficiency is 98%, for tracks

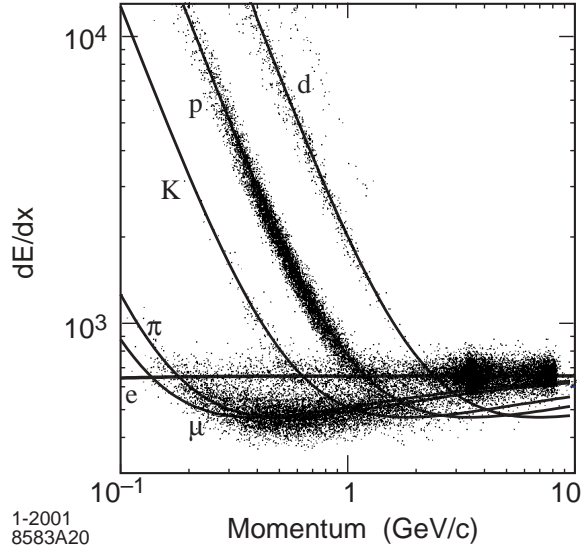


Figure 3.2: Measurement of  $dE/dx$  in the DCH as a function of track momenta.

with transverse momentum greater than 200 MeV/c.

There are five parameters which describe a track:  $d_0$  (DOCA XY),  $z_0$  (DOCA Z),  $\phi_0$ ,  $\omega$  and  $\tan\lambda$ . All parameters are measured at the point of closet approach to the beam axis (z-axis). The  $d_0$  parameter measures the position of this point of closet approach in the x-y plane, while the  $z_0$  parameter measures the distance of this point to the mean collision point. The parameter  $\omega = 1/p_t$  measures the curvature of the track. The angle  $\phi_0$  is the azimuthal angle, and  $\tan\lambda$  is the dip angle relative to the transverse plane.

The resolution for these parameters along with some specifications for the SVT and DCH are listed in Table 3.1.

### 3.2.4 Detector of Internally Reflected Cherenkov Light (DIRC)

The DIRC is a novel device consisting of optically flat bars of fused silica which run parallel to the beam direction just outside the DCH volume. When a particle passes through the bars it produces Cherenkov light which is transported by internal reflection, preserving the angle of emission, to the end of the bar where it is collected by an array of photomultiplier tubes. The front end of

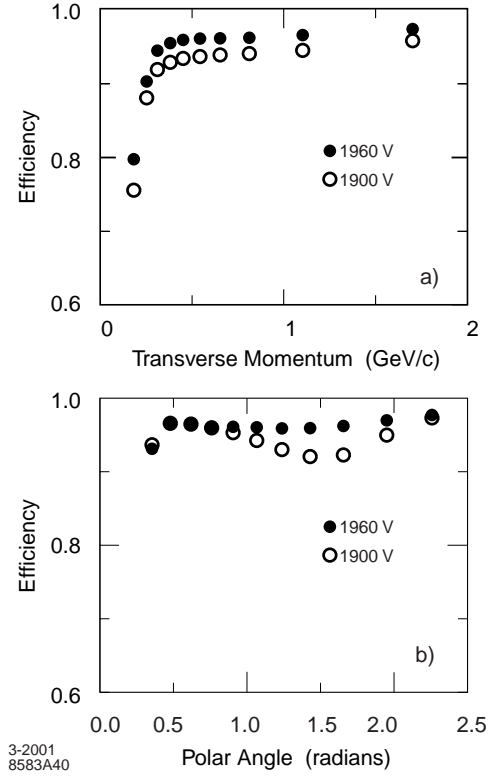


Figure 3.3: Track reconstruction efficiency in the DCH as a function of a) transverse momentum, b) polar angle.

the bars is equipped with a mirror so that the bars are read out only at the backward end of the detector. A fused silica wedge at the backward end of the bars reflects photons at large angles relative to the bar axis into a water filled expansion region, *standoff box (SOB)*, where the far side is instrumented with the photomultiplier tube (PMT) array. The PMTs are placed at a distance of about 1.2 m from the bar end.

The Cherenkov light pattern at the PMT array is a conic section, where the cone opening angle is essentially the Cherenkov production angle. The variable  $\theta_c$  is used to designate the Cherenkov angle,  $\cos\theta_c = 1/n\beta$  ( $\beta = v/c$ ),  $v =$  velocity of the particle and  $c =$  velocity of light. The DIRC provides three-dimensional imaging using the position and arrival time of the PMT signals, although the time information is not very precise and is mainly used for beam background suppression and helps to match the right track in the DCH with the

photon signal in the DIRC.

The reconstruction routine provides likelihood values for each of the five stable particle types ( $e, \mu, \pi, K, p$ ). The separation between kaons and pions, with which this analysis is especially concerned, is about  $4.2\sigma$  at  $3 \text{ GeV}/c$ .

### 3.2.5 Particle Identification System

Particle identification is based on information from the SVT, DCH and DIRC. Particle identification below  $700 \text{ MeV}/c$  comes primarily from the  $dE/dx$  information from the DCH and SVT. The DIRC provides separation of pions and kaons from about  $700 \text{ MeV}/c$  to  $4.2 \text{ GeV}/c$ .

Using the  $dE/dx$  measurements in the SVT and DCH and the angle and number of photons found in the DIRC, three sets of likelihoods values are calculated, one for each detector. Likelihood values for the stable particle types ( $\pi, K, p$ ) are calculated by multiplying together the likelihood values from the three detectors ( $L_\pi, L_K, L_p$ ). For the selection, cuts are made on the ratio between different hypothesis, where the value of the ratio,  $r$ , depends on the momentum of the track and the selection criteria [20].

There are five different charged kaon selection criteria,

- Very Tight :  $L_K > rL_\pi$  and  $L_K > rL_p$
- Tight :  $L_K > rL_\pi$  and  $L_K \geq rL_p$
- Loose :  $L_K > rL_\pi$
- Very Loose :  $L_K > rL_\pi$  or  $L_K > rL_p$
- Not a Pion :  $L_K \geq rL_\pi$  or  $L_\pi \leq rL_p$

In this analysis we use the Tight criteria for charged kaon identification. The kaon efficiency and pion mis-identification is shown in Figure 3.4 <sup>2</sup> for the Tight selection from  $D^*$  decays. The mean efficiency is 90% and the misidentification is 2.5%.

### 3.2.6 Electromagnetic Calorimeter (EMC)

The EMC is designed to measure electromagnetic showers and determine the energy and angular resolution over the energy range  $20 \text{ MeV}$  to  $4 \text{ GeV}$ . This range

---

<sup>2</sup>Figure from S.Spanier and G.Mancinelli.

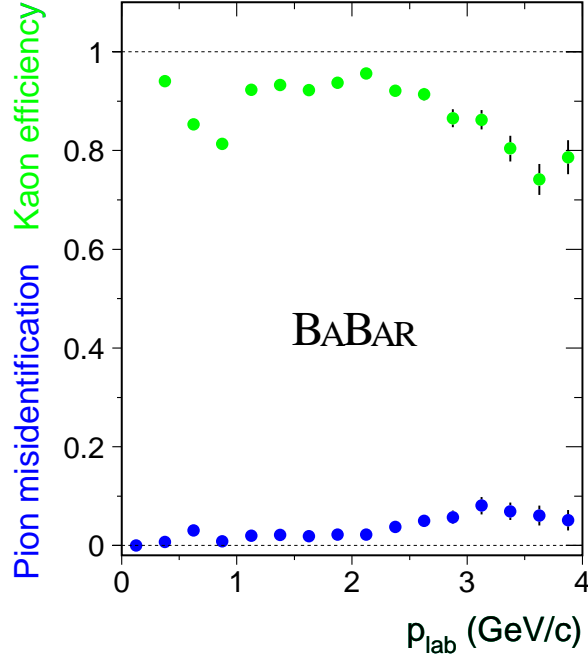


Figure 3.4: The kaon identification efficiency and pion misidentification for the Tight PID selection using the SVT, DCH and DIRC.

allows for detection of low energy  $\pi^0$ 's and  $\eta$ 's as well as high energy photons from radiative processes.

The EMC is composed of finely segmented arrays of thallium-doped cesium iodide (CsI(Tl)) crystals. The crystals are read-out with silicon photo-diodes that are matched to the spectrum of the scintillation light. The crystals are arranged in a cylindrical barrel outside of the DIRC and a forward end-cap, which corresponds to a solid angle coverage of about 90% in the center-of-mass system.

When a particle hits the EMC it produces an electromagnetic shower which can spread across many crystals. A group of neighboring crystals within which the energy is deposited is called a *cluster*. A cluster can result from one or more incident particles and therefore might have more than one local maximum. A pattern recognition algorithm is used to efficiently identify clusters and differentiate between single clusters with one energy maximum and merged clusters with more than one energy maximum, or *bump*. The algorithm also determines whether the bump is from a charged or neutral particle.

Figure 3.5 shows the energy resolution of the EMC as a function of pho-

ton energy measured by different processes which contribute in different energy ranges. (Note the log scale of the x-axis.) The resolution is about 12 MeV for photons with an energy of 2 GeV, which is the right range for the high energy photon candidates in our analysis. Figure 3.6 shows the angular resolution as a function of photon energy.

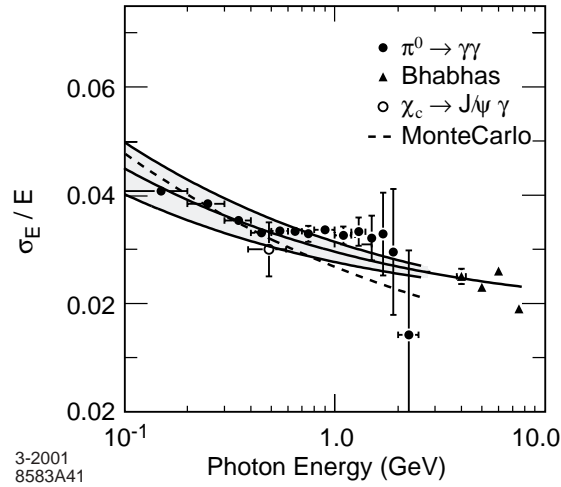


Figure 3.5: The energy resolution for the EMC measured for photons and electrons from various processes. The solid curve is a fit to an empirical equation and the indicated area denotes the rms error of the fit.

### 3.2.7 Instrumented Flux Return (IFR)

The IFR is designed to detect muons and neutral hadrons, primarily  $K_L^0$  and neutrons. This detector is not important for the  $b \rightarrow s\gamma$  analysis, but a short summary is presented here for completeness.

The IFR is instrumented in gaps in the steel flux return of the 1.5T magnet. The flux return acts as a muon filter and hadron absorber. The detectors are single gap resistive plate chambers (RPCs), with two-coordinate readout. The RPC's are installed in the barrel and end doors of the flux return. The basic construction of the RPC is a sandwich of aluminum strips on a mylar substrate, Bakelite sheets coated on the inside with linseed oil, with a gas filled gap in the middle. The aluminum readout strips are oriented perpendicular to each other on either side of the chamber. The RPC's detect streamers from ionizing particles and signals are readout capacitively on both sides of the gap.

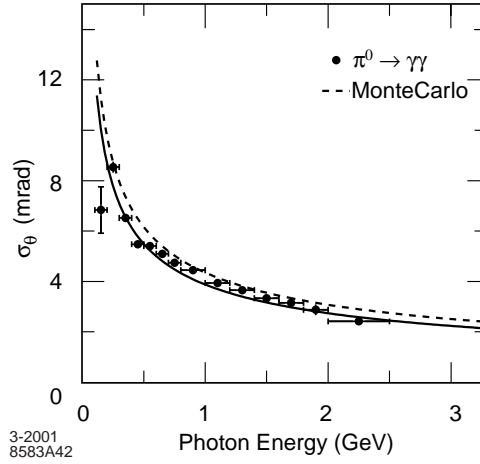


Figure 3.6: The angular resolution of the EMC for photons from  $\pi^0$  decays. The solid curve is a fit to an empirical equation.

Figure 3.7 shows the muon efficiency (left scale) and pion misidentification probability (right scale) as a function of laboratory track momentum and polar angle.

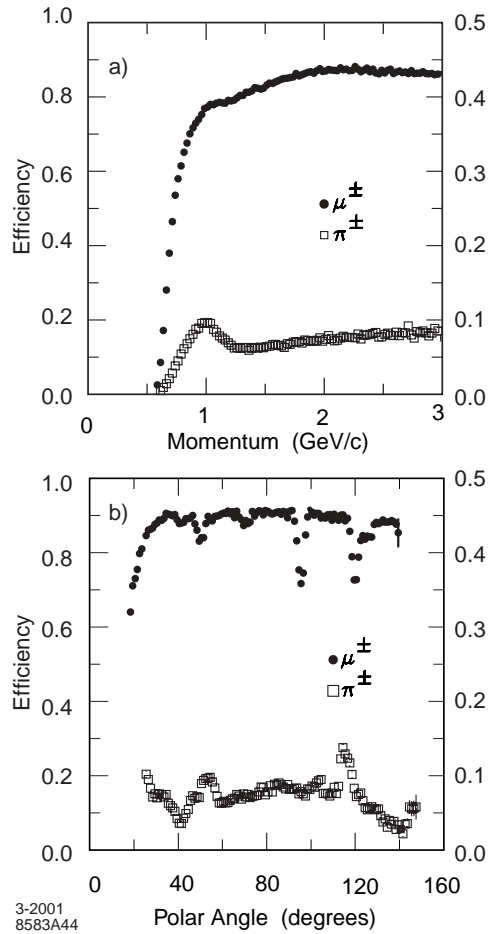


Figure 3.7: Muon efficiency (left scale) and pion misidentification probability (right scale) as a function of a) the laboratory track momentum, and b) the polar angle (for  $1.5 < p < 3.0$  GeV/ $c$  momentum), obtained with loose selection criteria.

# Chapter 4

## Analysis Method Summary

This chapter is meant to provide a summary of the analysis with references to the other chapters.

The goal of this analysis is to perform a measurement of the branching fraction for  $b \rightarrow s\gamma$  using a sum of exclusive states as a function of  $s$  hadronic mass. We then discuss how to convert this spectrum into a measurement of the inclusive branching fraction, although only preliminary results are presented.

In this semi-inclusive analysis twelve different final states are reconstructed. These twelve states include, on average, 45% of the total final states possible, as predicted by our Monte Carlo model, in the  $b \rightarrow s\gamma$  decay. The final states are constructed from a high energy photon candidate and a composite hadronic candidate containing strangeness. We consider modes with a hadronic multiplicity of at most four. We consider final states with one kaon and up to three pions. Only final states with at most one  $\pi^0$  are used. The kaons can be charged or neutral, although we do not consider final states with  $K_L$ 's, only  $K_S$ 's are used. We also only reconstruct  $K_S$ 's which decay to  $\pi^+\pi^-$ , and these reconstructed  $K_S$ 's are counted as the final state particle instead of the two charged pions. Table 4.1 lists the twelve final states used to reconstruct candidates in this analysis.

Ideally we would measure the partial branching fraction for each of the twelve modes separately. With the data sample used for this analysis ( $20.7 \text{ fb}^{-1}$ , 2000 data sample) we are statistics limited and therefore we must combine modes in order to have statistically significant samples. The simplest combination is to measure all twelve modes together. Another useful combination, which is used to investigate fragmentation effects, is to separate the modes by multiplicity, into *2-*, *3-*, or *4-body* events. This splits the twelve final states into three sets of four. Alternatively, to investigate isospin symmetry in the data, the modes are

$B^0\bar{B}^0$		$B^+B^-$	
Mode	categories	Mode	comment
$K\pi$	<i>2-body</i> , $\pi, K$	$K\pi^0$	<i>2-body</i> , $\pi^0, K$
$K_S\pi^0$	<i>2-body</i> , $\pi^0, K_S$	$K_S\pi$	<i>2-body</i> , $\pi, K_S$
$K\pi\pi^0$	<i>3-body</i> , $\pi^0, K$	$K_S\pi\pi^0$	<i>3-body</i> , $\pi^0, K$
$K_S\pi\pi$	<i>3-body</i> , $\pi, K_S$	$K\pi\pi$	<i>3-body</i> , $\pi, K$
$K_S\pi^0\pi\pi$	<i>4-body</i> , $\pi^0, K_S$	$K_S\pi\pi\pi$	<i>4-body</i> , $\pi, K_S$
$K\pi\pi\pi$	<i>4-body</i> , $\pi, K$	$K\pi^0\pi\pi$	<i>4-body</i> , $\pi^0, K$

Table 4.1: List of the twelve final states of the  $b \rightarrow s\gamma$  process which are used to reconstruct candidates in this analysis. The relevant final state categories are also listed.

split in two sets of six final states each by separating final states with or without a  $K_S$  ( $K, K_S$ ). The same can be done for states with and without a  $\pi^0$  ( $\pi, \pi^0$ ).

In the following sections the results will often be listed for eight final state categories (also shown in Table 4.1):

- *all*: 12/12 final states.
  - Split by hadronic multiplicity:
    - \* *2-body*: 4/12 final states with one kaon and one pion.
    - \* *3-body*: 4/12 final states with one kaon and two pions.
    - \* *4-body*: 4/12 final states with one kaon and three pions.
  - Split by states with and without a neutral pion:
    - \*  $\pi$ : 6/12 final states with no  $\pi^0$ 's.
    - \*  $\pi^0$ : 6/12 final states with one  $\pi^0$ .
  - Split by states with and without a k-short:
    - \*  $K$ : 6/12 final states with no  $K_S$ .
    - \*  $K_S$ : 6/12 final states with one  $K_S$ .

The results will also be presented in nine  $200\text{ MeV}/c^2$  bins in the hadronic mass ( $M_{Had}$ ) range 0.6 to 2.4  $\text{GeV}/c^2$ . In the range 0.6–1.0  $\text{GeV}/c^2$  (the first two bins) the signal Monte Carlo is composed of four exclusive  $K^*\gamma$  modes, while in the rest of the range, 1.0–2.4  $\text{GeV}/c^2$  (the last seven bins), the inclusive  $X_s\gamma$

Monte Carlo is used. The signal model is discussed in detail in Chapter 2.

Chapter 5 lists the Monte Carlo and data samples used in this analysis. We use  $20.7 \text{ fb}^{-1}$  of on-resonance data from 1999 and 2000. We use a sort of pseudo-truth matching in the signal Monte Carlo to separate real signal events from combinatoric background (cross-feed). This separates the signal Monte Carlo into two samples which are treated separately. This is discussed further below and in Section 7.2.

Chapter 6 details the event selection which is applied to pick out signal events and to reduce background from generic continuum and  $B\bar{B}$  events. The  $B$  candidate is constructed from a high energy photon ( $E_\gamma^* > 1.8 \text{ GeV}/c^2$ ) and a composite hadronic candidate which is reconstructed in one of the twelve final states listed in Table 4.1. In each event there is usually only one photon found which passes the quality selection, while there is often more than one hadronic candidate which passes the hadronic selection. There is often more than one  $B$  candidate formed per event which passes the selection. Therefore, on average, there is more than one final candidate per event. The best candidate is chosen as the one with the smallest  $\Delta E^*$ . Where  $\Delta E^*$  is the difference between the beam energy and the  $B$  candidate energy in the center of mass frame. After the selection and multiple candidate choice we are left with only one candidate per event.

The selection is not able to fully suppress the background and we are left with three different background components; continuum,  $B\bar{B}$  and cross-feed background. The continuum background comes from initial state radiation (ISR) events or events where a  $\pi^0$  or  $\eta$  decay produces a high energy photon candidate. The  $B\bar{B}$  background mostly stems from  $B \rightarrow D^{(*)}X$  decays, where the high energy photon candidate again comes mostly from a  $\pi^0$  or  $\eta$  decay. The cross-feed background consists of signal events which are incorrectly reconstructed. In Chapter 7 the backgrounds are discussed in detail.

The generic formula for the partial branching fraction for the  $i^{\text{th}}$   $M_{Had}$  bin and  $j^{\text{th}}$  final state category is:

$$PBF_{i,j} = N_{i,j}^{sig} / (\varepsilon_{i,j} * 2 * N_{bb}),$$

where  $N^{sig}$  is the signal yield,  $\varepsilon$  is the efficiency and  $N_{bb}$  is the number of  $B\bar{B}$  pairs in the data sample. In order to measure the partial branching fraction the quantities we need to determine are the signal efficiency and the signal yield.

The signal efficiency, detailed in Chapter 8, is obtained from the signal Monte Carlo sample. The truth matched events which pass the selection are counted as a function of  $M_{Had}$  and final state category. The efficiency in the  $i^{\text{th}}$   $M_{Had}$  bin and  $j^{\text{th}}$  final state category is defined as:

$$\varepsilon_{i,j} = N_{i,j}^{MCreco} / N_{i,j}^{MCgen}$$

where  $N_{i,j}^{MCreco}$  is the number of Monte Carlo truth matched events which pass the selection, and  $N_{i,j}^{MCgen}$  is the number of generated events in the initial Monte Carlo sample before the selection.

The signal yield is obtained from a fit to the data  $m_{ES}$  distribution with the various backgrounds subtracted.  $m_{ES}$  is the beam-energy substituted mass,  $M_{ES} = \sqrt{E_{beam}^2 - p_B^{*2}}$ . As the name suggests, the beam-energy is substituted for the  $B$  energy since the former is more precisely known. Some of the backgrounds peak in the signal  $m_{ES}$  region, but all contain a non-peaking component which is distributed over the full  $m_{ES}$  range. The non-peaking backgrounds are subtracted in the fit to the data while the peaking components are fit for in the Monte Carlo and subtracted directly from the data yield. The shape of the three background contributions are parameterized as follows:

- cross-feed background: Small peaking component. Parameterized by an Argus plus Crystal Ball shape function.
- continuum background: Non-peaking distribution and increases in magnitude with  $M_{Had}$ . Parameterized by an Argus shape function.
- $B\bar{B}$  background: Non-peaking plus peaking component at high  $M_{Had}$ . Very small contribution at low  $M_{Had}$ , (below 1.8 GeV/ $c^2$ ) but increases rapidly at higher  $M_{Had}$ . Parametrized by an Argus or Argus plus Crystal Ball shape above  $M_{Had} = 1.8$  GeV/ $c^2$ .

The Crystal Ball line-shape distribution:

$$C(m; m_0, \sigma, \alpha, n) = \frac{1}{N} \cdot \begin{cases} \exp(-(m - m_0)^2 / (2\sigma^2)) & , m > m_0 - \alpha\sigma \\ \frac{(n/\alpha)^n \exp(-\alpha^2/2)}{((m_0 - m)/\sigma + n/\alpha - \alpha)^n} & , m \leq m_0 - \alpha\sigma \end{cases}$$

is useful for fitting distributions with a radiative tail. It consists of a Gaussian signal peak matched to a power law tail. Note that the tail parameter,  $n$ , is not necessarily integer: lower values generate a longer tail. The parameter  $\alpha$

determines the crossover point from the Gaussian distribution to the power law tail distribution, in units of the peak width,  $\sigma$ .

The Argus distribution for the background shape is defined as:

$$A(m; m_0, c) = \frac{1}{N} \cdot m \sqrt{1 - (m/m_0)^2} \cdot \exp(c(1 - (m/m_0)^2)) \cdot \theta(m < m_0)$$

The Argus shape represents the natural shape of a phase space distribution of final state particles in two jets, near the kinematic limit where a particular combination of particles (the "B" candidate) balances to give zero total momentum. Note that  $m_0$ , the endpoint, represents the kinematic upper limit for the constrained mass and is held fixed at half of the center of mass energy (5.29 GeV/ $c^2$  for Y(4S) events) in the fits. The parameter  $c$  is what is usually referred to as the Argus parameter or Argus shape parameter in the text.

The background subtraction is performed as follows. The  $m_{ES}$  distribution in the data is fit to a Crystal Ball plus two Argus shapes, one for the cross-feed background and one for the sum of the continuum and  $B\bar{B}$  backgrounds. The two Argus shapes and the Crystal Ball shape parameters are fixed to values obtained from Monte Carlo fits. This is necessary because of the low statistics in some  $M_{Had}$  bins and final state categories. The peaking yield from the cross-feed and  $B\bar{B}$  background are fit for separately in the Monte Carlo samples and subtracted from the yield in the data fit. More details are found in Chapter 9.

The signal yield for the  $i^{\text{th}}$   $M_{Had}$  bin and  $j^{\text{th}}$  final state category is defined as:

$$N_{i,j}^{sig} = N_{i,j}^{data} - N_{i,j}^{xfeed} - N_{i,j}^{bb}.$$

The  $N$ 's are the peaking event yields from the fits,  $N = f_{CB} * N_{events}$ , where  $f_{CB}$  is the Crystal Ball fraction obtained from the fit and  $N_{events}$  is the total number of events that are fit.

The results from the fits are presented in Chapter 10.

In Chapter 11 the signal yield is combined with the signal efficiencies to obtain partial branching fractions (PBF). The results are *partial* branching fractions since they are defined in terms of the final states which we have used in this analysis, not for all possible  $b \rightarrow s\gamma$  final states.

$$PBF_{i,j} = N_{i,j}^{sig} / (\varepsilon_{i,j} * 2 * N_{bb}),$$

where  $N^{sig}$  is the signal yield,  $\varepsilon$  is the efficiency,  $N_{bb}$  is the number of  $B\bar{B}$  pairs in the data sample, the index  $i$  denotes the  $M_{Had}$  bin and  $j$  the final state category. For example,  $PBF_{i,all}$  is the partial branching fraction, in the  $i^{\text{th}}$   $M_{Had}$  bin, for

the 12 modes used in this analysis, since  $N_{i,all}^{sig}$  is the signal yield from the sum of those twelve modes, and  $\varepsilon_{i,all}$  is the efficiency averaged over the twelve modes. Or,  $PBF_{i,2body}$  is the partial branching fraction, in the  $i^{\text{th}}$   $M_{Had}$  bin, for the four modes which are two body decays (listed in Table 4.1).

The systematic errors for the partial branching fractions (PBF) are discussed in Chapter 12. Differences in detection efficiencies between data and Monte Carlo are accounted for with a shift in the efficiency and an associated systematic error. Systematic errors associated with the data and Monte Carlo fits give the largest contribution to the overall error.

We use the partial branching fractions for the different final state categories to examine differences between Monte Carlo and data. We compare the ratios of orthogonal categories,  $\pi^0/\pi$ ,  $K_S/K$ ,  $2/3\text{-body}$  and  $4/3\text{-body}$ , in data and MC. For the data the ratio is calculated using the PBF's. In the MC we use the ratio of the number of events at the generator level. We find that the  $K_S/K$  ratios agree between data and MC and also are consistent with isospin expectations of a ratio of 0.5. We do not find good agreement for the other ratios. This is a consequence of fragmentation differences in data and MC. What we see is that there are more states with  $\pi^0$ 's and less  $2\text{-body}$  states in the data than in the Monte Carlo. This comparison is made in Section 11.3.

Chapter 13 introduces a way to account for the differences between data and Monte Carlo fragmentation. The fragmentation gives the ratio between different final states. If we were measuring each final state separately, differences in the fragmentation between data and Monte Carlo would not matter. But, when we group states together we are averaging over their individual efficiencies weighted by the fragmentation determined from the Monte Carlo (since we obtain the signal efficiency from the Monte Carlo). The event yield is then measured in the data for a set of final states and divided by this average efficiency. If this Monte Carlo average efficiency is not a good approximation to the real efficiency, for this sum of states, the branching fraction will not be correct. We do not have enough statistics in the data ( $20.7fb^{-1}$ ), to measure each state individually, so we need a way to correct for these differences.

What we do is adjust the ratio of final states in the Monte Carlo to force it to match the data ratios. To do this we look at the ratio e.g. the  $\pi^0/\pi$  ratio in data and Monte Carlo and then adjust the efficiency, for e.g. the final states with a  $\pi^0$ , to force the ratio of ratios to be one.

$$R = (\pi^0/\pi)^{data}/(\pi^0/\pi)^{MC} \rightarrow 1$$

We look at this ratio of ratios,  $R$ , for  $\pi^0/\pi$ ,  $2/3$ -body and  $4/3$ -body. A plot of  $R$  as a function of  $M_{Had}$ , for each quantity, is fit to a straight line, and the  $y$ -offset is used to correct the generated and reconstructed number of events in the MC for that category. For example, we find that there are more  $\pi^0$ 's in data than in MC. This means that the  $R$  distribution has a positive  $y$ -offset. This  $y$ -offset is used to weight events with  $\pi^0$ 's in the MC, which effectively increases the number of events with  $\pi^0$ 's, and therefore increases the MC  $\pi^0/\pi$ , and brings  $R$  to 1. Note that this is an iterative procedure; only one correction is applied at a time. When the MC is adjusted to force one  $R$  to be one, the other  $R$ 's are effected, since e.g. the  $2$ -body category contains events with  $\pi^0$ . The consequence of this weighting is that the signal efficiency changes.

We first adjust the  $\pi^0/\pi$  ratio, then the  $2/3$ -body ratio, and then the  $\pi^0/\pi$  ratio again. The  $4/3$ -body ratio is not found to need adjustment. The final weighted signal Monte Carlo is used to obtain the weighted efficiencies. We also must redo all the fits adjusting the width of the Crystal Ball to that from fits to the weighted signal Monte Carlo.

These results are termed weighted partial branching fractions (WPBF) where the effects of fragmentation differences between data and Monte Carlo have been adjusted for.

The weighted partial branching fraction spectrum is the final experimental result presented in this document. Although, to compare with theoretical predictions, we need to correct for the  $b \rightarrow s\gamma$  final states that we don't measure to obtain the inclusive branching fraction and a hadronic mass spectrum which can be fit to extract theoretical model parameters. This method is discussed in Chapter 14, although only preliminary results are shown, since there are large uncertainties associated with the method. The results presented are calculated using the predictions from the Monte Carlo without any assigned errors. The correct error estimation is still being discussed inside the *BABAR* experiment and will be finalized before results are presented at summer conferences.

# Chapter 5

## Data and Monte Carlo Samples

We are using data events from Run-1 of *BABAR*, which includes data taken in 1999 and 2000 and Monte Carlo produced to match this data set<sup>1</sup>. The Monte Carlo event generation is done with Jetset [18], and the *BABAR* detector response is simulated with a Geant3 [21] based simulation.

This is a list of the samples used, together with some of the acronyms used to identify them:

- non-resonant signal Monte Carlo, neutral (**xs0**) and charged (**xsp**) final states. As described in Chapter 2 ( $BF(b \rightarrow s\gamma) = 3.2 \times 10^{-4}$  is assumed.):
  - Kagan & Neubert with  $m_b = 4.65$  GeV,  $\lambda_1 = -0.52$  GeV<sup>2</sup> and exponential shape function (**KN465**),  $125 fb^{-1}$ ,
  - Kagan & Neubert with  $m_b = 4.95$  GeV,  $\lambda_1 = -0.14$  GeV<sup>2</sup> and exponential shape function (**KN495**),  $48 fb^{-1}$ ,
- resonant signal Monte Carlo  $K^{*0}$  (892) (**ksg**) in the following decay modes,  $1062 fb^{-1}$  ( $BF(K^*\gamma) = 4.0 \times 10^{-5}$  is assumed):
  - $K^{*0} \rightarrow K\pi$  ( $K\pi$ )
  - $K^{*0} \rightarrow K_S(\rightarrow \pi\pi)\pi^0$  ( $K_S\pi^0$ )
  - $K^{*\pm} \rightarrow K\pi^0$  ( $K\pi^0$ )
  - $K^{*\pm} \rightarrow K_S(\rightarrow \pi\pi)\pi$  ( $K_S\pi$ )
- generic  $c\bar{c}$  Monte Carlo, (**ccb**),  $9.3 fb^{-1}$  ( $X_{sec} = 1.3nb$ ).

---

<sup>1</sup>Both the data and Monte Carlo were processed using BaBar reconstruction software releases from series 8

- generic  $uds$  Monte Carlo, (**uds**),  $8.7fb^{-1}$  ( $X_{sec} = 2.09nb$ ).
- generic  $B\bar{B}$  Monte Carlo, ( $X_{sec} = 1.13nb$ )  $14fb^{-1}$  and  $17fb^{-1}$  for the neutral (**b0g**) and charged mode (**bpg**), respectively.
- on-resonance data (**onr**),  $20.7fb^{-1}$ , which corresponds to  $(22.7 \pm 0.4) \times 10^6$   $B\bar{B}$  events.

It is important to point out that for the resonant signal Monte Carlo our sample consists of four specific modes. We do not generate any modes with a  $K_L$ , nor do we allow the  $K_S$  to decay to two  $\pi^0$ 's, while in the non-resonant  $X_s\gamma$  sample all modes are simulated. The four modes listed above include 2/3 of the total possible final states. These correspond to the modes that we measure. In order to simplify the interpretation of our results, we will correct the signal efficiency to account for the full k-short decays, i.e. include the  $K_S \rightarrow \pi^0\pi^0$  decays. This entails reducing the signal efficiency by a factor calculated using isospin factors. The calculation of the scaling factor for the different final state categories can be found in Appendix B. We do not correct for the states with  $K_L$ 's. Therefore, all results are with respect to the specific modes listed in Table 4.1, which includes modes with charged kaons and generic k-shorts (not generic neutral kaons).

In the sections that follow the signal Monte Carlo is often broken up into two separate samples labeled signal and cross-feed. After the reconstruction the signal Monte Carlo contains two categories of events, one where the true signal event has been reconstructed and one where the event has been incorrectly reconstructed. The combinatoric background is labeled cross-feed background and is discussed in more detail in Section 7.2.

To separate the signal and cross-feed samples we use a kind of Monte Carlo truth matching. For the signal sample we require that the true and reconstructed mode is the same and that the difference between the true and the reconstructed hadronic mass is within 50 MeV. The cross-feed sample contains all other events. In short:

- signal :  
reco mode = true mode &  $|trueM_{Had} - recoM_{Had}| < 0.05 \text{ GeV}/c^2$
- cross-feed :  
reco mode  $\neq$  true mode  
or  
reco mode = true mode &  $|trueM_{Had} - recoM_{Had}| > 0.05 \text{ GeV}/c^2$

Truth matched  $B$  mesons are found using the above method. The standard BaBar truth matching was not efficient enough to be used for the higher multiplicity modes.

# Chapter 6

## Selection

In the following, we describe the event selection criteria that we apply in the analysis. There are several steps:

- We preselect the events by running a filter. The filter requires at least one high energy photon, at least three good charged tracks and a maximum  $R_2^1$  cut. See Section 6.1 for details.
- We reconstruct B candidates from an energetic photon, a kaon and one to three pions. We reconstruct twelve exclusive final states. See Section 6.2 for details.
- Quality cuts on the photons, kaons and pions which were used to form the reconstructed B are applied. See Section 6.3 for details.
- We then combine event shape variables into a Fisher discriminant, and cut on it. See Section 6.4 for a definition of the Fisher discriminant and the variables used.
- After the selection there is usually more than one B candidate left in each event. We then choose the best candidate per event, taking the one with the minimum  $\Delta E^*$ . See Section 6.6 for details.

After the above steps we have a subset of events with one B candidate per event. The B mass ( $m_{ES}$ ) distribution of these events are fit and the background

---

<sup>1</sup> $R_2$  is the second Fox-Wolfram moment divided by the zero moment:  $R_2 \equiv H_2/H_0$  where  $H_n = \sum_{i,j} \frac{|p_i| \cdot |p_j|}{E_{Total}} \cdot P_n(\cos \theta_{ij})$ . The sum is taken over all the hadrons in the event,  $\theta_{ij}$  is the opening angle between hadron  $i$  and  $j$ ,  $E_{Total}$  is the total visible energy of the event and  $P_n(x)$  the  $n$ th Legendre polynomial.

subtraction, described in the following chapters, is applied. This yields the signal hadronic mass spectra. In the following sections, the different steps of the selection are described.

## 6.1 Filter

We start with an event filter which selects generic hadronic events with:

- $R2 < 0.9$ ,
- at least one photon with energy,  $E_\gamma^*$ , in the interval  $1.5 \text{ GeV}/c^2 < E_\gamma^* < 3.5 \text{ GeV}/c^2$  in the center of mass (CMS) frame,
- at least 3 good charged tracks. The quality cuts applied on the tracks are shown in Table 6.1.

Variable	Cut
Minimum Transverse momentum	0.1 GeV
Maximum momentum	10 GeV
Minimum number of DCH hits	12
Minimum fit $\chi^2$ probability	0
Maximum DOCA in XY plane	1.5 cm
Minimum Z DOCA	-10 cm
Maximum Z DOCA	10 cm

Table 6.1: Quality cuts applied for the good track selection.

Where the transverse momentum is measured with respect to the beam direction (Z-axis), and DOCA stands for the distance of closest approach to the beam spot.

The efficiencies, after the cuts in the filter are applied, for signal and background, are shown in Table 6.2.

## 6.2 Exclusive final states reconstruction

After the filter is applied,  $B$  mesons are reconstructed in the event. We attempt to reconstruct all possible hadronic combinations containing one kaon ( $K^+$  or  $K_S$ ), at most one  $\pi^0$ , and at most three charged pions.

Sample	efficiency (%)
$b \rightarrow s\gamma$ (KN465)	77.2
$c\bar{c}$	8.2
$uds$	13.9
generic $B\bar{B}$	2.5

Table 6.2: Efficiencies obtained from MC signal and background events after the filter is applied.

The hadronic candidate is combined with a high energy photon, and accepted as a  $B$  candidate if it satisfies cuts on a region surrounding the signal box identified by the following two variables:

- $\Delta E^*$ : the energy difference of a candidate  $B$  meson in the CMS frame<sup>2</sup>,  $E_B^*$ , should be equal to the CMS energy of the beam  $E_{beam}$  which is precisely known. We define:

$$\Delta E^* = E_B^* - E_{beam}, \quad (6.1)$$

where

$$E_B^* = E_K^* + \Sigma E_\pi^* + E_\gamma^*, \quad (6.2)$$

where  $E_K^*$  and  $\Sigma E_\pi^*$  are the energy of the kaon and the pions of the hadronic system.  $\Delta E^*$  should have a distribution centered at zero with a width dominated by the experimental resolution, in this case the high energy photon resolution.

For our initial selection of candidates we require  $-500 \text{ MeV}/c^2 < \Delta E^* < +500 \text{ MeV}/c^2$ .

- $m_{ES}$ : the other variable that identifies  $B$  mesons is the beam-energy substituted mass:

$$m_{ES} = \sqrt{E_{beam}^2 - p_B^{*2}}, \quad (6.3)$$

where  $p_B^*$  is the  $B$  momentum in the CMS frame. By substituting the beam energy instead of the measured  $B$  energy into the invariant mass equation, we increase our resolution.

For our initial selection of candidates we require  $5.2 \text{ GeV}/c^2 < m_{ES} < 5.3 \text{ GeV}/c^2$

---

<sup>2</sup>Note that variables in the CMS frame are denoted with a \* superscript

Only events with at least one reconstructed  $B$  passing the above selection are kept.

We have restricted ourselves to a maximum multiplicity of four for the hadronic system and a maximum of one  $\pi^0$ . In this case there are 12 distinct channels to consider, see Table 4.1.

These twelve channels cover on average 45% of the total  $X_s\gamma$  signal after  $M_{Had}=1.0$  GeV/ $c^2$  as shown in Section 2.4, while they correspond to 75% in the  $K^*\gamma$  region. Moreover, we make an initial cut on the mass of the hadronic system,  $M_{Had}$ :

$$0.6 \text{ GeV}/c^2 < M_{Had} < 2.4 \text{ GeV}/c^2$$

The upper cut corresponds to a cut on the photon energy:  $E_\gamma^* > 2.09$  GeV/ $c^2$ , using the equation:

$$M_{Had}^2 = m_B^2 - 2m_B E_\gamma^* \tag{6.4}$$

A looser hadronic mass cut would mean more background especially from  $B\bar{B}$  events.

The  $B$  reconstruction efficiency, i.e. how many events have at least one reconstructed  $B$  for the twelve modes, is given in Table 6.3. The  $B \rightarrow K^*\gamma$  sample is considered in the  $M_{Had}$  range 0.6–1.0 GeV/ $c^2$ , and the  $b \rightarrow s\gamma$  sample in the  $M_{Had}$  range 1.0–2.4 GeV/ $c^2$ .

Sample	<i>number of B &gt; 0:</i> efficiency (%)
$b \rightarrow s\gamma$ ( <b>KN465</b> )	47.8
$B \rightarrow K^*\gamma$	55.8
$c\bar{c}$	2.4
$uds$	4.9
generic $B\bar{B}$	0.3

Table 6.3: Efficiencies obtained from MC signal and background events after the filter and requiring at least one reconstructed  $B$ .

## 6.3 Quality cuts

### 6.3.1 High Energy Gamma Selection

The photons are created from neutral calorimetric objects which are single bumps not matched with any tracks, which have a minimum energy of 30 MeV, with a maximum lateral moment <sup>3</sup> of 0.8.

We require that the photon associated with the reconstructed  $B$  has at least an energy of 1.8 GeV.

As discussed in the previous section,  $E_\gamma^* = 2.09$  GeV corresponds to the upper  $M_{Had}$  cut-off,  $M_{HAD} = 2.4 \text{ GeV}/c^2$ . But,  $E_\gamma^*$  is smeared out by approximately  $\pm 150$  MeV due to the motion of the  $B$  meson in the Upsilon rest frame. Thus, we accept events with a photon energy down to 1.8 GeV.

#### Photon Quality Cuts

We implement quality cuts on the photon selection:

- the EMC cluster Second Moment <sup>4</sup>  $< 0.002$ ,
- the EMC cluster does not contain a noisy or dead crystal,
- the photon theta angle in the LAB frame,  $\theta_\gamma$ , is in the fiducial interval:  
 $-0.74 < \cos \theta_\gamma < 0.93$ ,

The second moment cut reduces background coming from merged  $\pi^0$ 's or  $\eta$ 's. The second moment is a measure of how circular the shower in the calorimeter is. If the two photons from a  $\pi^0$  or  $\eta$  decay are merged and form a cluster, this cluster is more likely to be oval shaped. Clusters from a single photon should be circular which gives a small second moment. The distributions for these variables can be found in Figure 6.1, for  $X_s\gamma$ , continuum and generic  $B\bar{B}$  background Monte Carlo.

---

<sup>3</sup>The lateral moment of a cluster is the ratio of the sum of energies of all but the two most energetic crystals weighted by the square of the distance to the cluster center and the same sum including all the crystals.

<sup>4</sup>The second moment of a cluster is defined as;  $S = \Sigma E_i(\Delta\Theta_i)^2 / \Sigma E_i$  where  $\Delta\Theta_i = \begin{pmatrix} \Theta_{clust} & -\Theta_i \\ \phi_{clust} & \phi_i \end{pmatrix}$  and  $\Theta_{clust} = \Sigma E_i\Theta_i / \Sigma E_i$  with a similar expression for  $\phi_{clust}$ . The sum is over the crystals in the cluster.

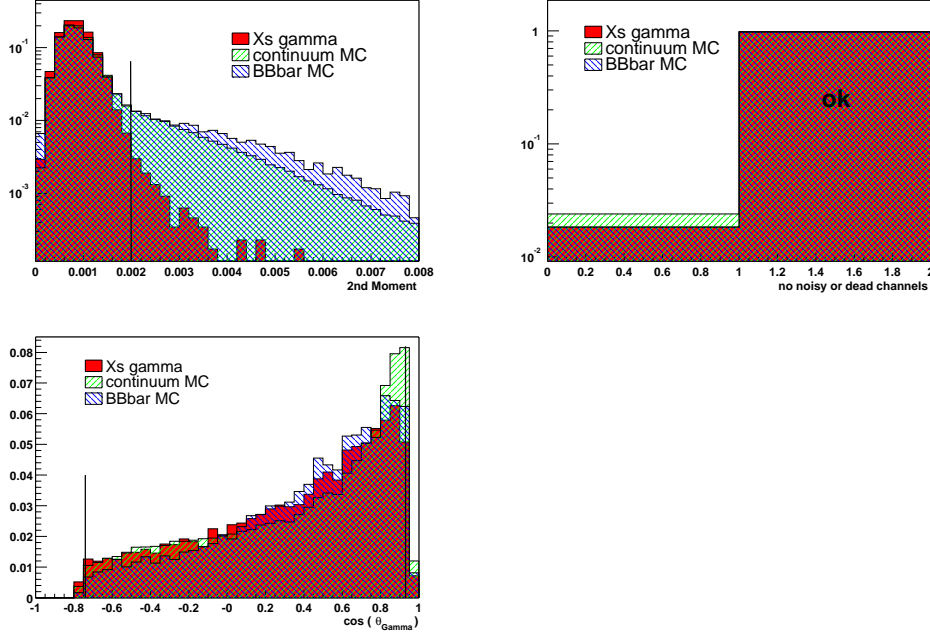


Figure 6.1: Photon selection variables for  $X_s\gamma$  signal MC (**KN465**), continuum and generic  $B\bar{B}$  background MC. The histograms are all normalized to 1.

### $\pi^0$ and $\eta$ vetoes

There is also a background component where one photon from an asymmetric  $\pi^0$  or  $\eta$  decay can have high enough energy to be considered as our high energy photon candidate. A  $\pi^0$  and  $\eta$  veto is implemented to remove this.

We look at the overlap of our high energy gamma with the lists of  $\pi^0(\rightarrow \gamma\gamma)$ <sup>5</sup> or  $\eta(\rightarrow \gamma\gamma)$ <sup>6</sup> in the event. The  $\pi^0$ 's are constructed from two photons with energies of at least 50 MeV, while the photons used to construct the  $\eta$ 's are required to have energies of at least 250 MeV.

If the high energy photon is found to be one of the daughters of a  $\pi^0$  or  $\eta$  and the corresponding  $\pi^0$  or  $\eta$  masses,  $m_{\pi^0}$  or  $m_{\eta}$ , are within a window around the  $\pi^0$  or  $\eta$  PDG masses, the event is rejected.

The mass windows within which the events are rejected, as optimized for the exclusive  $K^*\gamma$  analysis, are:

<sup>5</sup>The energy of the  $\pi^0$  is required to be at least 200 MeV/ $c^2$ . Their raw mass is constrained to the window 90 – 170 MeV/ $c^2$ . No mass constrained fit is applied

<sup>6</sup>A cut on the  $\eta$  mass between 470 and 620 MeV is applied.

$$115 \text{ MeV}/c^2 < m_{\pi^0} < 155 \text{ MeV}/c^2,$$

$$508 \text{ MeV}/c^2 < m_{\eta} < 588 \text{ MeV}/c^2.$$

In Figure 6.2, the closest masses per event (in case of overlap) to the  $\pi^0$  and  $\eta$  PDG masses are shown for a sample of  $X_s\gamma$  signal MC, continuum and generic  $B\bar{B}$  background MC. See Table 6.4 for the selection efficiencies.

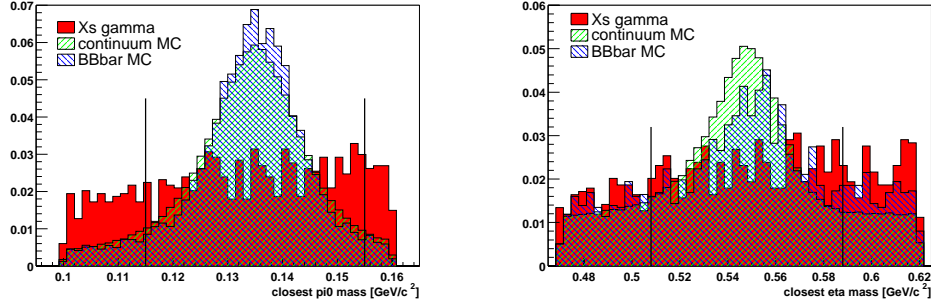


Figure 6.2: Closest masses per event (in case of overlap) to the  $\pi^0$  or  $\eta$  PDG masses for  $X_s\gamma$  signal MC, continuum and generic  $B\bar{B}$  background MC. The histograms are all normalized to an area of 1.

### Bump distance cut

Furthermore, in order to improve the suppression of background coming from  $\pi^0$  or  $\eta$  but not reconstructed within the vetoes, we implement an isolation cut on the photon bump.

In order to improve the isolation requirements on the photon, there is a cut on the distance between the photon bump and another charged or neutral bump in the event. If there is another bump within 25cm the photon is rejected. The corresponding distribution can be seen in Fig. 6.3. See Table 6.4 for the selection efficiencies.

### Summary

The selection efficiencies for the signal using truth matched photon candidates for each of these cuts are shown in Table 6.4 for the  $X_s\gamma$  sample. The cumulative signal efficiency after the photon quality cuts is 75%. Plots showing the selection for each cut in  $X_s\gamma$  signal MC, continuum and generic  $B\bar{B}$  background MC can be seen in Figures 6.1, 6.2 and 6.3. The histograms for the three samples are

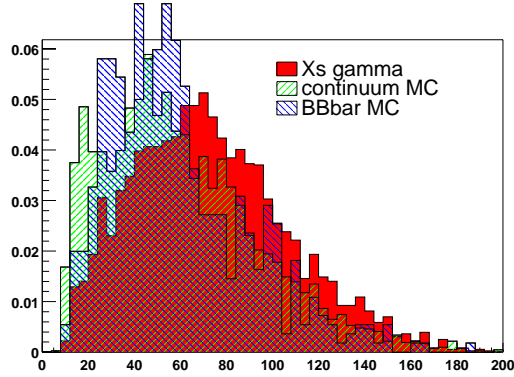


Figure 6.3: Bump distance distribution for  $X_s\gamma$  MC events, continuum and generic  $B\bar{B}$  background MC. The histograms are all normalized to an area of 1.

all normalized to an area of 1, therefore only their shapes can be compared, not their relative heights.

quality cut	Absolute $\varepsilon(\%)$
cluster Second Moment < 0.002	98.8
cluster does not contain a noisy or dead crystal	97.6
$-0.74 < \cos \theta_\gamma < 0.93$	96.7
$\pi^0$ veto	94.1
$\eta$ veto	95.1
Distance cut	91.4
Cumulative efficiency	75.4

Table 6.4: Efficiencies for each of the cuts on the photons using the MC signal events:  $X_s\gamma$  signal (**KN465**). The efficiencies are computed after the filter is applied. Each efficiency is computed with respect to the previous cut.

### 6.3.2 Charged pions and kaon selection

Tracks are requested to pass the good track selection, shown in Table 6.1. We do not apply particle identification (PID) on charged pions. We do require Tight PID (as defined in Section 3.2.5) for charged kaons, which has an efficiency

of 84% on our signal events. Requiring PID on the kaon helps to suppress the small expected background from  $b \rightarrow d\gamma$ .

Corrections for differences in data and Monte Carlo detection efficiencies are considered in the chapter dealing with systematic errors, Section 12.7.

### 6.3.3 $K_S$ selection

We reconstruct  $K_S \rightarrow \pi^+\pi^-$  candidates. The candidates are constructed from all pairs of oppositely charged tracks which are assigned the  $\pi$  mass. The pions are combined using a vertex fit. We do not reconstruct  $K_S \rightarrow \pi^0\pi^0$ . A number of cuts are made on the reconstructed  $K_S$  candidates to suppress non- $K_S$  backgrounds:

- a mass cut  $489 \text{ MeV}/c^2 < M_{K_S} < 507 \text{ MeV}/c^2$ ,
- a decay length cut,  $> 2 \text{ mm}$ ,
- convergence of the vertex fit.

Figure 6.4 shows the distributions for the  $K_S$  selection criteria in  $X_s\gamma$  signal MC, continuum and generic  $B\bar{B}$  background MC. The histograms are all normalized to an area of 1, so their shapes can be compared but not their relative heights.

The backgrounds to the  $K_S$  channels come primarily from real  $K_S$  (this is true both for continuum and  $B\bar{B}$  backgrounds). The selection efficiencies for the signal for each of these cuts are shown in Table 6.5. The cumulative efficiency on signal events for the  $K_S$  selection is 91%. Corrections for differences in data and Monte Carlo detection efficiencies are considered in the chapter dealing with systematic errors, Section 12.7.

cut	Absolute $\varepsilon(\%)$
mass cut $489 \text{ MeV}/c^2 < M_{K_S} < 507 \text{ MeV}/c^2$	94.6
decay length cut $> 2 \text{ mm}$	96.1
Converged vertex fit	99.9
Cumulative efficiency	90.8

Table 6.5: Efficiencies for each of the cuts on the  $K_S$  using the MC signal events:  $K^{*0}(\rightarrow K_S\pi^0)\gamma$ . The efficiencies are computed after the filter is applied. Each efficiency is computed with respect to the previous cut.

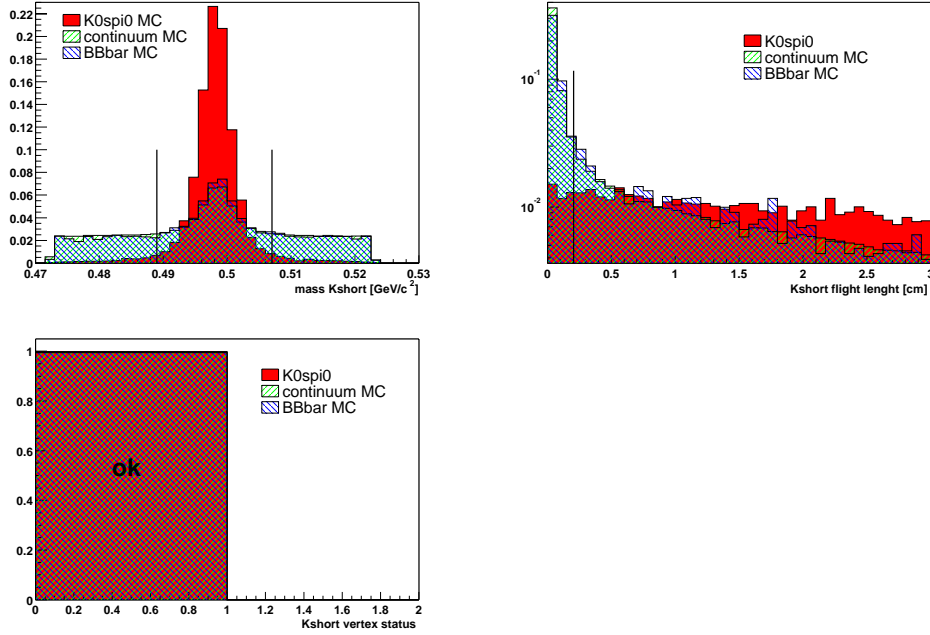


Figure 6.4: MC selection distributions for  $K_S$  candidates in  $K^{*0}(\rightarrow K_S\pi^0)\gamma$  signal events, continuum and generic  $B\bar{B}$  background.

### 6.3.4 Neutral Pion Identification

We use the default neutral pion candidates for our selection of neutral pions. The energy of the  $\pi^0$  is required to be at least 200 MeV. Their raw mass is constrained to be in the window 90 – 170 MeV. A mass constrained fit is applied.

Corrections for differences in data and Monte Carlo detection efficiencies are considered in the chapter dealing with systematic errors, Section 12.7.

## 6.4 Fisher Discriminant

Most of the background in the inclusive analysis comes from continuum production of a high energy photon either through initial state radiation (ISR) or through a  $\pi^0/\eta$  decay which escapes the vetoes that have been applied. These backgrounds are suppressed using event shape variables. As can be seen in Figure 6.5 the continuum backgrounds are both jet-like while the signal and  $B\bar{B}$

background events are isotropic. This difference in shape is what allows these event shape cuts to reduce the continuum background.

The shape variables we use are described in the following. Then, instead of applying a cut for each variable separately, they are combined using a linear multivariate method into a Fisher Discriminant described at the end of this section, in order to improve the total rejection power.

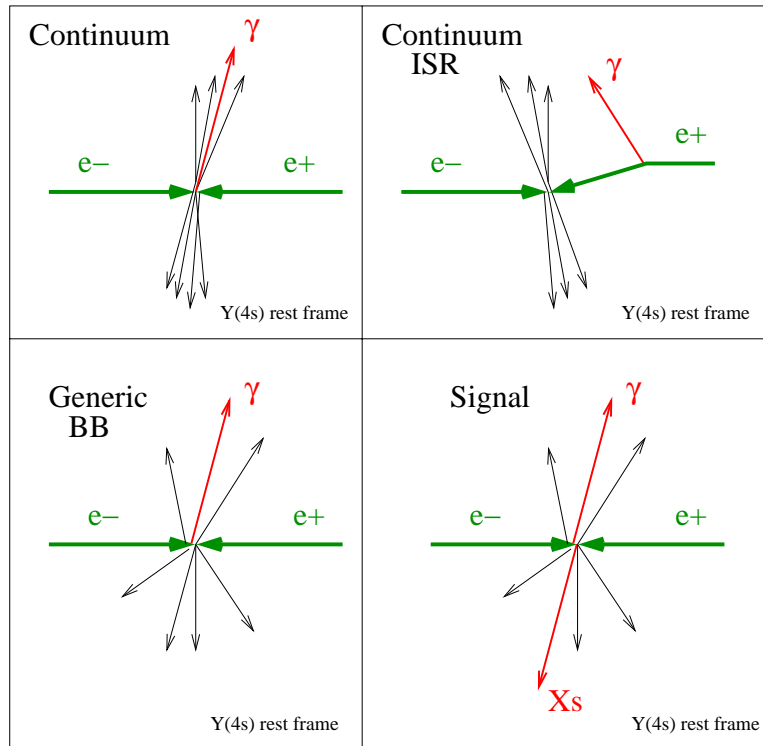


Figure 6.5: Illustrations of the shapes of the backgrounds and signal events.

### 6.4.1 Input variables for the Fisher Discriminant

The shape variables which are used as input to the Fisher Discriminant are described in the following.

$\cos \theta_T^*$  For each  $B$  candidate we calculate the angle  $\theta_T$  between the  $B$  daughters and the thrust of the event calculated (using charged and neutral candidates) excluding the  $B$  daughters. It is flat for signal, while rapidly increasing at  $\pm 1$  for the background.

- $\cos\theta_{B^*}$  The angle of the reconstructed  $B$  candidate with respect to the beam direction computed in the CMS frame.
- $E_f$  The energy flow in a  $20^\circ$  cone along the photon direction, excluding the photon energy, this should be low for signal events. Due to the small solid angle covered no leakage from the second  $B$  or the strange part of the signal  $B$  is expected. This will suppress continuum with initial state radiation.
- $E_b$  The expected energy flow in a  $40^\circ$  cone opposite the photon can be estimated by the known energy of the strange quark in the CMS. This is used to distinguish between signal and continuum events containing an ISR photon
- $R2$  The ratio of second to zeroth Fox-Wolfram moment. A lower  $R2$  characterizes signal events due to their isotropic decay, as opposed to Bhabha and tau events and continuum background.
- $R2'$  The ratio of Fox-Wolfram moment in the photon recoil system over the one in the CMS. The photon recoil system is defined by boosting the event to the the center of mass of the  $e^+e^-$  system minus the photon 4-vector. If the event is an ISR event, the topology will be jet-like in this frame. This is useful in further reducing continuum events with initial state radiation. By investigating the frame without the potential ISR photon the  $R2'$  value can filter out jetty continuum.

Plots of the shape variables are shown in Fig. 6.6. In order to select a purer sample of events we cut on the absolute value of  $\cos\theta_{T^*}$  at 0.7 when implementing the Fisher Discriminant, the distributions of the variables in the plots are shown after this cut (except  $\cos\theta_{T^*}$ ).

## 6.4.2 Description of the Fisher Discriminant

The Fisher Discriminant is calculated from a linear combination of input variables to provide the best separation between signal and background events. The linear coefficients are calculated by finding the axis in the  $N$  dimensional space of the discriminating variables such that signal and background are maximally separated. Signal and background training samples are used to obtain the values of the linear coefficients for each input variable and then these coefficients are used to calculate the Fisher Discriminant variable in the data sample. Finally, a cut is made on this calculated Fisher variable.

$\cos\theta_{T^*}$  is the most discriminating variable, and therefore, to reduce the number of events input to the Fisher Discriminant, a pre-cut is made on the absolute

value of  $\cos\theta_{T^*}$  at 0.7. The training was done on truth matched candidates to avoid the problem of multiple candidates per event. An independent signal Monte Carlo sample is used as a training sample. Both the generic continuum and  $B\bar{B}$  samples are used as the background training sample. After the training we checked that the **KN465** Fisher Discriminant shape was the same as the one from the training sample.

The variables are  $\cos\theta_{T^*}$ ,  $\cos\theta_{B^*}$ ,  $E_f$ ,  $E_b$ ,  $R2'$ ,  $R2/R2'$  and their coefficients (in the linear combination of the variables which gives the Fisher Discriminant) are: -1.09, -0.484, -0.726, -0.398, 3.084, -0.758, respectively. The Fisher Discriminant distribution is shown in Figure 6.7 for signal, continuum and  $B\bar{B}$  background Monte Carlo.

### 6.4.3 Optimization of the cut

The chosen optimization criterion of the cut on the Fisher Discriminant is to maximize  $S^2/(S+B)$ , where S and B are the expected signal and background, respectively. The corresponding optimization plot for the Fisher discriminant can be found in Fig. 6.8. The chosen cut which maximizes  $S^2/(S+B)$  is -0.8.

## 6.5 $\Delta E^*$ Window Selection

For the final analysis, the cut on  $\Delta E^*$  is tightened to the value:

$$-150 \text{ MeV} < |\Delta E^*| < +150 \text{ MeV}.$$

We use a symmetric cut because, as we discuss in the next section, if multiple  $B$  candidates per event pass the selection, the one with the smallest  $\Delta E^*$  is chosen as the final candidate. The  $\Delta E^*$  resolution for various modes can be seen in Figure 6.9.

## 6.6 Multiple Candidates

In each event a total of twelve channels are considered with a hadronic multiplicity up to four. It is probable that more than one  $B$  candidate per event can be formed and pass the selection.

For the final analysis, we would like to retain just one candidate per event. Multiple candidates in an event usually are constructed from the same gamma, but different hadronic combinations. The average number of multiple candidates

per event in the hadronic mass region from 0.6 to 0.8 GeV/ $c^2$  (corresponding to the  $K^*\gamma$  resonance region) is measured to be  $1.41 \pm 0.03$  from data events, which is in agreement with the estimation of  $1.47 \pm 0.08$  from full MC events. The difference between both estimates is  $0.05 \pm 0.08$  which is compatible with 0 within errors.

In order to study the multiple candidates selection we have first selected events in which one of the  $B$  candidates which pass the selection is truth matched. The pseudo-truth matching used is described in Chapter 5. For these events we have studied the number of candidates present in the exclusive final states after all the selection cuts are applied. In Table 6.6 the first column lists the twelve modes used. The next column ( $N_{events}$ ) list the number of events after the final selection. The third column ( $N_{events}^{Btrue}$ ) list the number of events after the final selection where one of the multiple candidates is truth matched. Figure 6.10 shows a plot of the number of candidates per event for the  $X_s\gamma$  Monte Carlo sample. It is clear from the distribution that, on average, there is more than one  $B$  candidate left after the selection per event.

Table 6.7 looks at how the multiple candidates are distributed over all the reconstructed modes. The first column lists the true mode, i.e. the mode that the event was generated with. The second column (Sig.) list the fraction of candidates (among all the multiple candidates) that are truth matched for each true mode. The next 12 columns lists the fraction of non-truth-matched candidates that are reconstructed in the other modes. For example, 59% of the candidates for events which are true  $K\pi$  events, have a truth-matched candidate. Out of the non-truth-matched candidates for true  $K\pi$  events 6% are reconstructed as  $K\pi$ , 16% are reconstructed as  $K\pi\pi^0$ , etc.

The best candidate is chosen from among the multiple candidates by taking the one with  $\Delta E^*$  closest to zero. We use the  $\Delta E^*$  criterion because we prefer to avoid using variables, such as  $m_{ES}$ , that are used for the background subtraction.

Table 6.8 shows the same numbers as Table 6.7 after the multiple candidate selection. This shows the fraction of correctly and incorrectly reconstructed events after the best candidate is chosen with the smallest (in absolute value)  $\Delta E^*$ .

To investigate the multiple candidate selection we can look at how far away, in  $\Delta E^*$ , the second best candidate was. The left plot in Figure 6.11 shows the  $\Delta E^*$  distribution for the best and second best candidate. We can plot the difference between the absolute value of the  $\Delta E^*$  of the best and the second best candidate, which will always be a negative quantity since the absolute value of the  $\Delta E^*$  for the best candidate will always be smaller. The right plot in the figure shows the difference between the absolute value of the  $\Delta E^*$  of the best

Mode	$N_{events}$	$N_{events}^{B_{true}}$
$K\pi$	711	210
$K_s\pi^0$	83	36
$K\pi\pi^0$	851	255
$K_s\pi\pi$	251	87
$K_s\pi^0\pi\pi$	137	5
$K\pi\pi\pi$	208	26
$K\pi^0$	268	58
$K_s\pi$	176	107
$K_s\pi\pi^0$	236	51
$K\pi\pi$	764	327
$K_s\pi\pi\pi$	46	5
$K\pi^0\pi\pi$	471	32

Table 6.6: For each final state (Mode), the table shows the total number of events ( $N_{events}$ ), and the number of events with a true B among the candidates ( $N_{B_{true}}^{events}$ ). This is for the  $X_s\gamma$  Monte Carlo sample with  $M_{Had}$  above 1.0 GeV/ $c^2$ .

and second best candidate.

## 6.7 Final Sample

We now have a sample of events which pass all our selection criteria and have one final  $B$  candidate reconstructed in one of the twelve modes. We then look at the  $m_{ES}$  distribution for the final candidates.

The major uncertainty in the determination of  $m_{ES}$  comes from the reconstructed photon energy. If we apply a kinematic constraint,  $\Delta E^* = 0$ , we can rescale the photon energy to correct for leakage effects. We then use this rescaled photon 4-vector to recalculate  $m_{ES}$ . This increases the  $m_{ES}$  resolution, but is less effective for modes which have a  $\pi^0$  in the final state since the leakage for the two photons which make up the  $\pi^0$  add to the width.

For our final selection, we retain events with a  $B$  candidate with  $m_{ES} > 5.21 \text{ GeV}/c^2$ .

true Mode	reconstructed mode						
	<i>Sig</i>	$K\pi$	$K_s\pi^0$	$K\pi\pi^0$	$K_s\pi\pi$	$K_s\pi^0\pi\pi$	$K\pi\pi\pi$
$K\pi$	0.59	0.06	0	0.16	0.01	0	0.03
$K_s\pi^0$	0.34	0	0.25	0	0.04	0	0
$K\pi\pi^0$	0.33	0	0	0.28	0.01	0.02	0.05
$K_s\pi\pi$	0.39	0	0	0	0.11	0.12	0.02
$K_s\pi^0\pi\pi$	0.38	0	0	0	0	0.46	0
$K\pi\pi\pi$	0.36	0	0	0.02	0	0.01	0.23
$K\pi^0$	0.47	0.05	0	0.23	0	0	0
$K_s\pi$	0.47	0	0.07	0	0.02	0	0
$K_s\pi\pi^0$	0.37	0	0.02	0.01	0.12	0.14	0
$K\pi\pi$	0.31	0.01	0	0.13	0.02	0.02	0.1
$K_s\pi\pi\pi$	0.37	0	0	0	0.15	0.37	0
$K\pi^0\pi\pi$	0.27	0	0	0.03	0	0	0.2

true Mode	reconstructed mode						
		$K\pi^0$	$K_s\pi$	$K_s\pi\pi^0$	$K\pi\pi$	$K_s\pi\pi\pi$	$K\pi^0\pi\pi$
$K\pi$		0.03	0.02	0.03	0.06	0	0.01
$K_s\pi^0$		0.02	0.1	0.26	0	0	0
$K\pi\pi^0$		0	0	0.01	0.09	0	0.21
$K_s\pi\pi$		0	0	0.2	0.02	0.13	0.02
$K_s\pi^0\pi\pi$		0	0	0	0	0.17	0
$K\pi\pi\pi$		0	0	0	0.01	0.04	0.33
$K\pi^0$		0.21	0.01	0.02	0.02	0	0
$K_s\pi$		0	0.1	0.31	0.01	0	0
$K_s\pi\pi^0$		0	0.01	0.3	0.01	0.03	0
$K\pi\pi$		0	0	0	0.1	0.01	0.31
$K_s\pi\pi\pi$		0	0	0.04	0	0.07	0
$K\pi^0\pi\pi$		0	0	0.02	0.02	0	0.47

Table 6.7: The fraction of reconstructed final candidates for each true mode for events where one of the multiple candidates is truth matched. Sig(nal) represents the truth matched candidates. This is for the  $X_s\gamma$  Monte Carlo sample for  $M_{Had}$  above 1.0 GeV/ $c^2$ .

true Mode	reconstructed mode						
	<i>Sig</i>	$K\pi$	$K_s\pi^0$	$K\pi\pi^0$	$K_s\pi\pi$	$K_s\pi^0\pi\pi$	$K\pi\pi\pi$
$K\pi$	0.8	0.12	0	0.04	0	0	0
$K_s\pi^0$	0.53	0	0.33	0	0	0	0
$K\pi\pi^0$	0.26	0	0	0.56	0	0	0.02
$K_s\pi\pi$	0.37	0	0	0	0.31	0.05	0.01
$K_s\pi^0\pi\pi$	0.2	0	0	0	0	0.6	0
$K\pi\pi\pi$	0.27	0	0	0.04	0	0	0.54
$K\pi^0$	0.26	0.03	0	0.07	0	0	0
$K_s\pi$	0.29	0	0.03	0	0	0	0
$K_s\pi\pi^0$	0	0	0	0	0.04	0.12	0
$K\pi\pi$	0.14	0.01	0	0.03	0	0.01	0.03
$K_s\pi\pi\pi$	0	0	0	0	0	0	0
$K\pi^0\pi\pi$	0	0	0	0	0	0	0
true Mode	reconstructed mode						
		$K\pi^0$	$K_s\pi$	$K_s\pi\pi^0$	$K\pi\pi$	$K_s\pi\pi\pi$	$K\pi^0\pi\pi$
$K\pi$		0.01	0	0	0.01	0	0
$K_s\pi^0$		0	0.03	0.11	0	0	0
$K\pi\pi^0$		0	0	0.01	0.05	0	0.08
$K_s\pi\pi$		0	0	0.17	0.01	0.07	0.01
$K_s\pi^0\pi\pi$		0	0	0	0	0.2	0
$K\pi\pi\pi$		0	0	0	0	0.04	0.12
$K\pi^0$		0.64	0	0	0	0	0
$K_s\pi$		0	0.56	0.11	0.01	0	0
$K_s\pi\pi^0$		0	0	0.82	0.02	0	0
$K\pi\pi$		0	0	0	0.68	0.01	0.1
$K_s\pi\pi\pi$		0	0	0	0	1	0
$K\pi^0\pi\pi$		0	0	0	0	0	1

Table 6.8: The fraction of reconstructed final candidates for each true mode after the best candidate selection. Sig(nal) represents the truth matched candidates. This is for the  $X_s\gamma$  Monte Carlo sample for  $M_{Had}$  above 1.0 GeV/ $c^2$ .

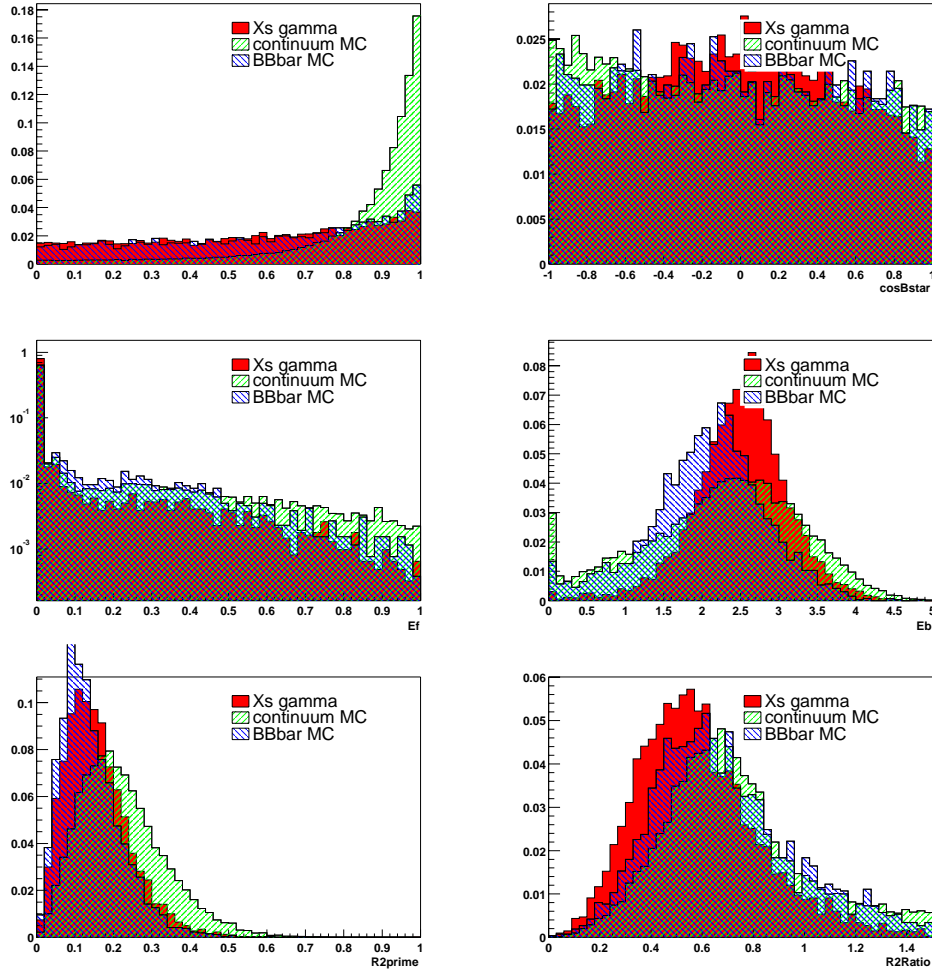


Figure 6.6: Distribution of the variables investigated as input to the Fisher Discriminant, for  $X_s\gamma$  MC events, **KN465**, continuum and generic  $B\bar{B}$  background MC. The histograms are all normalized to an area of 1.

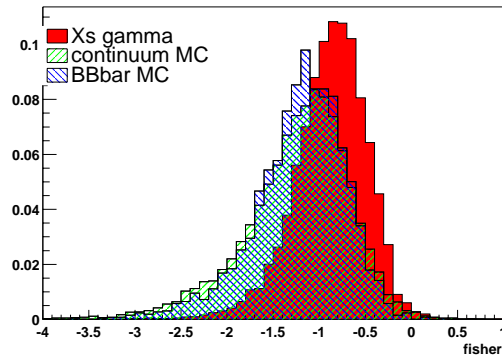


Figure 6.7: MC Fisher Discriminant distributions for  $X_s\gamma$  events (**KN465**), continuum and generic  $B\bar{B}$  background. The histograms are all normalized to an area of 1.

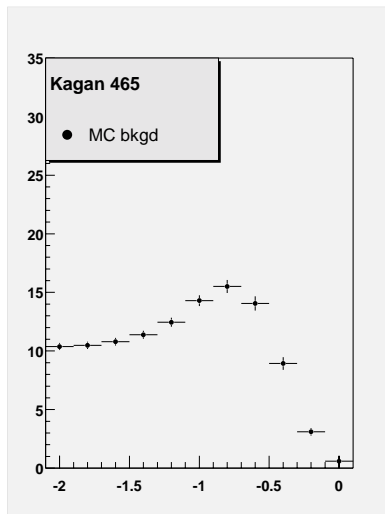


Figure 6.8: Optimization plots for the Fisher Discriminant made using just true B for the signal.

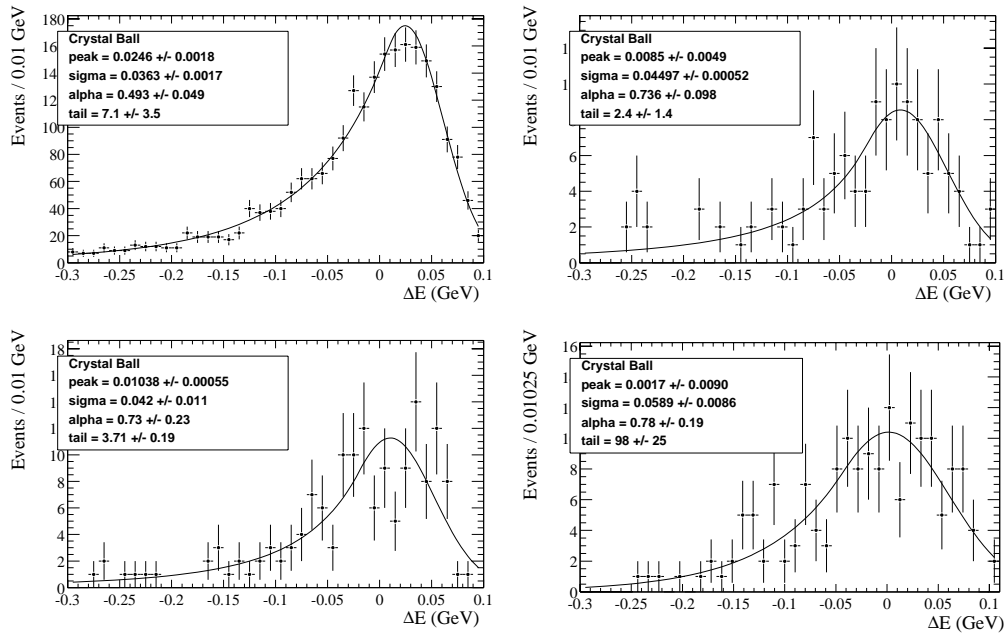


Figure 6.9:  $\Delta E^*$  resolution for the modes: Upper Left:  $K_s\pi$ , Upper Right:  $K_s\pi\pi$ , Lower Left:  $K\pi\pi$ , Lower Right:  $K\pi\pi^0$ .

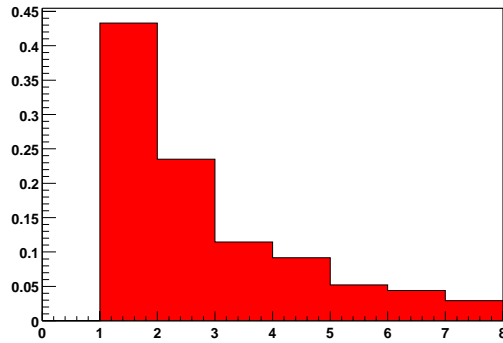


Figure 6.10: Plot of the number of candidates per event for the  $X_s\gamma$  Monte Carlo sample. The histogram is normalized to an area of 1.

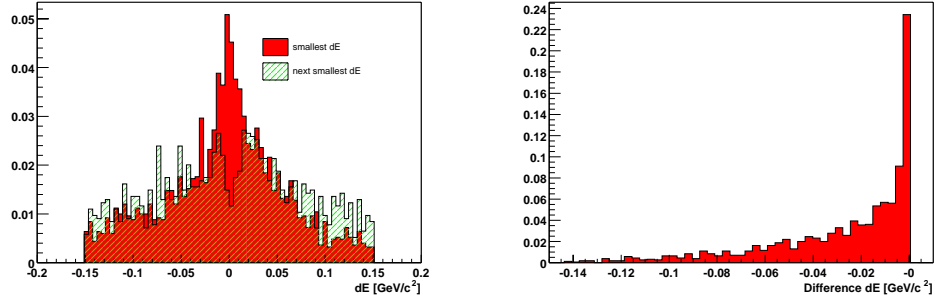


Figure 6.11: Left: Plot of  $\Delta E^*$  for the candidate with the smallest and the next to smallest  $\Delta E^*$  for  $X_s\gamma$ . Right: Plot of the difference between the  $\Delta E^*$  of the candidate with the smallest and next to the smallest  $\Delta E^*$  for  $X_s\gamma$ .

# Chapter 7

## Background Composition

There are three background sources for this analysis, continuum,  $B\bar{B}$ , and cross-feed. The cross-feed background comes from wrongly reconstructed signal and has a small peaking component. The  $B\bar{B}$  background comes mostly from decays where the high energy photon candidate is from an asymmetric  $\pi^0$  or  $\eta$  decay, and has a small peaking component at high  $M_{Had}$ . The continuum background is the largest of the three and comes from initial state radiation (ISR) or two-jet events where the high energy photon candidate is again from an asymmetric  $\pi^0$  or  $\eta$  decay. The continuum background does not peak in the signal  $m_{ES}$  region.

In the following, we describe the composition of the background after all selection cuts are applied and the best candidate is chosen. Figure 7.1 shows the background levels (over the full  $m_{ES}$  range 0.6–2.4 GeV/ $c^2$ , i.e. not just the peaking component) as a function of  $M_{Had}$  after the selection. The background subtraction method is described in the next chapter.

### 7.1 Composition of continuum and $B\bar{B}$ backgrounds

In Table 7.1 we show the breakdown of the backgrounds according to the final state. The first column lists the reconstructed final states. The next columns are the number of events in the generic Monte Carlo samples which have been reconstructed in each mode. All the numbers are scaled to the data luminosity (20.7 fb<sup>-1</sup>), and so can be directly compared. The numbers correspond to events in the full  $m_{ES}$  range, 5.21 to 5.3 GeV/ $c^2$ . The samples used (columns) are the generic  $B^0\bar{B}^0$ ,  $B^+B^-$ ,  $uds$  and  $c\bar{c}$ . The last two columns are the total  $B\bar{B}$  or

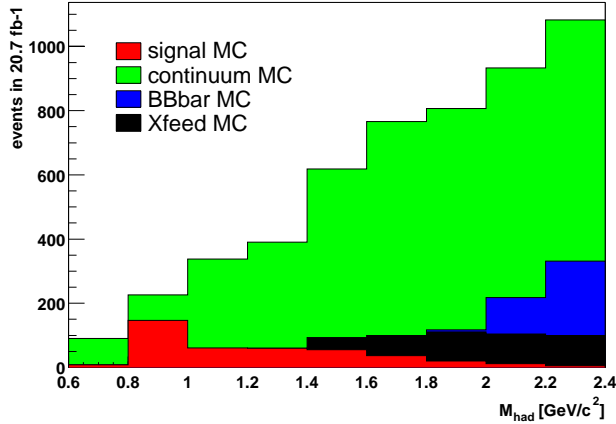


Figure 7.1: The different background levels after the full selection and over the full  $m_{ES}$  range,  $0.6\text{--}2.4\text{ GeV}/c^2$ , i.e. not just in the peaking region. The signal from the Monte Carlo is also shown for reference.

continuum samples respectively. The continuum contribution dominates for all final states, and the  $uds$  contribution is slightly larger than the  $c\bar{c}$  one since it has a larger cross-section.

The first six reconstructed final states listed (as in Table 4.1) are final states from  $B^0\bar{B}^0$  decays and the last six are from  $B^+B^-$  decays. Note that there is little correlation between the generation of  $B^0\bar{B}^0$  or  $B^+B^-$  events, and the reconstruction of  $B^0$  versus  $B^+$  candidates. For example, the  $K_S\pi\pi$  mode is a  $B^0$  decay mode and has 7 events from the  $B^0\bar{B}^0$  Monte Carlo and 6 events from the  $B^+B^-$  Monte Carlo. There are slightly more events from the correct type of  $B$  meson, but there is not a statistically significant difference. This indicates that it is quite likely that an additional charged pion from the other  $B$  has been added to the reconstructed state. This will change the sign from neutral to charged and vice versa.

Figure 7.2 shows the background in bins of hadronic mass for  $B\bar{B}$  and continuum Monte Carlo. The top plot shows the total  $B\bar{B}$  and continuum background. The bottom left plot shows the  $B\bar{B}$  background and the separate contributions from  $B^0\bar{B}^0$  and  $B^+B^-$  separately. The bottom right plot shows the continuum background and the separate contributions from  $uds$  and  $c\bar{c}$  separately. All the samples are normalized to  $20.7\text{ fb}^{-1}$ , and so can be directly compared.

Both continuum and  $B\bar{B}$  backgrounds increase as a function of  $M_{Had}$  (de-

mode	generic Monte Carlo sample					
	$B^0\bar{B}^0$	$B^+B^-$	$uds$	$c\bar{c}$	$B\bar{B}$	<i>continuum</i>
$K\pi$	9	7	250	145	16	394
$K_S\pi^0$	4	1	48	40	6	88
$K\pi\pi^0$	35	47	502	365	82	867
$K_S\pi\pi$	7	6	124	96	13	219
$K_S\pi^0\pi\pi$	34	35	193	158	69	351
$K\pi\pi\pi$	66	52	202	180	118	382
$K\pi^0$	3	7	150	100	10	250
$K_S\pi$	6	8	114	60	14	174
$K_S\pi\pi^0$	18	25	276	182	43	458
$K\pi\pi$	25	44	373	278	69	652
$K_S\pi\pi\pi$	24	22	105	76	45	180
$Kp\bar{i}^0\pi\pi$	120	157	664	558	277	1222

Table 7.1: Number of background events from  $B\bar{B}$  and continuum Monte Carlo for each final state. The entries are scaled to the data luminosity.

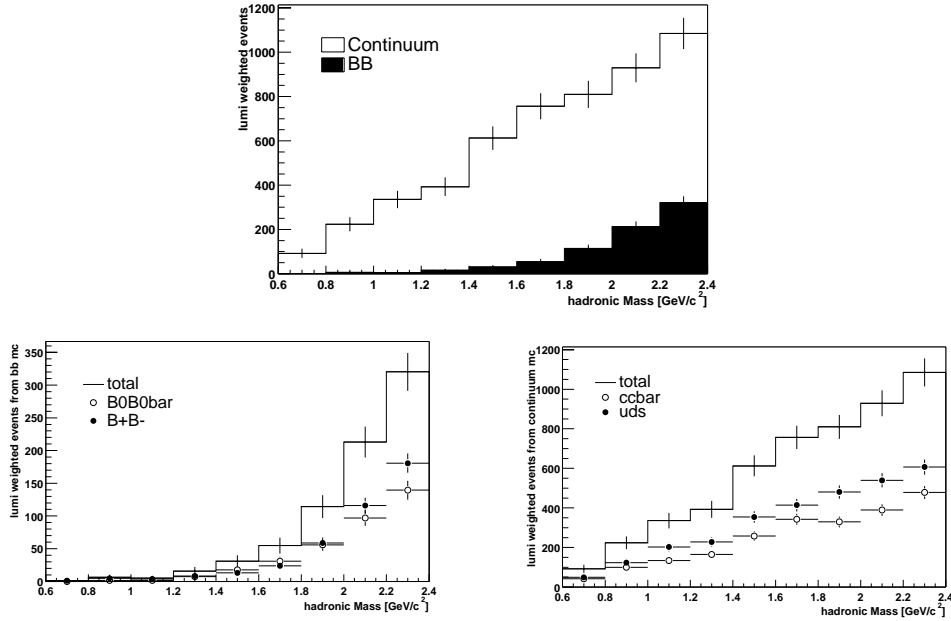


Figure 7.2: Dependence of  $B\bar{B}$  and continuum background on hadronic mass after all the selection cuts are applied and the choice of the best candidate made. All samples are normalized to  $20.7 \text{ fb}^{-1}$ .

crease as a function of  $E_\gamma^B$ ). For  $M_{Had} < 1.8 \text{ GeV}/c^2$  the level of  $B\bar{B}$  background is quite small, but at the highest mass considered,  $M_{Had} = 2.4 \text{ GeV}/c^2$ , the  $B\bar{B}$  background is significant, although still only about a third of the continuum background.

The continuum background is expected to be an even mixture of initial state radiation (ISR), in which a single high energy photon is radiated directly from the  $e^+$  or  $e^-$ , and of two-jet events ( $q\bar{q}$ ), in which the photon is usually the daughter of a  $\pi^0$  or  $\eta$ . Note, in Figure 7.2 (right plot), that the contributions from the **uds** and **ccb** generic Monte Carlo samples are almost equal, with a slight predominance of the **uds**. The continuum background  $m_{ES}$  distribution can be fit well by an Argus shape (see Appendix A for details about the PDF expression), see Figure 7.3.

The  $B\bar{B}$  backgrounds come mainly from decays with high multiplicity and therefore high hadronic mass where the high energy photon is the daughter of a

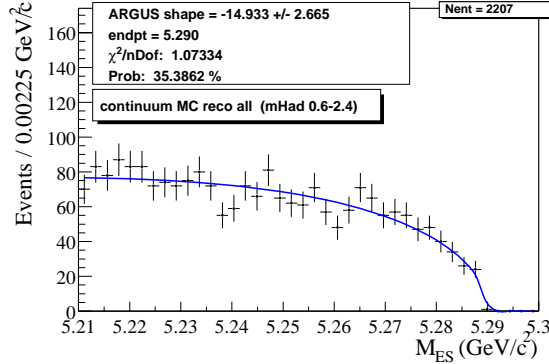


Figure 7.3: Fit of the Continuum background Monte Carlo (**uds** and **ccb**), over all  $M_{Had}$ , to an Argus shape. The Argus endpoint is fixed while the shape is fit. The sample used is  $8.7 \text{ fb}^{-1}$ .

$\pi^0$  or  $\eta$  which decayed asymmetrically. A large contribution is from  $B \rightarrow D^{(*)}X$  decays. To become a background event within the  $|\Delta E^*| < 0.15$  cut, it is usually necessary to add in a low energy track or  $\pi^0$  from the other  $B$  to replace the second unused photon from the  $\pi^0$  or  $\eta$  when reconstructing the  $B$ . Although we do not expect such a substitution to lead to a background that peaks strongly in the  $m_{ES}$  distribution, we do find some peaking component.

To investigate this we fit the generic  $B\bar{B}$  events (sum of  $B^0\bar{B}^0$  and  $B^+B^-$  with a luminosity of  $14.1 \text{ fb}^{-1}$ ) with an Argus background shape and a Crystal Ball signal shape (see Appendix A for details about the functions). The fits are shown in Figure 7.4. The top plot is over all  $M_{Had}$ . The bottom left is in the low  $M_{Had}$  region  $0.6\text{-}1.8 \text{ GeV}/c^2$ , and the bottom right plot is in the high  $M_{Had}$  region  $1.8\text{-}2.4 \text{ GeV}/c^2$ . Note that the fit in this figure was done fixing the Argus endpoint, and the Crystal Ball peak, tail and  $\alpha$  parameters to values from a fit to the signal Monte Carlo over the same  $M_{Had}$  range, (i.e. free parameters: Argus shape, Crystal Ball width and the CB fraction). These fits are shown just to have a feeling for the shape of the background. The final fits will be done slightly differently. The background subtraction method is discussed in Chapter 9.

Note that for all these studies the  $K^*\gamma$  and  $X_s\gamma$  signal events have been removed from the generic  $B\bar{B}$  sample by looking at the truth information and discarding them before any event selection is applied.

In the highest  $M_{Had}$  bins we find positive Crystal Ball yields that become significant compared to the signal yield. There is a small yield in the lower  $M_{Had}$

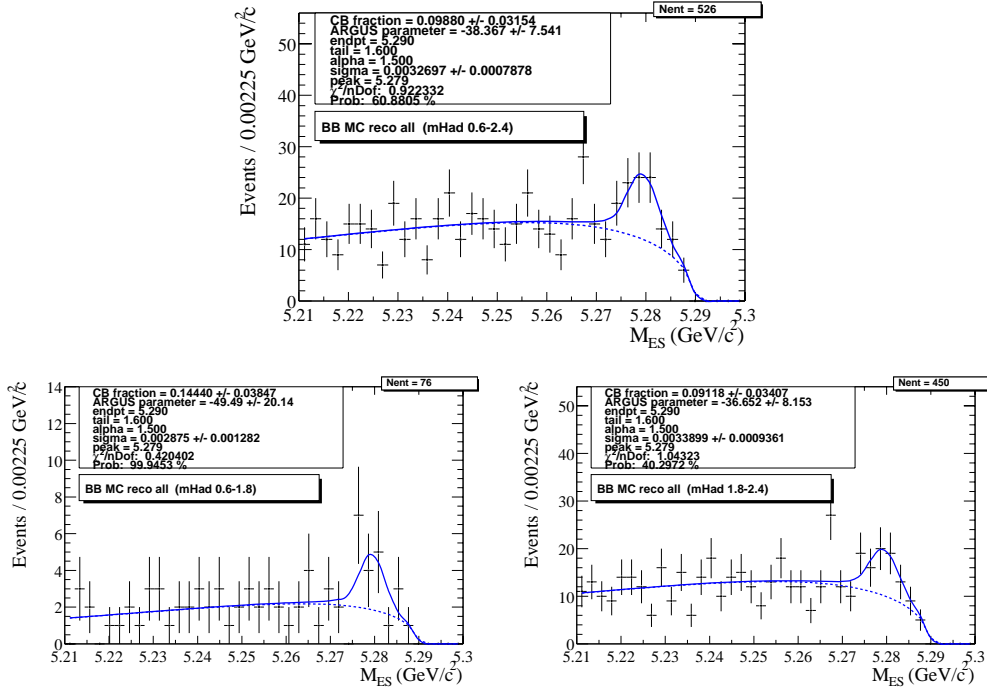


Figure 7.4: Fit of the  $B\bar{B}$  background (with luminosity  $14.1 \text{ fb}^{-1}$ ) to an Argus plus Crystal Ball function. The top plot is for the whole hadronic mass range, and the lower plots show 2 hadronic mass bins ( $0.6 - 1.8, 1.8 - 2.4$ )  $\text{GeV}/c^2$ .

region, but note that the lower left plot in Figure 7.4 corresponds to range in  $M_{Had}$  spanning  $1.2 \text{ GeV}/c^2$  and has only 76 events, while the right plot covers only  $0.6 \text{ GeV}/c^2$  and has 550 events. Splitting the lower  $M_{Had}$  range into  $200 \text{ MeV}/c^2$  bins will leave severely statistics limited distributions which will have a peaking yield consistent with zero. For now we neglect this very small contribution and consider the peaking contribution only above  $M_{Had} = 1.8 \text{ GeV}/c^2$ .

We have to correct for this peaking background in our  $b \rightarrow s\gamma$  yield since it will add to our data yield. This correction is made by subtracting directly the Crystal Ball yield from the final fits to the generic  $B\bar{B}$  Monte Carlo, scaled by luminosity, from the data yield in each  $M_{Had}$  bin. This is one aspect of this analysis which relies heavily on the Monte Carlo. We are clearly sensitive to the statistics of the  $B\bar{B}$  Monte Carlo sample. We have a  $14.1 \text{ fb}^{-1}$  sample of generic  $B\bar{B}$  Monte Carlo, which must be scaled by a factor of 1.5 to match the  $20.7 \text{ fb}^{-1}$  of on-resonance data.

To identify the origin of the peaking  $B\bar{B}$  background, we examine the Monte Carlo truth information for events within the signal region  $5.27 < m_{\text{ES}} < 5.29 \text{ GeV}/c^2$ , and find that for almost all of the events the high energy gamma comes from asymmetric  $\pi^0$  or  $\eta$  decays, as expected. Table 7.2 lists the percent of the time that the high energy gamma has a specific mother for all events in the region  $m_{\text{ES}} > 5.21 \text{ GeV}/c^2$  and also just in the signal region.

Parent of $\gamma$	$m_{\text{ES}} > 5.21 \text{ GeV}/c^2$		$m_{\text{ES}} > 5.27 \text{ GeV}/c^2$	
	$B^0$	$B^+$	$B^0$	$B^+$
$\pi^0$	68%	73%	62%	73%
$\eta$	26%	17%	35%	9.8%
$\eta'$	0.95%	1.2%	0%	2.4%
$\rho$	0%	2.5%	0%	2.4%
$\omega$	0%	0.6%	0%	2.4%
$e$	3.8%	1.2%	0%	2.4%
$K^*$	0%	0.6%	0%	0%
$n$	0.95%	1.9%	0%	2.4%
$B$	0%	0.6%	0%	2.4%
<i>string</i>	0.95%	0.6%	3.5%	2.4%

Table 7.2: Percentage of  $B\bar{B}$  MC events after all the cuts are applied and the best candidate chosen, listed according to the mother of the identified high energetic photon.

One way that these background events can escape our background rejection is if the other photon from the  $\pi^0$  or  $\eta$  decay was either not found in the reconstruction or was not used in our calculation of the  $\pi^0$  and  $\eta$  vetoes described in Chapter 6.

The most likely way that the other photon would not be found in the reconstruction is if it falls outside of the angular fiducial cuts in the photon selection. To investigate this we look at the angular distribution, at the Monte Carlo truth level, of the other daughter photon from the  $\pi^0$  or  $\eta$  decay for our  $B\bar{B}$  background events in the  $m_{\text{ES}}$  signal region. The left two plots in Figure 7.5 show the truth cosine of the theta angle in the lab frame for the other daughter photon. Most of the entries fall within the angular cut, and therefore most of the other daughter photons are not being cut out in this way.

Next we investigate if these other daughter photons are being used in the  $\pi^0$  and  $\eta$  vetoes. These vetoes are performed by checking for overlap between

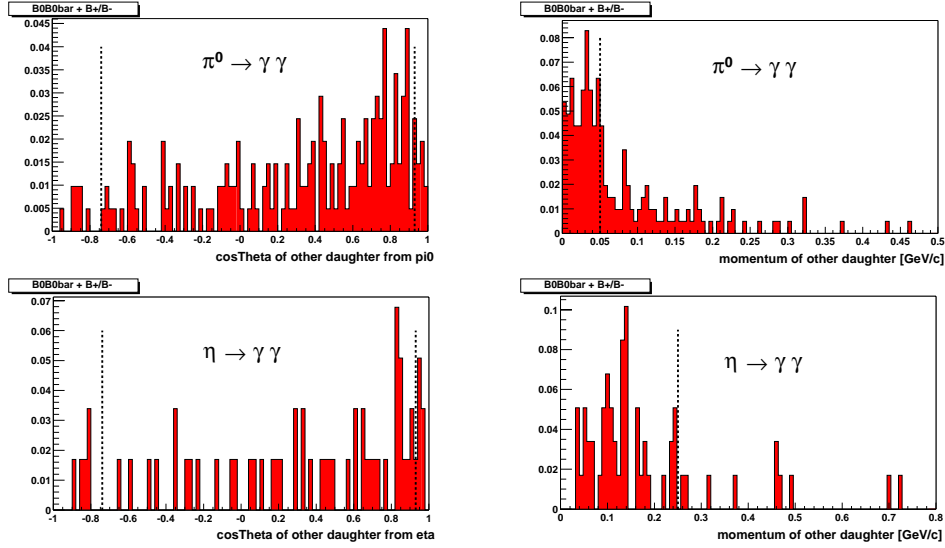


Figure 7.5: Momentum and  $\cos\theta$  distributions for the other daughter of a  $\pi^0$  or  $\eta$  decay which contributed a high energy photon in  $B\bar{B}$  background events. (The histograms have been normalized to an area of 1.)

the high energy photon candidate and a  $\pi^0$  or  $\eta$  list. If the high energy photon candidate can be combined with another photon in the event and forms a  $\pi^0$  or  $\eta$  with a reconstructed mass within a window around the nominal  $\pi^0$  or  $\eta$  mass, the high energy photon is rejected. There is a default momentum cut on the photons which are used to form the  $\pi^0$  or  $\eta$  list of  $50 \text{ MeV}/c$  for the  $\pi^0$  list and  $250 \text{ MeV}/c$  for the  $\eta$  list.

This momentum cut is a result of the assumption that most  $\pi^0$  or  $\eta$  decays are not very asymmetric. However, in this analysis, we expect that our background comes from very asymmetric  $\pi^0$  or  $\eta$  decays, because our signal photon has high energy. The default vetoes will be less effective for our analysis since the other daughter photon might not pass the momentum cut to be used in the veto.

The two right plots in Figure 7.5 shows the truth momentum of the other daughter photon from the high energy photon in  $B\bar{B}$  background events that pass all the selection, including the  $\pi^0$  and  $\eta$  vetoes, in the  $m_{\text{ES}}$  signal region. The top (bottom) right plot is for events where the high energy photon candidate came from a  $\pi^0$  ( $\eta$ ) decay. We can see that the distributions peak below the momentum cuts,  $50 \text{ MeV}/c$  for the  $\pi^0$  list and  $250 \text{ MeV}/c$  for the  $\eta$  list. These events are not being rejected by the  $\pi^0$  or  $\eta$  veto because the other daughter

does not pass the minimum momentum cut-off to be used in the vetoes.

There are systematic uncertainties due to our understanding of the generic Monte Carlo. We need to not only understand what is simulated, but also what might be missing from the generic sample. Especially at high  $M_{Had}$  there is not much that has been experimentally measured. We add a systematic error on the peaking  $B\bar{B}$  background yield to account for this.

We expect a small contribution to the background from  $b \rightarrow d\gamma$  decays. This contribution is suppressed by the square of  $V_{td}/V_{ts}$ , to an expectation of about 4%. Applying tight kaon PID reduces this further since the fake rate is small. At higher multiplicity we have several possible charged pions but the fake rate still should be less than 10%. This gives an expectation of less than 0.5% for the  $b \rightarrow d\gamma$  rate which is negligible.

## 7.2 Cross-Feed Background

In this section the third background source, cross-feed, is investigated. We first give a description and definition of the cross-feed background and then present a study of the hadronic mass resolution which helps justify our definition of this background. We also investigate the sources of the cross-feed background, by looking at the Monte Carlo truth.

### 7.2.1 Cross-feed background definition

A large source of background comes from signal events that have been wrongly reconstructed. This “cross-feed” background can be separated out from the correctly reconstructed, or “signal” events in the Monte Carlo and studied.

After the selection cuts are applied and the choice of the best candidate is performed in the reconstructed signal Monte Carlo, our sample is made of:

- “real signal” events, that is events for which the true B is identified.
- cross-feed background events, which indicates signal events whose hadronic system is not correctly identified. There are two categories of events which are of concern:
  - “feed-out” events in which the true B is found in the event before the choice of the best candidate, but an alternative candidate is chosen instead. These cases are summarized in Table 6.8.

- “feed-in” events in which the true B is not found, but an alternative candidate satisfies the selection cuts.

The twelve reconstructed modes can lead to feed-in due to finite detector efficiency. The modes not considered in the final analysis can only lead to feed-in. Collectively these give rise to a “cross-feed” background. Both feed-out and feed-in events are distributed over the full  $m_{ES}$  range.

To separate the “signal” and cross-feed samples we can use a kind of Monte Carlo truth matching. The signal events are selected by requiring that the true and reconstructed mode are the same and that the difference between the true and reconstructed hadronic mass is within  $50 \text{ MeV}/c^2$ . The cross-feed includes all other events. As shown earlier:

- “signal” :  
(reco mode = true mode) & ( $| \text{true}M_{Had} - \text{reco}M_{Had} | < 50 \text{ MeV}/c^2$ )
- cross-feed :  
reco mode  $\neq$  true mode or  
(reco mode = true mode) & ( $| \text{true}M_{Had} - \text{reco}M_{Had} | > 50 \text{ MeV}/c^2$ )

The cut on the difference between the true and reconstructed hadronic mass excludes events from the signal sample for which the correct mode is reconstructed but at least one daughter is not the true daughter. This is part of the “feed-in” sample described above and belongs in the cross-feed sample.

We can see that this hadronic mass difference cut makes sense by looking at the distribution of difference between the true and reconstructed hadronic mass (for the  $X_s\gamma$  Monte Carlo sample, with  $M_{Had} = 1.0 - 2.4 \text{ GeV}$ ). The left plot in Figure 7.6 shows the difference in the true and reconstructed  $M_{Had}$  for events where the true and reconstructed mode is the same. The lines show the  $50 \text{ MeV}/c^2$  cut, where 69% of the events fall within the cuts. The right plot in Figure 7.6 shows the same distribution for events where the true and reconstructed mode are not the same. The cross-feed sample is made up of all the events in the right plot plus the events outside of the  $50 \text{ MeV}/c^2$  cut in the left plot. Note that the y-axis has a log scale for both the plots.

These criteria separate well the “signal” (from now on just called signal) events from the wrongly reconstructed ones. It is clear that there is some background underneath the peak which we estimate to be on the order of 3%. The hadronic mass resolution is discussed further in the next section. There is also a systematic error associated with the  $50 \text{ MeV}/c^2$  cut in  $\Delta M_{Had}$  which is discussed

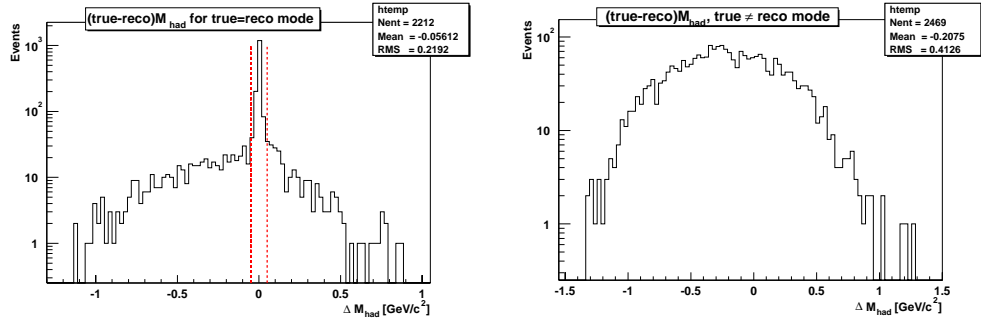


Figure 7.6: True minus reconstructed  $M_{Had}$  for events reconstructed with the true mode (left) or another mode (right). The lines show the 50  $\text{MeV}/c^2$  cut used to define the “signal” sample.

in Chapter 12.

Figure 7.7 shows the signal and cross-feed  $m_{ES}$  distributions for the  $M_{Had}$  range 1.0-2.4  $\text{GeV}/c^2$ . Chapter 9 discusses the method for fitting these distributions in bins of hadronic mass and Chapter 10 gives the results.

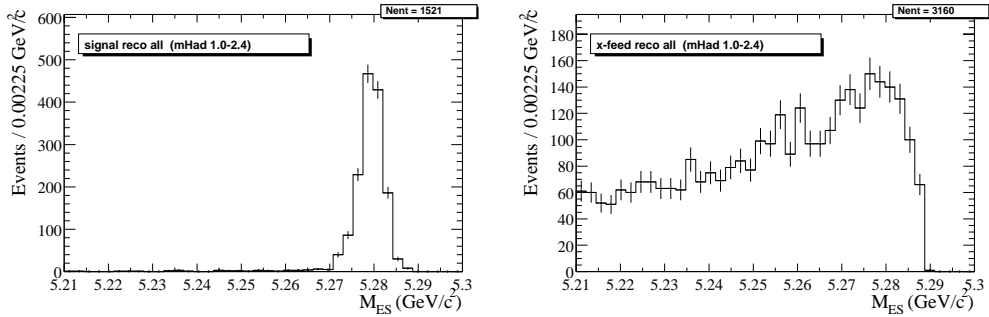


Figure 7.7: Sample signal and cross-feed distributions for  $M_{Had}$  1.0-2.4  $\text{GeV}/c^2$ .

We expect that the cross-feed peaks in the signal region, but it is not clear how to best describe the peaking behavior, or how strong it is.

As a quick check, we have fit the cross-feed over all  $M_{Had}$  (0.6-2.4  $\text{GeV}/c^2$ ), to obtain large statistics, to either a Crystal Ball plus Argus or just an Argus alone. We have summed up the  $K^*\gamma$  and  $X_s\gamma$  Monte Carlo samples with a luminosity

of  $125fb^{-1}$ . The fits can be seen in Figure 7.8. We have constrained the Crystal Ball parameters to values obtained from a fit to the signal sample in the same  $M_{Had}$  range.

It is clear from the fits that the distribution is not fit well with just an Argus function. There is clearly some sort of peaking contribution in the signal region. However, the Argus plus Crystal Ball function does not perfectly fit the distribution. If we had higher Monte Carlo statistics, we could examine other parameterizations for the cross-feed distribution.

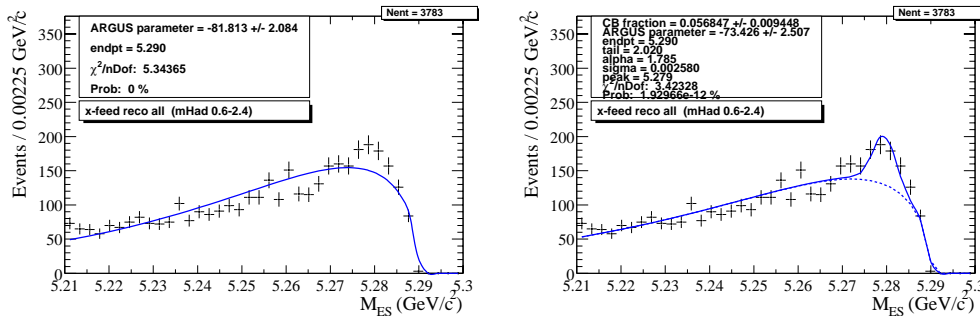


Figure 7.8: Fits to the cross-feed  $m_{ES}$  distribution over all  $M_{Had}$  (0.6-2.4  $GeV/c^2$ ), with either a Argus or Argus plus Crystal Ball function. The fit allowing for some peaking component is clearly better.

## 7.2.2 Hadronic mass resolution

In order to show that the reconstruction of the  $B$  candidates does not deform the hadronic mass spectra we have compared the generated and reconstructed hadronic mass distributions for signal Monte Carlo events.

We have broken up the event sample, after the full selection, into ten bins of true hadronic mass. We then split each of the ten samples again into nine bins of reconstructed hadronic mass.

For the first two true  $M_{Had}$  bins,  $M_{Had} = 0.6-0.8 GeV/c^2$  and  $0.8-1.0 GeV/c^2$ , only the  $K^*\gamma$  MC is considered since in this  $M_{Had}$  range only the resonance is considered. A combined sample of  $K\pi + K_s\pi^0 + K\pi^0 + K_S\pi$  is used. For the rest of the true  $M_{Had}$  bins the KN465  $Xs\gamma$  sample is used. The  $K^*\gamma$  samples are scaled down to match the luminosity of the  $Xs\gamma$ ,  $125 fb^{-1}$ .

We can start to separate the signal and cross-feed background by requiring that the true and reconstructed mode is the same. We don't apply the  $\Delta M_{Had} <$

50 MeV/ $c^2$  cut in the signal sample definition presented earlier since we want to investigate the  $M_{Had}$  distribution. We restrict our study to the peaking region of the  $m_{ES}$  distribution (5.27 to 5.29 GeV/ $c^2$ ). The  $M_{Had}$  resolution of the peaking events is an important quantity since leakage into or out of the background under the  $m_{ES}$  peak should not effect our measurement of the signal yield.

Table 7.3 shows the number of events for each selection for events where the true and reconstructed mode is the same. The number in parenthesis is the percent of reconstructed events in the true  $M_{Had}$  bin that fall in each reconstructed  $M_{Had}$  bin, i.e.  $N_{true,reco}/N_{true}$ . The small off-diagonal elements show that the leakage to neighboring bins is fairly small for events where the true and reconstructed modes are the same.

The last column of the table lists the total number (percent) of events for each true  $M_{Had}$  bin where the true and reconstructed mode is the same and the  $m_{ES}$  of the events is in the peaking region (5.27 to 5.29 GeV/ $c^2$ ). This is not quite our signal sample, but the background that is left is not very large. The percent decreases as  $M_{Had}$  increases due to two effects. As  $M_{Had}$  increases the final states that we reconstruct represent a smaller fraction of all the possible final states, roughly the fraction decreases from 65% to 25%. The states that we do not reconstruct can only show up as background and therefore there is more background at higher  $M_{Had}$ . The other effect is that events at higher  $M_{Had}$  are more likely to be higher multiplicity states which are less efficient to reconstruct.

Table 7.4 shows the number of events in the peaking  $m_{ES}$  region (5.27 to 5.29 GeV/ $c^2$ ) for events where the true and reconstructed mode are not the same. The denominator used to get the percent is still  $N_{true}$ , the number of reconstructed events after all the selection in one true  $M_{Had}$  bin. Looking vertically down the columns we see that this peaking background mostly comes from events where the true hadronic mass is outside the range it is reconstructed in.

To get a better idea of the width of the reconstructed  $M_{Had}$  distributions Figure 7.9 shows the difference between true and reconstructed  $M_{Had}$  for each event where the true and reconstructed mode is the same in the nine true  $M_{Had}$  bins, and where  $\Delta M_{Had} \leq 25$  MeV/ $c^2$ . This cut excludes only small tails in the  $\Delta M_{Had}$  distribution. Again, this is for events which fall in the peaking region of  $m_{ES}$  (5.27 to 5.29 GeV/ $c^2$ ). The distributions are fit with a Gaussian and linear function. Table 7.5 lists the widths from the fits in each true  $M_{Had}$  bin. The hadronic mass resolution for these events is on average 4.5 MeV/ $c^2$  which is small compared to the 200 MeV/ $c^2$  bins of  $M_{Had}$  in which the branching fractions are measured. This means that there is not much leakage from one  $M_{Had}$

true $M_{Had}$	reconstructed $M_{Had}$				
	0.6-0.8	0.8-1.0	1.0-1.2	1.2-1.4	1.4-1.6
0.6-0.8	42 (57.5)	3 (4.1)	1 (1.4)	0 (0)	0 (0)
0.8-1.0	6 (0.44)	883 (64.5)	10 (0.73)	3 (0.22)	2 (0.15)
1.0-1.2	1 (0.13)	12 (1.6)	358 (47.0)	11 (1.4)	15 (2.0)
1.2-1.4	2 (0.20)	3 (0.30)	19 (1.9)	354 (35.3)	32 (3.2)
1.4-1.6	0 (0)	1 (0.10)	4 (0.42)	21 (2.2)	327 (34.1)
1.6-1.8	0 (0)	1 (0.12)	1 (0.12)	2 (0.23)	16 (1.9)
1.8-2.0	0 (0)	0 (0)	0 (0)	1 (0.17)	4 (0.66)
2.0-2.2	0 (0)	0 (0)	0 (0)	1 (0.28)	1 (0.28)
2.2-2.4	0 (0)	0 (0)	0 (0)	0 (0)	0 (0)
> 2.4	0 (0)	0 (0)	0 (0)	0 (0)	0 (0)

true $M_{Had}$	reconstructed $M_{Had}$				
	1.6-1.8	1.8-2.0	2.0-2.2	2.2-2.4	sum
0.6-0.8	0 (0)	0 (0)	0 (0)	0 (0)	46 (63.0)
0.8-1.0	1 (0.07)	2 (0.15)	0 (0)	0 (0)	907 (66.2)
1.0-1.2	4 (0.53)	1 (0.13)	0 (0)	0 (0)	402 (52.8)
1.2-1.4	14 (1.4)	6 (0.60)	3 (0.30)	1 (0.10)	434 (43.2)
1.4-1.6	15 (1.6)	11 (1.1)	5 (0.52)	3 (0.31)	387 (40.4)
1.6-1.8	219 (25.7)	18 (2.1)	6 (0.70)	2 (0.23)	265 (31.1)
1.8-2.0	18 (3.0)	119 (19.7)	15 (2.5)	7 (1.2)	164 (27.2)
2.0-2.2	4 (1.1)	7 (1.9)	76 (21.0)	11 (3.0)	100 (27.6)
2.2-2.4	0 (0)	0 (0)	1 (0.63)	32 (20.1)	33 (20.8)
> 2.4	0 (0)	0 (0)	0 (0)	2 (2.3)	2 (2.3)

Table 7.3: The number of events, with (true = reco) mode and  $m_{ES}$  in the peaking region (5.27 to 5.29 GeV/ $c^2$ ), passing the full selection in bins of true and reconstructed  $M_{Had}$ . The sum (last column) is a horizontal sum in each true  $M_{Had}$  bin. The number in parenthesis is the percent of the total reconstructed events in the true  $M_{Had}$  bin.

true $M_{Had}$	reconstructed $M_{Had}$				
	0.6-0.8	0.8-1.0	1.0-1.2	1.2-1.4	1.4-1.6
0.6-0.8	0 (0)	1 (1.4)	2 (2.7)	2 (2.7)	1 (1.4)
0.8-1.0	4 (0.29)	9 (0.66)	21 (1.5)	33 (2.4)	32 (2.3)
1.0-1.2	3 (0.39)	4 (0.53)	14 (1.8)	29 (3.8)	29 (3.8)
1.2-1.4	4 (0.40)	11 (1.1)	15 (1.5)	20 (2.0)	35 (3.5)
1.4-1.6	1 (0.10)	4 (0.42)	7 (0.73)	23 (2.4)	26 (2.7)
1.6-1.8	0 (0)	1 (0.12)	2 (0.23)	11 (1.3)	25 (2.9)
1.8-2.0	0 (0)	1 (0.17)	1 (0.17)	10 (1.7)	15 (2.5)
2.0-2.2	0 (0)	0 (0)	0 (0)	0 (0)	4 (1.1)
2.2-2.4	0 (0)	0 (0)	0 (0)	0 (0)	0 (0)
> 2.4	0 (0)	0 (0)	0 (0)	0 (0)	1 (1.1)

true $M_{Had}$	reconstructed $M_{Had}$				
	1.6-1.8	1.8-2.0	2.0-2.2	2.2-2.4	sum
0.6-0.8	1 (1.4)	1 (1.4)	0 (0)	0 (0)	8 (11.0)
0.8-1.0	22 (1.6)	13 (0.95)	8 (0.58)	3 (0.22)	144 (10.5)
1.0-1.2	19 (2.5)	7 (0.92)	4 (0.53)	7 (0.92)	116 (21.8)
1.2-1.4	25 (2.5)	15 (1.5)	16 (1.59)	11 (1.1)	152 (15.1)
1.4-1.6	26 (2.7)	27 (2.8)	21 (2.2)	11 (1.1)	146 (15.2)
1.6-1.8	33 (3.9)	32 (3.8)	20 (2.3)	21 (2.5)	133 (15.6)
1.8-2.0	15 (2.5)	33 (5.5)	21 (3.5)	24 (4.0)	132 (21.9)
2.0-2.2	12 (3.3)	11 (3.0)	15 (4.1)	20 (5.5)	62 (17.1)
2.2-2.4	3 (1.9)	4 (2.5)	11 (6.9)	8 (5.0)	26 (16.4)
> 2.4	1 (1.1)	1 (1.1)	5 (5.7)	8 (9.1)	16 (18.2)

Table 7.4: The number of events in the peaking  $m_{ES}$  range (5.27 to 5.29 GeV/ $c^2$ ), with (true != reco) mode, passing the full selection in bins of true and reconstructed  $M_{Had}$ . The sum (last column) is a horizontal sum in each true  $M_{Had}$  bin. The number in parenthesis is the percent of the total reconstructed events in the true  $M_{Had}$  bin.

bin to another due to resolution for our signal events. Although, the wrongly reconstructed events can more easily move around in  $M_{Had}$ .

true $M_{Had}$	sigma MeV/ $c^2$
0.6-0.8	$2.6 \pm 0.2$
0.8-1.0	$3.0 \pm 0.1$
1.0-1.2	$3.9 \pm 0.2$
1.2-1.4	$4.9 \pm 0.4$
1.4-1.6	$5.5 \pm 0.5$
1.6-1.8	$6.3 \pm 0.7$
1.8-2.0	$5.2 \pm 0.9$
2.0-2.2	$4.6 \pm 1.0$
2.2-2.4	$3.9 \pm 1.0$

Table 7.5:  $M_{Had}$  resolution. The width of the Gaussian from the fits to the (true – reco)  $M_{Had}$  distribution for (true = reco) mode and  $m_{ES}$  in the peaking region (5.27 to 5.29 GeV/ $c^2$ ) shown in Figure 7.9.

### 7.2.3 Cross–feed Sources Study

To understand where the cross–feed comes from we have split the Monte Carlo signal sample into eight different truth categories by looking at the Monte Carlo truth.

We first divide the Monte Carlo into signal and cross–feed samples, using the definition given in Section 7.2.1. The signal sample is, by definition, made up of events where the true and reconstructed mode is the same. In the signal sample we can investigate how many of the true generated events pass our selection.

The cross–feed sample is then divided into 8 categories defined in Table 2.2 on page 17 :

- true 2-,3-,4-,5-,6-body (4 final states each),
- true  $2\pi^0$  (8 final states),
- true  $sss$  (4 final states)
- *other* (all other events which do not fall into one of the above categories)

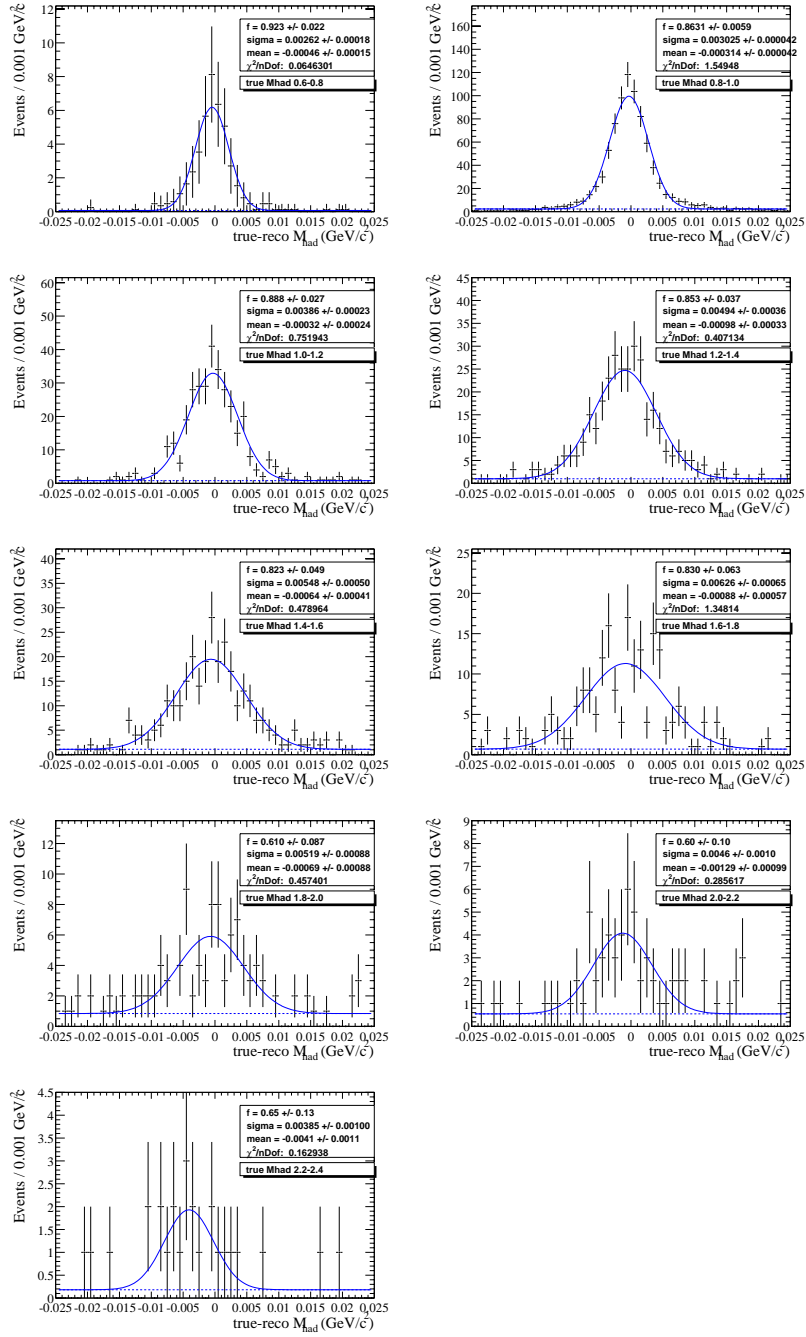


Figure 7.9: The difference between true and reconstructed (true – reco)  $M_{Had}$  in nine bins of true  $M_{Had}$  for events with true = reco mode and where  $|\text{true}M_{Had} - \text{reco}M_{Had}|$  less than  $25 \text{ MeV}/c^2$ , and  $m_{ES}$  in the peaking region ( $5.27$  to  $5.29 \text{ GeV}/c^2$ ). The distributions are fit with a Gaussian plus linear function.

We then look at how each event was reconstructed, as a *2-, 3-, 4-body* event, and divide things up again according to the reconstructed final state category

We count the number of events in each final state and truth category. Note that we do not do any fitting of the  $m_{\text{ES}}$  distribution, but only count the number of events in the full  $m_{\text{ES}}$  range, 5.21-5.3 GeV/ $c^2$ . Chapter 9 discusses the fitting procedure in order to pick out the peaking background from the cross-feed.

We present results in four bins of hadronic mass (instead of the usual nine) to increase statistics. The bins are 0.6-1.0 GeV/ $c^2$ , which is just  $K^*\gamma$ , 1.0-1.6 GeV/ $c^2$ , 1.6-2.0 GeV/ $c^2$  and 2.0-2.4 GeV/ $c^2$ , which are  $X_s\gamma$  events.

Tables 7.6 and 7.7 show the results. The first column shows the truth category and the second column lists the number of generated events in the Monte Carlo sample for each truth category. The next column lists the number of signal events, which is only defined for true *2,3,4-body* categories since the signal is required to have the same true and reconstructed mode. The numbers in parenthesis are the number of events in the peaking  $m_{\text{ES}}$  region (5.27 to 5.29 GeV/ $c^2$ ). On average 95% of the signal events are in the  $m_{\text{ES}}$  peaking region.

The next three columns present the events in the cross-feed sample broken up into reconstructed *2,3,4-body* categories. Summing down vertically we see that the amount of cross-feed increases with reconstructed multiplicity, i.e. the reconstructed *4-body* category has more cross-feed events than the reconstructed *2-body* category. We also see that the total amount of cross-feed increases slightly with increasing  $M_{\text{Had}}$ , although the amount of peaking cross-feed decreases slightly.

The contributions from the different truth categories are what we expect. The cross-feed events from the true 2-, 3-, and 4-body events mostly contribute to the reconstructed *2-, 3-, and 4-body* categories respectively. These are mostly cases where the event is reconstructed with the same multiplicity as it was generated with, but in the wrong mode, a  $\pi$  is replaced with a  $\pi^0$  or vice versa. There is also some contribution from events which are reconstructed with the same mode as they were generated with, but one of the daughters used in the reconstruction is not the true daughter and so the reconstructed  $M_{\text{Had}}$  is more than 50 MeV/ $c^2$  different from the truth one.

We can also examine how the true 2-, 3-, and 4-body events contribute to the other reconstructed categories. The largest contribution is to the next higher multiplicity. Therefore, the true 2-body events contribute mostly to the reconstructed *3-body* category. The true 3-body contribute more to the reconstructed *4-body* category than to the reconstructed *2-body* category. The true 4-body events hardly contribute to the reconstructed *2-body* category.

The true 5-, 6-body and sss events contribute mostly to the reconstructed

*4-body* category, while the true  $2\pi^0$  events contribute to both the reconstructed *3-* and *4-body* categories. The true “other” events contribute to all three reconstructed final state categories, but only a small fraction of the generated events make it into the final sample.

We can also look at how much of the peaking cross-feed comes from events with incorrectly reconstructed modes or correctly reconstructed modes but a  $\Delta M_{Had}$  which falls outside the  $50 \text{ MeV}/c^2$  cut.

Table 7.8 breaks the peaking cross-feed into these two categories. For example, the first row of the  $M_{Had} = 1.0-1.6 \text{ GeV}/c^2$  sections says: 24 events were generated and reconstructed in the same mode, but with a  $(trueM_{Had}-recoM_{Had}) > 50 \text{ MeV}/c^2$ ; 17 events were generated in a 2-body mode and reconstructed in a different 2-body mode; 34 events were generated in a 2-body mode but reconstructed in a 3-body mode; and 3 events were generated in a 2-body mode but reconstructed in a 4-body mode. Note that the number of events for the two samples add up to the total peaking cross-feed listed in parenthesis in Tables 7.6 and 7.7. We can see that for the n-body to n-body cross-feed both samples contribute at the same order.

Note that in this section the tables show the total number of events in the peaking region, not the events in the peak. As seen in Section 10.1.1 the peaking yield from a fit, scaled to the data luminosity is quite small in most cases.

$M_{Had}=0.6-1.0 \text{ GeV}/c^2$					
truth	gen. events	signal	x-feed reconstructed		
			<i>2-body</i>	<i>3-body</i>	<i>4-body</i>
2body	60153	7837 (7763)	445 (274)	41 (18)	0 (0)
$M_{Had}=1.0-1.6 \text{ GeV}/c^2$					
truth	gen. events	signal	x-feed reconstructed		
			<i>2-body</i>	<i>3-body</i>	<i>4-body</i>
2body	5888	499 (493)	76 (41)	76 (34)	5 (3)
3body	9324	496 (484)	21 (8)	302 (150)	66 (28)
4body	2445	70 (64)	1 (0)	37 (11)	96 (43)
5body	372	–	0 (0)	6 (1)	28 (13)
6body	30	–	0 (0)	0 (0)	4 (1)
$2\pi^0$	1286	–	4 (0)	39 (15)	37 (15)
sss	80	–	0 (0)	3 (1)	10 (3)
other	9112	–	9 (2)	32 (10)	34 (14)

Table 7.6: Number of events in the final selection split into signal and cross-feed, then into truth mode categories, then into reconstructed mode categories and finally presented in two bins of low  $M_{Had}$ . The number of generated events in the initial Monte Carlo sample is also shown for comparison. The numbers in parenthesis are the number of events in the peaking  $m_{ES}$  region (5.27 to 5.29  $\text{GeV}/c^2$ ).

$M_{Had}=1.6-2.0 \text{ GeV}/c^2$					
truth	gen. events	signal	x-feed reconstructed		
			<i>2-body</i>	<i>3-body</i>	<i>4-body</i>
2body	1651	98 (97)	41 (11)	98 (43)	20 (4)
3body	4182	163 (156)	11 (1)	223 (79)	169 (46)
4body	3693	85 (81)	0 (0)	40 (12)	187 (87)
5body	1712	–	0 (0)	3 (0)	64 (18)
6body	400	–	0 (0)	0 (0)	8 (1)
$2\pi^0$	1518	–	3 (0)	32 (7)	74 (19)
sss	247	–	0 (0)	6 (0)	33 (14)
other	9402	–	4 (1)	33 (5)	71 (18)
$M_{Had}=2.0-2.4 \text{ GeV}/c^2$					
truth	gen. events	signal	x-feed reconstructed		
			<i>2-body</i>	<i>3-body</i>	<i>4-body</i>
2body	687	35 (34)	22 (6)	80 (27)	36 (2)
3body	1778	47 (45)	6 (1)	180 (52)	209 (50)
4body	1951	28 (23)	1 (1)	41 (7)	193 (62)
5body	1425	–	0 (0)	3 (0)	61 (11)
6body	673	–	0 (0)	0 (0)	23 (3)
$2\pi^0$	1202	–	2 (0)	31 (6)	83 (14)
sss	111	–	0 (0)	0 (0)	25 (12)
other	9186	–	3 (0)	41 (9)	114 (22)

Table 7.7: Number of events in the final selection split into signal and cross-feed, then into truth mode categories, then into reconstructed mode categories and finally presented in two bins of high  $M_{Had}$ . The number of generated events in the initial Monte Carlo sample is also shown for comparison. The numbers in parenthesis are the number of events in the peaking  $m_{ES}$  region (5.27 to 5.29  $\text{GeV}/c^2$ ).

cross-feed						
$M_{Had}=0.6-1.0 \text{ GeV}/c^2$						
truth	(true = reco) mode			(true != reco) mode		
	2-body	3-body	4body	2-body	3-body	4body
2body	175	0	0	99	18	0
$M_{Had}=1.0-1.6 \text{ GeV}/c^2$						
truth	(true = reco) mode			(true != reco) mode		
	2-body	3-body	4body	2-body	3-body	4body
2body	24	–	–	17	34	3
3body	–	79	–	8	71	28
4body	–	–	23	0	11	20
$M_{Had}=1.6-2.0 \text{ GeV}/c^2$						
truth	(true = reco) mode			(true != reco) mode		
	2-body	3-body	4body	2-body	3-body	4body
2body	6	–	–	5	43	4
3body	–	46	–	1	33	46
4body	–	–	50	0	12	37
$M_{Had}=2.0-2.4 \text{ GeV}/c^2$						
truth	(true = reco) mode			(true != reco) mode		
	2-body	3-body	4body	2-body	3-body	4body
2body	4	–	–	2	27	2
3body	–	19	–	1	33	50
4body	–	–	39	1	7	23

Table 7.8: The number of cross-feed events in the peaking  $m_{ES}$  region (5.27 to 5.29  $\text{GeV}/c^2$ ), split two samples; one where the mode is reconstructed correctly but the  $\Delta M_{Had}$  of the event falls outside the  $50 \text{ MeV}/c^2$  cut ((true = reco) mode), and one where the mode is not correctly reconstructed ((true != reco) mode). The two samples are split into truth mode categories and then into reconstructed mode categories, and presented in four bins of  $M_{Had}$ .

# Chapter 8

## Signal Efficiency

The signal efficiency is one of the important quantities needed to calculate the branching fraction. In the previous chapter it was explained how the signal Monte Carlo is separated into signal and cross-feed samples. The definition of signal and cross-feed is repeated here for completeness:

- “signal” :  
(reco mode = true mode) & ( $|trueM_{Had} - recoM_{Had}| < 50 \text{ MeV}/c^2$ )
- cross-feed :  
reco mode  $\neq$  true mode or  
(reco mode = true mode) & ( $|trueM_{Had} - recoM_{Had}| > 50 \text{ MeV}/c^2$ )

This removes background events from the signal Monte Carlo making the signal efficiency simple to calculate. The yield,  $N_{i,j}^{reco}$ , or plainly the number of events passing the selection, in each  $M_{Had}$  bin and for each final event category is counted. The efficiency is defined as:

$$\epsilon_{i,j} = N_{i,j}^{reco} / N_{i,j}^{gen} \quad (8.1)$$

where  $i = M_{Had}$  bin and  $j =$  final state category (*all, 2,3,4-body* etc.). The denominator  $N_{i,j}^{gen}$  is the total number of generated events in the full Monte Carlo sample for each value of  $i$  and  $j$ . These numbers were obtained by looking at the generator level fractions for each final state in each  $M_{Had}$  bin and multiplying by the total number of events in the Monte Carlo sample.

Note that the efficiencies for the final state categories are with respect to the twelve reconstructed final states, or a sub-set thereof, see Table 4.1. This includes events with one kaon and up to three pions, where only up to one of the pions can be a  $\pi^0$ . The kaon can be charged or neutral, but only  $K_S$  are

used. We reconstruct only  $K_S \rightarrow \pi^+\pi^-$ , although generic  $K_S$  are counted in the denominator for the efficiency.

For the first two bins where we only consider the  $K * \gamma$  resonance, and only simulate four exclusive final states ( $K\pi$ ,  $K_S\pi^0$ ,  $K\pi^0$ ,  $K_S\pi$ ), where the  $K_S$  is constrained to decay to  $\pi^+\pi^-$ . We therefore need to include in the denominator ( $N_{i,j}^{gen}$ ) a factor to correct for the fraction of final states where  $K_S \rightarrow \pi^0\pi^0$ , since we want the denominator to be the total number of events that would be generated in a sample of  $B \rightarrow K^*\gamma, K^* \rightarrow K(K_S)$  (excluding  $K_L$ ), not constraining the  $K_S$  decay. Looking at the Clebsch-Gordan coefficients for the  $B^0$  and  $B^+$  decays (it is the same for the complex conjugate modes) this correction factor, for the *all* category, is 9/8. This factor is derived in detail in Appendix B. The denominator for the *all* final state category in the first  $M_{Had}$  bin, for example, is then:

$$N_{0,all}^{gen} = (N_{K\pi}^{gen} + N_{K_S\pi^0}^{gen} + N_{K\pi^0}^{gen} + N_{K_S\pi}^{gen}) * 9/8 \quad (8.2)$$

where all the samples are generated with the same luminosity. This type of correction is not needed for the  $X_s\gamma$  Monte Carlo since the  $K_S$  decays are not constrained at the generator level.

The signal  $m_{ES}$  distributions can be seen in Figures D.1 to D.9 in Appendix D. They are fit with a Crystal Ball function in order to determine the widths of the distribution which will be used later to fix the Crystal Ball shape in the fits to the peaking background and data. The fits are explained in detail in the next chapter. The fits are not needed for the efficiency calculation since the whole background subtracted distribution is treated as signal.

Table 8.1 presents the signal efficiency for the nine hadronic mass bins and the eight final state categories considered. Figure 8.1 shows the signal efficiency for the *all* final state category as a function of  $M_{Had}$ . These efficiencies, combined with the signal yield in data, will be used to calculate the partial branching fractions in each hadronic mass bin.

The efficiencies can be roughly understood in terms of:

- A  $1/M_{Had}$  dependence of the efficiency for each final state category
- A 60% efficiency ratio between  $\pi^0$  and  $\pi$  final states
- A 55% efficiency ratio between  $K_s$  and  $K$  final states
- A 60% efficiency factor between 3 and 2-body, and between 4 and 3-body final states.

$M_{Had}$	<i>all</i>	<i>2-body</i>	<i>3-body</i>	<i>4-body</i>
0.6-0.8	$16.0 \pm 0.8$	$16.0 \pm 0.8$	–	–
0.8-1.0	$11.4 \pm 0.1$	$11.4 \pm 0.1$	–	–
1.0-1.2	$7.6 \pm 0.4$	$9.7 \pm 0.6$	$5.6 \pm 0.5$	$5.9 \pm 2.3$
1.2-1.4	$5.7 \pm 0.3$	$7.7 \pm 0.6$	$5.1 \pm 0.4$	$2.8 \pm 0.6$
1.4-1.6	$5.2 \pm 0.3$	$7.6 \pm 0.7$	$5.4 \pm 0.4$	$2.7 \pm 0.4$
1.6-1.8	$4.1 \pm 0.3$	$6.0 \pm 0.8$	$4.4 \pm 0.4$	$2.8 \pm 0.4$
1.8-2.0	$3.0 \pm 0.3$	$5.8 \pm 0.9$	$3.2 \pm 0.4$	$1.7 \pm 0.3$
2.0-2.2	$2.8 \pm 0.3$	$5.7 \pm 1.1$	$3.1 \pm 0.5$	$1.4 \pm 0.3$
2.2-2.4	$2.1 \pm 0.3$	$4.2 \pm 1.2$	$1.9 \pm 0.5$	$1.4 \pm 0.4$
$M_{Had}$	$\pi$	$\pi^0$	$K$	$K_s$
0.6-0.8	$18.6 \pm 1.0$	$11.1 \pm 1.1$	$19.8 \pm 1.0$	$8.5 \pm 1.0$
0.8-1.0	$13.1 \pm 0.2$	$8.2 \pm 0.2$	$13.9 \pm 0.2$	$6.5 \pm 0.2$
1.0-1.2	$9.8 \pm 0.6$	$5.0 \pm 0.5$	$9.6 \pm 0.5$	$3.7 \pm 0.5$
1.2-1.4	$7.5 \pm 0.5$	$4.0 \pm 0.3$	$6.7 \pm 0.4$	$3.6 \pm 0.4$
1.4-1.6	$6.6 \pm 0.5$	$4.2 \pm 0.3$	$6.4 \pm 0.4$	$2.9 \pm 0.4$
1.6-1.8	$5.5 \pm 0.5$	$3.1 \pm 0.3$	$4.7 \pm 0.3$	$3.0 \pm 0.4$
1.8-2.0	$4.0 \pm 0.5$	$2.2 \pm 0.3$	$3.6 \pm 0.4$	$1.8 \pm 0.4$
2.0-2.2	$4.0 \pm 0.6$	$1.9 \pm 0.3$	$3.0 \pm 0.4$	$2.2 \pm 0.5$
2.2-2.4	$2.8 \pm 0.6$	$1.5 \pm 0.4$	$2.3 \pm 0.4$	$1.6 \pm 0.5$

Table 8.1: The signal efficiencies, in %, from the signal Monte Carlo sample. The  $m_{ES}$  distributions are shown in Figures D.1 to D.9. The efficiency is calculated by taking the number of events in the plots divided by the total generated events for each category in the Monte Carlo sample.

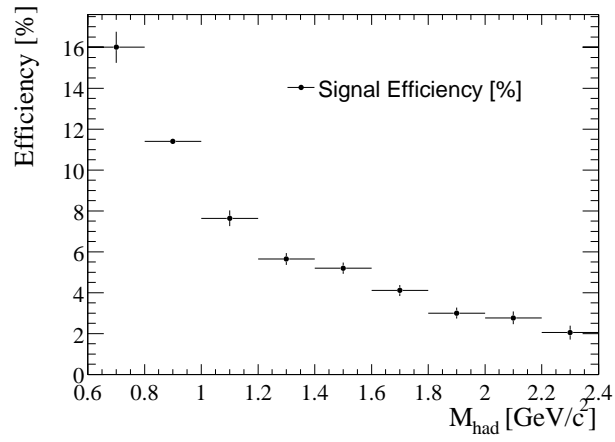


Figure 8.1: Signal efficiency as a function of  $M_{Had}$  for the *all* final state category.

# Chapter 9

## Background Subtraction

As we have seen in the previous chapters there are three different background sources in this analysis. In order to obtain the signal yield from a fit to the  $m_{\text{ES}}$  distribution in data a method of subtracting these backgrounds is needed. The background can be subtracted in two different ways. It can be parameterized in the  $m_{\text{ES}}$  distribution fit by adding a background function to the signal function or it can be directly subtracted from the  $m_{\text{ES}}$  data yield.

The contributions to the background vary over the  $M_{\text{Had}}$  spectrum and must be considered uniquely in each  $M_{\text{Had}}$  bin. In the following we will first describe a method for dealing with each background and then present a toy Monte Carlo study which shows that the method gives consistent results.

### 9.1 Method

After the event selection is performed, and the choice of the best candidate is made, the final data sample consists of signal, cross-feed background and background from continuum or  $B\bar{B}$  events. The functions used to parameterize the different contributions are:

- Signal: Crystal Ball function. A Crystal Ball instead of a Gaussian is used because of the radiative tail which can not be fully removed by  $\Delta E$  rescaling in events with a  $\pi^0$  in the final state.
- Cross-feed background: Argus plus Crystal Ball function. The addition of the Crystal Ball is needed to parameterize a small peaking component.
- Continuum background: Argus function. As discussed in Chapter 7 the continuum background does not have a peaking component and can be fit

to just an Argus function.

- $B\bar{B}$  background: Argus plus Crystal Ball at high  $M_{Had}$ . As discussed in Chapter 7 the  $B\bar{B}$  background does have a peaking contribution which becomes significant at higher hadronic masses after  $1.8 \text{ GeV}/c^2$ .

Ideally the data could be fit to a complicated function which incorporates all of these components directly, three Crystal Ball shapes plus three Argus shapes. With limited statistics in data and in Monte Carlo this is not practical.

Instead, we propose to treat the peaking and non-peaking components of the background in different ways. The non-peaking background from the cross-feed, continuum and  $B\bar{B}$  will be parameterized in the fit function, while the peaking components will be fit separately in the Monte Carlo and subtracted from the data Crystal Ball yield.

The data will therefore be fit to a single Crystal Ball plus two Argus functions. One Argus will be fixed from the cross-feed Monte Carlo fits and the other will be fixed from a fit to the combination of continuum and  $B\bar{B}$  Monte Carlo.

We choose two Argus shapes instead of three for simplicity. This choice is examined in the toy Monte Carlo study presented in the next section. There is also a systematic error associated with statistical uncertainty in the values of the Argus shape parameters fixed in the data fits. This error is examined in Chapter 12.

Because of low statistics in some hadronic mass bins and final state categories the Crystal Ball parameters from a fit to the signal Monte Carlo sample are used to fix the shapes in the fits to the peaking cross-feed,  $B\bar{B}$  and data samples. This is not ideal since there is no strong argument for assuming that the CB shape parameters, especially the width, should be the same as the signal. Systematic errors accounting for this assumption are studied in Chapter 12.

The signal yield  $N_{sig}$ , i.e., the data yield after the (peaking) background contribution is subtracted, for each  $M_{Had}$  bin and final state category, is given by:

$$N_{i,j}^{sig} = N_{i,j}^{data} - N_{i,j}^{xfeed} - N_{i,j}^{bb}, \quad (9.1)$$

where  $N_{i,j}$  is the yield, i.e. number of peaking events, per  $M_{Had}$  bin and final state category obtained from the various fits. The statistical error on the subtracted yield is equal to the sum in quadrature of the statistical error on the data, cross-feed and  $B\bar{B}$  yield. Therefore we are sensitive not only to the data, but also to the Monte Carlo, statistics. The toy-MC studies in the next section will examine this method of peaking background subtraction.

In summary, the functions and a description of the parameters used to fit the signal and background Monte Carlo and data samples are listed below. Example fits are shown in Figure 9.1. Figure 9.2 shows a diagram summarizing the fitting procedure. More technical details and results from the fits are presented in Chapter 10.

- **Signal:** The signal sample is fit with a Crystal Ball function. The peak, tail and  $\alpha$  parameters are fixed to values taken from fits in larger hadronic mass ranges. The width of the Crystal Ball is the only free parameter in the fit, since it is expected to vary for different categories and over the  $M_{Had}$  range.  
RESULTS: Crystal Ball parameters used to fix the peaking component shape in the background and data fits.
- **Cross-feed:** The cross-feed sample is fit with an Argus function plus a Crystal Ball function. The Crystal Ball parameters are fixed to the values from the signal fits. The free parameters are the Argus shape and the Crystal Ball fraction.  
RESULTS: Argus shape to be used in the data fits and cross-feed yield.
- **Continuum plus  $B\bar{B}$ :** The continuum (uds, ccb) and  $B\bar{B}$  (b0g, bpg) Monte Carlo samples are combined together with equal luminosity ( $8.7 fb^{-1}$ ) and fit with an Argus shape up to  $M_{Had}= 1.8 GeV/c^2$  and then an Argus plus Crystal Ball function above. The Crystal Ball parameters are fixed to the values from the signal fits. The free parameters are the Argus shape and the Crystal Ball fraction.  
RESULTS: Argus shape to be used in the data fits.
- **$B\bar{B}$ :** The  $B^0\bar{B}^0$  and  $B^+B^-$  samples are combined together with equal luminosity ( $14fb^{-1}$ ) and fit for  $M_{Had}$  above  $1.8 GeV/c^2$  to a Crystal Ball plus Argus function. The Crystal Ball parameters are fixed to the values from the signal fits. The free parameters are the Argus shape and the Crystal Ball fraction.  
RESULTS:  $B\bar{B}$  yield.
- **Data:** The data is fit with one Crystal Ball plus two Argus functions. The Crystal Ball parameters are fixed to the values from the signal MC fits. One Argus shape is fixed to the value from the cross-feed fits, and the other fixed to the value from the continuum plus  $B\bar{B}$  background fits. The only free parameter is the Crystal Ball fraction.  
RESULTS: Data yield.

## 9.2 Toy–MC studies

A toy–MC study is a way to test fitting hypothesis on high statistics samples without having to generate large samples of the full Monte Carlo. Distributions are generated according of pre-defined probability density functions. Distributions are generated for signal and background, and can be combined to simulate a data sample distribution. All that is generated is the final  $m_{\text{ES}}$  distribution for fitting, there is no particle generation or detector simulation.

A toy–MC study is used to investigate the method for fitting the data and Monte Carlo samples in order to consistently subtract the background and obtain the signal yield.

A detailed description of the method was given in the previous section. The next chapter lists the final parameters used in the fitting and the results of the fits.

As discussed in the previous section we treat the peaking and non-peaking backgrounds separately. There are two assumptions, one for each peaking and non-peaking background subtraction, that we will test with toy–MC studies in this section.

- Non-peaking background subtraction.

The data is composed of signal and three backgrounds, cross–feed, continuum and  $B\bar{B}$ . Instead of fitting the data with three Argus shapes, one for each background, we assume the continuum and  $B\bar{B}$  have similar shapes and use only one Argus function to parameterize them both. We therefore fit the data with two Argus functions instead of three.

- Peaking background subtraction.

The events in the peak of the  $m_{\text{ES}}$  distribution in data can have three sources; signal, cross–feed and  $B\bar{B}$  background. We fit the data with one Crystal Ball instead of three and then subtract from the data yield the yield from fits to the cross–feed and  $B\bar{B}$  background Monte Carlo samples to obtain the signal yield.

There are other assumptions that go into the fit method which will be discussed in the systematic error studies (Chapter 12). These include the statistical fluctuations in the fixed parameters used in the fits and the assumption that the Crystal Ball parameters, from the signal Monte Carlo fits, are used for all the peaking  $m_{\text{ES}}$  components.

### 9.2.1 Toy-MC Samples

Toy-MC events are generated according to pre-defined functions. The functions are obtained from fits to the  $m_{\text{ES}}$  distributions of the full Monte Carlo signal and background events. We generate a toy-MC sample to match the data and the four full Monte Carlo samples; signal, cross-feed, continuum, and  $B\bar{B}$ .

Note, that although throughout the text we split our events into several final state categories, here we will just use the *all* category since the fitting method study does not depend on the category. Finally, as throughout the text, we will look at the  $m_{\text{ES}}$  distribution in 200 MeV/ $c^2$  bins in the hadronic mass.

The values of the parameters used to generate each sample can be found in Table 9.1. The values in Table 9.1 are not listed with an associated error to emphasize that these are the values we use for the toy-MC generation. As discussed, the parameters for the Crystal Ball in the cross-feed and  $B\bar{B}$  (above  $M_{\text{Had}}=1.8\text{ GeV}/c^2$ ) fits are fixed to the ones from the fits to the signal sample. Therefore, they are only listed once in the signal table, and only the Crystal Ball fraction is listed in the other tables. This check of the fitting method assumes the functions used to fit a given sample and then used afterward to generate the toy-sample, are the correct ones.

The toy-events are generated according to the functions from the corresponding full Monte Carlo events with the parameters listed in Table 9.1. A total of 1M of events are generated for each sample.

- **toy-signal** events are generated with a Crystal Ball function.
- **toy-xfeed** events are generated with a Crystal Ball function and an Argus function.
- **toy-continuum** events are generated with an Argus function.
- **toy-bb** events are generated with just an Argus function up to 1.8 GeV/ $c^2$  and with a CB and an Argus function thereafter.
- **toy-data** events are generated according to the sum of the functions for all the contributions: signal, cross-feed, continuum and  $B\bar{B}$ . The corresponding fraction of each component over the whole  $m_{\text{ES}}$  range (5.21 to 5.3 GeV/ $c^2$ ) is shown in Table 9.2. The fractions are obtained from the expected signal and background events in full Monte Carlo after the selection and the choice of the best candidate is performed.

Signal					Cross-feed		
Crystal Ball					Argus & CB		
$M_{Had}$ (GeV)	peak (GeV)	width (MeV)	tail	$\alpha$	Argus Shape	end-point (GeV)	CB fraction %
0.6-0.8		2.43	4.05	1.61	-167.4		1.32
0.8-1.0		2.52	4.05	1.61	-144.8		31.87
1.0-1.2		2.59	1.64	1.86	-104.0		10.92
1.2-1.4		2.56	1.64	1.86	-110.5		10.29
1.4-1.6	5.27945	2.65	1.64	1.86	-116.0	5.29	2.91
1.6-1.8		2.68	1.64	1.86	-87.6		4.53
1.8-2.0		2.26	1.64	1.86	-64.1		3.73
2.0-2.2		2.67	1.64	1.86	-58.8		0.00
2.2-2.4		3.29	1.64	1.86	-20.7		6.94

Continuum			$B\bar{B}$		
Argus			Argus (& CB)		
$M_{Had}$ (GeV)	Argus Shape	end-point (GeV)	Argus Shape	end-point (GeV)	CB fraction %
0.6-0.8	-28.6		-		-
0.8-1.0	-8.3		-114.9		-
1.0-1.2	-26.7		-44.3		-
1.2-1.4	-16.2		-16.1		-
1.4-1.6	-9.6	5.29	-125.6	5.29	-
1.6-1.8	-6.8		-66.5		-
1.8-2.0	-15.4		-21.0		10.61
2.0-2.2	-12.0		-38.5		3.53
2.2-2.4	-21.9		-47.3		6.27

Table 9.1: Values of the fit function parameters extracted from the fits to the different MC samples. The Crystal Ball shape parameters for the cross-feed and  $B\bar{B}$  are fixed to the ones from the signal. Details are given in Chapter 10.

$M_{Had}$	$f_{sig}$ (%)	$f_{xfeed}$ (%)	$f_{continuum}$ (%)	$f_{B\bar{B}}$ (%)
0.6-0.8	7.2	3.0	89.8	0
0.8-1.0	37.8	1.7	58.7	1.9
1.0-1.2	14.3	5.2	79.1	1.4
1.2-1.4	11.7	8.9	76.2	3.2
1.4-1.6	7.1	10.1	79.3	3.6
1.6-1.8	3.9	9.3	81.2	5.6
1.8-2.0	1.9	9.4	77.5	11.1
2.0-2.2	1.0	7.6	74.2	17.7
2.2-2.4	0.4	6.3	71.6	21.7

Table 9.2: Fractions of signal,  $f_{sig}$ , cross-feed,  $f_{xfeed}$ , continuum,  $f_{continuum}$ , and  $B\bar{B}$  events,  $f_{B\bar{B}}$ , in the toy-data sample over the full  $m_{ES}$  range (5.21 to 5.3 GeV/ $c^2$ ).

## 9.2.2 Non-peaking Background Subtraction

As discussed earlier, the data is composed of signal and three backgrounds, cross-feed, continuum and  $B\bar{B}$ . These three backgrounds have a non-peaking component which can be parameterized by an Argus function.

We propose to fit the data with two, instead of three, Argus functions. We assume that the continuum and  $B\bar{B}$  backgrounds have similar shapes and use only one Argus function to parameterize them both. The Argus shape parameters can be seen in Table 9.3, for the  $B\bar{B}$  and continuum backgrounds (note that the  $B\bar{B}$  Argus parameters are slightly different than the ones for the final fit, in Chapter 10 since this study was done with a slightly smaller sample). Note that the continuum sample has higher statistics since the background level is higher. In the  $M_{Had}$  region less than 1.8 GeV/ $c^2$  there are hardly any  $B\bar{B}$  events, and therefore the Argus parameters are not very reliable. Any comparison should be made mostly in the last three bins. Moreover, it seems more natural to parametrize together all the “real” background, as opposed to the cross-feed, which is wrongly reconstructed signal (or combinatorial background).

Therefore, one of the two Argus shape parameters in the toy-data fits is fixed to the values used to generate the toy-xfeed (and listed in Table 9.1). The other is obtained from a fit to the combination of the toy-bb and toy-continuum distributions using high statistics (1M toy-events). The distribution is fit to a free Argus function below  $M_{Had}= 1.8$  GeV/ $c^2$ , and to an Argus plus Crystal Ball function above  $M_{Had}= 1.8$  GeV/ $c^2$ , where the Crystal Ball parameters are fixed

$M_{Had}$	Argus shape BB	Argus shape Continuum
0.6-0.8	--	$-28.6 \pm 20.1$
0.8-1.0	$-114.9 \pm 61.7$	$-8.3 \pm 12.9$
1.0-1.2	$-44.3 \pm 62.7$	$-26.7 \pm 10.4$
1.2-1.4	$-16.1 \pm 37.9$	$-16.2 \pm 9.8$
1.4-1.6	$-125.6 \pm 33.1$	$-9.6 \pm 7.8$
1.6-1.8	$-66.5 \pm 22.3$	$-6.8 \pm 7.0$
1.8-2.0	$-21.0 \pm 16.8$	$-15.4 \pm 6.8$
2.0-2.2	$-38.5 \pm 14.6$	$-12.0 \pm 6.3$
2.2-2.4	$-47.3 \pm 12.6$	$-21.9 \pm 5.8$

Table 9.3: The Argus shape parameters from a fit to the full MC  $B\bar{B}$  (2nd column) and full MC continuum events (3rd column) together with their corresponding fit error.

to those from the signal Monte Carlo fits. These fits are shown in Figure C.1 in Appendix C, and the Argus shape parameters from the fits are listed in Table 9.4. Also shown in the same table are the results of the same fit to a sample of BB+Continuum full MC events (smaller statistics). It can be seen that  $\chi^2/\text{dof}$  of the latter fits are good enough to justify our choice.

We therefore fit the toy-data events to two Argus functions with their shape parameters fixed as described above, and a Crystal Ball function. The Crystal Ball parameters, as always, are fixed to the ones for the signal sample shown in Table 9.1. These fits can be seen in Figure C.3 in Appendix C, and look reasonable.

We can try to simplify things further and fit the toy-data with a Crystal Ball and only one Argus function with a free shape. This is indeed a quite severe approximation. Using the toy-data sample generated with 3 Argus shape functions (cross-feed/BB/Continuum), we fit the resulting  $m_{ES}$  distributions using a single Argus shape function to parametrize the background. These fits can be seen in Figure C.2 in Appendix C. The  $\chi^2/\text{d.o.f.s}$  from the fits are shown in Table 9.5 and compared with the  $\chi^2/\text{d.o.f.s}$  from the fits with two Argus functions. Both fits are done with high statistics (1M events) toy-MC samples which is why the  $\chi^2/\text{d.o.f.s}$  are large.

The  $\chi^2/\text{d.o.f.s}$  is always lower for the fits with two Argus functions, except for the last  $M_{Had}$  bin where the statistics are low. This shows that the fit with

$M_{Had}$	Argus shape toy-(bb+cont.)	Argus shape full MC (bb+cont.)	$\chi^2 / dof$ full MC (bb+cont.)
0.6-0.8	$-28.51 \pm 0.12$	$-28.6 \pm 20.1$	0.18
0.8-1.0	$-9.34 \pm 0.13$	$-9.7 \pm 12.8$	0.69
1.0-1.2	$-26.42 \pm 0.12$	$-25.8 \pm 10.4$	0.99
1.2-1.4	$-20.19 \pm 0.12$	$-13.5 \pm 9.6$	0.84
1.4-1.6	$-11.90 \pm 0.13$	$-14.0 \pm 7.6$	0.72
1.6-1.8	$-7.47 \pm 0.13$	$-10.6 \pm 6.8$	0.79
1.8-2.0	$-17.77 \pm 0.14$	$-12.3 \pm 7.3$	1.33
2.0-2.2	$-18.07 \pm 0.16$	$-11.1 \pm 6.6$	0.78
2.2-2.4	$-16.91 \pm 0.16$	$-23.1 \pm 6.4$	0.56

Table 9.4: The Argus shape parameters from a fit to the toy–bb plus toy–continuum events (2nd column) shown in Figure C.1 in Appendix C. These values are used to fix one of the two Argus functions in the toy–data fits. Also shown Argus shape parameters from a fit to full MC (bb + cont) events (3rd column) together with the corresponding  $\chi^2/dof$  of the fit.

two Argus shapes is better, and therefore using a single Argus shape function to parametrize the background is a worse approximation. In our fits to the real data we will use two Argus functions.

### 9.2.3 Peaking background subtraction.

The goal of the fit to the data  $m_{ES}$  distribution is to measure the number of true signal events. However, there are three peaking components: the true signal events, cross–feed and  $B\bar{B}$  events. We assume that these three peaking components can be parameterized by a Crystal Ball shape. We also assume that the Crystal Ball shape for all the samples (signal, cross–feed and  $B\bar{B}$ ) is the same and fix the parameters to those found in a free fit to the signal sample. A systematic study testing these assumptions for the cross–feed and  $B\bar{B}$  events is presented in Chapter 12.

Fitting the data with three Crystal Ball functions would be the natural procedure. We propose to make an approximation by fitting the peak in the data with one Crystal Ball shape. We then subtract from the data yield the yields from separate fits to the cross–feed and  $B\bar{B}$  Monte Carlo.

To test this method we fit 1000 toy–data samples the size of the real data sample, with two Argus functions plus a Crystal Ball function. The Argus

$M_{Had}$	$\chi^2/dofs$ for 1 Argus + CB	$\chi^2/dofs$ for 2 Argus + CB
0.6-0.8	10.0	4.7
0.8-1.0	52.2	40.4
1.0-1.2	7.8	4.9
1.2-1.4	24.5	8.6
1.4-1.6	27.7	3.8
1.6-1.8	8.5	2.4
1.8-2.0	3.1	2.2
2.0-2.2	4.0	3.8
2.2-2.4	1.68	2.9

Table 9.5:  $\chi^2$  values for fits to the  $m_{ES}$  toy-data distribution using either one Argus and a Crystal Ball or the sum of two Argus and a Crystal Ball. The fits are performed in bins of the hadronic mass.

parameters are fixed to the cross-feed and continuum +  $B\bar{B}$  Argus shapes as discussed in the previous section. The Crystal Ball parameters are fixed to the signal ones listed in Table 9.1. The mean values of the Crystal Ball fraction with their respective errors (rms over all the samples), obtained from the toy-data fits can be seen in Table 9.6.

We know what fraction of cross-feed and  $B\bar{B}$  background was used to construct the toy-data Monte Carlo sample (see Table 9.2). Therefore, the measured fraction of true signal events in the toy-data,  $f^{sig}$ , is:

$$f^{sig} = f_{toy-data}^{CB} - f_{xfeed} * f_{toy-xfeed}^{CB} - f_{B\bar{B}} * f_{toy-bb}^{CB} \quad (9.2)$$

where  $f_{toy-data}^{CB}$  is the Crystal Ball fraction in the toy-data fits listed in Table 9.6,  $f_{toy-xfeed}^{CB}$  is the Crystal Ball fraction for the toy-xfeed listed in Table 9.1,  $f_{toy-bb}^{CB}$  is the Crystal Ball fraction in the toy-bb listed in Table 9.1, and  $f_{xfeed}$  and  $f_{B\bar{B}}$  are the fractions of toy-xfeed and toy-bb added to the toy-data as listed in Table 9.2. Results are shown in Table 9.7 and are compared to the generated fraction of signal events in the toy-data from Table 9.1.

Note that the difference between the measured fraction and the generated one is compatible with zero within errors for the statistics we are dealing with in the data sample. The errors are from the rms of the toy-data yield from fits to many samples. Therefore, the two approximations made in the fitting procedure (fitting the non-peaking background component with two Argus shapes and fitting the data with only one Crystal Ball, but subtracting the peaking background

$M_{Had}$	toy-data
0.6-0.8	$.064 \pm .037$
0.8-1.0	$.364 \pm .029$
1.0-1.2	$.150 \pm .027$
1.2-1.4	$.131 \pm .022$
1.4-1.6	$.075 \pm .018$
1.6-1.8	$.044 \pm .014$
1.8-2.0	$.032 \pm .012$
2.0-2.2	$.018 \pm .011$
2.2-2.4	$.024 \pm .010$

Table 9.6: Measured fraction of events in the Crystal Ball in the toy-data fits, obtained fitting 1000 toy-data samples of the size of the data. The error listed is the rms.

afterward to obtain the signal yield) do not introduce any significant bias in our measurement.

$M_{Had}$	Measured signal fraction (%)	Generated signal fraction (%)	(Measured-Generated) /Generated (%)
0.6-0.8	$6.36 \pm 3.70$	7.20	$-11.67 \pm 51.39$
0.8-1.0	$35.87 \pm 2.94$	37.76	$-5.02 \pm 7.81$
1.0-1.2	$14.43 \pm 2.75$	14.26	$1.21 \pm 19.36$
1.2-1.4	$12.18 \pm 2.38$	11.73	$3.90 \pm 20.33$
1.4-1.6	$7.21 \pm 1.82$	7.08	$1.79 \pm 25.76$
1.6-1.8	$3.98 \pm 1.46$	3.93	$1.34 \pm 37.23$
1.8-2.0	$1.67 \pm 1.25$	1.94	$-14.03 \pm 64.46$
2.0-2.2	$1.19 \pm 1.10$	0.99	$21.06 \pm 111.47$
2.2-2.4	$0.60 \pm 1.09$	0.38	$57.01 \pm 284.85$

Table 9.7: Measured and generated signal events in the toy-data. The third column shows the relative difference in the measured and generated signal events.

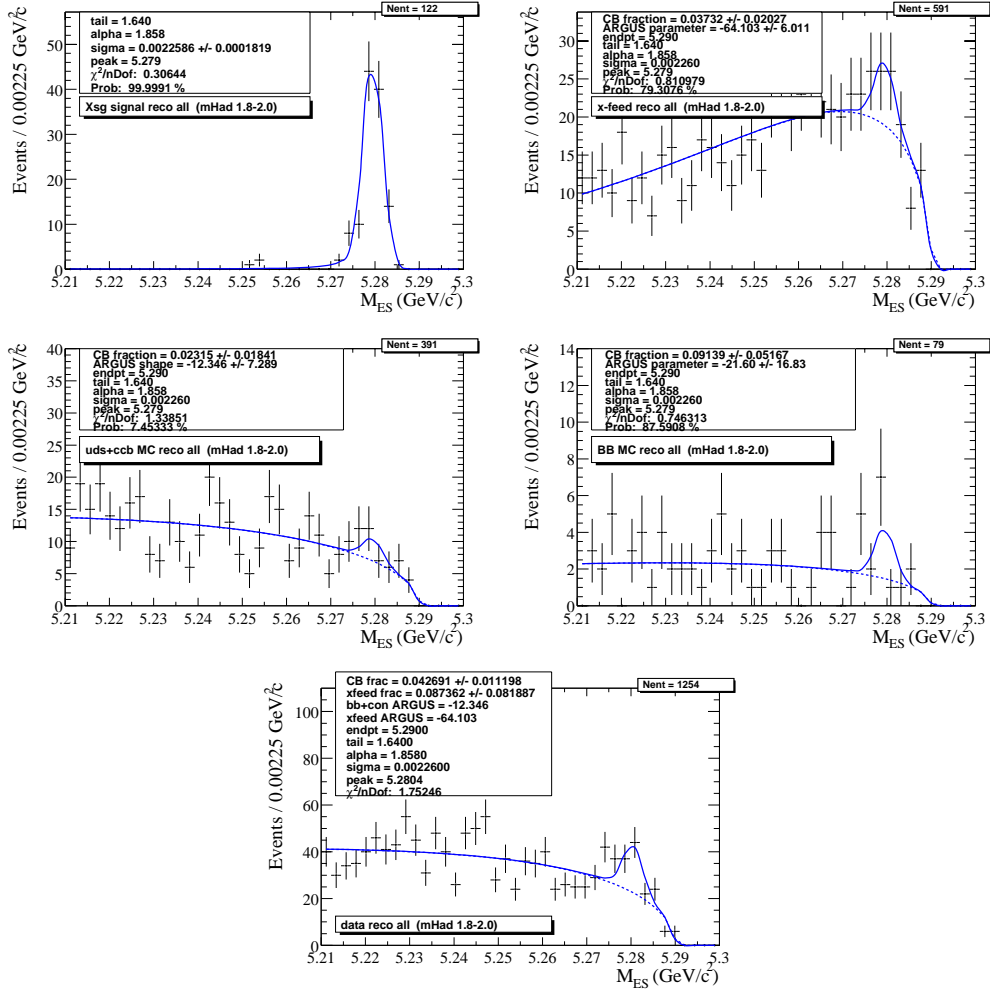


Figure 9.1: Example fits for the signal, cross-feed, continuum plus  $B\bar{B}$ ,  $B^+B^-$  and data samples in one  $200 \text{ MeV}/c^2 M_{Had}$  bin,  $1.8$  to  $2.0 \text{ GeV}/c^2$ .

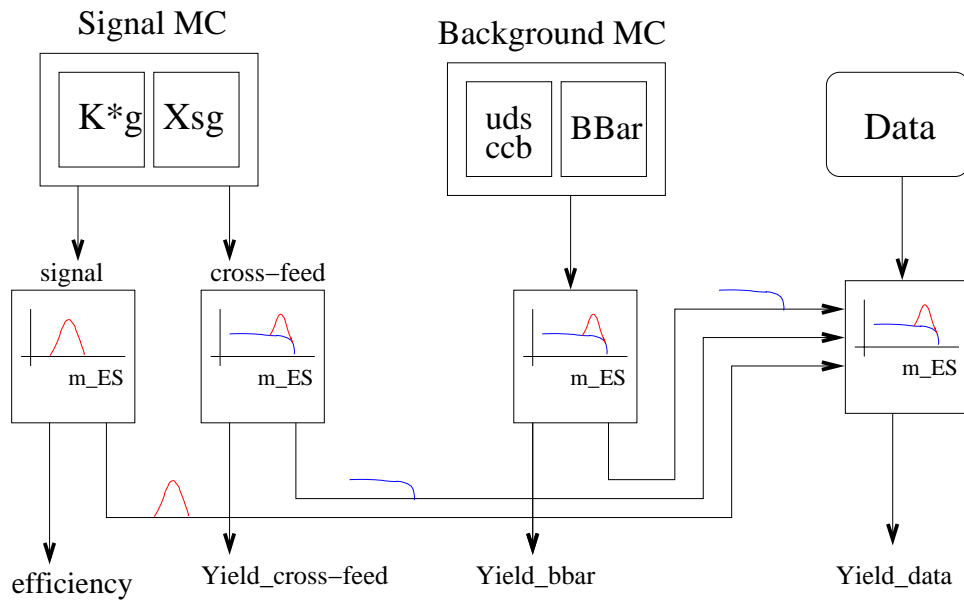


Figure 9.2: Diagram of the fitting procedure.

# Chapter 10

## Monte Carlo and Data Fit Results

In this chapter we show the results of the fits for the Monte Carlo and data samples. Only a few sample fits are shown in the text of the chapter but the complete set of fits can be found in Appendix D.

Note that in fits with a signal and background shape we have allowed  $f_{signal}$  to run negative which allows for a negative yield. This is necessary since the fraction can be quite small and otherwise we would not allow for the full range of statistical fluctuations, but would be artificially cut-off at zero. The negative yields are treated the same as the positive ones.

### 10.1 Fits to Monte Carlo

#### 10.1.1 Signal Monte Carlo

As described in the previous chapter the signal Monte Carlo is split into two components, signal and cross-feed which are defined as follows,

- signal :  
(reco mode = true mode) & ( $|trueM_{Had} - recoM_{Had}| < 50 \text{ MeV}/c^2$ )
- cross-feed :  
reco mode  $\neq$  true mode or  
(reco mode = true mode) & ( $|trueM_{Had} - recoM_{Had}| > 50 \text{ MeV}/c^2$ )

The full signal Monte Carlo events used in the following fits have two components, resonant,  $K^*\gamma$ , and non-resonant,  $X_s\gamma$ . The resonant  $K^*\gamma$  Monte Carlo

which is used in the first two  $M_{Had}$  bins, 0.6 to 1.0  $\text{GeV}/c^2$ , has a luminosity of  $1062 \text{ fb}^{-1}$ . Above 1.0  $\text{GeV}/c^2$  in  $M_{Had}$  the inclusive  $B \rightarrow X_s \gamma$  Monte Carlo is used. The model used in the generation is **KN465** and the sample has a luminosity of  $125 \text{ fb}^{-1}$ .

## Signal Sample

The signal sample is fit to a Crystal Ball function. The Crystal Ball parameters from these fits are used to fully constrain the Crystal Ball shape in the fits to other Monte Carlo samples and the data.

The peak of the Crystal Ball is a measurement of the beam energy smeared by the  $B$  momentum resolution, since,  $m_{ES} = \sqrt{E_{beam}^2 - p_B^{*2}}$ . We assume that it is the same for all the Monte Carlo samples but may be slightly different for the data. Because some fits will be done on low statistic samples we fix the peak value for all the fits. The peak is fixed to a value obtained from a free fit (all parameters free) to the signal sample in a high statistics bin,  $M_{Had} = 0.6$  to  $1.0 \text{ GeV}/c^2$ . The fit can be seen in Figure 10.1, giving a value of  $peak_{MC} = 5.27945 \pm 0.00006 \text{ GeV}/c^2$ .

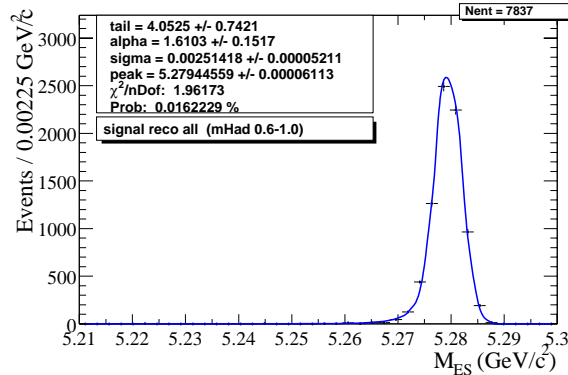


Figure 10.1: Free fit to MC signal sample in bin  $M_{Had} = 0.6-1.0 \text{ GeV}$  to obtain a value for the Crystal Ball peak,  $peak_{MC} = 5.27945 \pm 0.00006 \text{ GeV}/c^2$ .

The tail and  $\alpha$  Crystal Ball parameters are also fixed for the fits, so that when fitting low statistic samples (i.e.  $4$ -body events in the low  $M_{Had}$  region) they do not take on unreasonable values. These are fixed separately for each sample ( $2$ -body,  $3$ -body,  $4$ -body,  $\pi$ ,  $\pi^0$ ,  $K$ ,  $K_S$ ) in two  $M_{Had}$  ranges, 0.6 to 1.0  $\text{GeV}/c^2$  and 1.0 to 2.4  $\text{GeV}/c^2$ , instead of the usual nine, since we don't expect a large variation in these parameters. The fits can be seen in Figures 10.2 and

10.3, and the resulting parameters in Table 10.1. Systematic errors resulting from fixing these parameters are discussed in Chapter 12.

sample	$M_{Had}=0.6-1.0 \text{ GeV}/c^2$		$M_{Had}=1.0-2.4 \text{ GeV}/c^2$	
	tail	$\alpha$	tail	$\alpha$
<i>all</i>	$4.04 \pm 0.51$	$1.61 \pm 0.09$	$1.64 \pm 0.26$	$1.86 \pm 0.14$
<i>2-body</i>	$4.04 \pm 0.51$	$1.61 \pm 0.09$	$1.81 \pm 0.55$	$2.13 \pm 0.24$
<i>3-body</i>	—	—	$2.34 \pm 0.55$	$1.49 \pm 1.56$
<i>4-body</i>	—	—	$1.08 \pm 0.32$	$1.76 \pm 0.23$
$\pi$	$2.11 \pm 0.40$	$2.39 \pm 0.15$	$1.30 \pm 0.32$	$2.29 \pm 0.19$
$\pi^0$	$5.49 \pm 1.15$	$1.16 \pm 0.08$	$1.90 \pm 0.36$	$1.51 \pm 0.16$
$K$	$3.12 \pm 0.34$	$1.83 \pm 0.08$	$1.73 \pm 0.31$	$1.76 \pm 0.15$
$K_s$	$6.95 \pm 2.08$	$1.25 \pm 0.11$	$1.22 \pm 0.60$	$2.28 \pm 0.38$

Table 10.1: The Crystal Ball tail and  $\alpha$  parameters. From fits to the signal sample seen in Figure 10.2 and 10.3. The Crystal Ball peak is fixed, but all other parameters are free.

The last parameter left to determine is the width of the Crystal Ball function. This is expected to vary with  $M_{Had}$  and final state category, and so a unique value is obtained for each nine 200  $\text{MeV}/c^2$  bins of  $M_{Had}$  and for the eight final state categories. These values are obtained by fitting the signal sample to a Crystal Ball function with the peak, tail and  $\alpha$  parameters fixed to the values given above and the width free. The complete set of 72 plots can be seen in Appendix D in Figures D.1 to D.9, but two sample fits for the *all* final state category are shown in Figure 10.4, one in the low  $M_{Had}$  range 0.8 to 1.0  $\text{GeV}/c^2$  and one in the high  $M_{Had}$  range 1.8 to 2.0  $\text{GeV}/c^2$ .

Table 10.2 gives the results for the widths. The width varies from about 2-4  $\text{MeV}/c^2$ .

### Cross-feed Sample

The cross-feed sample is fit to an Argus plus Crystal Ball function. This incorporates a shape which falls with decreasing  $m_{ES}$  and a small peaking component. There is no overwhelming reason to pick this function, but with the limited statistics we have it fits well. A systematic study examining this choice is discussed in Chapter 12.

The Crystal Ball shape in the fits are fully constrained to the parameters from the signal sample fits. The Argus endpoint is also fixed to 5.29  $\text{GeV}/c^2$ .

$M_{Had}$	<i>all</i>	<i>2-body</i>	<i>3-body</i>	<i>4-body</i>
0.6-0.8	$2.42 \pm 0.10$	$2.42 \pm 0.10$	–	–
0.8-1.0	$2.52 \pm 0.02$	$2.52 \pm 0.02$	–	–
1.0-1.2	$2.59 \pm 0.11$	$2.62 \pm 0.14$	$2.55 \pm 0.18$	$1.81 \pm 0.85$
1.2-1.4	$2.56 \pm 0.11$	$2.48 \pm 0.15$	$2.57 \pm 0.17$	$2.28 \pm 0.01$
1.4-1.6	$2.65 \pm 0.12$	$2.51 \pm 0.18$	$2.54 \pm 0.17$	$3.06 \pm 0.41$
1.6-1.8	$2.68 \pm 0.16$	$2.50 \pm 0.25$	$2.58 \pm 0.01$	$2.71 \pm 0.35$
1.8-2.0	$2.26 \pm 0.18$	$2.19 \pm 0.36$	$2.26 \pm 0.28$	$2.17 \pm 0.32$
2.0-2.2	$2.67 \pm 0.28$	$1.78 \pm 0.30$	$3.04 \pm 0.49$	$3.04 \pm 0.63$
2.2-2.4	$3.29 \pm 0.47$	$3.02 \pm 0.72$	$3.45 \pm 0.71$	$2.74 \pm 0.88$
$M_{Had}$	$\pi$	$\pi^0$	$K$	$K_s$
0.6-0.8	$2.61 \pm 0.13$	$2.30 \pm 0.22$	$2.38 \pm 0.12$	$2.69 \pm 0.27$
0.8-1.0	$2.52 \pm 0.02$	$2.75 \pm 0.06$	$2.56 \pm 0.03$	$2.42 \pm 0.05$
1.0-1.2	$2.51 \pm 0.12$	$2.82 \pm 0.22$	$2.54 \pm 0.12$	$2.72 \pm 0.26$
1.2-1.4	$2.40 \pm 0.12$	$2.85 \pm 0.21$	$2.48 \pm 0.13$	$2.69 \pm 0.22$
1.4-1.6	$2.46 \pm 0.14$	$2.85 \pm 0.19$	$2.58 \pm 0.13$	$2.99 \pm 0.35$
1.6-1.8	$2.57 \pm 0.18$	$2.77 \pm 0.27$	$2.61 \pm 0.18$	$2.95 \pm 0.31$
1.8-2.0	$2.19 \pm 0.23$	$2.43 \pm 0.29$	$2.35 \pm 0.21$	$1.74 \pm 0.35$
2.0-2.2	$1.89 \pm 0.23$	$3.67 \pm 0.64$	$2.42 \pm 0.29$	$3.51 \pm 0.60$
2.2-2.4	$2.19 \pm 0.44$	$4.46 \pm 1.00$	$2.66 \pm 0.55$	$4.05 \pm 0.99$

Table 10.2: The width of the Crystal Ball function in  $\text{MeV}/c^2$ . From fits to signal MC shown in Figures D.1- D.9.

The free parameters in the fit are only the Crystal Ball fraction and the Argus shape.

The complete set of 72 plots for the cross-feed fits can be seen in Appendix D in Figures D.10 – D.18, but two sample fits for the *all* final state category are shown in Figure 10.5, one in the low  $M_{Had}$  range 0.8–1.0 GeV/ $c^2$  and one in the high  $M_{Had}$  range 1.8–2.0 GeV/ $c^2$ .

The resulting Argus shape parameters from the cross-feed fits are listed in Table 10.3. These parameters will be used later to fix one of the Argus shapes in the data fits.

$M_{Had}$	<i>all</i>	<i>2-body</i>	<i>3-body</i>	<i>4-body</i>
0.6-0.8	$-167.1 \pm 14.31$	$-167.1 \pm 14.31$	–	–
0.8-1.0	$-146.2 \pm 11.72$	$-148.2 \pm 13.06$	$-136.1 \pm 26.19$	–
1.0-1.2	$-104.0 \pm 14.65$	$-54.92 \pm 31.35$	$-117.1 \pm 19.07$	$-178.2 \pm 21.95$
1.2-1.4	$-110.5 \pm 10.06$	$-65.96 \pm 29.63$	$-113.9 \pm 12.93$	$-125.5 \pm 19.76$
1.4-1.6	$-116.0 \pm 7.373$	$-93.23 \pm 28.15$	$-117.2 \pm 10.74$	$-118.8 \pm 11.59$
1.6-1.8	$-87.64 \pm 6.752$	$-52.08 \pm 27.64$	$-89.80 \pm 10.61$	$-89.62 \pm 9.297$
1.8-2.0	$-64.10 \pm 6.011$	$-61.47 \pm 25.22$	$-56.32 \pm 10.16$	$-68.67 \pm 7.881$
2.0-2.2	$-58.78 \pm 6.088$	$-88.33 \pm 35.76$	$-80.69 \pm 10.65$	$-46.07 \pm 8.124$
2.2-2.4	$-20.66 \pm 6.724$	$-30.15 \pm 38.44$	$-1.587 \pm 12.89$	$-30.45 \pm 7.899$
$M_{Had}$	$\pi$	$\pi^0$	$K$	$K_s$
0.6-0.8	$-144.2 \pm 20.29$	$-188.7 \pm 20.35$	$-171.7 \pm 16.13$	$-152.8 \pm 30.73$
0.8-1.0	$-157.9 \pm 18.72$	$-136.1 \pm 15.37$	$-130.2 \pm 14.54$	$-177.8 \pm 20.20$
1.0-1.2	$-98.50 \pm 21.42$	$-103.5 \pm 21.25$	$-106.9 \pm 17.39$	$-98.49 \pm 27.40$
1.2-1.4	$-101.9 \pm 18.59$	$-111.4 \pm 12.51$	$-106.4 \pm 11.77$	$-123.4 \pm 20.07$
1.4-1.6	$-98.95 \pm 13.14$	$-122.7 \pm 9.518$	$-117.2 \pm 8.855$	$-114.8 \pm 13.80$
1.6-1.8	$-73.46 \pm 11.83$	$-92.79 \pm 8.343$	$-81.47 \pm 7.952$	$-104.5 \pm 12.98$
1.8-2.0	$-65.86 \pm 9.925$	$-62.51 \pm 7.691$	$-67.99 \pm 6.963$	$-52.88 \pm 11.74$
2.0-2.2	$-64.36 \pm 10.39$	$-57.46 \pm 7.986$	$-56.13 \pm 6.981$	$-66.47 \pm 12.73$
2.2-2.4	$-20.65 \pm 10.82$	$-18.81 \pm 9.085$	$-23.59 \pm 7.681$	$-18.03 \pm 13.13$

Table 10.3: The cross-feed Argus shape parameters, from fits to the cross-feed sample, shown in Figures D.10- D.18.

The yield in the signal region, from the Crystal Ball part of the fit, is also obtained. The yield is calculated as:

$$Y_{xfeed} = (f_{CB} * N) * (data\ lumi / signalMC\ lumi), \quad (10.1)$$

where  $f_{CB}$  is the Crystal Ball fraction from the fits, N is the number of events that are fit. As seen in the formula the yield is scaled down to the data luminosity so that it can be directly subtracted from the data yield to correct for the peaking cross-feed component. The yields from the fits are listed in Table 10.4 and are fairly small. Note that we have allowed  $f_{CB}$  to run negative which allows for a negative yield.

$M_{Had}$	<i>all</i>	<i>2-body</i>	<i>3-body</i>	<i>4-body</i>
0.6-0.8	$0.047 \pm 0.176$	$0.047 \pm 0.176$	–	–
0.8-1.0	$2.04 \pm 0.289$	$2.02 \pm 0.273$	$0.016 \pm 0.083$	–
1.0-1.2	$2.44 \pm 1.42$	$1.61 \pm 0.661$	$1.24 \pm 1.21$	–
1.2-1.4	$4.70 \pm 1.94$	$0.936 \pm 0.659$	$3.24 \pm 1.59$	$0.532 \pm 0.926$
1.4-1.6	$2.29 \pm 2.49$	$1.28 \pm 0.776$	$2.26 \pm 1.81$	$-1.52 \pm 1.92$
1.6-1.8	$3.97 \pm 2.33$	$0.401 \pm 0.456$	$2.16 \pm 1.58$	$1.61 \pm 1.82$
1.8-2.0	$3.65 \pm 1.98$	$-0.089 \pm 0.312$	$1.52 \pm 1.26$	$2.59 \pm 1.65$
2.0-2.2	$-0.167 \pm 1.99$	$-0.158 \pm 0.455$	$-2.65 \pm 1.38$	$2.11 \pm 1.81$
2.2-2.4	$6.58 \pm 2.12$	$0.33 \pm 0.321$	$2.82 \pm 1.21$	$3.07 \pm 1.71$

$M_{Had}$	$\pi$	$\pi^0$	$K$	$K_s$
0.6-0.8	$0.064 \pm 0.117$	$-0.019 \pm 0.135$	$-0.05 \pm 0.147$	$0.082 \pm 0.09$
0.8-1.0	$1.39 \pm 0.204$	$0.694 \pm 0.215$	$1.92 \pm 0.241$	$0.115 \pm 0.146$
1.0-1.2	$0.154 \pm 0.739$	$2.77 \pm 1.32$	$2.15 \pm 1.22$	$0.238 \pm 0.719$
1.2-1.4	$1.01 \pm 0.866$	$4.40 \pm 1.95$	$4.91 \pm 1.73$	$-0.202 \pm 0.808$
1.4-1.6	$0.868 \pm 1.14$	$1.72 \pm 2.55$	$1.35 \pm 2.17$	$0.585 \pm 1.30$
1.6-1.8	$0.099 \pm 0.953$	$4.43 \pm 2.28$	$4.09 \pm 2.02$	$-0.187 \pm 1.19$
1.8-2.0	$0.869 \pm 1.1$	$3.09 \pm 1.77$	$3.00 \pm 1.83$	$0.546 \pm 0.756$
2.0-2.2	$0.956 \pm 0.975$	$-1.71 \pm 2.17$	$0.785 \pm 1.62$	$-1.01 \pm 1.27$
2.2-2.4	$1.85 \pm 0.918$	$5.50 \pm 2.20$	$5.10 \pm 1.68$	$0.895 \pm 1.20$

Table 10.4: The cross-feed yield, from fits to the cross-feed sample, shown in Figures D.10- D.18. The yield is calculated by: num. ev. in plot \* CB fraction \* lumi factor, where the lumi factor is the scale factor to reduce the luminosity to the data luminosity ( $20.7 fb^{-1}$ ).

### 10.1.2 Background Monte Carlo

The background Monte Carlo consists of continuum (uds + ccb) and generic  $B\bar{B}$  events. The composition and behavior of these backgrounds are discussed in Chapter 7.

The sum of these two background contributions is parameterized by one Argus shape in the data fits. In order to obtain this background Argus shape parameter a fit is done to a  $8.7fb^{-1}$  combined sample of continuum and  $B\bar{B}$  Monte Carlo (uds, ccb, b0g, and bpg, where the luminosity is limited by the uds sample).

As discussed in Chapter 7, the continuum background can be parameterized by an Argus shape over all  $M_{Had}$  while the  $B\bar{B}$  background has a peaking component at high  $M_{Had}$ . The combined background sample is therefore fit to an Argus shape in the  $M_{Had}$  range 0.6 to 1.8 GeV/ $c^2$ , and an Argus plus Crystal Ball shape in the  $M_{Had}$  range 1.8 to 2.4 GeV/ $c^2$ , which is the last three  $M_{Had}$  bins.

In the fits the Argus endpoint is fixed to 5.29 GeV/ $c^2$ , while the shape is free. The Crystal Ball shape, when used, is fully fixed to the signal shape parameters, which is necessary with the limited statistics in the  $B\bar{B}$  sample. The Crystal Ball fraction is also a free parameter in the fits.

The complete set of 72 plots for the background fits can be seen in Appendix D in Figures D.19 – D.27, but two sample fits for the *all* final state category are shown in Figure 10.6, one in the low  $M_{Had}$  range 0.8 to 1.0 GeV/ $c^2$  and one in the high  $M_{Had}$  range 1.8 to 2.0 GeV/ $c^2$ .

The Argus shape parameters from the fits are listed in Table 10.5. These parameters will be used to fix one of the Argus shapes in the data fits.

## $B\bar{B}$ Yield

The peaking part of the  $B\bar{B}$  background has a significant yield at high  $M_{Had}$ , the last three bins. Since this yield will be directly subtracted from the data yield the uncertainty on it will directly contribute to the statistical uncertainty on the branching fraction measurement. In order to use the maximum statistics to measure the  $B\bar{B}$  yield the  $B\bar{B}$  sample is fit separately to an Argus plus Crystal Ball function. The Crystal Ball shape is again fully fixed to the signal parameters due to low statistics in the fits. The Argus shape is free and the endpoint is fixed to 5.29 GeV/ $c^2$ .

A  $14.1fb^{-1}$  generic  $B\bar{B}$  sample is fit in the last three  $M_{Had}$  bins, 1.8–2.4 GeV/ $c^2$ , and for each of the eight final state categories. The complete set of 24 plots can be seen in Appendix D in Figures D.28 – D.30, but a sample fits for the *all* final state category is shown in Figure 10.7, in the  $M_{Had}$  range 1.8–2.0 GeV/ $c^2$ .

The  $B\bar{B}$  background yield in the signal region is obtained from these fits. As

$M_{Had}$	<i>all</i>	<i>2-body</i>	<i>3-body</i>	<i>4-body</i>
0.6-0.8	$-28.6 \pm 20.1$	$-28.6 \pm 20.1$	–	–
0.8-1.0	$-9.70 \pm 12.8$	$-6.24 \pm 14.2$	$-24.6 \pm 29.4$	–
1.0-1.2	$-25.8 \pm 10.4$	$-16.1 \pm 16.4$	$-30.5 \pm 13.7$	$-83.8 \pm 75.4$
1.2-1.4	$-13.5 \pm 9.56$	$-28.6 \pm 18.3$	$-16.0 \pm 12.7$	$20.5 \pm 24.5$
1.4-1.6	$-14.0 \pm 7.63$	$-4.36 \pm 19.1$	$-23.8 \pm 10.3$	$-1.45 \pm 14.1$
1.6-1.8	$-10.6 \pm 6.79$	$-18.0 \pm 19.1$	$-4.67 \pm 9.91$	$-15.4 \pm 10.7$
1.8-2.0	$-12.3 \pm 7.29$	$-20.0 \pm 22.2$	$-4.73 \pm 12.4$	$-15.4 \pm 9.91$
2.0-2.2	$-11.1 \pm 6.62$	$-50.1 \pm 29.1$	$5.52 \pm 10.9$	$-21.2 \pm 9.07$
2.2-2.4	$-23.1 \pm 6.37$	$-33.9 \pm 28.6$	$-21.3 \pm 12.7$	$-22.6 \pm 7.43$
$M_{Had}$	$\pi$	$\pi^0$	$K$	$K_s$
0.6-0.8	$-55.7 \pm 25.5$	$20.1 \pm 35.3$	$-6.11 \pm 23.9$	$-92.3 \pm 41.4$
0.8-1.0	$-11.3 \pm 16.4$	$-7.21 \pm 20.5$	$3.21 \pm 15.0$	$-47.6 \pm 25.4$
1.0-1.2	$-15.3 \pm 16.3$	$-33.1 \pm 13.5$	$-24.4 \pm 12.6$	$-28.8 \pm 18.5$
1.2-1.4	$-16.5 \pm 15.1$	$-11.4 \pm 12.4$	$-16.9 \pm 10.8$	$-1.30 \pm 20.6$
1.4-1.6	$-22.1 \pm 12.3$	$-9.01 \pm 9.74$	$-21.7 \pm 9.07$	$4.20 \pm 14.2$
1.6-1.8	$-4.68 \pm 10.9$	$-14.4 \pm 8.67$	$-10.9 \pm 7.95$	$-9.83 \pm 13.1$
1.8-2.0	$-18.5 \pm 12.6$	$-9.38 \pm 9.07$	$-7.14 \pm 8.79$	$-26.0 \pm 12.7$
2.0-2.2	$-27.5 \pm 10.3$	$-2.50 \pm 8.86$	$-11.7 \pm 7.73$	$-10.0 \pm 13.0$
2.2-2.4	$-23.1 \pm 6.37$	$-19.4 \pm 8.87$	$-22.8 \pm 7.05$	$-27.1 \pm 13.0$

Table 10.5: The ( $B\bar{B}$  + continuum) background Argus shape parameters, from the fits shown in Figures D.19- D.27.

for the cross-feed, the yield is calculated as:

$$Y_{B\bar{B}} = (f_{CB} * N) * (data\ lumi / B\bar{B}MC\ lumi), \quad (10.2)$$

where  $f_{CB}$  is the Crystal Ball fraction from the fits,  $N$  is the number of events that are fit. As seen in the formula the yield is scaled up to the data luminosity so that it can be directly subtracted from the data yield to correct for the peaking background component. The yields from the fits are listed in Table 10.6 and are significant. Note that we have allowed  $f_{CB}$  to run negative which allows for a negative yield.

$M_{Had}$	<i>all</i>	<i>2-body</i>	<i>3-body</i>	<i>4-body</i>
1.8-2.0	$10.6 \pm 6.00$	–	$9.29 \pm 3.94$	$2.59 \pm 4.24$
2.0-2.2	$9.83 \pm 9.29$	$-1.62 \pm 2.4$	$14.0 \pm 5.58$	$-6.48 \pm 7.67$
2.2-2.4	$26.1 \pm 13.0$	$2.83 \pm 1.61$	$9.17 \pm 6.97$	$13.4 \pm 10.7$
$M_{Had}$	$\pi$	$\pi^0$	$K$	$K_s$
1.8-2.0	$6.24 \pm 1.90$	$4.08 \pm 4.43$	$6.75 \pm 4.94$	$3.21 \pm 3.19$
2.0-2.2	$1.79 \pm 4.14$	$8.69 \pm 9.79$	$7.26 \pm 7.81$	$2.35 \pm 5.19$
2.2-2.4	$26.1 \pm 13.0$	$12.8 \pm 14.0$	$25.5 \pm 10.9$	$-4.61 \pm 5.35$

Table 10.6: The  $B\bar{B}$  yield, from fits to the  $B\bar{B}$  MC sample ( $14.1\text{ fb}^{-1}$ ) The fits are shown in Figures D.28, D.29, and D.30 The yield is calculated by: num. ev. in plot \* CB fraction \* lumi factor, where the lumi factor is the scale factor to increase the lumi to the data lumi ( $20.7\text{ fb}^{-1}$ ).

To justify our choice of using only the last three bins in  $M_{Had}$ , 1.8-2.4  $\text{GeV}/c^2$ , we have fit the  $B\bar{B}$  sample for the *all* final state category also for the  $M_{Had}$  bin 1.6–1.8  $\text{GeV}/c^2$ . We obtain a negative yield which indicates that there are no events in the signal region. The scaled yield is  $Y_{B\bar{B}} = -1.98 \pm 4.08$ . Figure 10.8 shows the fit. We will not consider this yield in the final results.

The fits to the sum of the  $B\bar{B}$  and continuum samples, presented in the previous section can also give a yield for the peaking background in the last three bins. We can check that the results are the same, within statistical errors, as those to the fit of the  $B\bar{B}$  sample by itself. The combined sample of  $B\bar{B}$  and continuum is limited by the Monte Carlo statistics for the uds sample,  $8.7\text{ fb}^{-1}$ , while the  $B\bar{B}$  sample has a luminosity of  $14.1\text{ fb}^{-1}$ . Table 10.7 lists the yield for the fits to the two different samples. We list only the results for the *all* final

state category in the three bins. The numbers do agree within large statistical errors, although the errors are correlated since they are not independent samples. There is a trend, the fits to the  $B\bar{B}$  plus continuum provide a larger yield. In Section 12.6 we present results from a high-statistics toy–MC study from which we assign a 10% systematic shift and an error to correct for this discrepancy. The large difference seen in the table presented here are partly an artifact of the low statistics and are accompanied by a large statistical error. For the moment we will use the peaking values from the  $B\bar{B}$  fits.

$M_{Had}$	$B\bar{B}$	$B\bar{B} + \text{continuum}$
1.8-2.0	$10.6 \pm 6.00$	$19.73 \pm 15.69$
2.0-2.2	$9.83 \pm 9.29$	$24.69 \pm 18.76$
2.2-2.4	$26.1 \pm 13.0$	$47.51 \pm 25.70$

Table 10.7: The peaking yield for the *all* category from a fit to the  $B\bar{B}$  or the  $B\bar{B}$  plus continuum sample. (The yields are scaled to the data luminosity.)

## 10.2 Fits to data

The function used for the fits to the data events is made of two Argus functions for the background, cross–feed and  $B\bar{B}$  plus continuum, and a Crystal Ball function for the signal. As discussed earlier, to reduce the statistical uncertainty in the fitting, the two Argus shapes and the Crystal Ball parameters are fixed to values obtained from Monte Carlo fits.

The Crystal Ball parameters in the fits are all fixed to the values from the signal Monte Carlo fits, except the peak. The peak of the Crystal Ball measures the beam energy smeared by  $B$  momentum resolution,  $m_{ES} = \sqrt{E_{beam}^2 - p_B^{*2}}$ , which can be different in MC and data. The data peak is obtained from a fit to the high statistics  $M_{Had}$  range 0.6-1.0 GeV/ $c^2$ . The peak is left free in this fit, but the mean, tail, and  $\alpha$  parameters as well as the two background Argus shapes are fixed. The fixed parameter values are obtained from fits to the Monte Carlo samples in the same  $M_{Had}$  range. The fits can be seen in Figure 10.9 and the value for the data peak is found to be,  $peak_{data} = 5.28041 \pm 0.00032$  GeV/ $c^2$ . This value is used to fix the Crystal Ball peak parameter in all the data fits.

The background is parameterized by two Argus shapes: one for the cross–feed background and one for the  $B\bar{B}$  plus continuum background. The endpoints of

both Argus functions are fixed to  $5.29 \text{ GeV}/c^2$  and the shape parameters are also fixed to values from the Monte Carlo fits. The cross-feed Argus shape parameters are listed in Table 10.3. The Argus shape parameters from the fits to the combined  $B\bar{B}$  and continuum Monte Carlo are listed in Table 10.5. The Monte Carlo fits are discussed in the previous section.

To summarize, the parameters in the fit are defined as follows:

- Crystal Ball peak (fixed): fixed to value from data fit in  $M_{Had}$  range 0.6-1.0  $\text{GeV}/c^2$ , as described above.  $peak_{data} = 5.28041 \pm 0.00032 \text{ GeV}/c^2$
- Crystal Ball tail and  $\alpha$  parameters (fixed): both fixed to values from fits to signal Monte Carlo in two  $M_{Had}$  bins, 0.6-1.0 or 1.0-2.4  $\text{GeV}/c^2$ . The parameters are listed in Table 10.1.
- Crystal Ball width (fixed): fixed to values from the signal Monte Carlo fits for each bin and final state category. The parameters are listed in Table 10.2.
- Cross-feed Argus (fixed): endpoint fixed to  $5.29 \text{ GeV}/c^2$ , shape fixed to values from Monte Carlo fits for each bin and final state category. The shape parameters are listed in Table 10.3.
- $B\bar{B}$  plus continuum Argus (fixed): endpoint fixed to  $5.29 \text{ GeV}/c^2$ , shape fixed to values from Monte Carlo fits for each bin and final state category. The shape parameters are listed in Table 10.5.
- Crystal Ball fraction (free): the fraction between the Crystal Ball signal shape and the background (sum of two Argus shapes) is free in the fit.
- Cross-feed fraction (free): the fraction between the cross-feed and  $B\bar{B}$  plus continuum Argus function is left free in the fit.

The complete set of 72 plots for the data fits can be seen in Appendix D in Figures D.31 – D.39. Two sample fits for the *all* final state category are shown in Figure 10.11, one in the low  $M_{Had}$  range 0.8–1.0  $\text{GeV}/c^2$  and one in the high  $M_{Had}$  range 1.8–2.0  $\text{GeV}/c^2$ .

The resulting yields from the data fits are listed in Table 10.8. Note that the Crystal Ball fraction is allowed to go negative, in order to allow for the full range of statistical fluctuations, and a negative yield is obtained for some entries.

Table 10.9 shows the yields for the *all* final state category for data, cross-feed Monte Carlo  $B\bar{B}$  Monte Carlo and the resulting signal yield, where the cross-feed and  $B\bar{B}$  yield have been subtracted from the data yield. Figure ?? shows the data, cross-feed and  $B\bar{B}$  yields in colored histograms and the signal yield as the open histogram with the error bars. Table 10.10, 10.11 and 10.12 show the same results for the other final state categories.

$M_{Had}$	<i>all</i>	<i>2-body</i>	<i>3-body</i>	<i>4-body</i>
0.6-0.8	$10.38 \pm 5.911$	$10.38 \pm 5.911$	–	–
0.8-1.0	$119.6 \pm 13.22$	$120.8 \pm 12.34$	–	–
1.0-1.2	$27.42 \pm 8.14$	$11.00 \pm 4.995$	$14.83 \pm 6.184$	$0.9397 \pm 1.793$
1.2-1.4	$65.99 \pm 14.10$	$11.50 \pm 5.245$	$52.50 \pm 11.76$	$-3.843 \pm 4.709$
1.4-1.6	$73.18 \pm 13.95$	$18.63 \pm 5.741$	$41.94 \pm 10.08$	$15.79 \pm 7.547$
1.6-1.8	$44.55 \pm 14.73$	$4.875 \pm 4.561$	$20.92 \pm 9.606$	$22.12 \pm 11.25$
1.8-2.0	$53.53 \pm 14.04$	$4.134 \pm 3.340$	$30.94 \pm 9.712$	$19.88 \pm 10.59$
2.0-2.2	$32.04 \pm 13.60$	$-4.845 \pm 2.052$	$15.34 \pm 8.501$	$20.58 \pm 11.24$
2.2-2.4	$38.73 \pm 15.53$	$5.120 \pm 4.071$	$4.401 \pm 9.050$	$25.49 \pm 12.78$
$M_{Had}$	$\pi$	$\pi^0$	$K$	$K_s$
0.6-0.8	$6.676 \pm 3.886$	$-2.329 \pm 3.832$	$3.385 \pm 4.542$	$1.187 \pm 3.045$
0.8-1.0	$95.08 \pm 10.23$	$24.65 \pm 8.176$	$101.8 \pm 11.60$	$17.47 \pm 5.014$
1.0-1.2	$13.93 \pm 5.128$	$13.07 \pm 6.684$	$22.00 \pm 6.992$	$4.945 \pm 4.77$
1.2-1.4	$38.83 \pm 8.864$	$28.91 \pm 11.58$	$55.94 \pm 12.08$	$8.906 \pm 6.969$
1.4-1.6	$25.02 \pm 7.306$	$48.08 \pm 12.49$	$50.90 \pm 10.58$	$13.88 \pm 7.293$
1.6-1.8	$3.659 \pm 8.539$	$42.32 \pm 12.84$	$39.71 \pm 12.75$	$4.374 \pm 8.025$
1.8-2.0	$22.05 \pm 8.757$	$33.82 \pm 11.62$	$29.67 \pm 12.42$	$11.87 \pm 5.469$
2.0-2.2	$10.81 \pm 5.955$	$17.17 \pm 15.32$	$15.78 \pm 9.457$	$16.72 \pm 9.107$
2.2-2.4	$18.18 \pm 8.210$	$25.01 \pm 15.05$	$24.88 \pm 12.63$	$11.01 \pm 6.984$

Table 10.8: The data yield, from the fits shown in Figures D.31– D.39. The yield is calculated by: num. ev. in plot \* signal fraction

### 10.3 Comparison of Final State Category Yields

As a consistency check, we sum the *2-*, *3-*, and *4-body* yields and compare them to the *all* final state category yield. The same can be done with the sum of the  $\pi$  and  $\pi^0$  categories and the  $K$  and  $K_S$  categories. Table 10.13 shows

$M_{Had}$	data	bbbar	x-feed	result
0.6-0.8	$10.38 \pm 5.91$	–	$0.05 \pm 0.18$	$10.34 \pm 5.91$
0.8-1.0	$119.6 \pm 13.22$	–	$2.04 \pm 0.29$	$117.6 \pm 13.22$
1.0-1.2	$27.42 \pm 8.14$	–	$2.44 \pm 1.42$	$24.98 \pm 8.26$
1.2-1.4	$65.99 \pm 14.10$	–	$4.70 \pm 1.94$	$61.29 \pm 14.23$
1.4-1.6	$73.18 \pm 13.95$	–	$2.29 \pm 2.49$	$70.89 \pm 14.17$
1.6-1.8	$44.55 \pm 14.73$	–	$3.97 \pm 2.33$	$40.58 \pm 14.91$
1.8-2.0	$53.53 \pm 14.04$	$10.61 \pm 6.00$	$3.65 \pm 1.98$	$39.27 \pm 15.40$
2.0-2.2	$32.04 \pm 13.60$	$9.83 \pm 9.29$	$-0.17 \pm 1.99$	$22.38 \pm 16.59$
2.2-2.4	$38.73 \pm 15.53$	$26.10 \pm 13.02$	$6.58 \pm 2.12$	$6.05 \pm 20.38$

Table 10.9: The yield from the various samples for the *all* final state category in the nine  $M_{Had}$  bins.

the difference between the sums and the *all* final state category yields. The differences are all quite small. Therefore we claim the yields are consistent.

reco 2-body				
$M_{Had}$	data	bbbar	x-feed	result
0.6-0.8	$10.38 \pm 5.91$	–	$0.05 \pm 0.18$	$10.34 \pm 5.91$
0.8-1.0	$120.8 \pm 12.34$	–	$2.02 \pm 0.27$	$118.8 \pm 12.34$
1.0-1.2	$11.00 \pm 5.00$	–	$1.61 \pm 0.66$	$9.39 \pm 5.04$
1.2-1.4	$11.50 \pm 5.25$	–	$0.94 \pm 0.66$	$10.56 \pm 5.29$
1.4-1.6	$18.63 \pm 5.74$	–	$1.28 \pm 0.78$	$17.35 \pm 5.79$
1.6-1.8	$4.88 \pm 4.56$	–	$0.40 \pm 0.46$	$4.47 \pm 4.58$
1.8-2.0	$4.13 \pm 3.34$	–	$-0.09 \pm 0.31$	$4.22 \pm 3.35$
2.0-2.2	$-4.85 \pm 2.05$	$-1.62 \pm 2.40$	$-0.16 \pm 0.46$	$-3.07 \pm 3.19$
2.2-2.4	$5.12 \pm 4.07$	$2.83 \pm 1.61$	$0.33 \pm 0.32$	$1.96 \pm 4.39$
reco 3-body				
$M_{Had}$	data	bbbar	x-feed	result
0.6-0.8	–	–	–	–
0.8-1.0	$-1.47 \pm 2.47$	–	$0.02 \pm 0.08$	$-1.49 \pm 2.47$
1.0-1.2	$14.83 \pm 6.18$	–	$1.24 \pm 1.21$	$13.59 \pm 6.30$
1.2-1.4	$52.50 \pm 11.76$	–	$3.24 \pm 1.59$	$49.26 \pm 11.87$
1.4-1.6	$41.94 \pm 10.08$	–	$2.26 \pm 1.81$	$39.69 \pm 10.24$
1.6-1.8	$20.92 \pm 9.61$	–	$2.16 \pm 1.58$	$18.77 \pm 9.74$
1.8-2.0	$30.94 \pm 9.71$	$9.29 \pm 3.94$	$1.52 \pm 1.26$	$20.13 \pm 10.56$
2.0-2.2	$15.34 \pm 8.50$	$13.96 \pm 5.59$	$-2.65 \pm 1.38$	$4.03 \pm 10.26$
2.2-2.4	$4.40 \pm 9.05$	$9.17 \pm 6.97$	$2.82 \pm 1.21$	$-7.59 \pm 11.49$
reco 4-body				
$M_{Had}$	data	bbbar	x-feed	result
0.6-0.8	–	–	–	–
0.8-1.0	–	–	–	–
1.0-1.2	$0.94 \pm 1.79$	–	–	$0.94 \pm 1.79$
1.2-1.4	$-3.84 \pm 4.71$	–	$0.53 \pm 0.93$	$-4.38 \pm 4.80$
1.4-1.6	$15.79 \pm 7.55$	–	$-1.52 \pm 1.92$	$17.31 \pm 7.79$
1.6-1.8	$22.12 \pm 11.25$	–	$1.61 \pm 1.82$	$20.51 \pm 11.40$
1.8-2.0	$19.88 \pm 10.59$	$2.59 \pm 4.24$	$2.59 \pm 1.65$	$14.71 \pm 11.53$
2.0-2.2	$20.58 \pm 11.24$	$-6.48 \pm 7.67$	$2.11 \pm 1.81$	$24.95 \pm 13.73$
2.2-2.4	$25.49 \pm 12.78$	$13.35 \pm 10.67$	$3.07 \pm 1.71$	$9.07 \pm 16.74$

Table 10.10: The yield from the various samples for the *2-body*, *3-body* and *4-body* final state categories in nine  $M_{Had}$  bins.

reco $\pi$				
$M_{Had}$	data	bbbar	x-feed	result
0.6-0.8	$6.68 \pm 3.89$	–	$0.06 \pm 0.12$	$6.61 \pm 3.89$
0.8-1.0	$95.08 \pm 10.23$	–	$1.39 \pm 0.20$	$93.69 \pm 10.24$
1.0-1.2	$13.93 \pm 5.13$	–	$0.15 \pm 0.74$	$13.78 \pm 5.18$
1.2-1.4	$38.83 \pm 8.86$	–	$1.01 \pm 0.87$	$37.82 \pm 8.91$
1.4-1.6	$25.02 \pm 7.31$	–	$0.87 \pm 1.14$	$24.16 \pm 7.40$
1.6-1.8	$3.66 \pm 8.54$	–	$0.10 \pm 0.95$	$3.56 \pm 8.59$
1.8-2.0	$22.05 \pm 8.76$	$6.24 \pm 1.90$	$0.87 \pm 1.10$	$14.94 \pm 9.03$
2.0-2.2	$10.81 \pm 5.96$	$1.79 \pm 4.14$	$0.96 \pm 0.98$	$8.06 \pm 7.32$
2.2-2.4	$18.18 \pm 8.21$	$11.33 \pm 6.14$	$1.85 \pm 0.92$	$5.00 \pm 10.29$
reco $\pi^0$				
$M_{Had}$	data	bbbar	x-feed	result
0.6-0.8	$-2.33 \pm 3.83$	–	$-0.02 \pm 0.14$	$-2.31 \pm 3.83$
0.8-1.0	$24.65 \pm 8.18$	–	$0.69 \pm 0.22$	$23.96 \pm 8.18$
1.0-1.2	$13.07 \pm 6.68$	–	$2.77 \pm 1.32$	$10.33 \pm 6.81$
1.2-1.4	$28.91 \pm 11.58$	–	$4.40 \pm 1.95$	$24.51 \pm 11.74$
1.4-1.6	$48.08 \pm 12.49$	–	$1.72 \pm 2.55$	$46.36 \pm 12.75$
1.6-1.8	$42.32 \pm 12.84$	–	$4.43 \pm 2.28$	$37.89 \pm 13.04$
1.8-2.0	$33.82 \pm 11.62$	$4.08 \pm 4.44$	$3.09 \pm 1.77$	$26.65 \pm 12.56$
2.0-2.2	$17.17 \pm 15.32$	$8.69 \pm 9.79$	$-1.71 \pm 2.17$	$10.20 \pm 18.31$
2.2-2.4	$25.01 \pm 15.05$	$12.79 \pm 13.97$	$5.5 \pm 2.2$	$6.72 \pm 20.65$

Table 10.11: The yield from the various samples for  $\pi$  and  $\pi^0$  final state categories in nine  $M_{Had}$  bins.

reco $K$				
$M_{Had}$	data	bbbar	x-feed	result
0.6-0.8	$3.39 \pm 4.54$	–	$-0.05 \pm 0.15$	$3.43 \pm 4.55$
0.8-1.0	$101.8 \pm 11.6$	–	$1.92 \pm 0.24$	$99.85 \pm 11.60$
1.0-1.2	$22.00 \pm 6.99$	–	$2.15 \pm 1.22$	$19.85 \pm 7.10$
1.2-1.4	$55.94 \pm 12.08$	–	$4.91 \pm 1.73$	$51.03 \pm 12.20$
1.4-1.6	$50.90 \pm 10.58$	–	$1.35 \pm 2.17$	$49.55 \pm 10.80$
1.6-1.8	$39.71 \pm 12.75$	–	$4.09 \pm 2.02$	$35.63 \pm 12.91$
1.8-2.0	$29.67 \pm 12.42$	$6.75 \pm 4.94$	$3.00 \pm 1.83$	$19.92 \pm 13.49$
2.0-2.2	$15.78 \pm 9.46$	$7.27 \pm 7.81$	$0.79 \pm 1.62$	$7.73 \pm 12.37$
2.2-2.4	$24.88 \pm 12.63$	$25.52 \pm 10.92$	$5.10 \pm 1.68$	$-5.74 \pm 16.78$
reco $K_S$				
$M_{Had}$	data	bbbar	x-feed	result
0.6-0.8	$1.19 \pm 3.05$	–	$0.08 \pm 0.09$	$1.11 \pm 3.05$
0.8-1.0	$17.47 \pm 5.01$	–	$0.12 \pm 0.15$	$17.35 \pm 5.02$
1.0-1.2	$4.95 \pm 4.77$	–	$0.24 \pm 0.72$	$4.71 \pm 4.82$
1.2-1.4	$8.91 \pm 6.97$	–	$-0.20 \pm 0.81$	$9.11 \pm 7.02$
1.4-1.6	$13.88 \pm 7.29$	–	$0.59 \pm 1.30$	$13.30 \pm 7.41$
1.6-1.8	$4.37 \pm 8.03$	–	$-0.19 \pm 1.19$	$4.56 \pm 8.11$
1.8-2.0	$11.87 \pm 5.47$	$3.21 \pm 3.20$	$0.55 \pm 0.76$	$8.12 \pm 6.38$
2.0-2.2	$16.72 \pm 9.11$	$2.35 \pm 5.19$	$-1.01 \pm 1.27$	$15.39 \pm 10.56$
2.2-2.4	$11.01 \pm 6.98$	$-4.61 \pm 5.35$	$0.90 \pm 1.20$	$14.73 \pm 8.88$

Table 10.12: The yield from the various samples for  $K$  and  $K_S$  final state categories in nine  $M_{Had}$  bins.

<i>(2-body + 3-body + 4-body) - all</i>				
$M_{Had}$	data	bbbar	x-feed	result
0.6-0.8	0	–	0	0
0.8-1.0	-0.27	–	-0.0038	-0.27
1.0-1.2	-0.66	–	0.41	-1.1
1.2-1.4	-5.8	–	0.0091	-5.8
1.4-1.6	3.2	–	-0.26	3.5
1.6-1.8	3.4	–	0.2	3.2
1.8-2.0	1.4	1.3	0.36	-0.22
2.0-2.2	-0.96	-4	-0.54	3.5
2.2-2.4	-3.7	-0.74	-0.36	-2.6
<i>(<math>\pi + \pi^0</math>) - all</i>				
$M_{Had}$	data	bbbar	x-feed	result
0.6-0.8	-6	–	-0.002	-6
0.8-1.0	0.1	–	0.042	0.059
1.0-1.2	-0.41	–	0.49	-0.9
1.2-1.4	1.7	–	0.71	1
1.4-1.6	-0.074	–	0.3	-0.38
1.6-1.8	1.4	–	0.56	0.87
1.8-2.0	2.3	-0.29	0.31	2.3
2.0-2.2	-4.1	0.65	-0.59	-4.1
2.2-2.4	4.5	-2	0.77	5.7
<i>(<math>K + K_S</math>) - all</i>				
$M_{Had}$	data	bbbar	x-feed	result
0.6-0.8	-5.8	–	-0.015	-5.8
0.8-1.0	-0.39	–	-0.008	-0.38
1.0-1.2	-0.47	–	-0.053	-0.42
1.2-1.4	-1.1	–	0.0098	-1.2
1.4-1.6	-8.4	–	-0.35	-8
1.6-1.8	-0.46	–	-0.072	-0.39
1.8-2.0	-12	-0.65	-0.11	-11
2.0-2.2	0.47	-0.21	-0.063	0.74
2.2-2.4	-2.8	-5.2	-0.59	2.9

Table 10.13: The difference in the yields between the sum of 2-, 3-, 4-body, or  $\pi$ ,  $\pi^0$ , or  $K$ ,  $K_s$  final state categories and the *all* final state category in nine  $M_{Had}$  bins.

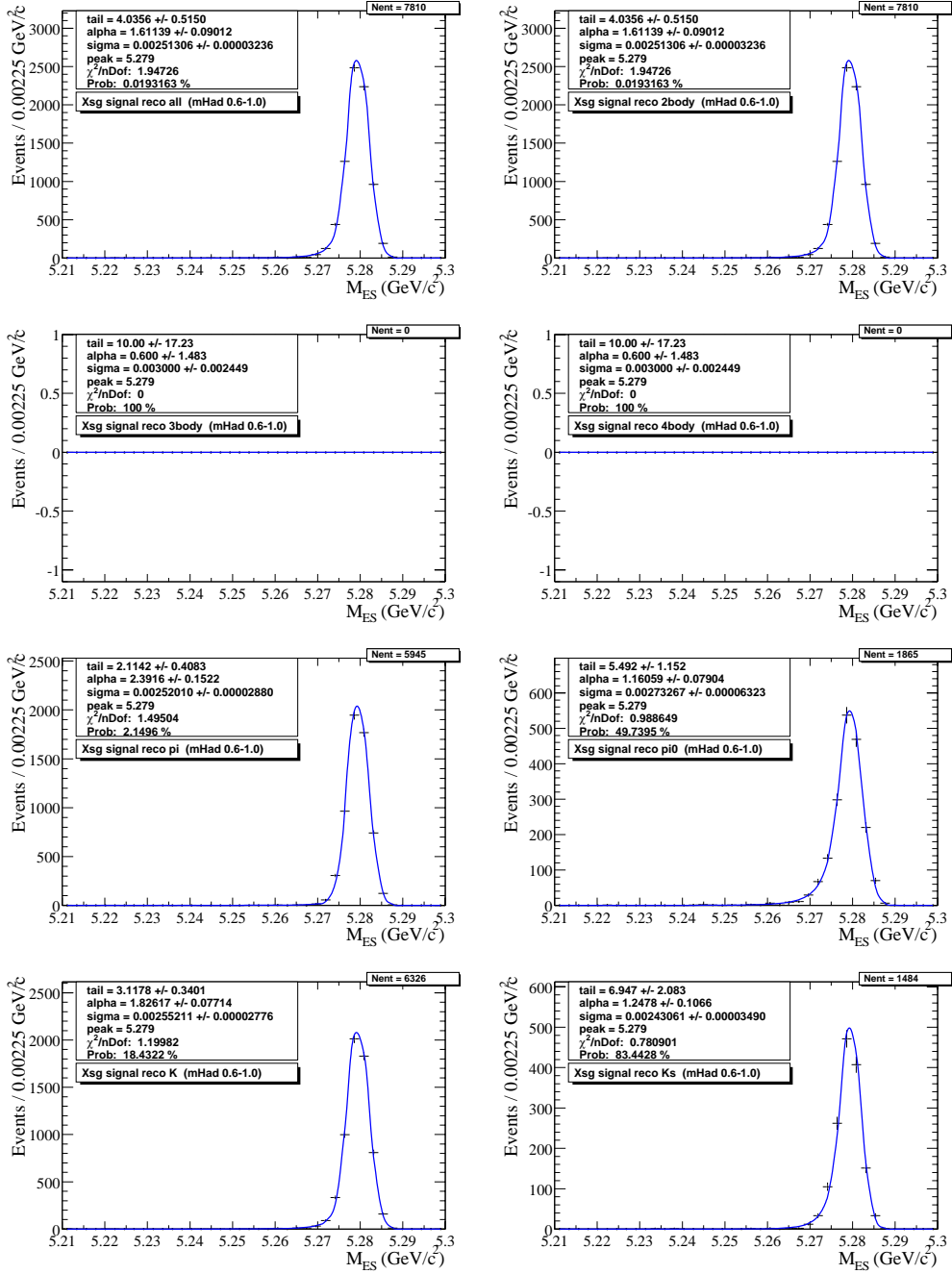


Figure 10.2: MC signal fit over the wide  $M_{Had}$  bin, 0.6-1.0 GeV/c<sup>2</sup>.

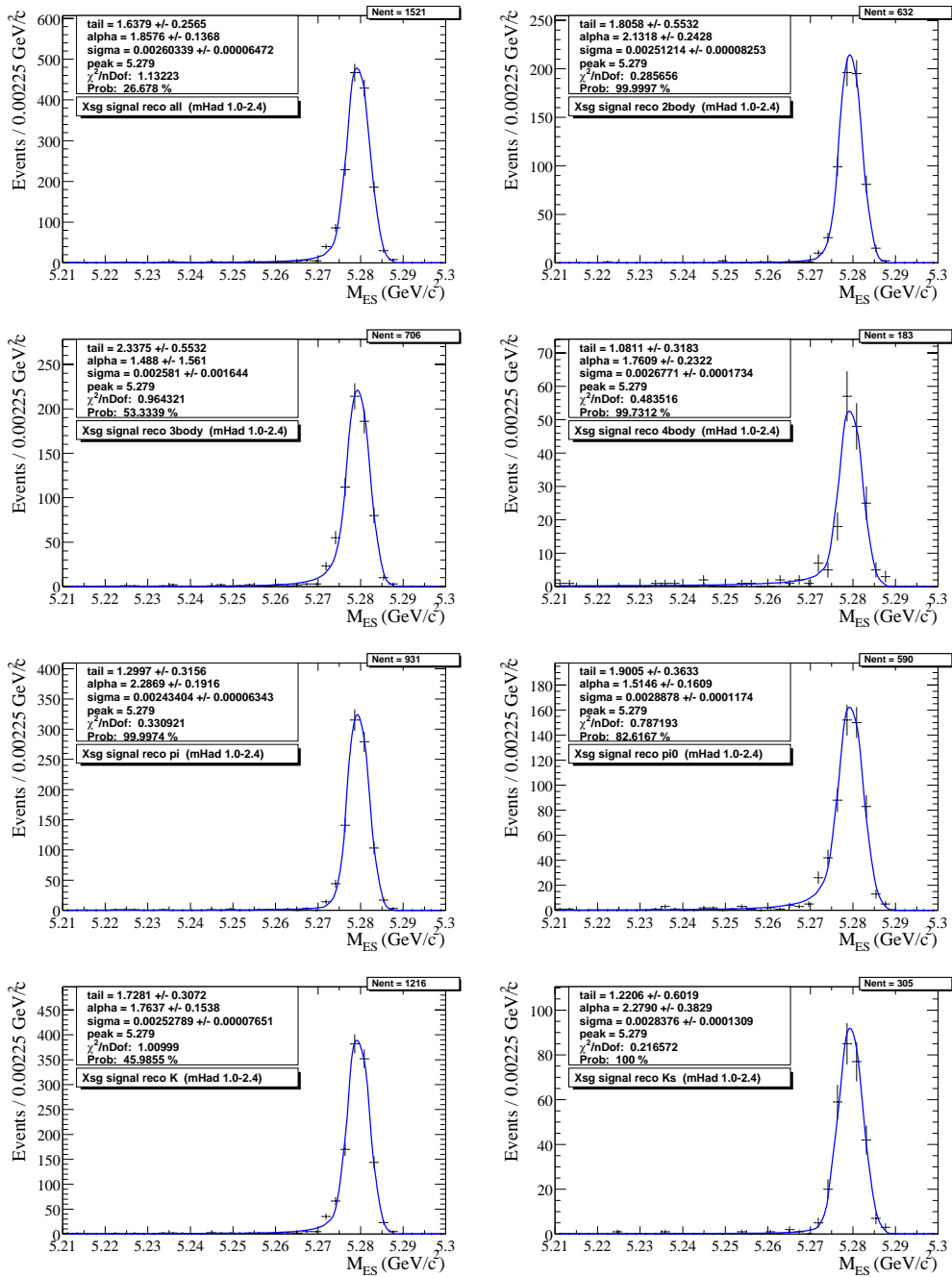


Figure 10.3: MC signal fit over the wide  $M_{Had}$  bin, 1.0-2.4 GeV.

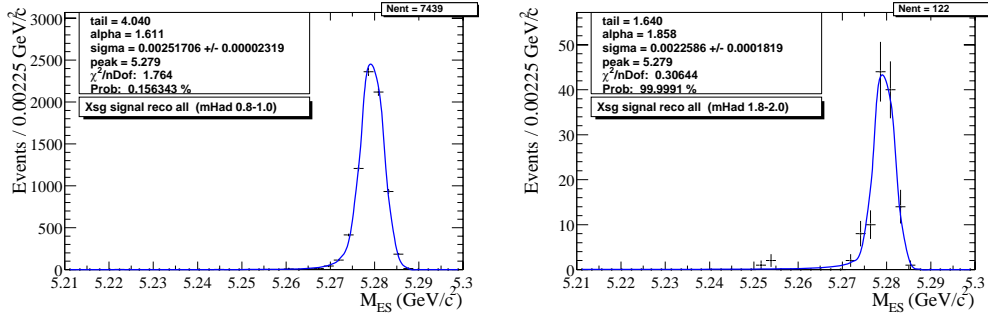


Figure 10.4: Sample MC signal fits.

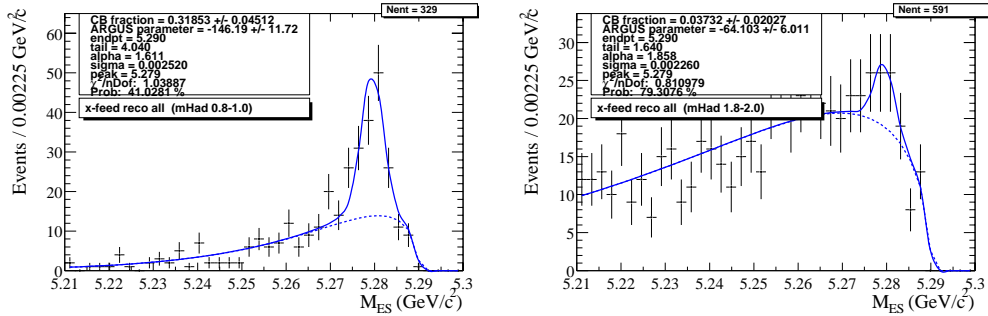


Figure 10.5: Sample MC cross-feed fits.

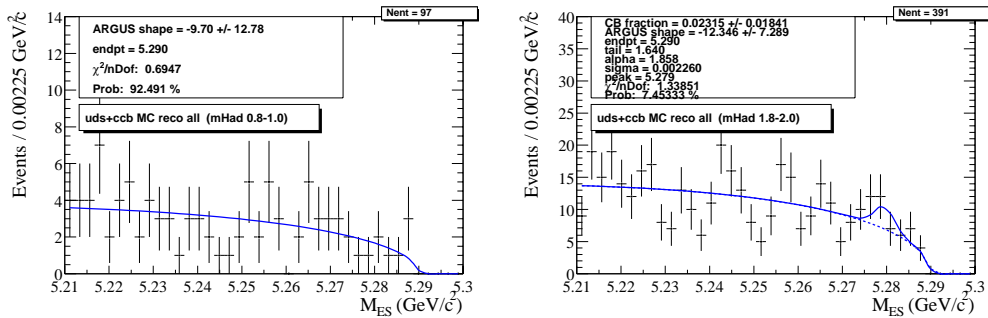


Figure 10.6: Sample MC background (continuum plus  $B\bar{B}$ ) fits.

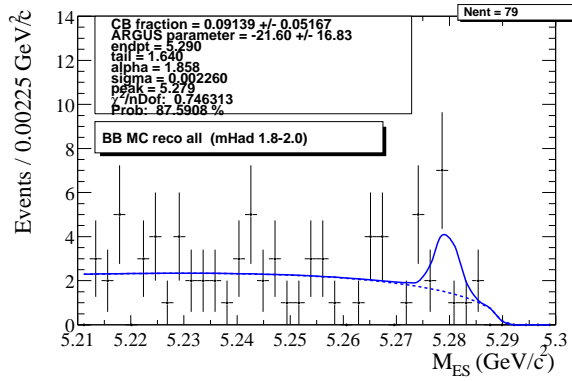


Figure 10.7: Sample MC  $B\bar{B}$  background fit.

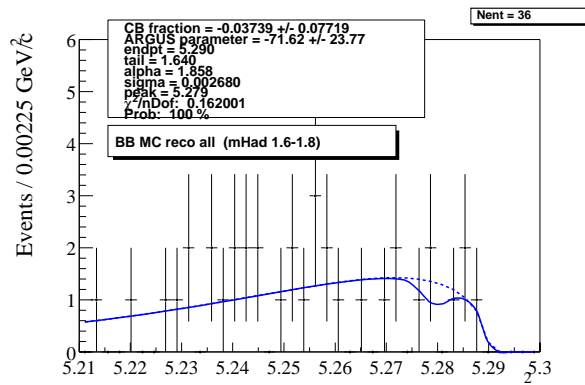


Figure 10.8:  $B\bar{B}$  fit for the *all* category in  $M_{Had}$  1.6-1.8  $\text{GeV}/c^2$ .

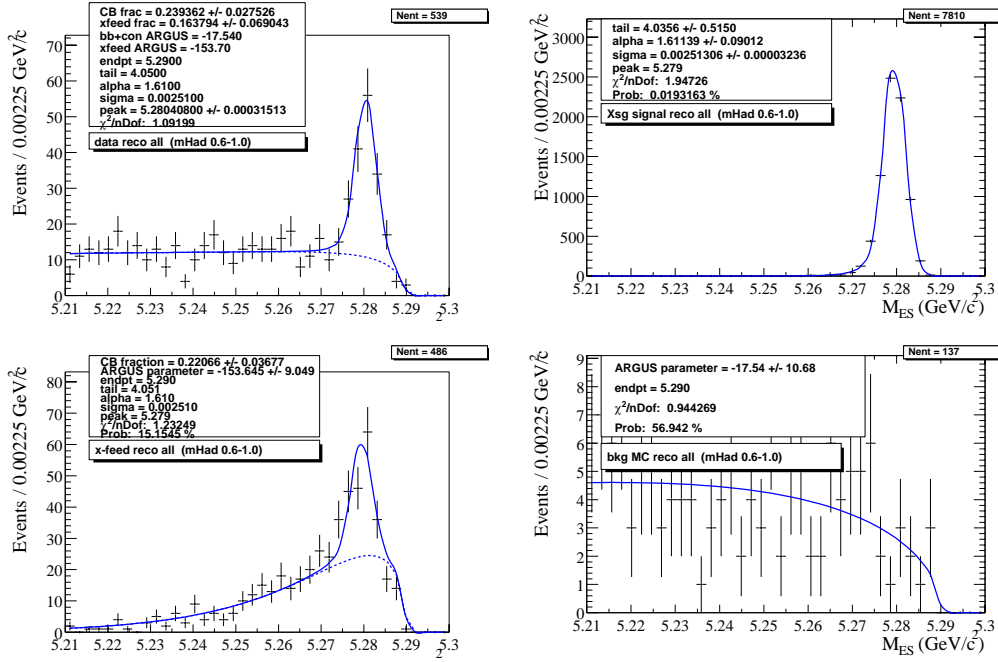


Figure 10.9: Fits to obtain the Crystal Ball peak parameter. The data sample (*all* final state category) is fit (top left) in the  $M_{Had}$  range 0.6-1.0, leaving the peak free, but fixing the other Crystal Ball parameters to the values obtained from a fit to the signal Monte Carlo (top right). The two Argus shape parameters are fixed to values from fits to the cross-feed (bottom left) and  $B\bar{B}$  plus continuum (bottom right).

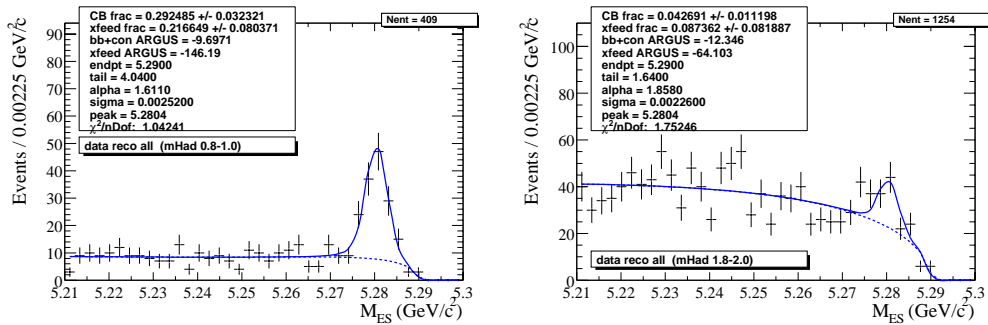


Figure 10.10: Sample data fits.

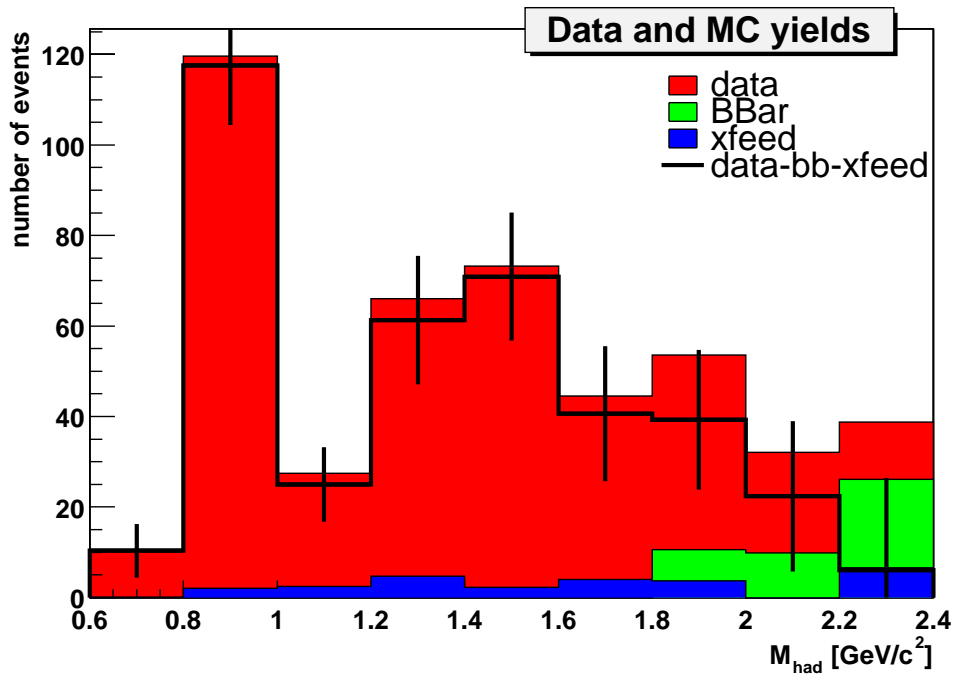


Figure 10.11: The data, cross-feed,  $B\bar{B}$  and signal yields as a function of  $M_{Had}$ .

# Chapter 11

## Determination of Partial Branching Fractions using the MC Expectations

In this chapter we will describe the method for calculating the Partial Branching Fractions (PBF), and present the results with statistical errors. A computational study of the results is also performed. These are *partial* branching fractions since they are with respect to the limited number of modes we measure, not with respect to all the possible final states from the  $b \rightarrow s\gamma$  transition. We also limit this measurement to the hadronic mass range 0.6 to 2.4 GeV/ $c^2$ .

The partial branching fractions are the quantities that are measured in this analysis, although they are not easily compared to theoretical predictions. To obtain the inclusive  $b \rightarrow s\gamma$  branching fraction we need to correct for the states we do not measure and sum over the full  $M_{Had}$  range. This procedure is discussed in Chapter 14, although only preliminary results are presented. There are issues with the extrapolation to states that we don't measure that are beyond the scope of this document.

Although the final results are not presented in this chapter since, as we see in the next two chapters, these PBFs need to be corrected for detection and fragmentation differences between data and Monte Carlo.

### 11.1 Partial Branching Fraction Definition

All the previous chapters have been dedicated to the measurement of the signal yield and signal efficiency. Moreover, we have split the data into nine bins of hadronic mass in order to reconstruct the hadronic mass spectrum which can

be compared to theoretical spectrum. We then split up the sample in each  $M_{Had}$  bin according to the final state multiplicity (*2-body*, *3-body*, *4-body*) or whether the final state contains a charged or neutral kaon or pion, ( $K/K_S$ ,  $\pi/\pi^0$ ). There is also a category, *all*, which is the sum of all the twelve final states that we consider.

We can therefore calculate the PBF for each hadronic mass bin using the *all* category or as a sum of the sub samples: *2+3+4-body*,  $\pi + \pi^0$  or  $K + K_S$ . The four PBFs should be identical within the uncorrelated errors if there are no differences between the hadronization in the Monte Carlo and in data. As is shown in the next section, there are differences which need to be accounted for.

The PBF is defined, per each hadronic mass bin  $i$  and final state category  $j$ , as:

$$PBF_{i,j} = \frac{N_{i,j}^{Sig}}{\varepsilon_{i,j} 2N_{BC}} \quad (11.1)$$

where  $N_{i,j}$  is the yield of the signal events in the  $i^{\text{th}}$   $M_{Had}$  bin and  $j^{\text{th}}$  final state category, as given in Tables 10.9, 10.10, 10.11 and 10.12. Table 8.1 lists the signal efficiency,  $\varepsilon$ , in bins of  $M_{Had}$  and final state categories.  $N_{BC} = (22.7 \pm 0.4) \times 10^6$  is the number of  $B\bar{B}$  events in the on-resonance data sample obtained from B-counting studies.

## 11.2 Partial Branching Fraction results

In the following the PBFs for the different final state categories are shown in the tables and plots. Note that the corresponding error comes only from the statistical error from each component as listed in Tables 10.9, 10.10, 10.11, 10.12 and 8.1. The systematic studies and associated errors are discussed in Chapter 12.

Table 11.1 lists the results for the PBFs in the nine bins of hadronic mass and for the different final state categories. Figure 11.1 shows some plots of the results. The top left plot shows the signal yield, for the *all* final state category, versus  $M_{Had}$ . The  $K^*\gamma$  resonant peak can be seen below  $M_{Had} = 1.0 \text{ GeV}/c^2$ , and the non-resonant distribution above.

The top right plots shows the partial branching fraction, for the *all* final state category, versus  $M_{Had}$ . This is just the yield plot divided by the efficiency and a constant ( $2N_{BC}$ ). You can see how the efficiency decreases with  $M_{Had}$  by how the PBF distribution at high  $M_{Had}$  is larger with respect to the  $K^*\gamma$  peak.

The next six plots show the PBFs for the different final state categories. On the left the three divisions are shown,  $2/3/4$ -body,  $K/K_S$  and  $\pi/\pi^0$ . On the right a comparison of the distribution for the *all* final state category and the bin-by-bin sum within each division ( $2+3+4$ -body,  $K+K_S$  and  $\pi+\pi^0$ ) are shown. If the Monte Carlo correctly modeled the data the two distributions should be exactly the same, but they are not.

$M_{Had}$	<i>all</i>	<i>2-body</i>	<i>3-body</i>	<i>4-body</i>
0.6-0.8	$1.42 \pm 0.816$	$1.42 \pm 0.816$	–	–
0.8-1.0	$22.6 \pm 2.56$	$22.9 \pm 2.39$	–	–
1.0-1.2	$7.2 \pm 2.41$	$2.13 \pm 1.15$	$5.35 \pm 2.52$	$0.353 \pm 0.688$
1.2-1.4	$23.9 \pm 5.67$	$3.04 \pm 1.54$	$21.2 \pm 5.33$	$-3.42 \pm 3.82$
1.4-1.6	$30 \pm 6.21$	$5.02 \pm 1.74$	$16.3 \pm 4.38$	$14.2 \pm 6.72$
1.6-1.8	$21.8 \pm 8.12$	$1.63 \pm 1.69$	$9.49 \pm 5.01$	$16.0 \pm 9.11$
1.8-2.0	$28.9 \pm 11.6$	$1.61 \pm 1.3$	$13.7 \pm 7.41$	$19.1 \pm 15.4$
2.0-2.2	$17.8 \pm 13.3$	$-1.19 \pm 1.26$	$2.87 \pm 7.33$	$38.3 \pm 23.0$
2.2-2.4	$6.5 \pm 21.9$	$1.04 \pm 2.34$	$-8.73 \pm 13.4$	$13.9 \pm 26.0$
$M_{Had}$	$\pi$	$\pi^0$	$K$	$K_s$
0.6-0.8	$0.784 \pm 0.463$	$-0.458 \pm 0.762$	$0.382 \pm 0.506$	$0.285 \pm 0.78$
0.8-1.0	$15.8 \pm 1.74$	$6.43 \pm 2.2$	$15.8 \pm 1.85$	$5.84 \pm 1.69$
1.0-1.2	$3.11 \pm 1.18$	$4.51 \pm 3.01$	$4.55 \pm 1.65$	$2.79 \pm 2.88$
1.2-1.4	$11.1 \pm 2.70$	$13.7 \pm 6.65$	$16.9 \pm 4.15$	$5.52 \pm 4.3$
1.4-1.6	$8.12 \pm 2.55$	$24.6 \pm 7.03$	$17.1 \pm 3.87$	$10.2 \pm 5.84$
1.6-1.8	$1.42 \pm 3.43$	$27.0 \pm 9.68$	$16.8 \pm 6.23$	$3.36 \pm 5.99$
1.8-2.0	$8.20 \pm 5.05$	$25.6 \pm 12.5$	$12.2 \pm 8.37$	$9.98 \pm 8.1$
2.0-2.2	$4.48 \pm 4.12$	$11.6 \pm 20.9$	$5.59 \pm 8.98$	$15.3 \pm 11.0$
2.2-2.4	$3.87 \pm 8.01$	$9.91 \pm 30.6$	$-5.57 \pm 16.3$	$20.2 \pm 13.9$

Table 11.1: The partial branching fraction ( $10^{-6}$ ) for all the different final state categories as a function of  $M_{Had}$ .

### 11.3 Interpretation of the PBF results

In the following sections we investigate the difference in the fragmentation between data and Monte Carlo. To do this we compare at the ratios in data

and Monte Carlo for  $K_S/K$ ,  $\pi^0/\pi$ ,  $2/3$ -body and  $4/3$ -body. We also look at some simple isospin arguments to see what we should expect for the ratios.

We calculate the ratios in two ways, in order to investigate two things. The first way is to compare the ratio of the PBFs to the MC generated events. In the PBFs the data yield has been corrected for any detector effects by dividing by the efficiency. These numbers are what we can compare with expectations from isospin calculations. To be clear we define, e.g. for the  $\pi^0/\pi$  ratio:

$$(\pi^0/\pi)_{corr}^{data} = PBF_{\pi^0}/PBF_{\pi} \quad (11.2)$$

$$(\pi^0/\pi)_{corr}^{MC} = N_{\pi^0}^{gen}/N_{\pi}^{gen} \quad (11.3)$$

where the ratios are labeled *corr* to note that they are after the data corrections.

The second way is to compare the data yields to the reconstructed MC yields. This looks at the data before any corrections for the detector efficiency. The detector corrections in the data basically weight the different bins by  $1/\text{efficiency}$  in that bin. This gives a larger weight to bins with small efficiencies. This gives a larger weight to bins with low statistics and distorts the comparison between data and MC. To be clear we define, e.g. for the  $\pi^0/\pi$  ratio:

$$(\pi^0/\pi)_{raw}^{data} = N_{\pi^0}^{sig}/N_{\pi}^{sig} \quad (11.4)$$

$$(\pi^0/\pi)_{raw}^{MC} = N_{\pi^0}^{reco}/N_{\pi}^{reco} \quad (11.5)$$

where the ratios are labeled *raw* to note that they are before the efficiency corrections.  $N^{sig}$  is the peaking signal yield as defined in the Equation 9.1,  $N^{sig} = N^{data} - N^{xfeed} - N^{BB}$ , and  $N^{reco}$  is the number of reconstructed events in the MC signal sample, after the cross-feed is removed.

### 11.3.1 $K_S$ production

By dividing the data into sub-samples in the previous sections ( $K$  and  $K_S$  final state categories) we can explicitly check the ratio, for data and MC, between events with charged and neutral kaons,  $K_S/K$ .

We assume there is equal production of  $B^+$  and  $B^0$  at the  $\Upsilon(4S)$ . We also assume that there is no isospin violation in the  $b \rightarrow s\gamma$  amplitude itself. In this case we expect equal numbers of  $K^+$  and  $K^0$ , leading to a distribution of final states  $K^+ : K_S : K_L = 2 : 1 : 1$ .

Table 11.2 shows the results for the ratios which are defined above. The  $(K_S/K)_{corr}$  values are consistent with a 1:2 ratio ( $K_S/K = 0.5$ ) within statistical errors.

We present the ratios in larger bins of  $M_{Had}$ . The last bin  $M_{Had}= 2.0\text{--}2.4\text{ GeV}/c^2$ , is dominated by the negative yield in the  $200\text{ MeV}/c^2$   $M_{Had}$  bin  $2.2\text{--}2.4\text{ GeV}/c^2$ . This is what increases the average fraction over all  $M_{Had}$ , which is listed in the last row. The second to last row in the table shows the fraction if we exclude that bin in our average. (Note that our definition of  $K_S$  includes both  $\pi^+\pi^-$  and  $\pi^0\pi^0$  decays, even though we only detect the former).

We see no significant difference between Monte Carlo and data and therefore do not have to correct for any fragmentation differences in these categories.

$M_{Had}$	$(K_S/K)_{corr}^{data}$	$(K_S/K)_{corr}^{MC}$	$(K_S/K)_{raw}^{data}$	$(K_S/K)_{raw}^{MC}$
0.6-1.0	$0.378 \pm 0.124$	0.500	$0.179 \pm 0.0608$	0.235
1.0-1.6	$0.48 \pm 0.215$	0.497	$0.225 \pm 0.0994$	0.228
1.6-2.0	$0.459 \pm 0.384$	0.493	$0.228 \pm 0.201$	0.291
2.0-2.4	$1960 \pm 20000$	0.495	$15.1 \pm 158$	0.358
0.6-2.2	$0.595 \pm 0.214$	0.499	$0.257 \pm 0.0734$	0.237
0.6-2.4	$0.876 \pm 0.35$	0.499	$0.314 \pm 0.0858$	0.237

Table 11.2: The ratios for the  $K_S$  and  $K$  final state categories as a function of  $M_{Had}$ .

### 11.3.2 $\pi^0$ production

Table 11.3 shows the ratios for the  $\pi^0 : \pi$  final state categories as a function of the hadronic mass.

Note that the ratios increase from lower to higher hadronic masses. The agreement between data and MC is not very good, there are more  $\pi^0$  modes in the data. This discrepancy is due to differences in data and MC fragmentation. The contributions to the  $\pi^0$  final states at high  $M_{Had}$  are not very well known and therefore are not well modeled in the Monte Carlo. Another contribution to this effect could be from having a poorly modeled  $\pi^0$  efficiency, but since the  $(\pi^0/\pi)_{corr}^{data}$  ratio in the first bin matches our expectations, as discussed in the next section, we don't think this is the main contribution. Chapter 13 discusses the method we use to weight the MC events to correct for this difference.

We can try to understand what we expect the ratio to be using some isospin calculations. But, the ratio  $\pi^0 : \pi$  is more difficult to estimate than the ratio  $K_S : K$ , because it depends on the resonant substructure of the  $Kn\pi$  system. To demonstrate this we perform some simple isospin estimates.

$M_{Had}$	$(\pi^0/\pi)_{corr}^{data}$	$(\pi^0/\pi)_{corr}^{MC}$	$(\pi^0/\pi)_{raw}^{data}$	$(\pi^0/\pi)_{raw}^{MC}$
0.6-1.0	$0.36 \pm 0.15$	0.50	$0.216 \pm 0.0931$	0.314
1.0-1.6	$1.92 \pm 0.56$	1.07	$1.07 \pm 0.304$	0.58
1.6-2.0	$5.47 \pm 3.84$	1.41	$3.49 \pm 2.55$	0.793
2.0-2.4	$2.57 \pm 5.23$	1.43	$1.29 \pm 2.46$	0.719
0.6-2.2	$2.13 \pm 0.63$	0.66	$0.876 \pm 0.189$	0.356
0.6-2.4	$2.16 \pm 0.86$	0.67	$0.888 \pm 0.215$	0.357

Table 11.3: The ratios for the  $\pi^0$  and  $\pi$  final state categories as a function of  $M_{Had}$ .

### $\pi^0$ production $2$ -body final states

For the  $2$ -body final states, we assume that all  $X_s$  systems are  $I = 1/2$   $K^{*(*)}$  resonances. It follows that the final states are distributed as for  $K^*(892)$ :

$$K\pi : K\pi^0 : K_s\pi : K_s\pi^0 = 0.667 : 0.333 : 0.333 : 0.167 \quad (11.6)$$

$$\pi^0 : \pi = 0.500 \quad (2 - \text{body}) \quad (11.7)$$

This is consistent with our observed ratio,  $(\pi^0/\pi)_{corr}^{data} = 0.36 \pm 0.15$ , in the lowest  $M_{Had}$  range, 0.6–1.0 GeV/ $c^2$ , listed in Table 11.3. Our number is slightly low, but consistent within statistical errors.

### $\pi^0$ production in $3$ -body final states

The resonance sub-structure for  $3$ -body final states is not well known. We can make some assumptions and see what they predict to understand how the ratio increases with higher multiplicity states.

For the  $3$ -body final states we assume that the  $X_s$  is an  $I = 1/2$   $K^{**}$  resonance. We consider two possible resonance substructures:  $K\rho$  and  $K^*\pi$ . Note that a preliminary analysis by BELLE indicates that these modes dominate the  $3$ -body final states, and contribute almost equally [16].

Using Clebsch-Gordon coefficients for Isospin  $1 \times 1/2$  the  $K\rho$  fractions are:

$$K\rho^0 : K\rho^+ : K_S\rho^0 : K_S\rho^+ = 0.333 : 0.667 : 0.167 : 0.333 \quad (11.8)$$

and since  $\rho^0 \rightarrow \pi^+\pi^-$  100%,  $\rho^+ \rightarrow \pi^+\pi^0$  100%,

$$\pi^0 : \pi = 2.000 \quad 2\pi^0 : 1\pi^0 + \pi = 0.000 \quad (K\rho) \quad (11.9)$$

Similarly the  $K^*\pi$  fractions are:

$$K^{*0}\pi^+ : K^{*0}\pi^0 : K^{*+}\pi^- : K^{*+}\pi^0 = 0.667 : 0.333 : 0.667 : 0.333 \quad (11.10)$$

which combined with the 2-body  $K^*$  decay fractions gives:

$$K\pi\pi : K\pi\pi^0 : K_S\pi\pi : K_S\pi\pi^0 : K\pi^0\pi^0 : K_S\pi^0\pi^0 \quad (11.11)$$

$$0.444 : 0.444 : 0.222 : 0.222 : 0.111 : 0.056 \quad (11.12)$$

$$\pi^0 : \pi = 1.000 \quad 2\pi^0 : 1\pi^0 + \pi = 0.125 \quad (K^*\pi) \quad (11.13)$$

The conclusion of this study is that the ratio  $\pi^0 : \pi$  is expected to be about 1.5 for *3-body* final states, and should not be greater than 2.0. The observed ratio in our data in the  $M_{Had}$  range 1.0–1.6 GeV/ $c^2$  where 3-body events dominate, agrees with this prediction, although the central value is high. Note that contributions from *4-body* states are also included in this range in the data.

#### $\pi^0$ production in *4-body* final states

The  $\pi^0$  production in *4-body* final states is an even more difficult fraction to estimate. We consider four possible resonance substructures of an  $I = 1/2$   $K^{**}$  resonance:  $K\omega, Ka_1, K^*\rho, K^{**}\pi$ . Note that this list is not comprehensive. Using Clebsch-Gordon coefficients we get predicted *4-body* final states for different resonant substructures as shown in Table 11.4.

	$K\pi\pi\pi$	$K\pi\pi\pi^0$	$K_S\pi\pi\pi$	$K_S\pi\pi\pi^0$	$K\pi\pi^0\pi^0$	$K_S\pi\pi^0\pi^0$
$K\omega$	—	0.667	—	0.333	—	—
$Ka_1$	0.125	0.250	0.063	0.125	0.125	0.063
$K^*\rho$	0.111	0.278	0.056	0.139	0.111	0.056
$K^{**}\pi$	0.141	0.233	0.071	0.117	0.120	0.056
MC	0.198	0.300	0.054	0.110	0.092	0.048

Table 11.4: Predicted *4-body* final states for different resonant substructures.

It can be seen that  $K\omega$  is in a separate class from the other three hypotheses.

$$\pi^0 : \pi = \infty \quad 2\pi^0 + 3\pi^0 : 1\pi^0 + \pi = 0.0 \quad (K\omega) \quad (11.14)$$

$$\pi^0 : \pi = 2.0 \quad 2\pi^0 + 3\pi^0 : 1\pi^0 + \pi = 0.32 \quad (Ka_1, K^*\rho, K^{**}\pi) \quad (11.15)$$

This does not increase the predicted  $\pi^0 : \pi$  ratio. Although this is clearly not a comprehensive list of possible contributions. Our measured values at high  $M_{Had}$  still agree with a ratio of 2, but with slightly high central values and large statistical errors.

### 11.3.3 Hadronic multiplicity

We make the natural assumption that the mean multiplicity increases with  $M_{Had}$  and that the width of the multiplicity distribution also increases. This means that we want to compute the mean multiplicity in bins of the hadronic mass. We reconstruct only events with a multiplicity of up to four. Therefore, in the data, we can only compute a “truncated” multiplicity, meaning that we use only *2-, 3- and 4-body* events. We do the same in the Monte Carlo in order to compare to the data multiplicity.

We compute the mean multiplicity per each mass bin as the weighted average of the PBF for each multiplicity category (i.e. *2, 3 and 4 body*) for the data.

$$M_{data} = \frac{(PBF_{2body} * 2) + (PBF_{3body} * 3) + (PBF_{4body} * 4)}{PBF_{2body} + PBF_{3body} + PBF_{4body}} \quad (11.16)$$

For the MC signal events, we compute the weighted average over the generated events for the *2, 3 and 4 body* categories.

$$M_{MC} = \frac{(Ngen_{2body} * 2) + (Ngen_{3body} * 3) + (Ngen_{4body} * 4)}{Ngen_{2body} + Ngen_{3body} + Ngen_{4body}} \quad (11.17)$$

The corresponding values are shown in Table 11.5 for data and MC. Figure 11.2 shows the same distributions. Note that contrary to expectations the multiplicity can be higher than 4.0. This can happen when one of the PBFs is negative (due to statistical fluctuations in the signal yield). We can see that at high  $M_{Had}$  the data multiplicity is higher than the Monte Carlo prediction.

To investigate where that difference is coming from, we can look at ratios between the three categories, *2/3-body* and *4/3-body*. Tables 11.6 and 11.7 lists these ratios in each  $M_{Had}$  bin above  $M_{Had}=1.0 \text{ GeV}/c^2$ . One can see that there is more 2-body events (higher *2/3-body* ratio) in Monte Carlo than in data, while the *4/3-body* ratio are consistent within large errors. In Chapter 13 a method to correct the Monte Carlo for this difference is presented.

$M_{Had}$	0.6-0.8	0.8-1.0	1.0-1.2
MC Mean	2.0	2.0	2.52
Data Mean	2.0	2.0	$2.77 \pm 0.17$
$M_{Had}$	1.2-1.4	1.4-1.6	1.6-1.8
MC Mean	2.80	3.02	3.18
Data Mean	$2.69 \pm 0.26$	$3.26 \pm 0.16$	$3.53 \pm 0.21$
$M_{Had}$	1.8-2.0	2.0-2.2	2.2-2.4
MC Mean	3.26	3.28	3.29
Data Mean	$3.51 \pm 0.25$	$3.99 \pm 0.19$	$5.07 \pm 6.47$

Table 11.5: Parameterization of truncated hadronic multiplicity in signal MC and data.

$M_{Had}$	$(2b/3b)_{corr}^{data}$	$(2b/3b)_{corr}^{MC}$	$(2b/3b)_{raw}^{data}$	$(2b/3b)_{raw}^{MC}$
1.0-1.2	$0.40 \pm 0.29$	1.03	$0.69 \pm 0.49$	1.8
1.2-1.4	$0.14 \pm 0.08$	0.56	$0.21 \pm 0.12$	0.84
1.4-1.6	$0.31 \pm 0.14$	0.43	$0.44 \pm 0.18$	0.62
1.6-1.8	$0.17 \pm 0.20$	0.40	$0.24 \pm 0.27$	0.56
1.8-2.0	$0.12 \pm 0.11$	0.39	$0.21 \pm 0.20$	0.69
2.0-2.2	$-0.41 \pm 1.14$	0.38	$-0.76 \pm 2.10$	0.71
2.2-2.4	$-0.12 \pm 0.33$	0.39	$-0.26 \pm 0.70$	0.85

Table 11.6: Ratios of 2/3-body for  $M_{Had}$  above  $1.0 \text{ GeV}/c^2$  for data and Monte Carlo.

$M_{Had}$	$(4b/3b)_{corr}^{data}$	$(4b/3b)_{corr}^{MC}$	$(4b/3b)_{raw}^{data}$	$(4b/3b)_{raw}^{MC}$
1.0-1.2	$0.07 \pm 0.13$	0.04	$0.07 \pm 0.14$	0.05
1.2-1.4	$-0.16 \pm 0.19$	0.21	$-0.09 \pm 0.10$	0.11
1.4-1.6	$0.87 \pm 0.47$	0.48	$0.44 \pm 0.23$	0.24
1.6-1.8	$1.68 \pm 1.31$	0.80	$1.10 \pm 0.83$	0.52
1.8-2.0	$1.40 \pm 1.36$	1.01	$0.73 \pm 0.69$	0.53
2.0-2.2	$13.3 \pm 35$	1.08	$6.2 \pm 16$	0.50
2.2-2.4	$-1.59 \pm 3.85$	1.13	$-1.2 \pm 2.9$	0.85

Table 11.7: Ratio of 4/3-body for  $M_{Had}$  above  $1.0 \text{ GeV}/c^2$  for data and Monte Carlo.

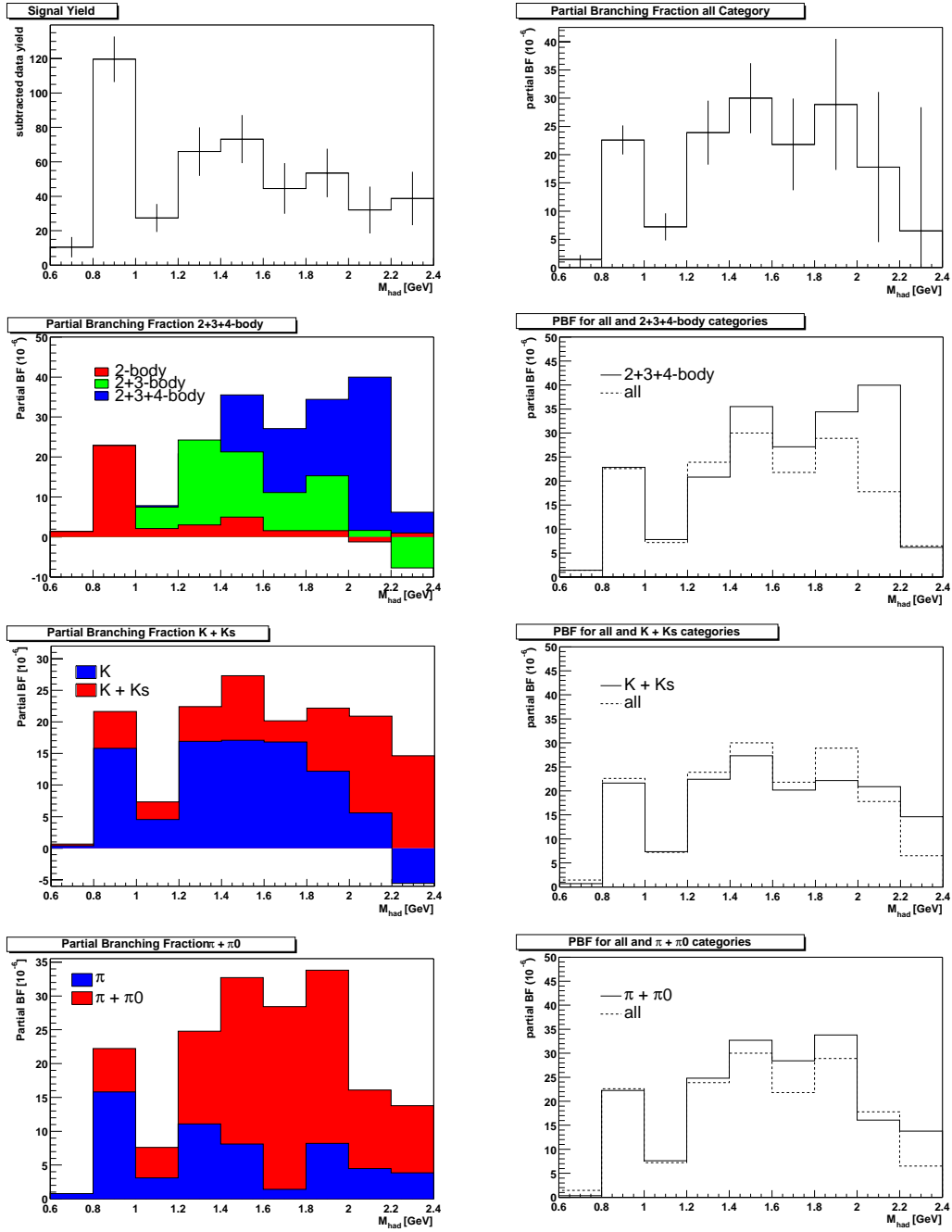


Figure 11.1: Signal yield and PBF for the different final state categories. When the error is shown it is just a statistical error.

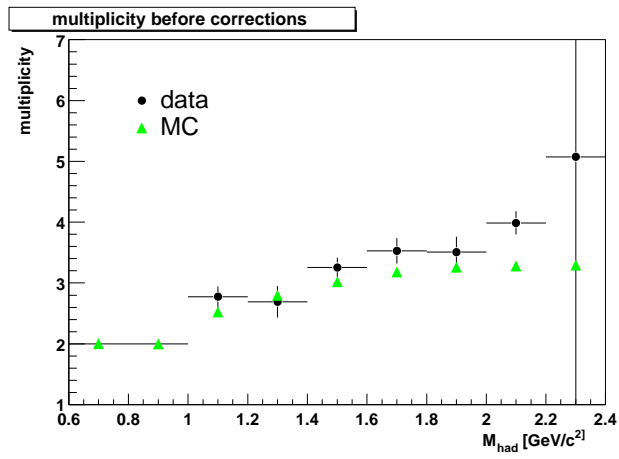


Figure 11.2: Truncated hadronic multiplicity in signal MC and data.

# Chapter 12

## Systematic Errors

In this chapter we describe the different sources of systematic errors on the partial branching fractions. We divide them into different components:

- Errors which do not depend on the final state investigated (e.g.  $K\pi$ ,  $K_S\pi^0$  etc.) or on  $M_{Had}$ . This category includes the photon systematics, the B-counting error, the error on selection variables like  $\cos\theta_{T^*}$  and the Fisher Discriminant.
- Errors due to the fitting procedure and signal definition. This gives the highest contribution to the systematic error.
- Errors due to the uncertainty in the detection efficiency (excluding the photon detection efficiency). Here we also consider the correction factors which need to be applied to the MC signal efficiency due to the disagreement between data and MC for some basic quantities (e.g. tracking efficiency, PID killing, etc.). Therefore, there is not only a systematic error associated with the efficiency but also a shift, (which causes accordingly a shift in the PBF central values).
- Signal Model Errors. We include two errors in the signal efficiency. One due to the variation in an assumption made in our signal model; the cut-off between the  $K^*\gamma$  and  $X_S\gamma$  events at  $1.0 \text{ GeV}/c^2$ . The other due to the signal model, KN465, used to calculate the efficiencies. Other model dependence comes in the calculation of the inclusive BF and will be presented in Chapter 14.

In the following, we will describe the different sources of systematic errors.

## 12.1 Photon systematics

The uncertainties related to the detection of and quality cuts on the high energy photon are the same for all the hadronic final states. They are summarized in Table 12.1, and described in the sections below. The total contribution to the systematic error is 3.7 %.

Systematic From	Error on BF
Photon efficiency	$\pm 1.3\%$
Photon energy scale	$\pm 1.0\%$
Photon energy resolution	$\pm 2.5\%$
$\pi^0(\eta)$ Vetoes	$\pm 1.0\%$
Bump distance cut	$\pm 2.0\%$
Total	$\pm 3.7\%$

Table 12.1: Photon systematics

**Photon Efficiency:** The photon efficiency systematic was measured by the neutrals working group in *BABAR*. They compared the rate of tau decays to  $\pi^+\pi^0$  and  $\pi^+\pi^0\pi^0$  in Monte Carlo and data. The decay fractions of these modes are known to within 1% and therefore the ratio is sensitive to the  $\pi^0$  efficiency. There is a difference found between data and Monte Carlo which can be corrected for by killing 2.5% of the photons in the Monte Carlo [22]. This is a systematic bias that must be applied to the signal MC efficiency. This factor is not dependent on the hadronic final state and so the same factor is applied for all final state categories in the whole  $M_{Had}$  range. This uniformly decreases the signal efficiency. There is an associated uncertainty on this bias which is listed in Table 12.1,  $\pm 1.3\%$ .

The rest of the photon systematics were calculated for the exclusive  $K^*\gamma$  analysis [14][23]. Our photon selection is the same. Below we present a short description of the different studies.

**Photon Energy Scale:** The photon energy scale was studied using symmetric  $\eta$  decays to two photons. Deviations of the measured  $\eta$  mass from the nominal value of  $547.3 \text{ MeV}/c^2$  gives a measurement of the uncertainty of the energy scale. This uncertainty effects the efficiency of the  $\Delta E^*$  cut by  $\pm 1\%$ , which is taken as the systematic error due to the photon energy scale.

**Photon Energy Resolution:** The Neutral Analysis Working Group have found that the  $\pi^0/\eta$  mass spectra are up to 10% wider in the data compared to Monte Carlo [24]. The effect of this resolution difference is studied by smearing the reconstructed photon energy spectrum by a Gaussian distribution in the signal MC. The  $\Delta E^*$  cut efficiency decreases smoothly with increased smearing. For a 10% degradation in the width they find a 2.5% change in the efficiency. This is taken as our systematic error due to the photon energy resolution.

**$\pi^0/\eta$  Vetoes:** The  $\pi^0$  and  $\eta$  vetoes are designed to discard events where the high energy photon candidate comes from  $\pi^0$  or  $\eta$  decays. These vetoes are checked by embedding signal photons into data and background Monte Carlo samples and comparing the efficiencies. The MC and data efficiencies agree within 1% and therefore we assign a 1% systematic error.

**Bump Distance Cut:** The bump distance cut requires that there is not another bump in the calorimeter within 25cm of the bump corresponding to the signal photon. The systematic on the efficiency of this cut is studied by embedding photon clusters extracted from radiative Bhabha events into data and generic  $B\bar{B}$  Monte Carlo events. The corresponding efficiencies are seen to agree within 2%, and so this is taken as our systematic error for this cut.

## 12.2 B-counting systematics

The total number of  $B$  mesons in our data sample is needed to normalize the Branching Fractions. This number is obtained by comparing the ratio of generic hadronic events to muon pairs in the on- and off-resonance data; the increase in the ratio for the on-resonance sample is assumed to due to  $\nu(4s)$  production. This study was performed by the Inclusive Charmonium analysis working group in  $BABAR$ . There are uncertainties associated with the number of  $\nu(4s)$  events found and with the efficiency of the selection. Overall a systematic error 1.6% is estimated [25].

## 12.3 Errors associated with the selection variables

There is also a systematic uncertainty coming from the use of  $\cos\theta_T$  and Fisher Discriminant cuts to suppress continuum backgrounds. We have com-

pared these distributions in off-resonance data and continuum MC events after all the other cuts are applied. The corresponding plots can be found in Figure 12.1 from which we see that data and MC events are in agreement within the limited statistics. To quantify the error on  $\cos\theta_{T^*}$  and the Fisher discriminant, we have looked at the distributions for the exclusive  $K^*(892)$  data and MC samples. We assign a systematic error based on the difference in the efficiency for the  $K^*(892)$  channel when we vary the shapes of the distributions within the range allowed by the statistics of the MC samples. The corresponding error is 1.0 %.

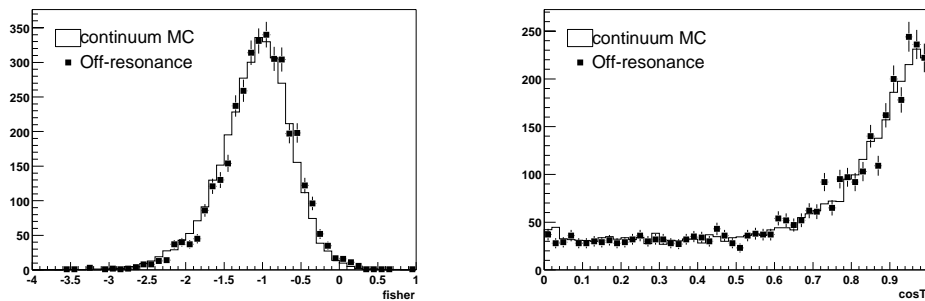


Figure 12.1: Fisher discriminant and  $\cos\theta_{T^*}$  distribution for off-resonance data (dots) and continuum MC after all the selection cuts are applied. MC events and off-resonance data are normalized to the same number of events.

## 12.4 Fit Systematics

In order to study the error due to the background subtraction which affects the PBF computation, we have looked at the effect of varying the fixed parameters used in the fits.

In most of the studies below the parameters varied change the results of the fits to more than one of the samples (data and various Monte Carlo samples). The numbers presented in the tables (e.g. Table 12.2) are the percent changes in the yields from the different samples, (i.e. data, cross-feed MC and  $B\bar{B}$  MC) and the last column is the percent change in the signal yield, which is the same as the percent error on the PBF, since  $PBF = N_{sig}/\epsilon 2N_{bb}$ . The signal yield is peaking background subtracted data yield,  $N_{sig} = N_{data} - N_{xfeed} - N_{BB}$ . The percent change is how much the yield has changed divided by the central value

for the yield, e.g.  $\Delta Data = (N'_{data} - N_{data})/N_{data}$ , where  $N'$  is the yield with the changed parameter. The percent change in the signal yield is not directly obtainable from the percent change in the other yields. It is defined as,

$$\begin{aligned} \Delta signal &= (N'_{sig} - N_{sig})/N_{sig} \\ &= \frac{(N'_{data} - N'_{xfeed} - N'_{BB}) - (N_{data} - N_{xfeed} - N_{BB})}{N_{data} - N_{xfeed} - N_{BB}} \end{aligned} \quad (12.1)$$

Usually the average percent  $\Delta signal$ , if the changes are symmetric, or the maximum percent  $\Delta signal$  is assigned as the systematic error, and is listed in the last column of the tables.

### 12.4.1 Crystal Ball Width

The width of the Crystal Ball function is fixed in the fits to the cross-feed, the  $B\bar{B}$  Monte Carlo and the data. The values which are used are obtained from the fits to the signal Monte Carlo sample for each  $M_{Had}$  bin and final state category. The values for the widths vary from 1.74 to 4.46 MeV/ $c^2$  and are listed in Table 10.2. To obtain a systematic error on the PBF, we vary the width by 0.2 MeV/ $c^2$ , and calculate the change in the PBF. The value of 0.2 MeV/ $c^2$  is the average over  $M_{Had}$  of the statistical error on the width for the *all* final state category.

The Crystal Ball width is fixed not only in the data fits, but also in the fits to the cross-feed and  $B\bar{B}$  to obtain the background yields which are subtracted from the data yield. We therefore change the fixed width in all the three fits simultaneously. We re-fit the samples twice, adding or subtracting 0.2 MeV/ $c^2$  from the fixed width.

Table 12.2 shows the percent change in the cross-feed,  $B\bar{B}$  and data yields averaged over the  $\pm 0.2$  MeV/ $c^2$  change. The last column shows the percent change in the signal yield (data - cross-feed -  $B\bar{B}$ ), which is the same as the systematic error on the PBF. The change in all the yields increased with the larger width (+0.2 MeV/ $c^2$ ) and decreased with the smaller width (-0.2 MeV/ $c^2$ ) symmetrically. The values in the table are the average of the magnitudes of the changes in the yields.

In practice, changing the width of the Crystal Ball in the fits also changes the Argus shape parameters which are obtained from fits to the cross-feed and  $B\bar{B}$  plus continuum Monte Carlo samples and used to fix the two Argus shapes in the data fits. If we now take the new Argus shapes, obtained from the fits with the increased or decreased widths, as well as change the Crystal Ball width, we obtain a slightly different systematic. These results are shown in Table 12.3 and

are very similar to the ones in Table 12.2, with the exception of the statistically limited last  $M_{Had}$  bin. This shows that the Argus shapes are not greatly affected by the change in the Crystal Ball width.

The values from the fits with both the width and Argus shapes adjusted, listed in Table 12.3, will be used.

$M_{Had}$	$\Delta data$	$\Delta X feed$	$\Delta B\bar{B}$	$error$
0.6-0.8	3.75	33.1	–	3.61
0.8-1.0	3.88	5.94	–	3.84
1.0-1.2	0.655	15.2	–	0.764
1.2-1.4	7.07	9.47	–	6.88
1.4-1.6	5.41	23	–	4.84
1.6-1.8	6.37	4.71	–	6.53
1.8-2.0	7.12	6.56	3.83	8.06
2.0-2.2	4.76	102	12.9	0.855
2.2-2.4	3.67	6.57	2.98	3.46

Table 12.2: Average percent change in data, cross-feed,  $B\bar{B}$  yield and systematic error, when changing the fixed Crystal Ball width for the *all* final state category.

A consistency check has been performed to study the assumption of using the same Crystal Ball parameters obtained from fits to the signal Monte Carlo to parametrize the Crystal Ball width for the cross-feed peaking component. The cross-feed distributions for the *all* final state category was re-fit leaving the Crystal Ball width free, but fixing the other parameters including the Crystal Ball fraction. The results are shown in Table 12.4, where the new fitted Crystal Ball width for the cross-feed is compared to the Crystal Ball width obtained from fits to the signal Monte Carlo, for each  $M_{Had}$  bin. In all cases the widths are consistent within ( $1 \sigma$ ) errors. We do not assign a systematic error for this difference.

We can also perform a similar cross-check for the data width by simply comparing the Monte Carlo Crystal Ball width to one from a fit to the data where the width is left free. We fit the data in the high statistics bin,  $M_{Had} = 0.8-1.0 \text{ GeV}/c^2$ , and obtain a width of,  $\sigma_{data} = 2.4 \pm 0.3 \text{ MeV}/c^2$ . This is consistent with the signal Monte Carlo value of  $\sigma_{MC} = 2.52 \pm 0.02 \text{ MeV}/c^2$ , as listed in

$M_{Had}$	$\Delta data$	$\Delta X feed$	$\Delta B\bar{B}$	$error$
0.6-0.8	3.77	33.1	–	3.64
0.8-1.0	3.97	5.94	–	3.94
1.0-1.2	0.785	15.2	–	0.622
1.2-1.4	7.12	9.47	–	6.94
1.4-1.6	5.41	23.0	–	4.85
1.6-1.8	6.42	4.71	–	6.59
1.8-2.0	6.89	6.56	3.83	7.75
2.0-2.2	4.69	102	12.9	0.853
2.2-2.4	5.12	6.57	2.98	12.8

Table 12.3: Average percent change in data, cross-feed,  $B\bar{B}$  yield and systematic error, when changing the fixed Crystal Ball width and adjusting the Argus shape parameters for the *all* final state category.

Table 10.2. We do not assign a systematic error for this.

## 12.4.2 Crystal Ball $\alpha$ and tail

In all the fits the Crystal Ball  $\alpha$  and tail parameters are fixed to values obtained from fits over two  $M_{Had}$  ranges, 0.6-1.0 GeV/ $c^2$  and 1.0-2.4 GeV/ $c^2$  for each final state category. The values can be found in Table 10.1.

The Crystal Ball function is a Gaussian with a power law tail on one side. The  $\alpha$  parameter signifies how many sigma away from the mean of the Gaussian the power law distribution starts. The tail parameter determines the order of the power law. We expect that these parameters do not depend on the hadronic mass since they are concerned with the radiative tail of the  $m_{ES}$  distribution. The radiative tail depends on the beam energy spread and the photon energy resolution and therefore will increase slightly for events with a  $\pi^0$ , but should not be  $M_{Had}$  dependent.

The two parameters are anti-correlated (60–90%). We consider, as a systematic error, the effect of varying the alpha and tail parameters to their extreme values listed in Table 10.1. We pick the smallest and largest value in the table for the  $\alpha$  and tail parameter separately, and then combine the smallest  $\alpha$  with the largest tail, and vice-versa. The two sets of values we use are:  $\alpha = 1.16$ , tail = 6.95; and  $\alpha = 2.39$ , tail = 1.22. We redo all the fits and also adjust the Argus

$M_{Had}$	$\sigma_{X-feed}$	$\sigma_{Signal}$	$\Delta\sigma/\delta_{stat}$
0.6-0.8	$3.15 \pm 1.27$	$2.43 \pm 0.10$	0.57
0.8-1.0	$2.83 \pm 0.37$	$2.52 \pm 0.02$	0.84
1.0-1.2	$3.73 \pm 1.15$	$2.59 \pm 0.11$	0.99
1.2-1.4	$3.38 \pm 1.03$	$2.56 \pm 0.11$	0.79
1.4-1.6	$3.72 \pm 1.51$	$2.64 \pm 0.12$	0.71
1.6-1.8	$2.50 \pm 1.23$	$2.68 \pm 0.16$	-0.15
1.8-2.0	$2.38 \pm 0.09$	$2.26 \pm 0.18$	0.60
2.0-2.2	$0 \pm 1$	$2.67 \pm 0.28$	-0.003
2.2-2.4	$4.14 \pm 0.87$	$3.29 \pm 0.473$	0.86

Table 12.4: Crystal Ball width [MeV/ $c^2$ ] obtained from fits to Signal Monte Carlo (second column) and from fits to cross-feed Monte Carlo (first column) and their relative difference (third column), where  $\delta_{stat}$  takes into account the uncertainties of both  $\sigma$ 's.

parameters in the data fits.

Table 12.5 shows the percent change in the cross-feed,  $B\bar{B}$  and data yields averaged over the two cases. The last column shows the percent change in the signal yield (data - cross-feed -  $B\bar{B}$ ), which is the same as the systematic error on the PBF. The average of the magnitudes of the changes is shown, since the change in the yields have the same magnitude but opposite signs for the two variations. Setting the parameters at their maximum values increased all the yields, while setting the parameters at their minimum decreased the yields.

### 12.4.3 Monte Carlo Crystal Ball Peak

For the Monte Carlo fits to the cross-feed and background samples, the peak of the Crystal Ball function is fixed to a value obtained from a free fit in the high statistics  $M_{Had}$  bin, 0.8-1.0 GeV/ $c^2$  corresponding to the  $K^*\gamma$  resonance region.

We consider, as a systematic error, the effect of varying the peak value by its statistical error for the Monte Carlo fits. The Monte Carlo peak value is,  $5.27945 \pm 0.00006$  GeV/ $c^2$ . We therefore re-fit the samples with the Crystal Ball peak set to 5.27951 and 5.27939 GeV/ $c^2$ . The variation is small and so we expect only a small change, which is what we see.

We re-fit the cross-feed, and  $B\bar{B}$  samples to obtain an average change in the yield. This changes the total signal yield.

Table 12.6 shows the average percent change in the cross-feed and  $B\bar{B}$  yields

$M_{Had}$	$\Delta data$	$\Delta X feed$	$\Delta B\bar{B}$	$error$
0.6-0.8	4.47	18	–	4.41
0.8-1.0	3.13	5.95	–	3.08
1.0-1.2	1.76	6.22	–	2.17
1.2-1.4	4.41	3.8	–	4.46
1.4-1.6	4.43	7.1	–	4.34
1.6-1.8	5.85	9.48	–	5.5
1.8-2.0	6.67	4.58	6.86	6.82
2.0-2.2	2.72	1.91	10.8	3.2
2.2-2.4	4.99	5.83	3.37	11

Table 12.5: Average percent change in data, cross-feed,  $B\bar{B}$  yield and systematic error, when changing the fixed Crystal Ball  $\alpha$  and tail parameters and adjusting the Argus shape parameters. For the *all* final state category.

due to varying the fixed peak value, and the average change of the signal yield (data - cross-feed -  $B\bar{B}$ ), which is the same as the percent systematic error on the PBF.

The percent systematic is small, especially compared to the other systematics, therefore we will neglect this in the final results.

#### 12.4.4 Data Crystal Ball Peak

In the data fits the peak of the Crystal Ball function is fixed to a value obtained from a free fit in the high statistics  $M_{Had}$  bin, 0.8-1.0 GeV/ $c^2$  corresponding to the  $K^*\gamma$  resonance region, for all the fits. We consider, as a systematic error, the effect of varying the peak value by its statistical error for the data fits. The data peak value is,  $5.2804 \pm 0.0003$  GeV/ $c^2$ . We therefore refit the data with the Crystal Ball peak set to 5.2807 and 5.2801 GeV/ $c^2$ , and find the difference in the data yield due to this change.

Table 12.7 shows the percent change in the data yield due to varying the fixed peak value, for both the plus and minus changes, and the same values for the signal yield (data - cross-feed -  $B\bar{B}$ ) which is the same as the percent systematic error on the PBF. The last column lists the absolute value of the larger change in the signal yield. This will be used as a conservative estimate for the percent systematic error.

$M_{Had}$	$\Delta x_{feed}$	$\Delta B\bar{B}$	$error$
0.6-0.8	7.2	–	0.045
0.8-1.0	0.043	–	0.0046
1.0-1.2	0.04	–	0.0039
1.2-1.4	1.2	–	0.13
1.4-1.6	3.4	–	0.11
1.6-1.8	0.15	–	0.016
1.8-2.0	0.84	1.4	0.49
2.0-2.2	1.4	0.87	0.41
2.2-2.4	0.22	0.73	0.9

Table 12.6: Percent change in cross–feed and  $B\bar{B}$  yield and percent systematic error on the partial branching fraction when changing the fixed Monte Carlo Crystal Ball peak for the *all* final state category.

The % change in the signal yield is not symmetric and not even consistently the same or opposite sign. This inconsistent variation is due to the fact that we are fitting fairly low statistics distributions. Changing the peak value slightly causes one or more points to fall in or out of the fixed width of the signal peak and therefore changes the yield but not significantly within statistics. To be conservative we will take the largest absolute variation as the percent systematic error on the partial branching fraction.

### 12.4.5 Cross–Feed Argus Shape

The Argus shape obtained from a fit to the cross–feed sample is used to constrain one of the two Argus shapes in the data fit. These shapes are obtained uniquely for each  $M_{Had}$  bin and final state category. We vary these Argus shape parameters by plus and minus their statistical errors in the data and cross–feed Monte Carlo fits to obtain a systematic error on the PBF. The parameters along with their statistical errors are listed in Table 10.3.

Table 12.8 shows the percent change in the data yield and the cross–feed yield when changing the Argus shapes by plus and minus the statistical errors, and the same values for the signal (data - cross–feed -  $B\bar{B}$ ) yield, which is equivalent to the percent systematic error on the PBF. The last column lists the absolute value of the larger change in the signal yield. This will be used as a conservative

$M_{Had}$	$\Delta data+$	$\Delta data-$	$\Delta signal+$	$\Delta signal-$	$error$
0.6-0.8	3.9	-5.3	4.0	-5.4	5.4
0.8-1.0	-0.67	-0.15	-0.68	-0.15	0.68
1.0-1.2	2.9	-3.6	3.2	-4.0	4.0
1.2-1.4	-2.5	1.6	-2.7	1.7	2.7
1.4-1.6	-1.1	0.34	-1.1	0.35	1.1
1.6-1.8	-1.2	0.51	-1.3	0.56	1.3
1.8-2.0	-2.1	1.7	-2.9	2.3	2.9
2.0-2.2	-3.9	3.0	-5.6	4.3	5.6
2.2-2.4	3.4	-3.7	22	-24	24

Table 12.7: Percent change in data yield and percent systematic error on the partial branching fraction when changing the fixed Crystal Ball peak in the data fits for the *all* final state category.

estimate for the percent systematic error.

The % change in the data and therefore in the signal yield is not symmetric and not even consistently the same or opposite sign. This inconsistent variation is due to the fact that we are fitting fairly low statistics distributions in the data. Changing the Argus shape parameter slightly causes the background shape under the signal distribution to change slightly and therefore change the yield but not significantly within statistics.

In contrast the changes in the cross-feed yields are directly correlated with the change in the Argus shape. Adding the statistical error to the Argus shape makes it less negative and therefore increases the yield. Subtracting the statistical error makes the Argus shape more negative and therefore decreases the yield. The percent changes listed in the table are large, but the cross-feed yields themselves are quite small (see Table 10.4), and therefore the percent changes in the signal yield are reasonable.

### 12.4.6 Background Argus Shape

The Argus shape obtained from a fit to the background ( $B\bar{B}$  plus continuum) sample is used to constrain one of the Argus shapes used in the data fit. These shapes are obtained uniquely for each  $M_{Had}$  bin and final state category. We vary these Argus shape parameters by plus and minus their statistical errors in the data fits to obtain a systematic error on the PBF. The parameters along with their statistical errors are listed in Table 10.5.

$M_{Had}$	$\Delta data+$	$\Delta data-$	$\Delta xf+$	$\Delta xf-$	$\Delta sig+$	$\Delta sig-$	$error$
0.6-0.8	2.4	6.3	160	-160	1.7	7.0	7.0
0.8-1.0	-0.3	-0.98	6.1	-6.0	-0.41	-0.9	0.9
1.0-1.2	2.7	2.9	29	-29	0.16	6.1	6.1
1.2-1.4	-2.0	-2.8	20	-19	-3.7	-1.6	3.7
1.4-1.6	-1.1	-0.93	57	-56	-3.0	0.84	3.0
1.6-1.8	0.0097	-2.3	29	-29	-2.8	0.27	2.8
1.8-2.0	-2.0	-2.2	24	-24	-5.0	-0.72	5.0
2.0-2.2	-2.8	-5.1	620	-630	-8.7	-2.6	8.7
2.2-2.4	3.5	0.22	17	-17	4.5	20	20

Table 12.8: Percent change in data and cross-feed (xf) yield and percent systematic error on the partial branching fraction when changing the fixed cross-feed Argus shape for the *all* final state category.

Table 12.9 shows the percent change in the data yield when changing the Argus shapes by plus and minus the statistical errors, and the same value for the signal (data - cross-feed -  $B\bar{B}$ ) yield, which is equivalent to the percent systematic error on the PBF. The last column lists the absolute value of the larger change in the signal yield. This will be used as a conservative estimate for the percent systematic error.

The % change in the signal yield is not symmetric and not even consistently the same or opposite sign. This inconsistent variation is due to the fact that we are fitting fairly low statistics distributions. Changing the Argus shape parameter slightly causes the background shape under the signal distribution to change slightly and therefore change the yield.

## 12.4.7 Summary of Fit Systematics

Adding the previous fit systematics in quadrature for each  $M_{Had}$  bin will give the total percent systematic error on the partial branching fraction from the fitting procedure for the *all* final state category.

Table 12.10 lists the percent errors and the sum.

$M_{Had}$	$\Delta data+$	$\Delta data-$	$\Delta signal+$	$\Delta signal-$	$error$
0.6-0.8	-12	-13	-12	-13	13
0.8-1.0	-2.8	1.3	-2.9	1.3	2.9
1.0-1.2	21	-16	23	-18	23
1.2-1.4	-7.1	1.6	-7.6	1.7	7.6
1.4-1.6	-5.1	-10	-5.3	-11	11
1.6-1.8	-6.4	4.0	-7.0	4.3	7.0
1.8-2.0	-5.8	-6.5	-7.9	-8.9	8.9
2.0-2.2	-8.1	0.4	-12	0.58	12
2.2-2.4	19	-0.14	120	-0.91	120

Table 12.9: Percent change in data yield and percent systematic error on the partial branching fraction when changing the fixed background Argus shape for the *all* final state category.

$M_{Had}$	width	$\alpha$ -tail	data peak	xfeed Argus	bkg Argus	total
0.6-0.8	3.64	4.41	5.4	7.0	13	17
0.8-1.0	3.94	3.08	0.68	0.9	2.9	5.9
1.0-1.2	0.622	2.17	4.0	6.1	23	24
1.2-1.4	6.94	4.46	2.7	3.7	7.6	12
1.4-1.6	4.85	4.34	1.1	3.0	11	13
1.6-1.8	6.59	5.5	1.3	2.8	7.0	12
1.8-2.0	7.75	6.82	2.9	5.0	8.9	15
2.0-2.2	0.853	3.2	5.6	8.7	12	16
2.2-2.4	12.8	11	24	20	120	125

Table 12.10: Percent systematic errors from the fitting procedure for the *all* final state category.

## 12.5 Signal Definition Systematic

The reconstructed “signal” Monte Carlo samples ( $K^*\gamma$  and  $X_s\gamma$ ) are separated into signal and cross-feed events. The definitions, presented earlier, are:

- signal :  
 $\text{reco mode} = \text{true mode} \ \& \ | M_{Had}^{true} - M_{Had}^{reco} | < 0.05 \text{ GeV}/c^2$
- cross-feed :  
 $\text{reco mode} \neq \text{true mode}$   
or  
 $\text{reco mode} = \text{true mode} \ \& \ | M_{Had}^{true} - M_{Had}^{reco} | > 0.05 \text{ GeV}/c^2$

We consider, as a systematic error, the change in the branching fraction if we vary the  $50 \text{ MeV}/c^2$   $\Delta M_{Had}$  cut. This change will affect the signal and cross-feed distributions and therefore the efficiency and all the fits.

After varying the  $\Delta M_{Had}$  cut, the new signal distribution is used to recalculate the efficiency and re-fit to get the new Crystal Ball widths which will be used in the rest of the fits. The new cross-feed and old continuum plus  $B\bar{B}$  and  $B\bar{B}$  Monte Carlo samples are re-fit with the new Crystal Ball widths yielding new cross-feed and  $B\bar{B}$  yields, and new Argus shape parameters for the data fits. The data is then fit with the new Crystal Ball width and Argus shape parameters to get a new data yield. The new efficiency and yields are used to calculate a new partial branching fraction.

Table 12.11 shows the percent change in the various yields, in the efficiency and in the partial branching fraction for the *all* final state category. The top section shows the change when increasing the  $\Delta M_{Had}$  upper limit to  $100 \text{ MeV}/c^2$  and the bottom section shows the same when decreasing the  $\Delta M_{Had}$  upper limit to  $30 \text{ MeV}/c^2$ . As we expect, the change in the efficiency and the change in the signal yield mostly balance each other out causing the change in the partial branching fraction to be small. This happens since adding (or subtracting) events from the signal sample subtracts (or adds) events to the cross-feed sample.

Therefore, the systematic error (which is the same as the % change in the PBF) is smaller than a few percent, except in the last two hadronic mass bins where the statistics are low. As a conservative estimate we will take the larger (between the 100 and 30  $\text{ MeV}/c^2$  upper limit) of the errors for each bin.

$\Delta M_{Had} = 100 \text{ MeV}/c^2$						
$M_{Had}$	$\Delta Y_{data}$	$\Delta Y_{xfeed}$	$\Delta Y_{B\bar{B}}$	$\Delta Y_{sig}$	$\Delta \varepsilon$	$\Delta PBF$
0.6-0.8	2.0	-160	–	2.7	4.0	-1.3
0.8-1.0	1.0	-56	–	2.0	1.7	0.31
1.0-1.2	0.36	-25	–	2.9	3.3	-0.39
1.2-1.4	4.7	9.5	–	4.4	4.4	-0.054
1.4-1.6	4.0	-68	–	6.4	8.7	-2.1
1.6-1.8	1.7	-59	–	7.6	11	-2.8
1.8-2.0	7.4	-2.4	4.3	9.1	11	-1.4
2.0-2.2	4.2	-550	15	3.8	19	-13
2.2-2.4	9.1	-0.35	4.2	40	29	9.1
$\Delta M_{Had} = 30 \text{ MeV}/c^2$						
$M_{Had}$	$\Delta Y_{data}$	$\Delta Y_{xfeed}$	$\Delta Y_{B\bar{B}}$	$\Delta Y_{sig}$	$\Delta \varepsilon$	$\Delta PBF$
0.6-0.8	-0.13	240	–	-1.2	-1.3	0.14
0.8-1.0	-0.67	58	–	-1.7	-1.4	-0.28
1.0-1.2	-0.37	32	–	-3.5	-3.5	0.032
1.2-1.4	-4.4	10	–	-5.5	-3.0	-2.5
1.4-1.6	-4.0	14	–	-4.6	-6.0	1.5
1.6-1.8	-3.7	14	–	-5.5	-6.2	0.85
1.8-2.0	-5.6	11	-2.8	-7.9	-7.4	-0.53
2.0-2.2	-7.3	91	-18	-3.5	-11	8.0
2.2-2.4	-17	-16	-11	-46	-14	-37

Table 12.11: Percent changes in the yields, efficiency and PBF from varying the  $\Delta M_{Had}$  cut in the signal sample definition for the *all* final state category.

## 12.6 $B\bar{B}$ Peaking Yield

The yield from the peaking  $B\bar{B}$  background is obtained from a fit to the generic  $B\bar{B}$  sample to a Crystal Ball plus Argus function, where the Crystal Ball parameters are fixed to the signal Monte Carlo values and the Argus shape parameter is free. Alternatively, we could obtain the  $B\bar{B}$  yield from a fit to the  $B\bar{B}$  plus continuum distribution. As we saw in Section 10.1.2 in Table 10.7, the yield from the fit to the combined  $B\bar{B}$  plus continuum sample is greater than the yield from the fit to the  $B\bar{B}$  sample alone, although it is consistent within statistical errors.

This trend is not due to any peaking contribution from the continuum background. As can be seen in Figure 7.3, the continuum fits well to an Argus function and does not have any peaking component. The difference can be explained by the fact that the continuum and  $B\bar{B}$  distributions do not have exactly the same shape, and so the Argus parameters from the fits to the  $B\bar{B}$  or  $B\bar{B}$  plus continuum are different. Note also that the magnitude of the continuum background is at least three times greater than the  $B\bar{B}$  background even in the high hadronic mass range, see Figure 7.2. Therefore the continuum shape dominates the Argus shape parameter in the combined fit.

A toy-mc study was performed to investigate this effect. A high-statistics sample was produced, 4M events. A toy-background sample was generated with a Crystal Ball plus Argus for the  $B\bar{B}$  plus an Argus for the continuum, where the parameters were fixed as in Chapter 9. This toy-background sample was then fit with one Argus plus Crystal Ball to simulate the  $B\bar{B}$  plus continuum fits. The fit ( $B\bar{B}$  plus continuum) and generated ( $B\bar{B}$ ) peaking fraction is shown in Table 12.12. As expected the fraction from the fits are larger than the generated fraction.

$M_{Had}$	CB-fraction Generated	CB-fraction Fitted	% Difference
1.8-2.0	0.0133	$0.0143 \pm 0.0002$	$7.5 \pm 1.5$ %
2.0-2.2	0.0066	$0.0083 \pm 0.0002$	$25 \pm 3$ %
2.2-2.4	0.0146	$0.0160 \pm 0.0002$	$9.6 \pm 1.4$ %

Table 12.12: Comparison of the generated and fit Crystal Ball fraction from a toy-MC sample of  $B\bar{B}$  plus continuum.

To account for this trend, we will increase the  $B\bar{B}$  yield by  $(10 \pm 10)\%$ . This changes the central value of the PBF in these last three bins, as well as adds an

additional systematic error. This shift is included in the PBF results presented in Table 12.22.

We also add here an uncertainty due to the fact that we do not trust that the composition of the generic  $B\bar{B}$  Monte Carlo correctly models the background in the data. A large component of the peaking background is from  $B \rightarrow D^{(*)}\rho$  for which the branching fraction is known to about 10% accuracy. We then have to account for other possible peaking contributions, some of which may not be in MC at all. To account for this we increase the  $\pm 10\%$  systematic error on the peaking  $B\bar{B}$  yield to  $\pm 20\%$ .

To get the percent systematic error on the PBF, the systematic error of  $\pm 20\%$  is applied to the shifted  $B\bar{B}$  yield and then the PBF is recalculated. Table 12.13 lists the central value for the PBF (including the 10% shift in the central value of the  $B\bar{B}$  yield), the PBF after changing the  $B\bar{B}$  yield by  $\pm 20\%$  and the percent change in the central PBF, which is considered as a systematic error on the PBF.

$M_{Had}$	central	+20%	-20%	error
1.8-2.0	$33.3 \pm 13.5$	31.3	35.3	7 %
2.0-2.2	$18.4 \pm 14.5$	16.5	20.2	10 %
2.2-2.4	$6.01 \pm 25.4$	-1.13	13.2	120 %

Table 12.13: The change in the PBF when applying a 20% systematic error to the  $B\bar{B}$  yield, after the 10% shift has been applied.

## 12.7 Efficiency Systematics

The effects of a number of residual differences between simulated and data events, observed using data control samples and Monte Carlo events, must be corrected for when computing the signal efficiency. These differences give not only a systematic error on the efficiency, but also a shift in the central value, which causes accordingly a shift in the PBF central values.

### 12.7.1 Difference between data and MC detection efficiencies

We do not expect that the Monte Carlo exactly models the working detector. Therefore, there are corrections which need to be applied to the Monte Carlo signal efficiency due to the disagreement between data and Monte Carlo for some basic quantities. For our analysis the relevant quantities are, tracking efficiency, particle identification (PID) for charged Kaons,  $K_S$  and  $\pi^0$  detection efficiencies.

The detection efficiency systematic studies have been performed by various working groups within the experiment. These groups then provide recipes on how to calculate the errors for the different systematics which we apply to our analysis. The studies and recipes are summarized below.

**Tracking efficiency:** The tracking reconstruction is investigated by comparing the efficiency in data and MC for reconstructing tracks. Tracks found in the SVT are used to signal the presence of a charged track. The number of tracks reconstructed in the DCH divided by the number of tracks reconstructed in the SVT defines the efficiency. This efficiency is calculated as a function of the DCH high voltage setting, the total charged multiplicity in the event, the transverse momentum, the polar angle and azimuth of the charged track. The efficiencies for both data and MC are calculated and the difference is tabulated as a function of the above listed variables [26]. These tables are used weight each charged track in the Monte Carlo, and therefore correct the MC track efficiency. Moreover, in order to account, at least globally, for possible data-MC inconsistencies in areas such as material description, internal detector alignment, or magnetic-field map, a smearing of the transverse momentum of the tracks is applied.

A typical correction factor for charged tracks in our analysis is 98%.

**$K_S$ :** The  $K_S$  reconstruction is investigated by comparing the  $K_S$  rate in background subtracted data and  $B\bar{B}$  MC. Correction tables are provided to adjust for the difference in rates [27]. The tables are binned in 2-D  $K_S$  flight length only, from 1 to 40 cm in 1 cm bins. Two sets of tables are provided: one with a  $p_T(K_S) \geq 1 \text{ GeV}/c$  cut, and one for all  $p_T$ . The recommendation is to base the central value of the correction on the former (irrespective of the  $p_T$  of the  $K_S$  under consideration) because it is considered more reliable, and to treat the difference between the two tables as a systematic error. In addition, the efficiency again has to be computed separately for the 1900 and 1960V data sets. The average value of the correction, computed as suggested is found to be +3.0%.

**Charged Kaon:** There are differences in kaon detection efficiency between data control samples and Monte Carlo. The MC is found to be more efficient than the data [20], and therefore we want to “kill” some of the reconstructed kaons in the MC before our event selection. The differences between the Monte Carlo and data efficiency are tabulated as a function of momentum and  $\theta$ . In the “PID-killing” method, the original kaon list is replaced by new list constructed as follows. Given the true particle type of a reconstructed charged track (K in this example), the kaon-identification probability of the track is computed from the tables. These corrections are important, especially for kaons with momentum  $0.5 < p < 1 \text{ GeV}/c$ , because the raw simulation overestimates the single-kaon identification efficiency by 10-15%. The validity range of the tables ( $0.25 \text{ GeV}/c \leq p \leq 5 \text{ GeV}/c$ ,  $0.35 \leq \theta \leq 2.55$ ), combined with the effective coverage of the SVT ( $\theta \leq 2.54$ ), define the charged kaon kinematic cuts imposed in the selection.

$\pi^0$ : The  $\pi^0$  efficiency systematic was measured by the neutrals working group in *BABAR*. They compared the rate of tau decays to  $\pi^+\pi^0$  and  $\pi^+\pi^0\pi^0$  in Monte Carlo and data. The decay fractions of these modes are known to within 1% and therefore the ratio is sensitive to the  $\pi^0$  efficiency. The  $\pi^0$  efficiencies agree to within 5% between data and MC. Thus, 5 % of the MC  $\pi^0$  are killed [22].

We apply the above corrections to the signal Monte Carlo sample and compute new signal efficiencies. We weight each photon by 97.5 % (see Section 12.1), weight each track according to the tracking tables, weight each  $K_s$  by 103 %, kill the charged kaons, and finally each  $\pi^0$  is weighted by 95.0 %. The track smearing is also applied. Table 12.14 shows the corrected efficiencies. The ratio of the corrected efficiency with respect to the original one is shown in parenthesis. The weighted cross-feed sample is also re-fit and the yields change slightly.

### 12.7.2 Systematic errors on difference between data and MC efficiencies

Table 12.15 shows the systematic errors on the difference between data and Monte Carlo detection efficiencies obtained from studies of data control samples, as described above and reported in the various references.

The errors are first computed for each final state, as listed in Table 12.16, using the values in Table 12.15. Errors from the same sources are considered 100% correlated, while errors from different sources are considered uncorrelated. For example, for the  $K\pi$  mode the error is,  $\delta\varepsilon = ((1.2 + 1.2)^2 + 3.0^2)^{1/2} = 3.8$ ,

$M_{Had}$	<i>all</i>	<i>2-body</i>	<i>3-body</i>	<i>4-body</i>
0.6-0.8	$15.0 \pm 1.0$ (94)	$15.0 \pm 1.0$ (94)	–	–
0.8-1.0	$10.6 \pm 0.2$ (93)	$10.6 \pm 0.2$ (93)	–	–
1.0-1.2	$7.2 \pm 0.4$ (94)	$9.3 \pm 0.6$ (96)	$5.0 \pm 0.5$ (88)	$6.3 \pm 2.4$ (108)
1.2-1.4	$5.3 \pm 0.3$ (94)	$7.5 \pm 0.6$ (98)	$4.7 \pm 0.4$ (92)	$2.2 \pm 0.5$ (80)
1.4-1.6	$4.6 \pm 0.3$ (88)	$7.1 \pm 0.7$ (94)	$4.5 \pm 0.4$ (83)	$2.5 \pm 0.4$ (92)
1.6-1.8	$3.8 \pm 0.3$ (92)	$5.4 \pm 0.7$ (90)	$4.0 \pm 0.4$ (92)	$2.7 \pm 0.4$ (94)
1.8-2.0	$2.6 \pm 0.2$ (86)	$5.1 \pm 0.9$ (89)	$2.7 \pm 0.4$ (82)	$1.5 \pm 0.3$ (90)
2.0-2.2	$2.6 \pm 0.3$ (92)	$4.8 \pm 1.0$ (84)	$2.9 \pm 0.5$ (95)	$1.4 \pm 0.3$ (98)
2.2-2.4	$1.8 \pm 0.3$ (86)	$3.7 \pm 1.2$ (88)	$1.7 \pm 0.5$ (88)	$1.2 \pm 0.4$ (83)
$M_{Had}$	$\pi$	$\pi^0$	$K$	$K_s$
0.6-0.8	$15.8 \pm 1.2$ (85)	$13.4 \pm 1.6$ (121)	$18.8 \pm 1.3$ (95)	$7.4 \pm 1.2$ (87)
0.8-1.0	$12.3 \pm 0.2$ (94)	$7.3 \pm 0.2$ (90)	$12.9 \pm 0.2$ (93)	$6.1 \pm 0.2$ (94)
1.0-1.2	$9.2 \pm 0.6$ (94)	$4.7 \pm 0.5$ (94)	$8.8 \pm 0.5$ (92)	$3.8 \pm 0.5$ (104)
1.2-1.4	$7.3 \pm 0.5$ (97)	$3.5 \pm 0.3$ (89)	$6.2 \pm 0.4$ (93)	$3.5 \pm 0.4$ (97)
1.4-1.6	$5.9 \pm 0.4$ (90)	$3.6 \pm 0.3$ (86)	$5.5 \pm 0.3$ (86)	$2.8 \pm 0.4$ (97)
1.6-1.8	$5.1 \pm 0.5$ (92)	$2.8 \pm 0.3$ (91)	$4.2 \pm 0.3$ (90)	$2.9 \pm 0.4$ (98)
1.8-2.0	$3.4 \pm 0.4$ (86)	$2.0 \pm 0.3$ (87)	$3.0 \pm 0.3$ (83)	$1.7 \pm 0.4$ (97)
2.0-2.2	$3.5 \pm 0.6$ (89)	$1.9 \pm 0.3$ (96)	$2.7 \pm 0.4$ (90)	$2.2 \pm 0.5$ (97)
2.2-2.4	$1.8 \pm 0.3$ (86)	$1.4 \pm 0.4$ (92)	$1.9 \pm 0.4$ (83)	$1.6 \pm 0.5$ (97)

Table 12.14: The corrected signal efficiencies in % after the data–MC corrections are applied. The ratio of the corrected and the original efficiencies is given in parenthesis.

where the first term is the tracking efficiency error for the kaon and pion, and the second term is the charged kaon identification error. These errors are applied as weights for each event according to its mode, and the weighted efficiencies are calculated. The systematic error is the percent change between the weighted and un-weighted efficiency.

Table 12.17 shows the corresponding systematic error per each mass bin for the *all* final state category due to detection efficiency differences in data and Monte Carlo.

Reference	Systematic From	$\delta\varepsilon$
[26]	Tracking efficiency	$\pm 1.2\%$ per track
[23]	Charged kaon identification	$\pm 3.0\%$ per kaon
[22]	$\pi^0$ efficiency	$\pm 2.5\%$ per $\pi^0$
[27],[23]	$K_S^0$ efficiency	$\pm 4.0\%$ per $K_S^0$

Table 12.15: Systematic errors on difference between data and MC efficiencies from data control samples.

Final State	$\delta\varepsilon$
$K\pi$	3.8%
$K_S\pi^0$	4.7%
$K\pi\pi^0$	4.6%
$K_S\pi\pi$	4.5%
$K_S\pi^0\pi\pi$	5.3%
$K\pi\pi\pi$	4.7%
$K\pi^0$	4.1%
$K_S\pi$	4.2%
$K_S\pi\pi^0$	4.9%
$K\pi\pi$	4.7%
$K_S\pi\pi\pi$	5.4%
$K\pi^0\pi\pi$	5.3%

Table 12.16: Detection efficiency systematics for each final state using Table 12.15.

$M_{Had}$	$all$
0.6-0.8	3.95
0.8-1.0	3.96
1.0-1.2	4.21
1.2-1.4	4.40
1.4-1.6	4.49
1.6-1.8	4.58
1.8-2.0	4.56
2.0-2.2	4.56
2.2-2.4	4.61

Table 12.17: The total systematic error in % per each mass bin and for the *all* final state category due to the smearing and killing factors.

## 12.8 Transition between resonant and non-resonant Monte Carlo.

The Monte Carlo model introduces systematic uncertainties. This type of systematics are important in the inclusive BF determination, and will be discussed further in the following chapters.

In the determination of the PBF in bins of hadronic mass, there is some model dependence associated with the sharp mass-cut-off at 1.0 GeV between the  $K^*\gamma$  resonant Monte Carlo and the non-resonant  $X_s\gamma$  Monte Carlo. This is the Kagan & Neubert recipe, described in Chapter 2.

To investigate the systematic from this cut-off, we vary the 1.0 GeV/ $c^2$  cut off to 1.2 GeV/ $c^2$ . We then count only the  $K^*\gamma$  resonance in the 1.0-1.2 GeV/ $c^2$  mass bin instead of only the  $X_s\gamma$  contribution. This change in the hadronic mass cut-off will have an effect on the signal efficiency as well as the cross-feed yield for that bin.

The signal efficiency for this particular bin is shown in Table 12.18, where the the estimation using the  $K^*\gamma$  resonance MC is compared with the one estimated using the  $X_s\gamma$  contribution. The results are compatible within ( $1.2\sigma$ ) statistical errors. We consider the 10% variation as systematic error in this bin from the Monte Carlo modeling. This error will be quoted separately along with the other model dependent errors coming from the determination of the inclusive BF.

In order to estimate the cross-feed yield using the  $K^*\gamma$  Monte Carlo for this bin, the cross-feed  $M_{ES}$  distribution has been re-fit. The measured cross-feed

Signal Efficiency $\epsilon$ . $M_{Had}$ : 1.0–1.2 GeV			
reco-body	$X_s\gamma$	$K^*\gamma$	$\Delta\epsilon/\sigma$
<i>2-body</i>	$0.0970 \pm 0.0061$	$0.0876 \pm 0.0048$	1.2

Table 12.18: Signal Efficiency estimated using the  $X_s\gamma$  contribution (first column) or  $K^*\gamma$  (second column), together with their statistical agreement (third column), where  $\sigma$  takes into account the statistical uncertainty of both estimations.

yields are presented in Table 12.19. The cross-feed yields from the  $X_s\gamma$  Monte Carlo are slightly higher, although the values are small and therefore this will not significantly change the signal yield. We do not assign a systematic error in this case.

Cross-feed yield. $M_{Had}= 1.0\text{--}1.2 \text{ GeV}/c^2$		
reco-body	$K^*\gamma$	$X_s\gamma$
<i>all</i>	$0.46 \pm 0.30$	$2.4 \pm 1.4$
<i>2-body</i>	$0.57 \pm 0.23$	$1.75 \pm 0.71$
<i>3-body</i>	$0 \pm 0.0001$	$1.23 \pm 1.22$

Table 12.19: Cross-feed yield estimated using the  $K^*\gamma$  contribution (first column) and  $X_s\gamma$  (second column).

## 12.9 Generator error due to model dependence

In order to estimate any possible  $X_s\gamma$  model dependence of the signal efficiency, we use the KN495 model instead of the KN465 to estimate the efficiency for each  $M_{Had}$  bin. All the systematic corrections that have been applied to the KN465 model, have been calculated and applied to the KN495 Monte Carlo model as well.

The resulting efficiencies are compared between the two models, and in Table 12.20 the difference in efficiency is shown for the *all* final state category and for each  $M_{Had}$  bin, together with the statistical error of the estimation. As it can be seen, the efficiency differences agree within statistics with zero.

The weighted average efficiency difference between the two models, is found to be  $-0.0032 \pm 0.0019$ , which correspond to a relative systematic uncertainty on the efficiencies which ranges from  $-2.1\% \pm 1.3\%$  to  $-17.8\% \pm 11\%$ , calculated with respect to Table 13.6. On average the correction is  $-9.9\% \pm 5.8\%$ . Even though the obtained result is in reasonable agreement with no offset, due to limited statistics we take the absolute value of the difference as our systematic uncertainty, which we round to  $\pm 10\%$ .

This model dependence also effects the cross-feed yield. The systematic error associated with this is found to be negligible with respect to the on average 50% statistical error.

$M_{Had}$	$\Delta\epsilon$
1.0-1.2	$-0.0092 \pm 0.0049$
1.2-1.4	$-0.0064 \pm 0.0040$
1.4-1.6	$-0.0036 \pm 0.0041$
1.6-1.8	$-0.0045 \pm 0.0045$
1.8-2.0	$0.0048 \pm 0.0054$
2.0-2.2	$0.0028 \pm 0.0073$
2.2-2.4	$0.0147 \pm 0.0115$
combination	$-0.0032 \pm 0.0019$

Table 12.20: Efficiency difference for each  $M_{Had}$  bin between the  $X_S\gamma$  models KN495 and KN465. The combination is a weighted average over  $M_{Had}$ .

## 12.10 Summary of the systematic errors

The results of our systematic studies will not only provide a systematic error on our PBFs, but also causes a shift in the central values due to the shifts in the Monte Carlo efficiencies presented in Table 12.14. We will first present a summary of the systematic errors on the PBFs and then in the next section present the PBFs calculated with the shifted efficiencies.

The total contributions to the systematic errors from the different sources discussed above is shown in Table 12.21, excluding the model errors. The column labeled general includes the contribution from the photon efficiency, B-counting and selection variable systematics. The model dependent errors presented in Sections 12.9 and 12.8 will be listed separately and are 10% except in the  $M_{Had}$

bin 1.0-1.2 GeV/ $c^2$  where the error is 14%. Note that the systematic errors are less than the statistical errors in all  $M_{Had}$  bins.

$M_{Had}$	General 12.1- 12.3	Fit 12.4	Signal 12.5	$B\bar{B}$ Yield 12.6	Eff. 12.7	Total Syst.	Stat. err.
0.6-0.8		17	1.3	–	3.95	18.0	58
0.8-1.0		5.9	0.31	–	3.96	8.2	11
1.0-1.2		24	0.39	–	4.21	24.7	36
1.2-1.4		12	2.5	–	4.40	13.7	24
1.4-1.6	4.2	13	2.1	–	4.49	14.5	21
1.6-1.8		12	2.8	–	4.58	13.8	36
1.8-2.0		15	1.4	7	4.56	17.7	41
2.0-2.2		16	13	10	4.56	23.7	79
2.2-2.4		125	37	120	4.61	177	423

Table 12.21: Percent systematic errors from all the systematic contributions, except the signal modeling, for the *all* final state category.

## 12.11 Partial BFs with systematic errors

Here we present the results for the PBF using the shifts in the Monte Carlo efficiencies from the systematic studies presented above. The shifted efficiencies are listed in Table 12.14. The shift (+10%) in the  $B\bar{B}$  peaking yield is also applied.

We show here updated tables for the hadronic multiplicity (Table 12.23, *2/3-body* and *4/3-body* ratios (Tables 12.24 and 12.25),  $K_S/K$  (Table 12.26) and  $\pi^0/\pi$  (Table 12.27) ratios as discussed in Chapter 11. These values have not changed significantly with the systematic shifts, although the Monte Carlo multiplicity values have moved in the right direction. The data multiplicities have changed only slightly since only the cross-feed yield changed due to the corrections to the signal Monte Carlo, except in the last three bins where the shift in the  $B\bar{B}$  peaking yield is applied.

We see that there is still a disagreement (as expected) between the data and MC values for the  $\pi^0/\pi$  and *2/3-body* ratios. Chapter 13 presents a method for correcting for these differences.

Table 12.28 presents the PBF results for the *all* final state category with the statistical and systematic errors.

$M_{Had}$	<i>all</i>	<i>2-body</i>	<i>3-body</i>	<i>4-body</i>
0.6-0.8	$1.52 \pm 0.876$	$1.52 \pm 0.876$	–	–
0.8-1.0	$24.4 \pm 2.76$	$24.6 \pm 2.58$	–	–
1.0-1.2	$7.21 \pm 2.57$	$2.2 \pm 1.21$	$5.27 \pm 2.8$	$0.33 \pm 0.643$
1.2-1.4	$25.3 \pm 6.04$	$2.99 \pm 1.57$	$23.1 \pm 5.79$	$-4.5 \pm 4.83$
1.4-1.6	$33.3 \pm 7.09$	$5.53 \pm 1.86$	$19.2 \pm 5.28$	$13.8 \pm 7.21$
1.6-1.8	$24.6 \pm 8.87$	$1.9 \pm 1.88$	$10.5 \pm 5.47$	$17.9 \pm 9.77$
1.8-2.0	$33.3 \pm 13.5$	$1.81 \pm 1.47$	$16.4 \pm 9.11$	$21.4 \pm 17.1$
2.0-2.2	$18.4 \pm 14.5$	$-1.64 \pm 1.51$	$0.926 \pm 7.72$	$40.1 \pm 23.7$
2.2-2.4	$6.01 \pm 25.4$	$0.961 \pm 2.66$	$-10.3 \pm 15.3$	$15.9 \pm 31.4$
$M_{Had}$	$\pi$	$\pi^0$	$K$	$K_s$
0.6-0.8	$0.917 \pm 0.548$	$-0.363 \pm 0.63$	$0.384 \pm 0.53$	$0.452 \pm 0.911$
0.8-1.0	$16.8 \pm 1.86$	$7.21 \pm 2.46$	$17.1 \pm 2.0$	$6.17 \pm 1.81$
1.0-1.2	$3.15 \pm 1.26$	$4.61 \pm 3.2$	$4.6 \pm 1.79$	$2.55 \pm 2.8$
1.2-1.4	$11.6 \pm 2.8$	$15.2 \pm 7.45$	$18.1 \pm 4.47$	$5.56 \pm 4.42$
1.4-1.6	$8.94 \pm 2.86$	$27.8 \pm 8.19$	$19.3 \pm 4.52$	$10.7 \pm 6.07$
1.6-1.8	$1.74 \pm 3.72$	$30.9 \pm 10.7$	$19.3 \pm 6.97$	$3.58 \pm 6.12$
1.8-2.0	$9.11 \pm 5.93$	$30.4 \pm 14.5$	$14.6 \pm 10.1$	$9.72 \pm 8.34$
2.0-2.2	$4.99 \pm 4.62$	$10.6 \pm 21.7$	$5.33 \pm 9.95$	$15.8 \pm 11.4$
2.2-2.4	$3.38 \pm 9.72$	$14.1 \pm 33.4$	$-8.81 \pm 19.8$	$20.3 \pm 14.3$

Table 12.22: The partial branching fraction ( $10^{-6}$ ) for the different final state categories as a function of  $M_{Had}$  using the shifted efficiencies.

$M_{Had}$	0.6-0.8	0.8-1.0	1.0-1.2
MC Mean	2.0	2.0	2.52
Data Mean	2.0	2.0	$2.76 \pm 0.18$
$M_{Had}$	1.2-1.4	1.4-1.6	1.6-1.8
MC Mean	2.80	3.02	3.18
Data Mean	$2.65 \pm 0.32$	$3.21 \pm 0.16$	$3.53 \pm 0.20$
$M_{Had}$	1.8-2.0	2.0-2.2	2.2-2.4
MC Mean	3.26	3.28	3.29
Data Mean	$3.50 \pm 0.26$	$4.10 \pm 0.25$	$8.11 \pm 61.3$

Table 12.23: Parameterization of truncated hadronic multiplicity in signal MC and data.

$M_{Had}$	$(2b/3b)_{corr}^{data}$	$(2b/3b)_{corr}^{MC}$	$(2b/3b)_{raw}^{data}$	$(2b/3b)_{raw}^{MC}$
1.0-1.2	$0.42 \pm 0.32$	1.03	$0.77 \pm 0.58$	1.9
1.2-1.4	$0.13 \pm 0.08$	0.56	$0.21 \pm 0.12$	0.89
1.4-1.6	$0.29 \pm 0.13$	0.43	$0.46 \pm 0.19$	0.69
1.6-1.8	$0.18 \pm 0.20$	0.40	$0.25 \pm 0.27$	0.55
1.8-2.0	$0.12 \pm 0.12$	0.39	$0.23 \pm 0.22$	0.75
2.0-2.2	$8.34 \pm 319$	0.38	$14 \pm 520$	0.63
2.2-2.4	$-0.07 \pm 0.24$	0.39	$-0.15 \pm 0.53$	0.85

Table 12.24: Ratios of 2/3-body for  $M_{Had}$  above  $1.0 \text{ GeV}/c^2$  for data and Monte Carlo after systematic corrections.

$M_{Had}$	$(4b/3b)_{corr}^{data}$	$(4b/3b)_{corr}^{MC}$	$(4b/3b)_{raw}^{data}$	$(4b/3b)_{raw}^{MC}$
1.0-1.2	$0.06 \pm 0.13$	0.04	$0.078 \pm 0.15$	0.055
1.2-1.4	$-0.20 \pm 0.22$	0.21	$-0.093 \pm 0.099$	0.097
1.4-1.6	$0.72 \pm 0.43$	0.48	$0.4 \pm 0.23$	0.26
1.6-1.8	$1.70 \pm 1.28$	0.80	$1.1 \pm 0.83$	0.53
1.8-2.0	$1.36 \pm 1.35$	1.01	$0.78 \pm 0.76$	0.58
2.0-2.2	$-195 \pm 7450$	1.08	$-94 \pm 3600$	0.52
2.2-2.4	$-1.14 \pm 3.07$	1.13	$-0.82 \pm 2.2$	0.8

Table 12.25: Ratios of 4/3-body for  $M_{Had}$  above  $1.0 \text{ GeV}/c^2$  for data and Monte Carlo after systematic corrections.

$M_{Had}$	$(K_S/K)_{corr}^{data}$	$(K_S/K)_{corr}^{MC}$	$(K_S/K)_{raw}^{data}$	$(K_S/K)_{raw}^{MC}$
0.6-1.0	$0.38 \pm 0.12$	0.500	$0.18 \pm 0.061$	0.24
1.0-1.6	$0.45 \pm 0.20$	0.497	$0.23 \pm 0.10$	0.25
1.6-2.0	$0.39 \pm 0.34$	0.493	$0.22 \pm 0.20$	0.33
2.0-2.4	$-4.81 \pm -14.80$	0.495	$-6.7 \pm -33$	0.40
0.6-2.2	$0.55 \pm 0.20$	0.498	$0.26 \pm 0.075$	0.24
0.6-2.4	$0.86 \pm 0.37$	0.498	$0.32 \pm 0.089$	0.24

Table 12.26: The ratios for the  $K_S$  and  $K$  final state categories as a function of  $M_{Had}$ .

$M_{Had}$	$(\pi^0/\pi)_{corr}^{data}$	$(\pi^0/\pi)_{corr}^{MC}$	$(\pi^0/\pi)_{raw}^{data}$	$(\pi^0/\pi)_{raw}^{MC}$
0.6-1.0	$0.39 \pm 0.15$	0.50	$0.22 \pm 0.093$	0.31
1.0-1.6	$2.02 \pm 0.60$	1.07	$1.1 \pm 0.3$	0.55
1.6-2.0	$5.82 \pm 4.25$	1.41	$3.8 \pm 2.9$	0.79
2.0-2.4	$2.98 \pm 7.10$	1.43	$1.5 \pm 3.2$	0.78
0.6-2.2	$2.20 \pm 0.65$	0.74	$0.87 \pm 0.19$	0.37
0.6-2.4	$2.32 \pm 0.93$	0.75	$0.9 \pm 0.22$	0.37

Table 12.27: The ratios for the  $\pi^0$  and  $\pi$  final state categories as a function of  $M_{Had}$ .

$M_{Had}$	$PBF \pm stat \pm syst \pm model$
0.6-0.8	$1.52 \pm 0.876 \pm 0.27 \pm 0.15$
0.8-1.0	$24.4 \pm 2.76 \pm 2.0 \pm 2.4$
1.0-1.2	$7.21 \pm 2.57 \pm 1.78 \pm 1.0$
1.2-1.4	$25.3 \pm 6.04 \pm 3.47 \pm 2.5$
1.4-1.6	$33.3 \pm 7.09 \pm 4.83 \pm 3.3$
1.6-1.8	$24.6 \pm 8.87 \pm 3.39 \pm 2.5$
1.8-2.0	$33.3 \pm 13.5 \pm 5.89 \pm 3.3$
2.0-2.2	$18.4 \pm 14.5 \pm 4.36 \pm 1.8$
2.2-2.4	$6.01 \pm 25.4 \pm 10.6 \pm 0.6$

Table 12.28: The partial branching fraction ( $10^{-6}$ ) for the *all* final state category as a function of  $M_{Had}$  using the shifted efficiencies and showing the statistical and systematic errors.

# Chapter 13

## Weighted Partial Branching Fractions

In this chapter we describe the method for re-weighting the Monte Carlo to take into account the actual production of particles in the final state. We then recalculate the PBF's after the corrections are applied (Weighted Partial Branching Fraction, WPBR).

The Monte Carlo re-weighting is associated with differences between the fragmentation of the  $X_s$  system in the signal Monte Carlo, and the fragmentation in data, which has to be inferred from the observed distribution of the signal among the final states. The MC fragmentation is done by a general package (JetSet).

In general, the correct approach would be to measure the PBFs for each of the twelve investigated final states. The sum of all the PBFs for each bin would give the correctly fragmented PBF. In our case, we cannot look at each final state individually, because we lack statistics in data (when dividing the sample into 9 mass bins and 12 final states). We instead re-weight the Monte Carlo signal events to reproduce the behavior found in data. The details of the method and the results are given in the following.

### 13.1 Weighting procedure

As discussed in the previous chapters, the ratio of the  $\pi^0$  and  $\pi$  categories and the multiplicities show a different behavior in data and Monte Carlo. We want to correct the signal Monte Carlo distribution, and therefore the efficiencies, to bring the Monte Carlo into agreement with the data.

Given two orthogonal categories (e.g.  $\pi^0$  and  $\pi$ ), we want to correct their relative ratio, such that the ratio of the ratios in data and MC are equal to one, e.g.

$$R = (\pi^0/\pi)^{data}/(\pi^0/\pi)^{MC} \rightarrow 1 \quad (13.1)$$

The ratio in data is computed as the ratio of the yield in data, less the contribution from the  $B\bar{B}$  yield in the last three bins in the hadronic mass, of the two categories under consideration. The ratio in MC is given by the ratio of the MC reconstructed events in the signal sample for each of the two categories under consideration.

$$(\pi^0/\pi)^{data} = (N_{\pi^0}^{data} - N_{\pi^0}^{bb})/(N_{\pi}^{data} - N_{\pi}^{bb}) \quad (13.2)$$

$$(\pi^0/\pi)^{MC} = N_{\pi^0}^{reco}/N_{\pi}^{reco} \quad (13.3)$$

In particular, we consider the ratios  $\pi^0/\pi$ , *2-body/3-body*, *4-body/3-body*. We calculate the equivalent of R, the ratio of the ratios in data and Monte Carlo, in each  $M_{Had}$  bin, and fit the R distribution to a straight line. The fit is to a zero-degree polynomial and the y-intercept from the fit provides a constant factor,  $S$ , with which to weight the Monte Carlo events to force R to equal 1, i.e. the distribution will be centered around R=1.

The process is iterative, as the weight due to the  $\pi^0/\pi$  will effect also the ratio of *2-body/3-body* and *4-body/3-body*, and vice-versa. The weight is applied to both the generated and reconstructed events in the Monte Carlo.

The weights will adjust the efficiency for all the categories except for the ones used to generate the weights. For example, if we weight the reconstructed and generated events with a constant factor,  $S$ , derived from a fit to the ratio of the  $\pi^0/\pi$  ratios distribution, the new efficiency for the  $\pi^0$  category,  $\varepsilon'_{\pi^0}$ , will be:

$$\varepsilon'_{\pi^0} = (S * n_{\pi^0}^{recoed})/(S * n_{\pi^0}^{gener}) = (n_{\pi^0}^{recoed})/(n_{\pi^0}^{gener}) = \varepsilon_{\pi^0} \quad (13.4)$$

where  $n_{\pi^0}^{recoed}$  and  $n_{\pi^0}^{gener}$  are the recoed and generated events, respectively, in the  $\pi^0$  category. From the above equation it is clear that, as the constant amount  $S$  simplifies, the new efficiency is equal to the old efficiency for the category for which the weight is determined. The same is true for any orthogonal category, as it will not contain  $\pi^0$  events.

If the category contains some  $\pi^0$  events, the new efficiency will depend on the factor  $S$ . E.g. for the *2-body* events:

$$\varepsilon'_{2b} = (S * n_{2b-\pi^0}^{recoed} + n_{2b-\pi}^{recoed})/(S * n_{2b-\pi^0}^{gener} + n_{2b-\pi}^{gener}) \quad (13.5)$$

where  $n_{2b-\pi^0}^{recoed}$ ,  $n_{2b-\pi}^{recoed}$ ,  $n_{2b-\pi^0}^{gener}$ , and  $n_{2b-\pi}^{gener}$  are the number of recoed *2-body* events in the  $\pi^0$  category, the number of recoed *2-body* events in the  $\pi$  category, the

number of generated *2-body* events in the  $\pi^0$  category, and the number of generated *2-body* events in the  $\pi$  category, respectively.

In the following, we first correct the  $\pi^0$  category, then we look at the multi-body categories. Note that according to our model we need a weighted efficiency only for the  $X_s\gamma$  events, thus our weights just start after 1.0 GeV/ $c^2$ .

We look at the ratio in data and Monte Carlo for the three different cases:  $\pi^0/\pi$ , *2/3-body*, and *4/3-body*, as a function of the hadronic mass. Figure 13.1 shows the ratios for the three cases. The errors are just statistical errors. The bin for the range 1.6-1.8 GeV/ $c^2$  in  $M_{Had}$  in the  $\pi^0/\pi$  R plot is quite high and has large statistical errors. This is due to a statistical fluctuation in the data yield for the  $\pi$  category, which is quite low compared to neighboring bins, yielding a large ratio. The second to last bin in the *2/3-body* and *4/3-body* R plots is not seen on the graph. This is because the *3-body* signal yield is very small in this bin and the ratio blows up. Note that these are effects coming from our limited statistics. In order to show the ratios in a more reasonable scale, we magnify the y-axis of the plots and show them again in Figure 13.2. We fit the points with a constant line (P0). Note that the fit includes any points off scale as well. The choice of the function to be used in the fit is an assumption we make, dictated by the fact that the fit has a good  $\chi^2$ .

## 13.2 $\pi^0$ weights

We first want to correct the  $\pi^0/\pi$  ratio. According to the fit values, our weight is 1.907. All signal events which belong to the  $\pi^0$  category are weighted by this factor. The signal MC weighted events are then used such to get the new efficiencies. The efficiencies of the categories  $\pi^0$  and  $\pi$  are unchanged as the the weights are obtained from the  $\pi^0$  category while the  $\pi$  category is orthogonal. Few percent changes in the other categories are observed. The ratios of the new weighted efficiencies with respect to the un-weighted ones are shown in Table 13.1. These weighted efficiencies are used to recalculate the ratios for the Monte Carlo, the data ratios do not change.

We look again at the ratio of ratios in data and Monte Carlo for the three different cases:  $\pi^0/\pi$ , *2/3-body*, and *4/3-body*, as a function of the hadronic mass, after the  $\pi^0$  weight is applied. The corresponding picture is shown in Figure 13.3. Note that the  $\pi^0/\pi$  ratio is now centered around one.

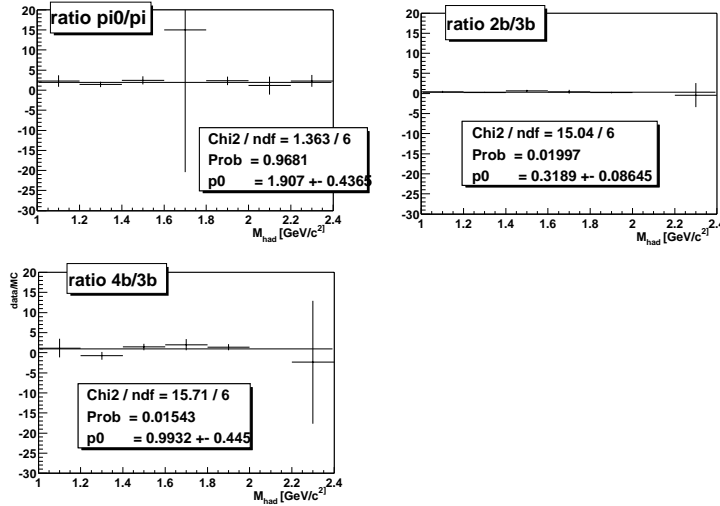


Figure 13.1: Data over MC ratios of the following ratios (in clockwise order) as a function of the hadronic mass:  $\pi^0/\pi$ , 2/3 bodies, and 4/3 bodies. No weights are yet applied. A zero-degree polynomial is used for fitting.

### 13.3 $\pi^0$ and 2-body weights

We then weight the two *2-body* events according to the fit to the *2/3-body* ratio distribution as seen in Figure 13.3. This corresponds to a weight of 0.3805.

The signal MC weighted events are then used to get the new efficiencies. The ratio of the new weighted efficiencies with respect to the un-weighted ones are shown in Table 13.2.

We look again at the ratio of ratios in data and Monte Carlo for the three different cases:  $\pi^0/\pi$ , *2/3-body*, and *4/3-body*, as a function of the hadronic mass, after the  $\pi^0$  and *2-body* weights have been applied. The corresponding picture is shown in Figure 13.4.

### 13.4 $\pi^0$ , 2-body and $\pi^0$ (second iteration) weights

After the  $\pi^0$  and the 2 body corrections are applied, we see that the  $\pi^0/\pi$  ratio is lower than 1 (Fig. 13.4). The  $\pi^0/\pi$  ratio has been modified by the 2 body weight as the two categories,  $\pi^0$  and *2-body*, are not orthogonal. The *4/3-body* R distribution has been affected by the weighting but partly since the statistics are low the changes have not been significant and the ratio of ratios are still

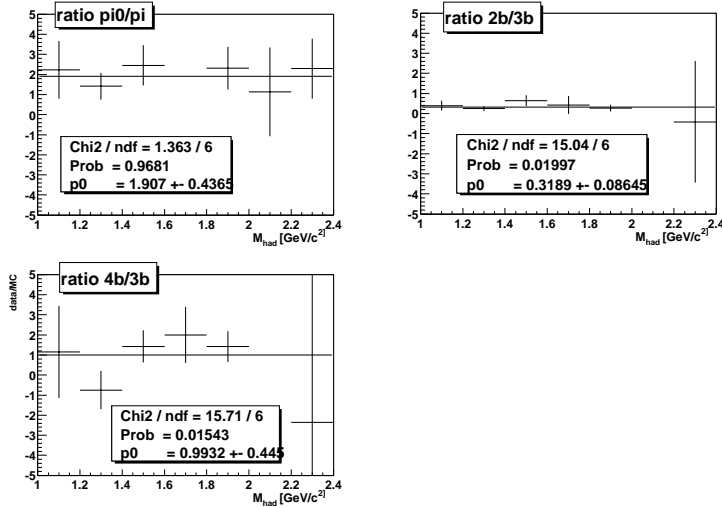


Figure 13.2: Data over MC ratios of the following ratios (in clockwise order) as a function of the hadronic mass:  $\pi^0/\pi$ ,  $2/3$ -body, and  $4/3$ -body. No weights are yet applied. A zero-degree polynomial is used for fitting. This plot is the magnification of Fig. 13.1.

consistent with zero. We therefore, apply a correction on the  $\pi^0$  events again, to bring the ratio back to 1.

The signal MC weighted events are then used to get the new efficiencies. The ratios of the new efficiencies to the original ones are shown in Table 13.3.

The new ratio of ratios plots are shown in Figure 13.5, all are consistent with 1 within the errors. Figure 13.6 show the same plots, but with a larger y-scale, to see how some of the points off-scale in Figure 13.5 have adjusted.

## 13.5 Weighted Partial Branching Fraction Results

The Monte Carlo signal distribution is what is being weighted. Therefore, the weights change not only the efficiency but also the shape of the signal and cross-feed distributions. The weighted efficiencies are listed in Table 13.6. The weights slightly change the Crystal Ball signal parameters (see Table 13.4). The widths, on average, increase compared to Table 10.2. This is expected since we are giving more weight to events with  $\pi^0$ 's which have a slightly larger signal

$M_{Had}$	<i>all</i>	<i>2-body</i>	<i>3-body</i>	<i>4-body</i>
1.0-1.2	89.2	88.9	93.6	97.6
1.2-1.4	89.2	89.5	91.9	101
1.4-1.6	93.2	92.8	95	104.0
1.6-1.8	92.2	88.6	95.8	96.1
1.8-2.0	91.2	89.8	102	91.6
2.0-2.2	90.3	93	93.7	96.2
2.2-2.4	92.0	91	88.9	106
$M_{Had}$	$\pi$	$\pi^0$	$K$	$K_s$
1.0-1.2	100	100	88.8	90.4
1.2-1.4	100	100	87.9	93.2
1.4-1.6	100	100	94.1	89.9
1.6-1.8	100	100	92.1	92.9
1.8-2.0	100	100	91.4	91.5
2.0-2.2	100	100	90.7	89.7
2.2-2.4	100	100	93.1	89.7

Table 13.1: Ratio of the  $\pi^0$  weighted efficiency and the original efficiency in %.

width, and giving less weight to *2-body* events which have a slightly smaller width, although the changes are not large.

Since the signal Crystal Ball parameters are used to fix the peaking shape in the fits to the other Monte Carlo samples and the data, all the are redone. In this way we also obtain a new set of cross-feed Argus parameters to use in the data fits (see Table 13.5). We refit  $B\bar{B}$  sample to obtain a new  $B\bar{B}$  yield, and the  $B\bar{B}$  plus continuum sample to obtain new Argus shape parameters to use in the data fits. Using the new Crystal Ball and Argus shape parameters we also obtain a new set of data yields. The corresponding new weighted partial branching fractions, using the updated yields and efficiencies, are shown in Table 13.7 and in Figure 13.7. These results include the systematic shifts in the efficiencies and in the  $B\bar{B}$  yield presented in Chapter 12.

Tables 13.8, 13.9, 13.10, 13.11, and 13.12 show the new multiplicities, multiplicity ratios and the new ratios for  $K_S/K$  and  $\pi^0/\pi$  which show a better agreement between data and Monte Carlo than before. This can also be seen from the plot of the multiplicity versus  $M_{Had}$  shown in Figure 13.8, which can be compared to the same distribution before any corrections were applied, shown in Figure 11.2.

It can be noticed from Figure 13.7, that the comparison of the WPBF ob-

$M_{Had}$	<i>all</i>	<i>2-body</i>	<i>3-body</i>	<i>4-body</i>
1.0-1.2	78.7	88.9	93.6	97.6
1.2-1.4	81.1	89.5	91.9	101
1.4-1.6	85.9	92.8	95.9	104
1.6-1.8	88.3	88.6	95.8	96.1
1.8-2.0	83.1	89.8	102	91.67
2.0-2.2	83.1	93	93.7	96.2
2.2-2.4	83.6	91	88.9	106
$M_{Had}$	$\pi$	$\pi^0$	$K$	$K_s$
1.0-1.2	84.7	95.2	79	77.8
1.2-1.4	91	95.8	79.6	86.1
1.4-1.6	89.5	96.9	88.6	75.8
1.6-1.8	94.2	101	87	92.4
1.8-2.0	82.3	96.6	81.9	87.8
2.0-2.2	86.5	97.1	82.6	84.6
2.2-2.4	82.6	97.1	86.2	77.6

Table 13.2: Ratio of the  $\pi^0$  and 2 body weighted efficiency and the original efficiency in %.

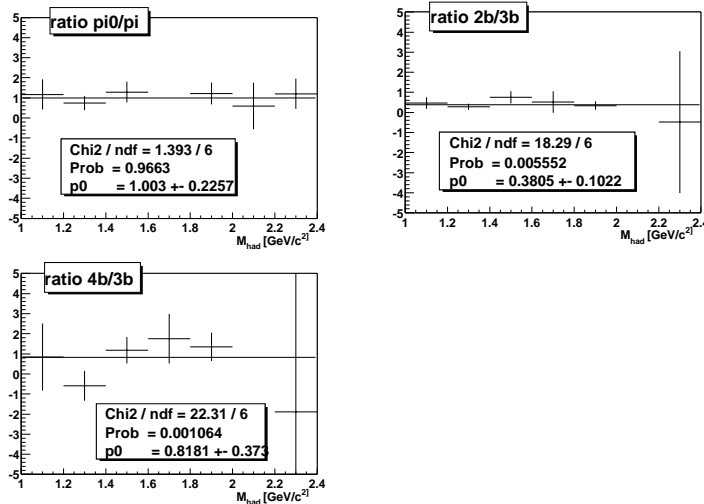


Figure 13.3: Data over MC ratios of the following ratios (in clockwise order) as a function of the hadronic mass:  $\pi^0/\pi$ ,  $2/3$ -body, and  $4/3$ -body. The  $\pi^0$  weight is applied. A zero-degree polynomial is used for fitting.

tained from the *all* category with respect to the sum  $(2+3+4)$ -body categories also agree well, since systematic errors coming from the failure of the MC to reproduce the data distribution have been taken into account. This is also true for the comparison with the sum of  $(K + K_S)$  categories and the sum of  $(\pi + \pi^0)$  categories. Nevertheless, we would not expect the two distributions to be exactly the same unless we had infinite statistics. Even though both results are obtained from the same data sample, they are in fact two independent methods of measuring the same quantity, and therefore they make different use of the available information in the data. Thus, we expect them to be compatible (if no other systematic effect is present). Note that compared to the same plots before the weighting, Figure 11.1, the agreement in most bins has improved, although in the last bins there are some fluctuation. These bins, especially the last bin, have such large statistical errors that they do not contribute much to the fit to R, and therefore the corrections applied to all bins do not necessarily correct them in a consistent way.

$M_{Had}$	<i>all</i>	<i>2-body</i>	<i>3-body</i>	<i>4-body</i>
1.0-1.2	81.2	92.9	95.3	97.4
1.2-1.4	84.2	93.3	94.6	101
1.4-1.6	87.8	95.6	96.7	104
1.6-1.8	90.7	92.5	98	97.4
1.8-2.0	84.7	93.5	101	93.2
2.0-2.2	85.3	97.4	95.4	97
2.2-2.4	85.2	95.2	91.6	105
$M_{Had}$	$\pi$	$\pi^0$	$K$	$K_s$
1.0-1.2	84.7	95.2	81.5	80.2
1.2-1.4	91	95.8	83	88
1.4-1.6	89.5	96.9	90	79.1
1.6-1.8	94.2	101	89.6	94.2
1.8-2.0	82.3	96.6	84	87.9
2.0-2.2	86.5	97.1	84.9	86.7
2.2-2.4	82.6	97.1	88.2	78

Table 13.3: Ratio of the  $\pi^0$  (two iterations) and 2 body weighted efficiency and the original efficiency in %.

$M_{Had}$	<i>all</i>	<i>2-body</i>	<i>3-body</i>	<i>4-body</i>
1.0-1.2	$2.7 \pm 0.1$	$2.7 \pm 0.2$	$2.8 \pm 0.2$	$1.7 \pm 0.5$
1.2-1.4	$2.7 \pm 0.1$	$2.6 \pm 0.2$	$2.8 \pm 0.2$	$2.2 \pm 0.4$
1.4-1.6	$2.9 \pm 0.2$	$2.4 \pm 0.3$	$2.9 \pm 0.2$	$3.0 \pm 0.4$
1.6-1.8	$3.0 \pm 0.2$	$2.6 \pm 0.5$	$3.0 \pm 0.2$	$3.0 \pm 0.4$
1.8-2.0	$2.2 \pm 0.2$	$2.5 \pm 0.7$	$2.4 \pm 0.2$	$2.0 \pm 0.3$
2.0-2.2	$3.7 \pm 0.3$	$2.1 \pm 0.6$	$3.6 \pm 0.4$	$4.1 \pm 0.7$
2.2-2.4	$3.6 \pm 0.5$	$3.0 \pm 1.1$	$4.0 \pm 0.8$	$3.0 \pm 0.7$
$M_{Had}$	$\pi$	$\pi^0$	$K$	$K_s$
1.0-1.2	$2.6 \pm 0.2$	$3.0 \pm 0.2$	$2.7 \pm 0.2$	$2.7 \pm 0.3$
1.2-1.4	$2.5 \pm 0.2$	$3.0 \pm 0.2$	$2.5 \pm 0.1$	$2.7 \pm 0.2$
1.4-1.6	$2.4 \pm 0.2$	$3.3 \pm 0.2$	$2.6 \pm 0.1$	$3.4 \pm 0.3$
1.6-1.8	$2.6 \pm 0.2$	$3.3 \pm 0.2$	$2.8 \pm 0.2$	$2.9 \pm 0.3$
1.8-2.0	$2.0 \pm 0.2$	$2.5 \pm 0.3$	$2.2 \pm 0.2$	$1.8 \pm 0.3$
2.0-2.2	$2.0 \pm 0.3$	$4.3 \pm 0.5$	$3.2 \pm 0.4$	$3.9 \pm 0.6$
2.2-2.4	$2.6 \pm 0.6$	$4.0 \pm 0.7$	$3.0 \pm 0.5$	$4.6 \pm 1.2$

Table 13.4: The width of the CB function for the signal events after the weights are applied, in  $\text{MeV}/c^2$ .

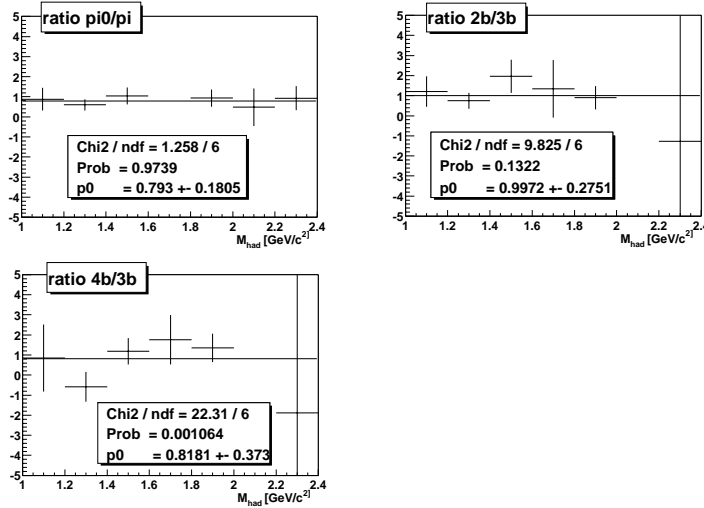


Figure 13.4: Data over MC ratios of the following ratios (in clockwise order) as a function of the hadronic mass:  $\pi^0/\pi$ ,  $2/3$ -body, and  $4/3$ -body. The  $\pi^0$  and 2-body weights are applied. A zero-degree polynomial is used for fitting.

## 13.6 Systematics due to the weights

To take into account a systematic error on the weighting method, we have varied the weights associated with each category, namely  $\pi^0$  and 2-body, by one sigma up and down in a correlated way. The values for the weights, along with their statistical errors, are listed in Table 13.13, where the weight for each step is shown. The difference between the efficiencies before and after the change in the weights is shown in Table 13.14. We take the maximum variation of the efficiency in the two cases as a systematic error. This systematic error is added (in quadrature) to the total in Table 12.21.

Table 13.15 lists the results for the weighted partial branching fractions in bins of  $M_{Had}$  with their statistical and total systematic error for the *all* final state category.

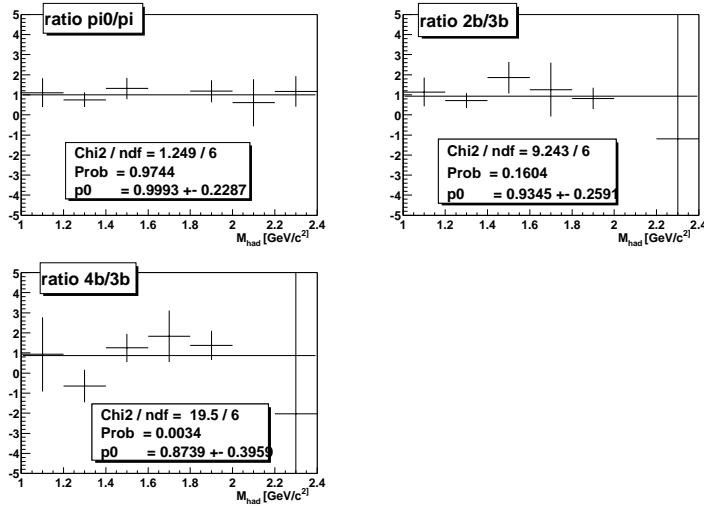


Figure 13.5: Data over MC ratios of the following ratios (in clockwise order) as a function of the hadronic mass:  $\pi^0/\pi$ ,  $2/3$ -body, and  $4/3$ -body. The  $\pi^0$  (two iterations) and 2 body weights are applied. A zero-degree polynomial is used for fitting.

$M_{Had}$	<i>all</i>	<i>2-body</i>	<i>3-body</i>	<i>4-body</i>
1.0-1.2	$-105 \pm 16$	$-83 \pm 45$	$-104 \pm 19$	$-159 \pm 14$
1.2-1.4	$-119 \pm 10$	$-51 \pm 53$	$-123 \pm 12$	$-118 \pm 17$
1.4-1.6	$-113 \pm 7$	$-113 \pm 40$	$-115 \pm 10$	$-110 \pm 10$
1.6-1.8	$-90 \pm 10$	$-76 \pm 39$	$-89 \pm 10$	$-90 \pm 10$
1.8-2.0	$-68 \pm 5$	$-60 \pm 38$	$-60 \pm 9$	$-73 \pm 7$
2.0-2.2	$-59 \pm 6$	$-65 \pm 57$	$-751 \pm 10$	$-52 \pm 7$
2.2-2.4	$-18 \pm 6$	$17 \pm 65$	$10 \pm 12$	$-31 \pm 7$
$M_{Had}$	$\pi$	$\pi^0$	$K$	$K_s$
1.0-1.2	$-108 \pm 27$	$-98 \pm 20$	$-108 \pm 20$	$-98 \pm 26$
1.2-1.4	$-100 \pm 21$	$-121 \pm 11$	$-116 \pm 12$	$-128 \pm 18$
1.4-1.6	$-101 \pm 14$	$-115 \pm 8$	$-114 \pm 8$	$-115 \pm 13$
1.6-1.8	$-74 \pm 12$	$-94 \pm 7$	$-84 \pm 7$	$-102 \pm 12$
1.8-2.0	$-69 \pm 11$	$-68 \pm 6$	$-72 \pm 6$	$-56 \pm 11$
2.0-2.2	$-67 \pm 11$	$-58 \pm 7$	$-55 \pm 7$	$-70 \pm 12$
2.2-2.4	$-2 \pm 13$	$-21 \pm 7$	$-22 \pm 7$	$-7 \pm 13$

Table 13.5: The x-feed Argus shape parameters after the weights are applied.

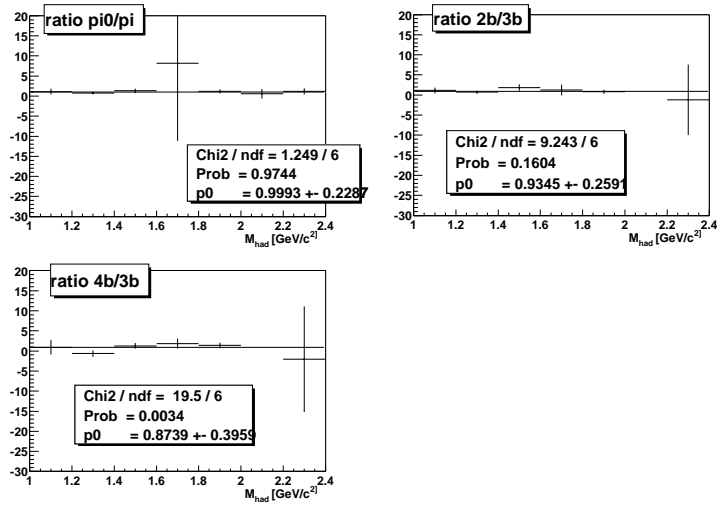


Figure 13.6: Data over MC ratios of the following ratios (in clockwise order) as a function of the hadronic mass:  $\pi^0/\pi$ ,  $2/3$ -body, and  $4/3$ -body. The  $\pi^0$  (two iterations) and 2-body weights are applied. A zero-degree polynomial is used for fitting. The y scale is increased with respect to Figure 13.5.

$M_{Had}$	all	2-body	3-body	4-body
0.6-0.8	$15.0 \pm 1.0$	$15.0 \pm 1.0$	–	–
0.8-1.0	$10.6 \pm 0.2$	$10.6 \pm 0.2$	–	–
1.0-1.2	$5.8 \pm 0.4$	$8.6 \pm 0.9$	$4.8 \pm 0.4$	$6.1 \pm 1.9$
1.2-1.4	$4.5 \pm 0.3$	$7.0 \pm 0.8$	$4.5 \pm 0.3$	$2.3 \pm 0.5$
1.4-1.6	$4.0 \pm 0.2$	$6.8 \pm 1.0$	$4.3 \pm 0.3$	$2.6 \pm 0.3$
1.6-1.8	$3.4 \pm 0.2$	$5.0 \pm 1.0$	$3.9 \pm 0.3$	$2.6 \pm 0.3$
1.8-2.0	$2.2 \pm 0.2$	$4.8 \pm 1.2$	$2.7 \pm 0.3$	$1.4 \pm 0.2$
2.0-2.2	$2.2 \pm 0.3$	$4.7 \pm 1.6$	$2.8 \pm 0.4$	$1.4 \pm 0.3$
2.2-2.4	$1.5 \pm 0.3$	$3.5 \pm 1.7$	$1.5 \pm 0.4$	$1.3 \pm 0.3$
$M_{Had}$	$\pi$	$\pi^0$	$K$	$K_s$
0.6-0.8	$15.8 \pm 1.2$	$13.4 \pm 1.6$	$18.8 \pm 1.3$	$7.4 \pm 1.2$
0.8-1.0	$12.3 \pm 0.2$	$7.3 \pm 0.2$	$12.9 \pm 0.2$	$6.1 \pm 0.2$
1.0-1.2	$7.8 \pm 0.6$	$4.5 \pm 0.4$	$7.2 \pm 0.5$	$3.1 \pm 0.5$
1.2-1.4	$6.6 \pm 0.5$	$3.4 \pm 0.3$	$5.1 \pm 0.3$	$3.1 \pm 0.4$
1.4-1.6	$5.2 \pm 0.5$	$3.5 \pm 0.3$	$4.9 \pm 0.3$	$2.2 \pm 0.3$
1.6-1.8	$4.8 \pm 0.5$	$2.8 \pm 0.2$	$3.7 \pm 0.3$	$2.8 \pm 0.4$
1.8-2.0	$2.8 \pm 0.4$	$1.9 \pm 0.2$	$2.5 \pm 0.3$	$1.5 \pm 0.3$
2.0-2.2	$3.1 \pm 0.6$	$1.8 \pm 0.3$	$2.3 \pm 0.3$	$1.9 \pm 0.4$
2.2-2.4	$1.9 \pm 0.6$	$1.3 \pm 0.3$	$1.7 \pm 0.3$	$1.2 \pm 0.4$

Table 13.6: The weighted signal efficiencies (%).

$M_{Had}$	<i>all</i>	<i>2-body</i>	<i>3-body</i>	<i>4-body</i>
1.0-1.2	$8.77 \pm 3.22$	$2.57 \pm 1.3$	$5.06 \pm 3.02$	$1.47 \pm 0.783$
1.2-1.4	$31.3 \pm 7.53$	$3.53 \pm 1.74$	$25.4 \pm 6.41$	$-4.39 \pm 4.61$
1.4-1.6	$39.7 \pm 7.93$	$5.66 \pm 2.08$	$20.2 \pm 5.49$	$13.2 \pm 6.89$
1.6-1.8	$29.1 \pm 10.7$	$1.99 \pm 2.12$	$11.2 \pm 6.14$	$19.5 \pm 10.5$
1.8-2.0	$38 \pm 16.2$	$1.83 \pm 1.67$	$17.8 \pm 9.44$	$20.8 \pm 17.9$
2.0-2.2	$24.7 \pm 21.4$	$-3.41 \pm 2.2$	$1.73 \pm 9.02$	$47.8 \pm 29.8$
2.2-2.4	$6.8 \pm 32.3$	$1.16 \pm 2.87$	$-14.5 \pm 18.6$	$17.7 \pm 32.6$
$M_{Had}$	$\pi$	$\pi^0$	$K$	$K_s$
1.0-1.2	$3.84 \pm 1.51$	$4.18 \pm 3.45$	$5.57 \pm 2.23$	$3.07 \pm 3.49$
1.2-1.4	$13.2 \pm 3.11$	$15.8 \pm 8.26$	$21.7 \pm 5.47$	$6.52 \pm 5.1$
1.4-1.6	$9.97 \pm 3.19$	$31.1 \pm 8.68$	$21.5 \pm 5.05$	$14 \pm 8.39$
1.6-1.8	$1.93 \pm 4.02$	$35.1 \pm 11.2$	$22.2 \pm 8.17$	$3.34 \pm 6.35$
1.8-2.0	$9.45 \pm 7.43$	$30.7 \pm 15.3$	$16 \pm 11.8$	$11.1 \pm 9.72$
2.0-2.2	$5.6 \pm 5.66$	$12.4 \pm 26$	$7.94 \pm 14.5$	$17.1 \pm 14.3$
2.2-2.4	$6.67 \pm 13.3$	$2.49 \pm 33.9$	$-8.48 \pm 25.2$	$39.1 \pm 24.5$

Table 13.7: WPBR (in  $10^{-6}$ ) results after the weights are applied.

$M_{Had}$	0.6-0.8	0.8-1.0	1.0-1.2
MC Mean	2.0	2.0	2.78
Data Mean	2.0	2.0	$2.88 \pm 0.16$
$M_{Had}$	1.2-1.4	1.4-1.6	1.6-1.8
MC Mean	3.02	3.21	3.36
Data Mean	$2.68 \pm 0.27$	$3.19 \pm 0.16$	$3.54 \pm 0.21$
$M_{Had}$	1.8-2.0	2.0-2.2	2.2-2.4
MC Mean	3.44	3.45	3.45
Data Mean	$3.47 \pm 0.26$	$4.11 \pm 0.25$	$6.68 \pm 23.9$

Table 13.8: Parameterization of truncated hadronic multiplicity in signal MC and data after the weights are applied.

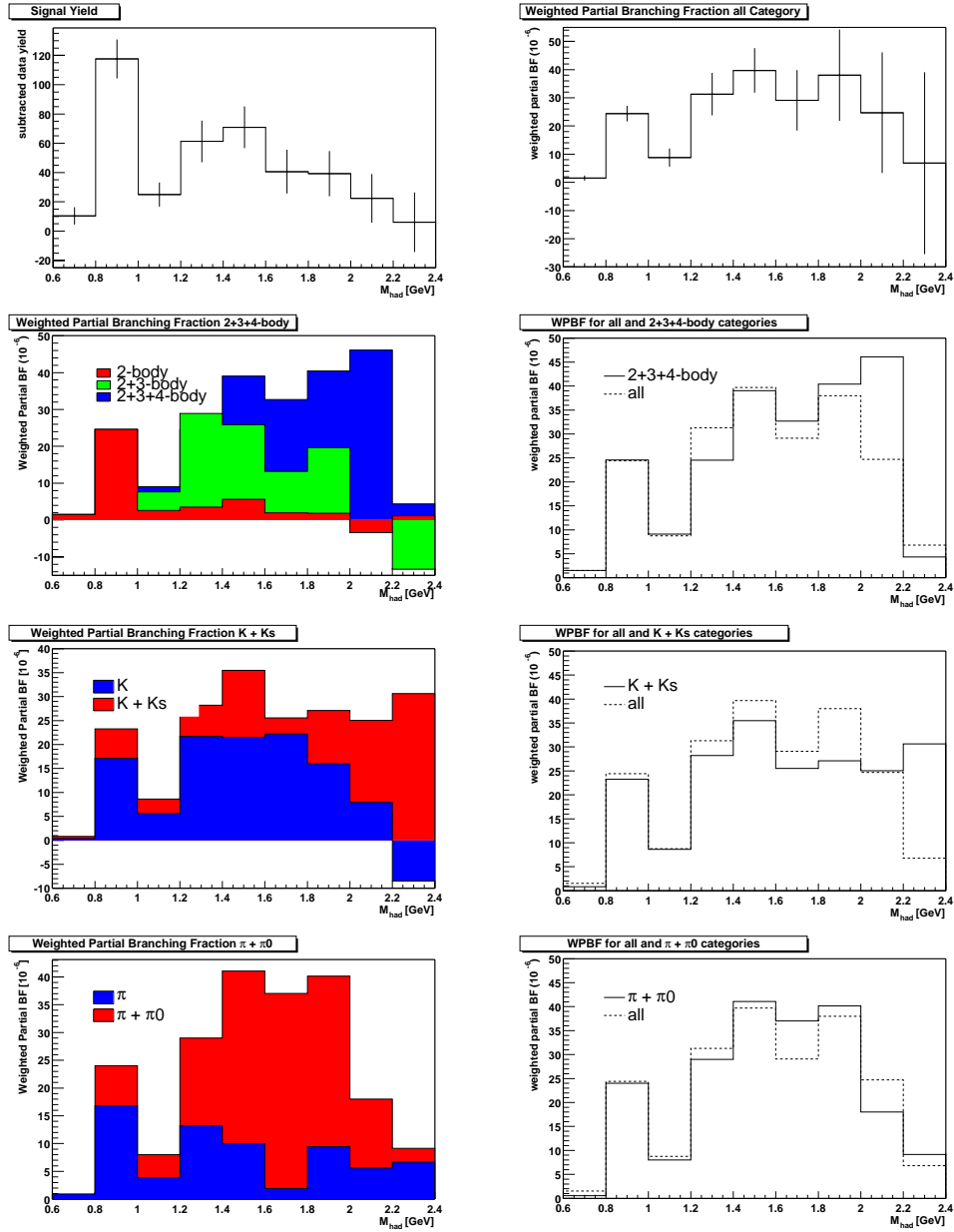


Figure 13.7: Signal yield and WPBF for the all the categories with  $\pi^0$  (2 iterations) and 2 body weight. When the error is shown is just a statistical error.

$M_{Had}$	$(2b/3b)_{corr}^{data}$	$(2b/3b)_{corr}^{MC}$	$(2b/3b)_{raw}^{data}$	$(2b/3b)_{raw}^{MC}$
1.0-1.2	$0.51 \pm 0.40$	0.36	$0.92 \pm 0.71$	0.65
1.2-1.4	$0.14 \pm 0.08$	0.20	$0.22 \pm 0.12$	0.31
1.4-1.6	$0.28 \pm 0.13$	0.15	$0.44 \pm 0.19$	0.24
1.6-1.8	$0.18 \pm 0.21$	0.14	$0.23 \pm 0.27$	0.19
1.8-2.0	$0.10 \pm 0.11$	0.14	$0.18 \pm 0.19$	0.24
2.0-2.2	$-1.91 \pm 9.53$	0.13	$-3.2 \pm 16$	0.21
2.2-2.4	$-0.08 \pm 0.22$	0.13	$-0.19 \pm 0.49$	0.29

Table 13.9: Ratios of 2/3-body for  $M_{Had}$  above  $1.0 \text{ GeV}/c^2$  for data and Monte Carlo after weights are applied.

$M_{Had}$	$(4b/3b)_{corr}^{data}$	$(4b/3b)_{corr}^{MC}$	$(4b/3b)_{raw}^{data}$	$(4b/3b)_{raw}^{MC}$
1.0-1.2	$0.29 \pm 0.23$	0.05	$0.37 \pm 0.27$	0.068
1.2-1.4	$-0.17 \pm 0.19$	0.22	$-0.088 \pm 0.093$	0.11
1.4-1.6	$0.66 \pm 0.39$	0.50	$0.39 \pm 0.22$	0.30
1.6-1.8	$1.73 \pm 1.33$	0.87	$1.1 \pm 0.86$	0.58
1.8-2.0	$1.17 \pm 1.17$	1.13	$0.62 \pm 0.60$	0.60
2.0-2.2	$26 \pm 130$	1.15	$13 \pm 63$	0.56
2.2-2.4	$-1.23 \pm 2.65$	1.14	$-1.0 \pm 2.1$	0.93

Table 13.10: Ratios of 4/3-body for  $M_{Had}$  above  $1.0 \text{ GeV}/c^2$  for data and Monte Carlo after weights are applied.

$M_{Had}$	$(K_S/K)_{corr}^{data}$	$(K_S/K)_{corr}^{MC}$	$(K_S/K)_{raw}^{data}$	$(K_S/K)_{raw}^{MC}$
0.6-1.0	$0.38 \pm 0.12$	0.500	$0.18 \pm 0.06$	0.24
1.0-1.6	$0.48 \pm 0.23$	0.497	$0.23 \pm 0.11$	0.25
1.6-2.0	$0.38 \pm 0.33$	0.503	$0.21 \pm 0.20$	0.35
2.0-2.4	$-115 \pm -6.81e + 03$	0.505	$16 \pm 180$	0.40
0.6-2.2	$0.55 \pm 0.21$	0.500	$0.26 \pm 0.076$	0.24
0.6-2.4	$0.95 \pm 0.42$	0.500	$0.33 \pm 0.093$	0.25

Table 13.11: The ratios for the  $K$  and  $K_S$  final state categories as a function of  $M_{Had}$ . The  $\pi^0$  (two iterations) and 2 body weight is applied.

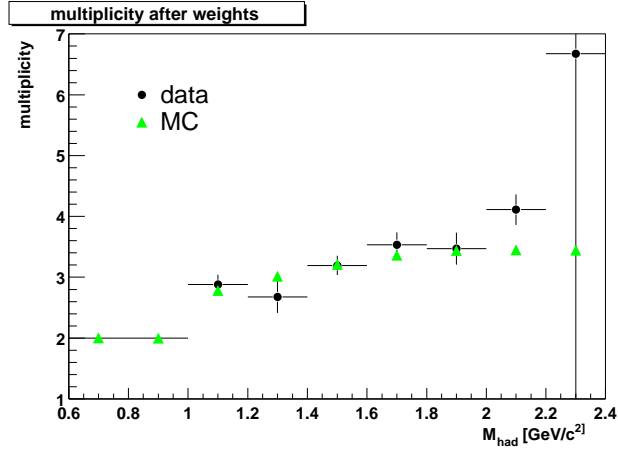


Figure 13.8: Truncated hadronic multiplicity in signal MC and data after weighting.

$M_{Had}$	$(\pi^0/\pi)_{corr}^{data}$	$(\pi^0/\pi)_{corr}^{MC}$	$(\pi^0/\pi)_{raw}^{data}$	$(\pi^0/\pi)_{raw}^{MC}$
0.6-1.0	$0.40 \pm 0.15$	0.50	$0.22 \pm 0.094$	0.31
1.0-1.6	$1.89 \pm 0.57$	1.91	$1.1 \pm 0.31$	1.1
1.6-2.0	$5.77 \pm 4.53$	2.39	$4.4 \pm 3.6$	1.5
2.0-2.4	$1.21 \pm 3.60$	2.40	$0.86 \pm 2.2$	1.5
0.6-2.2	$2.20 \pm 0.68$	0.95	$0.92 \pm 0.2$	0.43
0.6-2.4	$2.02 \pm 0.85$	0.98	$0.9 \pm 0.22$	0.44

Table 13.12: The ratios for the  $\pi^0$  and  $\pi$  final state categories as a function of  $M_{Had}$ . The  $\pi^0$  (two iterations) and 2 body weight is applied.

category	weight
1. $\pi^0$	$1.9 \pm 0.4$
2. <i>2-body</i>	$0.38 \pm 0.10$
3. $\pi^0$	$0.79 \pm 0.18$

Table 13.13: The weights used along with their statistical errors, listed according to category and in the order applied.

$M_{Had}$	plus	minus	error
1.0-1.2	2.7	2.9	2.9
1.2-1.4	4.5	6.3	6.3
1.4-1.6	2.2	3.2	3.2
1.6-1.8	3.8	5.6	5.6
1.8-2.0	1.7	2.3	2.3
2.0-2.2	3.1	4.5	4.5
2.2-2.4	1.6	2.1	2.1

Table 13.14: The percent change of the signal efficiencies obtained with the weights changed by plus or minus 1 sigma. The systematic error used is the larger of the two changes.

$M_{Had}$	$WPBF \pm stat \pm syst \pm model$
0.6-0.8	$1.52 \pm 0.876 \pm 0.27 \pm 0.15$
0.8-1.0	$24.4 \pm 2.76 \pm 2.0 \pm 2.4$
1.0-1.2	$8.77 \pm 3.22 \pm 2.18 \pm 1.2$
1.2-1.4	$31.3 \pm 7.53 \pm 4.68 \pm 3.1$
1.4-1.6	$39.7 \pm 7.93 \pm 5.88 \pm 4.0$
1.6-1.8	$29.1 \pm 10.7 \pm 4.38 \pm 2.9$
1.8-2.0	$38.0 \pm 16.2 \pm 6.77 \pm 3.8$
2.0-2.2	$24.7 \pm 21.4 \pm 5.98 \pm 2.5$
2.2-2.4	$6.8 \pm 32.3 \pm 12.0 \pm 0.68$

Table 13.15: The weighted partial branching fractions with statistical and systematic errors for the *all* final state category.

# Chapter 14

## Inclusive Branching Fractions

In this chapter we describe the method for calculating the  $b \rightarrow s\gamma$  Branching Fraction from the measured partial Branching Fractions. Preliminary results are calculated, although the treatment of the model dependent errors will not be dealt with fully here. A more complete treatment is under discussion within the *BABAR* experiment.

For comparison with results from other experiments, and with theoretical predictions, we also present plots of our results in terms of the photon energy in the rest frame of the  $B$ :

$$E_\gamma^B = \frac{M_B^2 - M_{Had}^2}{2M_B} \quad (14.1)$$

This variable is completely equivalent to  $M_{Had}$ . Our 200 MeV/ $c^2$  bins in  $M_{Had}$  convert into  $E_\gamma^B$  bins with variable widths ranging from 27 to 87 MeV/ $c^2$ . The resolution on  $M_{Had}$  of  $\approx 10$  MeV/ $c^2$ , which is shown in Chapter 7.2.2, converts into an  $E_\gamma^B$  resolution of 1-5 MeV/ $c^2$  which is 10 $\times$  better than the intrinsic resolution of the calorimeter, and almost 100 $\times$  better than the resolution on the photon energy in the  $\Upsilon(4S)$  rest frame,  $E_\gamma^*$ , which is smeared by the momentum of the  $B$  in the center-of-mass frame,  $p_B \approx 300$  MeV/ $c$ . Table 14.1 shows the numerical conversion between  $M_{Had}$  and  $E_\gamma^*$  (and vice-versa) according to the kinematical equation given above.

### 14.1 Branching Fraction Formula

The branching fraction (BF) is determined by weighting the PBFs by the fraction of the total final states that are measured:

$$BF_i = \frac{PBF_{i,j}}{f_{i,j}}, \quad (14.2)$$

$M_{Had}$	$E_\gamma^B$	$M_{Had}$	$E_\gamma^B$
0.650	2.60	0.6	2.606
0.975	2.55	0.8	2.579
1.216	2.50	1.0	2.545
1.416	2.45	1.2	2.504
1.592	2.40	1.4	2.454
1.750	2.35	1.6	2.398
1.895	2.30	1.8	2.333
2.029	2.25	2.0	2.261
2.156	2.20	2.1	2.222
2.275	2.15	2.2	2.182
2.388	2.10	2.3	2.139
2.496	2.05	2.4	2.095
2.600	2.00	2.5	2.048

Table 14.1: Table showing the conversion between recoil hadronic mass and  $E_\gamma^B$ , the photon energy in the B rest frame. The units are GeV.

where  $PBF_{i,j}$  is the partial branching fraction in the  $i^{\text{th}}$   $M_{Had}$  bin and  $j^{\text{th}}$  final state category, and  $f_{i,j}$  is the fraction of  $b \rightarrow s\gamma$  final states which we reconstruct in our analysis for the  $j^{\text{th}}$  final state category in that  $M_{Had}$  bin. This gives us a BF spectrum as a function of  $M_{Had}$ . The inclusive branching fraction is obtained by summing or fitting this spectrum.

There is some dependence on the  $b \rightarrow s\gamma$  BF in the PBF expression which we need to remove. The  $PBF_{i,j}$  expression:

$$PBF_{i,j} = \frac{N_{i,j}^{Sig}}{\varepsilon_{i,j} 2N_{BC}}, \quad (14.3)$$

where  $\varepsilon_{i,j}$  is the signal efficiency for the  $i^{\text{th}}$   $M_{Had}$  bin and  $j^{\text{th}}$  final state category,  $N_{BC} = 22.7 \times 10^6$  is the number of  $B\bar{B}$  events in our data sample and  $N_{i,j}^{Sig}$  is the yield measured in data less the yield from the  $B\bar{B}$  and cross-feed events.  $N_{i,j}^{Sig}$  thus depends linearly on the cross-feed yield. The cross-feed yield is scaled to the data luminosity using the BF( $b \rightarrow s\gamma$ ) predicted by theory. Thus, if we make explicit the dependence on the BF on the cross-feed yield in Equation 14.2, we can solve the first order equation, and write the BF as:

$$BF_i = \frac{(N_{i,j}^{DATA} - N_{i,j}^{BB})}{(\varepsilon_{i,j}^{sig} + \varepsilon_{i,j}^{xfeed}) 2N_{BC} f_{i,j}} \quad (14.4)$$

where  $N_{i,j}^{DATA}$  and  $N_{i,j}^{BB}$  are the yield in data and BB events,  $\varepsilon_{i,j}^{sig}$  and  $\varepsilon_{i,j}^{xfeed}$  are the signal and cross-feed efficiencies. The cross-feed efficiency is not a very interesting quantity, it is mainly a convenient way to take out the dependence of the BF in scaling the cross-feed yield to the data luminosity. It is defined as the cross-feed yield (cross-feed peaking component) divided by the generated events, the same denominator as is used for the signal efficiency. The values for the cross-feed efficiency for the *all* final state category are listed in Table 14.2.

Note that each final state category can give a value for the BF in each  $M_{Had}$  bin, although we will present results for the *all* final state category only (due to the small statistics for the individual different final state categories). The other categories were used to investigate and correct for differences between the data and Monte Carlo in the PBF.

$M_{Had}$	<i>all</i>
0.6–0.8	$0.07 \pm 0.50$
0.8–1.0	$0.23 \pm 0.03$
1.0–1.2	$0.63 \pm 0.22$
1.2–1.4	$0.56 \pm 0.20$
1.4–1.6	$0.39 \pm 0.24$
1.6–1.8	$0.39 \pm 0.23$
1.8–2.0	$0.48 \pm 0.27$
2.0–2.2	$-0.16 \pm 0.51$
2.2–2.4	$2.11 \pm 0.69$

Table 14.2: Cross-feed efficiencies (in %) for the *all* final state category, in 200 MeV/ $c^2$  bins of the hadronic mass.

## 14.2 Final State Fractions

The crucial element in determining the inclusive branching fraction is estimating the final state fractions; the fraction of generated events for the  $j=all$  category,  $f_{i,all}$ , in the  $i^{\text{th}}$   $M_{Had}$  bin, from now on referred to as just  $f_i$ . This is the fraction of all possible final states that our 12 reconstructed final states represent. It is used to effectively correct the  $\varepsilon_i$  to obtain the efficiency for finding any  $b \rightarrow s\gamma$  event.

The  $f_i$ s can be easily obtained from the Monte Carlo at the generator level. The values for the *all* final state category are listed in Table 14.3. In the following

we will use these  $f_i$ s to calculate the BF in each  $M_{Had}$  bin.

$M_{Had}$	$all$
0.6–0.8	75
0.8–1.0	75
1.0–1.2	66.4
1.2–1.4	64.8
1.4–1.6	55.2
1.6–1.8	44.9
1.8–2.0	35.2
2.0–2.2	27.3
2.2–2.4	21.5
average	51.7

Table 14.3: The  $f_i$ s in percent, at the generator level, for the *all* final state category, in 200 MeV/ $c^2$  bins of the hadronic mass.

We would like to understand how well the Monte Carlo represents the final state fractions, although it is not straight forward. We have already seen that the multiplicity in data and Monte Carlo is not the same. We have corrected for that by weighting the Monte Carlo signal efficiencies in the calculation of the PBF's, but these differences will also affect the  $f_i$ s. There also could be uncertainties in the composition of the Monte Carlo itself, especially at high  $M_{Had}$  where there is not much experimental knowledge.

We can investigate the contributions to the fraction of events that we do not measure,  $1 - f_i$ , i.e. the missing fraction. There are several contributions to this factor:

- $K_L$  final states,
- Final states with  $> 1\pi^0$ , where states with  $2\pi^0$  are the largest contribution,
- Final states with  $> 3\pi$  (hadronic multiplicity “ $\geq 5$ -body”),
- Final states with an  $\eta$  or  $\eta'$ ,
- Other more exotic states, such as  $s\bar{s}$ .

Table 14.4 lists the missing fractions,  $(1 - f_i)$ , broken into the above categories derived from the signal Monte Carlo. We do not assign any errors to these numbers here, although in a complete treatment we should estimate the errors for

the different contributions.

	Hadronic Mass						
	1.0-1.2	1.2-1.4	1.4-1.6	1.6-1.8	1.8-2.0	2.0-2.2	2.2-2.4
$K_L$	25	25	25	25	25	25	25
$2\pi^0$	4.0	4.5	5.3	5.6	4.9	4.0	3.3
$> 3\pi$		0.3	4.5	10.8	18.0	21.9	24.0
$\eta/\eta'$	4.6	5.0	7.6	8.7	9.4	10.3	11.1
$s\bar{s}s$			1.2	2.9	4.2	6.2	7.4
Other		0.4	1.2	2.1	3.3	5.3	7.7
Total	33.6	35.2	44.8	55.1	64.8	72.7	78.5

Table 14.4: Percent generator missing fractions.

Below we discuss briefly what we know about the above categories and how we would start to assign errors to the missing fractions.

We have investigated differences between the MC and data, and corrected for them in the signal efficiency used to calculate the partial branching fractions. This is possible since we are comparing measured quantities in the data against MC predictions. It is more complicated to extend these corrections to quantities which are not measured.

Specifically, in Section 12.11, Table 12.27 and Table 12.24, we see disagreement between data and MC ratios of different categories of final states. We see that there are more final states with a  $\pi^0$  in the data than in the MC (higher  $\pi^0/\pi$  ratio in data than in MC), and that there are less final states with *2-body* events in the data than in the MC (lower *2/3-body* ratio in data than in MC). These measurements are with respect to the twelve final states used in our analysis. It is not clear how to extend these relations to other categories not measured, such as modes with  $2\pi^0$ s or *5-body* modes.

One might assume that since we see a higher  $\pi^0/\pi$  fraction in the data, there should be a higher  $2\pi^0/(\pi + \pi^0)$  fraction as well, but as seen in the discussion in Section 11.3.2, for certain modes the fraction of modes with  $2\pi^0$ s should decrease as the  $1\pi^0$  fraction increases. This is not a complete discussion, but only illustrates how the relationship between modes that we do and don't measure is not straight forward.

There is perhaps information to be gained from the difference in multiplicity between data and MC. What we see is that there is fewer *2-body* final states in data than in MC (the *2/3-body* ratio is lower in data than in MC). One could

look at the multiplicity distribution, event yield versus multiplicity, in the data and try to extend it out beyond  $4$ -body. Although, the distribution consists of just three points in the data, and it is not obvious how much we can rely on the MC shape to extend it.

The one place where we do have some information is the  $K_L$  category. We assume that the  $K_L$  contribution is the same as the  $K_S$  one, and from Table 12.26 we see that the data agree with the isospin expectation of  $K_S/K = 0.5$ . Therefore we assume that prediction of 25% for the  $K_L$  component of the missing fraction is reliable.

To make a better estimation of the errors on the missing fractions we would need to either measure more modes, or attempt to adjust the Monte Carlo generator parameters to better match the data. We can also consider running over a Monte Carlo sample composed of a sum of the resonant modes, instead of the non-resonant  $X_s\gamma$  MC, or some combination of both.

### 14.3 Inclusive Branching Fraction Results

Table 14.5 shows the inclusive BF with the statistical and systematic errors, although with no error assigned to the missing fractions. We consider all the systematic error sources as 100% correlated between  $M_{Had}$  bins, except for the errors from the fitting procedure, which we consider uncorrelated. The two contributions to the systematic error are also shown in the table. The errors of the sum have been computed taking into account the correlations between bins. The sum is very sensitive to the large statistical and systematic errors in the last two bins. Note that the statistical and systematic errors are on the same order for all of the bins. The last line in the table is the sum of the  $M_{Had}$  bins.

Table 14.6 shows the cumulative inclusive BF with the statistical and systematic errors in the  $M_{Had}$  range 0.6-2.4 GeV/ $c^2$ . To extend this over the full phase space we look at the fraction of the phase space that this region represents, as predicted by the Monte Carlo. In Section 2.4, Table 2.3, we see that the KN465 model predicts that 75% of the  $X_s\gamma$  final states falls in the  $M_{Had}$  range 1.0-2.4 GeV/ $c^2$ . If we add to that the 13% from the resonant  $K^*\gamma$  peak in the range  $M_{Had} = 0.6$ -1.0 GeV/ $c^2$ , we find that we measure 88% of the spectrum. We can therefore correct for this 12% and we obtain  $BF(b \rightarrow s\gamma) = (5.2 \pm 1.3 \pm 1.5) \times 10^{-4}$ .

Figure 14.1 shows plots of the BF as a function of the hadronic mass and plotted in terms of  $E_\gamma^B$  or  $M_{Had}$ . The errors shown are only statistical errors.

A better way to extrapolate from the measured to the full phase space would be to fit the  $M_{Had}$  distribution to the theoretical spectral function. The generator parameters could also be varied in the fit and the best fitting function used to integrate over all  $M_{Had}$ . This would not only provide a measurement of the HQET parameters and a better measurement of the BF, but also reduce the error in the BF compared to taking a straight sum over  $M_{Had}$  bins. The fitting method is not presented here since they are still under development within *BABAR* but a preliminary number for the inclusive branching fraction integrated over all  $M_{Had}$  is,  $(4.3 \pm 0.5 \pm 0.8 \pm 1.3) \times 10^{-4}$ , where the errors are statistical, systematic and model dependent (this includes a large error on the missing fractions) [28][29].

$M_{Had}$	$BF \pm stat \pm syst$	Syst. Error	
		Uncorrelated	Correlated
0.6–0.8	$2.27 \pm 1.32 \pm 0.50$	0.4	0.3
0.8–1.0	$36.3 \pm 4.0 \pm 4.7$	2.1	4.2
1.0–1.2	$14.2 \pm 4.4 \pm 4.0$	3.4	2.2
1.2–1.4	$47.1 \pm 10.4 \pm 8.5$	5.7	6.3
1.4–1.6	$69.9 \pm 13.3 \pm 12.5$	9.1	8.6
1.6–1.8	$63.6 \pm 21.6 \pm 11.5$	7.6	8.6
1.8–2.0	$98.2 \pm 38.3 \pm 20.0$	14.7	13.6
2.0–2.2	$94.5 \pm 88.0 \pm 24.8$	15.1	19.7
2.2–2.4	$33.4 \pm 62.8 \pm 59.3$	41.8	42.1
0.6–2.4	$459.5 \pm 118.1 \pm 116.3$	48.8	105.6

Table 14.5: Inclusive Branching Fraction in  $10^{-6}$  and their corresponding statistical and systematic error for each  $M_{Had}$  bin. The last two columns show for each bin how the systematic error breaks down into correlated and uncorrelated errors.

## 14.4 Comparison

We can compare our result for the inclusive BF,  $(5.2 \pm 1.3 \pm 1.3) \times 10^{-4}$ , with the measurements from other experiments. Table 1.2 is repeated here. It lists the measurements of the inclusive  $b \rightarrow s\gamma$  BF from other experiments, as well as our unofficial world average. The first error listed is the statistical error, and the second (and third) errors give the systematic uncertainties, including

$M_{Had}$	$BF \pm stat \pm syst$
0.6–0.8	$2.27 \pm 1.32 \pm 0.50$
0.6–1.0	$38.6 \pm 4.2 \pm 5.0$
0.6–1.2	$52.8 \pm 6.1 \pm 7.8$
0.6–1.4	$99.9 \pm 12.1 \pm 14.8$
0.6–1.6	$169.8 \pm 17.9 \pm 24.5$
0.6–1.8	$233.4 \pm 28.1 \pm 33.2$
0.6–2.0	$331.6 \pm 47.5 \pm 48.2$
0.6–2.2	$426.1 \pm 100.0 \pm 68.3$
0.6–2.4	$459.5 \pm 118.1 \pm 116.3$
total	$522.2 \pm 134.2 \pm 132.2$

Table 14.6: Cumulative Inclusive Branching Fraction in  $10^{-6}$ .

model dependence where this is quoted separately. The ALEPH measurement was done using Z-decays, and will not be specifically compared with.

Experiment	$\text{Br}(b \rightarrow s\gamma) \times 10^{-4}$
CLEO 2001 [9]	$3.21 \pm 0.43 \pm 0.27^{+0.18}_{-0.10}$
ALEPH 1998 [10]	$3.11 \pm 0.80 \pm 0.72$
BELLE 2001 [11]	$3.36 \pm 0.53 \pm 0.42 \pm 0.52$
Unofficial World Average	$3.24 \pm 0.34 \pm 0.35$

Table 14.7: Published measurements of the inclusive rate  $b \rightarrow s\gamma$ .

We see right away that the central value for our number is higher than the other measurements, although it does agree within the large errors. Summing in quadrature the statistical and systematic errors we obtain,  $BF(b \rightarrow s\gamma) = (5.22 \pm 1.88) \times 10^{-4}$ . One thing that we do which is not done in BELLE or CLEO is to weight the MC by the fragmentation differences (Chapter 13). The equivalent number to the one quoted above, but using the PBFs before the weighting we obtain a BF of  $4.3 \times 10^{-4}$ . This is in better agreement with the other experiments.

We also see that our statistical error (26%) is about double that of BELLE (16%) or CLEO (13%) while our data sample is much larger:  $21.7fb^{-1}$ , compared to  $5.8fb^{-1}$  for BELLE and  $9.1fb^{-1}$  for CLEO. As noted at the end of the previous section our statistical errors will decrease after performing a fit to the  $M_{Had}$  spectrum since more information is used in the determination of the BF.

However, this still will give us errors on the same order at the other experiments, which is due to differences in the analyzes.

The CLEO analysis is quite advanced and uses a combination of both the fully inclusive and semi-inclusive methods. They use four independent data samples obtained with different selection criteria which they combine with different weights, which increases significantly their statistics. They also use their large off-resonance data sample to subtract the continuum background. *BABAR* runs only 12% of the time off-resonance which is not a large enough sample to use for background subtraction in this analysis.

BELLE uses a similar semi-exclusive technique, although they reconstruct also 5-body modes which increases their measured channels from twelve to sixteen. They use a Super-Fox-Wolfram sideband to model the continuum background shape which has high statistics. They also have a much smaller statistical error on the peaking  $B\bar{B}$  background yield (20% compared to our on average 70%), which directly effects the statistical error on the BF.

Our systematic error (25%) is comparable to the others, BELLE (20%) and CLEO (30%). x

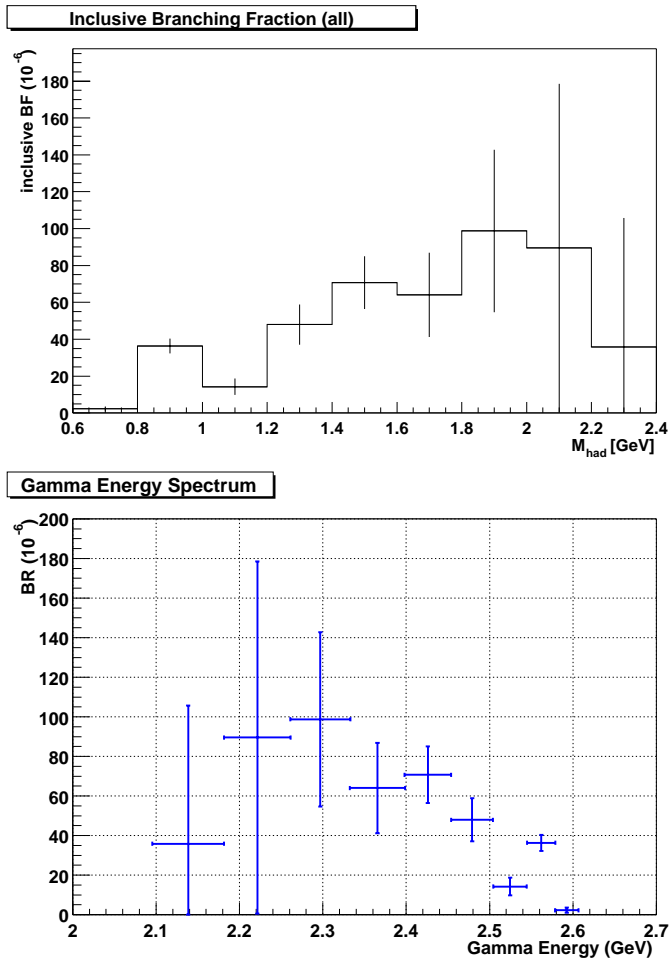


Figure 14.1: Upper plot: Inclusive branching fraction as a function of the hadronic mass. Lower plot: Inclusive branching fraction as a function of  $E_{\gamma}^B$ .

# Chapter 15

## Conclusions

We have investigated the radiative penguin process  $b \rightarrow s\gamma$  using a pseudo-reconstruction method. We reconstruct twelve exclusive final states with a kaon, one to three pions and an energetic photon.

We have applied a selection which makes use of a Fisher discriminant in order to reduce the background. The background comes from several sources; continuum,  $B\bar{B}$  and cross-feed events. Cross-feed is defined as the background coming either from signal final states which are not part of the twelve states we reconstruct, or incorrectly reconstructed final states. The background is an increasing function of the hadronic mass of the  $s$ -system (higher masses means more background). Moreover, the cross-feed and the  $B\bar{B}$  events have a peaking component in the signal region of the energy-substituted  $B$  mass,  $m_{\text{ES}}$ . The background subtraction performed to obtain the peaking signal event yield is complicated by the presence of the three different background components and their peaking shapes. The non-peaking component is subtracted in the fit to the data  $m_{\text{ES}}$  spectrum, while the peaking components are estimated in the Monte Carlo and explicitly subtracted from the peaking data yield. A detailed study of the fitting method is performed in the analysis.

After the background is subtracted, the partial branching fractions (PBFs) for the investigated final states are studied as a function of the hadronic mass. However, as we do not have enough statistics to make a mass dependent study of each final state alone, we measure the PBF for all the twelve states together which, effectively, is a weighted sum of the individual states. We correct for observed differences in data and Monte Carlo fragmentation which change the weights for each final state.

The partial branching fraction spectrum, shown in Figure 15.1 with statistical error bars, is the final measured quantity presented here. The systematic

errors, where the largest contribution comes from the background subtraction method, are of the same order as the statistical errors. The measured spectral shape matches theoretical predictions where only the  $K^*\gamma$  resonant peak is considered separately. The higher resonances are wide enough that they are overlapping and along with the non-resonant contributions are parameterized by a non-resonant spectral shape at hadronic masses above the  $K^*\gamma$  peak.

This is a large step toward the measurement of the inclusive branching fraction. To obtain the inclusive rate the fraction of final states we do not reconstruct must be approximated. To illustrate the method we take the value for this missing fraction from the Monte Carlo prediction and follow the calculation through to obtain a value of  $BF(b \rightarrow s\gamma)^{(0.6-2.4\text{GeV})} = (4.6 \pm 1.2 \pm 1.2) \times 10^{-4}$ , over our measured  $M_{Had}$  range of 0.6–2.4 GeV/ $c^2$ , where the first error is statistical and the second is systematic. Extending over the full phase space we obtain a value of  $BF(b \rightarrow s\gamma) = (5.2 \pm 1.3 \pm 1.3) \times 10^{-4}$ , which is consistent with the standard model prediction within the large errors. These values neglect a possibly quite large systematic error associated with the model dependence of the missing fractions. This is due to limited understanding of the high  $M_{Had}$  region of the Monte Carlo parameterization.

A more complete treatment of model dependent errors and a fit to the  $M_{Had}$  spectrum to perform a more precise measurement of the inclusive branching fraction is underway within the *BABAR* experiment. Preliminary results are expected during the summer of this year (2002).

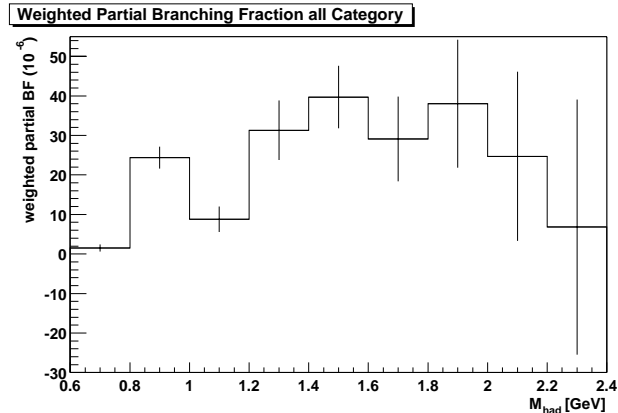


Figure 15.1: PBF for the *all* final state category as a function of  $M_{Had}$ .

# Appendix A

## The PDFs used in the fits

### A.1 Argus Background Distribution

The ARGUS distribution for the background shape defined:

$$A(m; m_0, c) = \frac{1}{N} \cdot m \sqrt{1 - (m/m_0)^2} \cdot \exp(c(1 - (m/m_0)^2)) \cdot \theta(m < m_0)$$

Note that  $m_0$  represents the kinematic upper limit for the constrained mass and is usually held fixed at half of the center of mass energy (nominally 5.29 GeV/ $c^2$  for Y(4S) events) in a fit. The minimum value of  $m_0$  must be  $\geq$  the maximum value of  $m$ . The parameter  $c$  is what is usually referred to as the Argus parameter or Argus shape parameter in the text.

### A.2 Crystal Ball Lineshape Distribution

The Crystal Ball lineshape distribution:

$$C(m; m_0, \sigma, \alpha, n) = \frac{1}{N} \cdot \begin{cases} \exp(-(m - m_0)^2/(2\sigma^2)) & , m > m_0 - \alpha\sigma \\ \frac{(n/\alpha)^n \exp(-\alpha^2/2)}{((m_0 - m)/\sigma + n/\alpha - \alpha)^n} & , m \leq m_0 - \alpha\sigma \end{cases}$$

is useful for fitting a radiative tail. It consists of a Gaussian signal peak matched to a power law tail. Note that the tail parameter,  $n$ , is not necessarily integer, and is usually held fixed in a fit: lower values generate a longer tail. The parameter  $\alpha$  determines the crossover point from the Gaussian distribution to the power law tail distribution, in units of the peak width,  $\sigma$ . Typical values for  $|\alpha|$  are 0.6–1.1. With  $\alpha > 0$  the tail is below the peak, and with a negative value and the two ranges switched the tail is above the peak.

# Appendix B

## Isospin Correction for $K_S \rightarrow \pi^0\pi^0$ in $K^*\gamma$

In the  $M_{Had}$  region 0.6 to 1.0 GeV/ $c^2$ , we use resonant  $K^*\gamma$  Monte Carlo as our signal Monte Carlo. This sample was generated in four separate requests for the four decay modes from  $B \rightarrow K^*\gamma$ , two for each charged ( $K^+\pi^0, K_S\pi^+$ ) and neutral ( $K\pi, K_S\pi^0$ ) B's. These specific decays were generated with some constraints. The  $K^*$  only decays to charged Kaons or  $K_S, K_L$  are not allowed. Also,  $K_S$ 's from the  $K^*$  only decay to  $\pi^+\pi^-$ , decays to  $\pi^0\pi^0$  are not generated.

In the inclusive  $X_s\gamma$  Monte Carlo which is used above 1.0 GeV/ $c^2$ , there are no constraints on the decays of the daughter particles of the  $X_s$ .

The Monte Carlo signal efficiency is defined as:

$$\epsilon_{i,j} = N_{i,j}^{reco} / N_{i,j}^{gen} \quad (\text{B.1})$$

where  $i = M_{Had}$  bin and  $j =$  final event category (*all, 2,3,4-body* etc.). The denominator  $N_{i,j}^{gen}$  is the total number of generated events in the full Monte Carlo sample for each value of  $i$  and  $j$ . These numbers were obtained by looking at the generator level fractions for each final state in each  $M_{Had}$  bin and multiplying by the total number of events in the Monte Carlo sample.

In our denominator we do not want to constrain the  $K_S$  decay, i.e. we want to include generated events for generic  $K_S$ , not just  $K_S \rightarrow \pi^+\pi^-$ . Therefore, in the  $K^*\gamma$  sample we need to correct the generated number of events in the specific Monte Carlo samples to obtain the total number of events that would be generated in a sample of  $B \rightarrow K^*\gamma, K^* \rightarrow K(K_S)$  (excluding  $K_L$ ). The  $X_s\gamma$  Monte Carlo does not need to be corrected.

The missing  $K_L$  factor will be added when we move from partial to inclusive branching fractions. Therefore we are measuring our PBF's with respect to modes with charged Kaons or  $K_S$ 's not generic neutral Kaons.

Below we will derive the factors needed to correct the  $K^*\gamma$  Monte Carlo for  $K_S \rightarrow \pi^0\pi^0$  for the different final state categories. The categories which need corrections are the *all*,  $\pi$ ,  $\pi^0$ , and  $K_S$  categories. The  $K$  category has no  $K_S$  modes in it to correct and there are no *3-* and *4-body* final states in the resonant region. The *2-body* category is equivalent to the *all* category.

## B.1 Four Resonant Modes

Here we list the four resonant modes with the their isospin factors:

$$B^0 \rightarrow K^{*0}\gamma : 1$$

$$K^{*0} \rightarrow K^+\pi^- : 2/3$$

$$K^{*0} \rightarrow K^0\pi^0 : 1/3$$

$$K^0 \rightarrow K_L : 1/2$$

$$K^0 \rightarrow K_S : 1/2$$

$$K_S \rightarrow \pi^+\pi^- : 2/3$$

$$K_S \rightarrow \pi^0\pi^0 : 1/3$$

$$B^+ \rightarrow K^{*+}\gamma : 1$$

$$K^{*+} \rightarrow K^+\pi^0 : 1/3$$

$$K^{*+} \rightarrow K^0\pi^+ : 2/3$$

$$K^0 \rightarrow K_L : 1/2$$

$$K^0 \rightarrow K_S : 1/2$$

$$K_S \rightarrow \pi^+\pi^- : 2/3$$

$$K_S \rightarrow \pi^0\pi^0 : 1/3$$

Remember that we want to correct for only for  $K_S \rightarrow \pi^0\pi^0$  not for  $K_L$ .

We first calculate what we have, i.e. the total fraction of decay modes that we use excluding the  $K_S \rightarrow \pi^0\pi^0$ , and then the missing fraction. What we want

is what we have plus the missing fraction.

The factor we are looking for will multiply the denominator of the efficiency, therefore it will be  $f_{\pi^0\pi^0} = (want/have)$ .

## B.2 Correction for the *all* final state category

Here we will calculate the correction factor for the *all* final state category.

What we have in the *all* category:

$$B^0(K^+\pi^-) + B^0(K_S(\pi^+\pi^-)\pi^0) + B^+(K^+\pi^0) + B^+(K_S(\pi^+\pi^-)\pi^+) = \\ (2/3) + (1/3)(1/2)(2/3) + (1/3) + (2/3)(1/2)(2/3) = 24/18 = have$$

What we add:

$$B^0(K_S(\pi^0\pi^0)\pi^0) + B^+(K_S(\pi^0\pi^0)\pi^+) = \\ (1/3)(1/2)(1/3) + (2/3)(1/2)(1/3) = 3/18 = add$$

What we want is what we have plus the added  $\pi^0\pi^0$  modes;  
 $have + add = 24/18 + 3/18 = 27/18 = want$

Therefore,

$$f_{\pi^0\pi^0}^{all} = (want/have) = (27/18)/(24/18) = 9/8$$

## B.3 Correction for the $\pi$ final state category

Here we will calculate the correction factor for the  $\pi$  final state category.

What we have in the  $\pi$  category:

$$B^0(K^+\pi^-) + B^+(K_S(\pi^+\pi^-)\pi^+) = \\ (2/3) + (2/3)(1/2)(2/3) = 16/18 = have$$

What we add:

$$B^+(K_S(\pi^0\pi^0)\pi^+) = \\ (2/3)(1/2)(1/3) = 2/18 = add$$

What we want is what we have plus the added  $\pi^0\pi^0$  modes;  
 $have + add = 16/18 + 2/18 = 18/18 = 1 = want$

Therefore,

$$f_{\pi^0\pi^0}^\pi = (\textit{want}/\textit{have}) = 1/(16/18) = 9/8$$

## B.4 Correction for the $\pi^0$ final state category

Here we will calculate the correction factor for the  $\pi^0$  final state category.

What we have in the  $\pi^0$  category:

$$B^0(K_S(\pi^+\pi^-)\pi^0) + B^+(K^+\pi^0) = \\ (1/3)(1/2)(2/3) + (1/3) = 8/18 = \textit{have}$$

What we add:

$$B^0(K_S(\pi^0\pi^0)\pi^0) = \\ (1/3)(1/2)(1/3) = 1/18 = \textit{add}$$

What we want is what we have plus the added  $\pi^0\pi^0$  modes;

$$\textit{have} + \textit{add} = 8/18 + 1/18 = 9/18 = \textit{want}$$

Therefore,

$$f_{\pi^0\pi^0}^{\pi^0} = (\textit{want}/\textit{have}) = (9/18)/(8/18) = 9/8$$

## B.5 Correction for the $K_S$ final state category

Here we will calculate the correction factor for the  $K_S$  final state category. We expect it to be 3/2, but let's check.

What we have in the  $K_S$  category:

$$B^0(K_S(\pi^+\pi^-)\pi^0) + B^+(K_S(\pi^+\pi^-)\pi^+) = \\ (1/3)(1/2)(2/3) + (2/3)(1/2)(2/3) = 6/18 = \textit{have}$$

What we add:

$$B^0(K_S(\pi^0\pi^0)\pi^0) + B^+(K_S(\pi^0\pi^0)\pi^+) = \\ (1/3)(1/2)(1/3) + (2/3)(1/2)(1/3) = 3/18 = \textit{add}$$

What we want is what we have plus the added  $\pi^0\pi^0$  modes;  
 $have + add = 6/18 + 3/18 = 9/18 = want$

Therefore,

$$f_{\pi^0\pi^0}^{K_S} = (want/have) = (9/18)/(6/18) = 3/2$$

# Appendix C

## Plots for the toy–MC studies

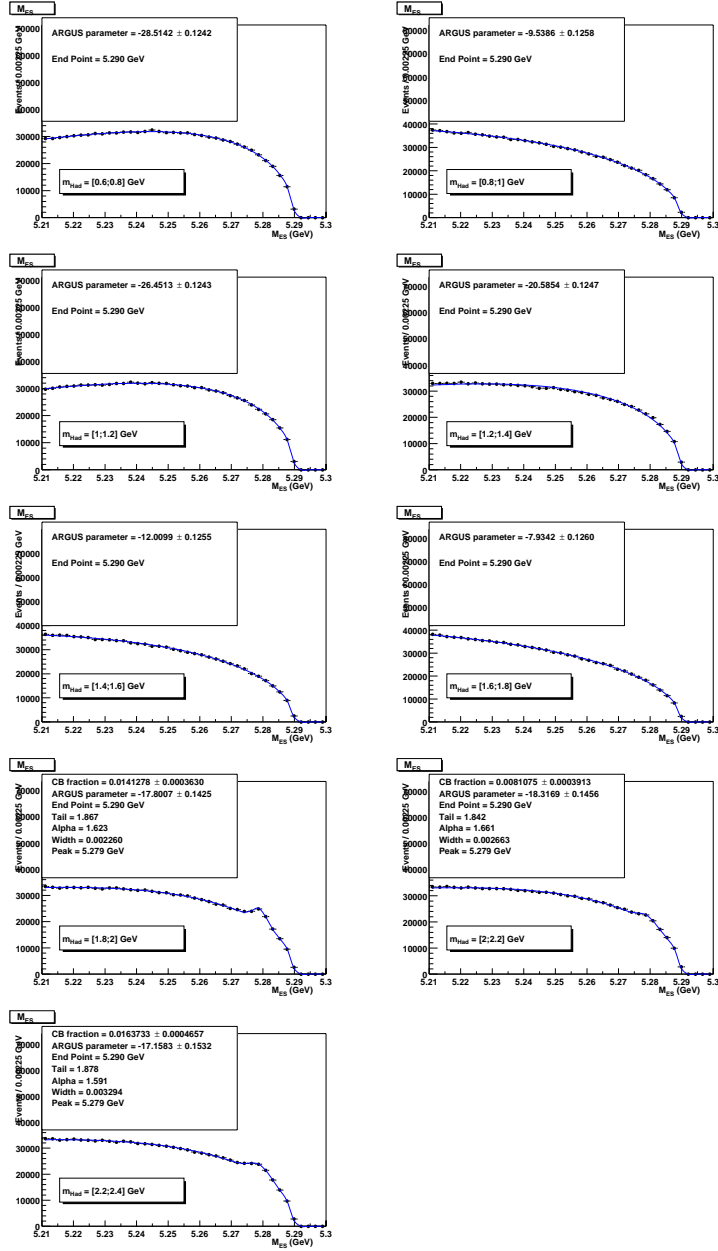


Figure C.1: Toy-background (toy-bb plus toy-cont) fits with a fixed CB and an Argus function. Free parameters: the normalization, the ratio among the CB and the Argus function and the Argus function shape.

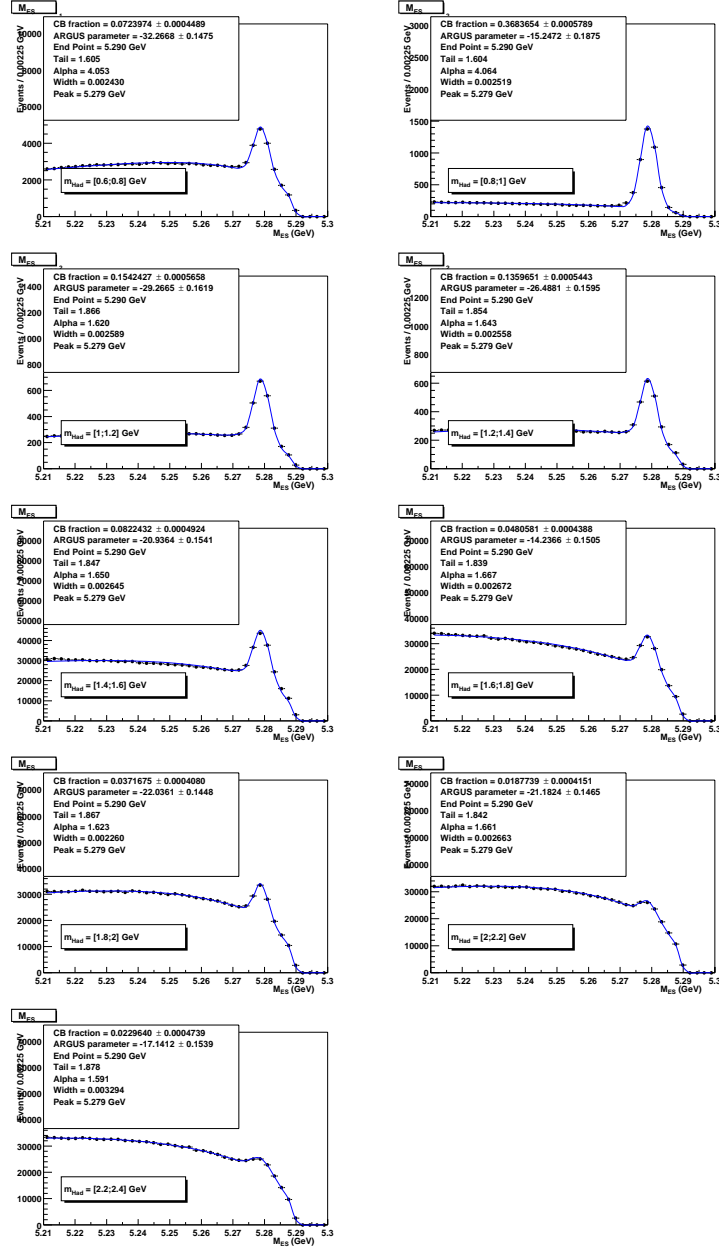


Figure C.2: Toy-data fits with a fixed CB and an Argus function. Free parameters: the normalization, the ratio among the CB and the Argus function and the Argus function shape.

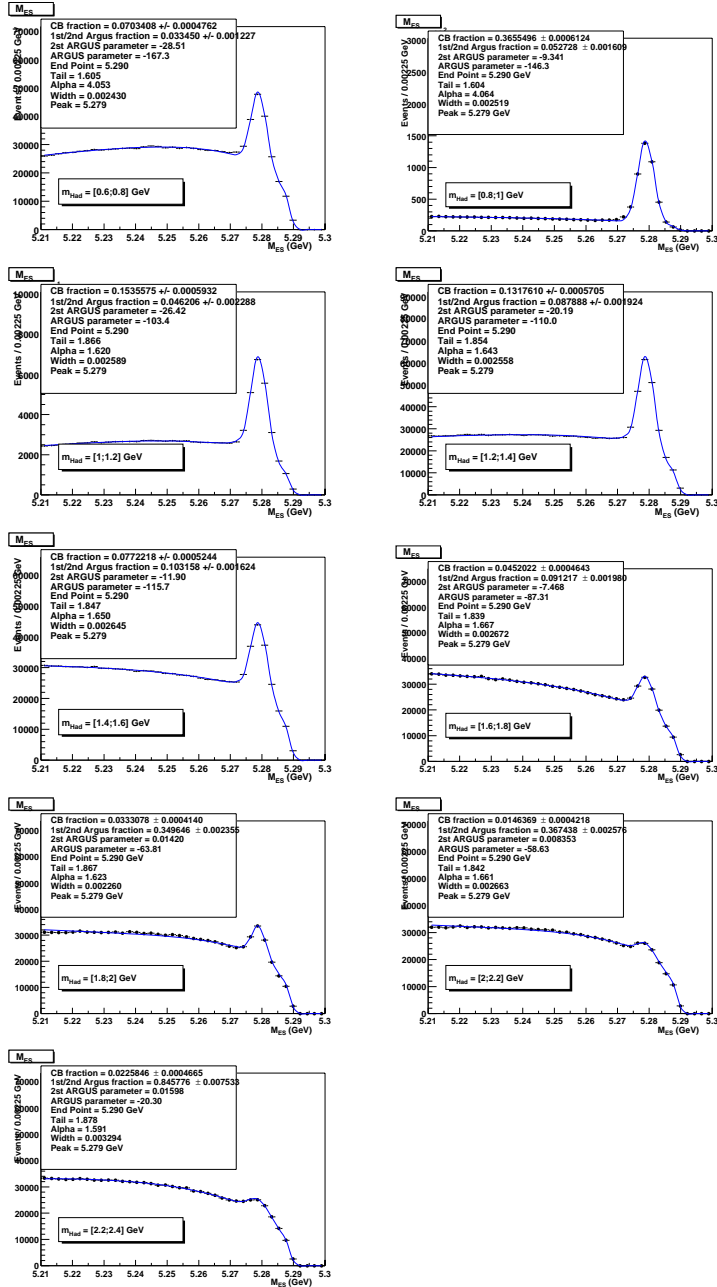


Figure C.3: Toy-data fits with a fixed CB and two Argus functions. Free parameters: the normalization, the ratio among functions and the Argus function shapes.

# Appendix D

## Plots for all the fits

### D.1 Signal Monte Carlo Fits

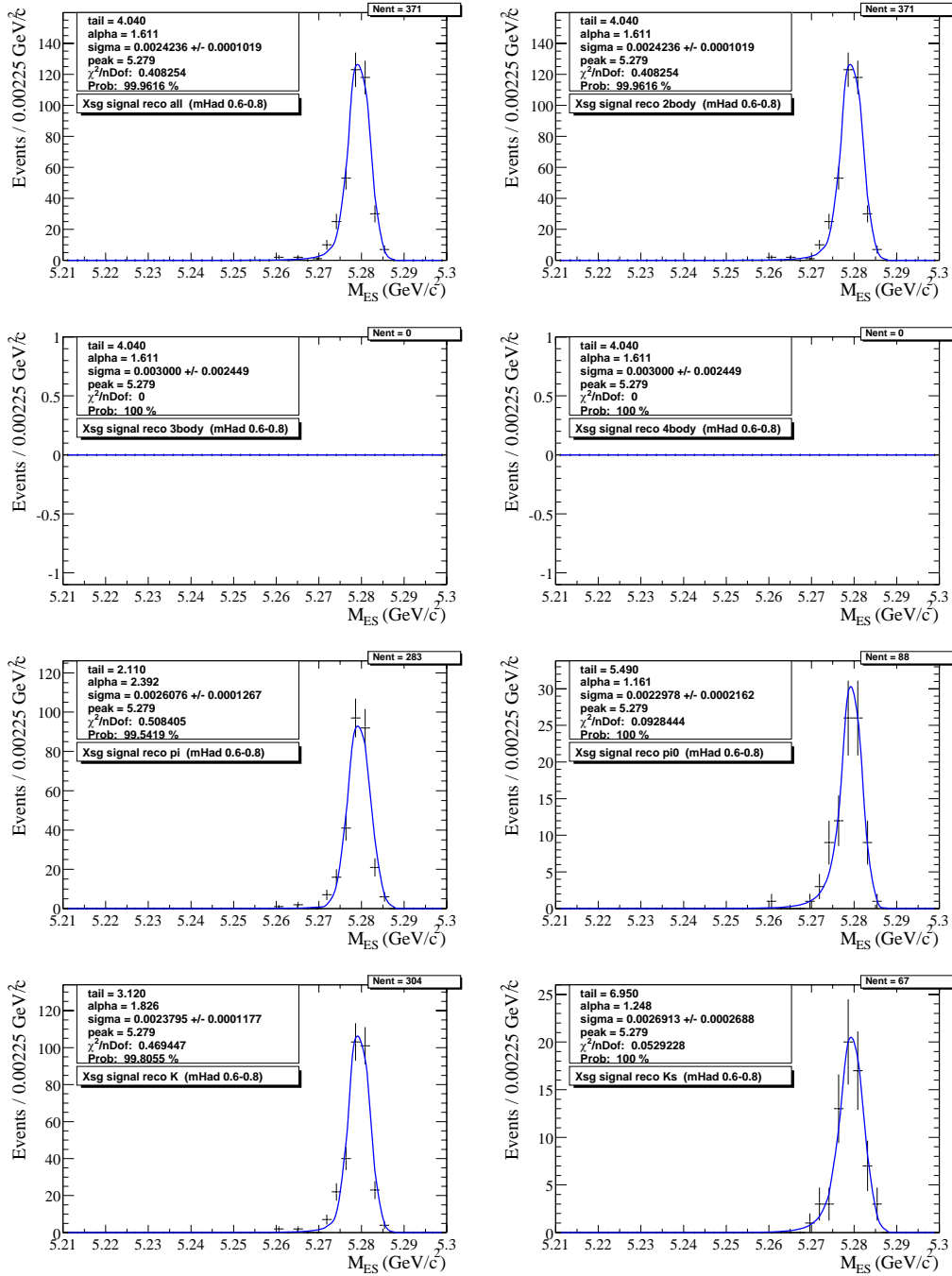


Figure D.1: MC signal fits for  $M_{Had} = 0.6-0.8 \text{ GeV}/c^2$ .

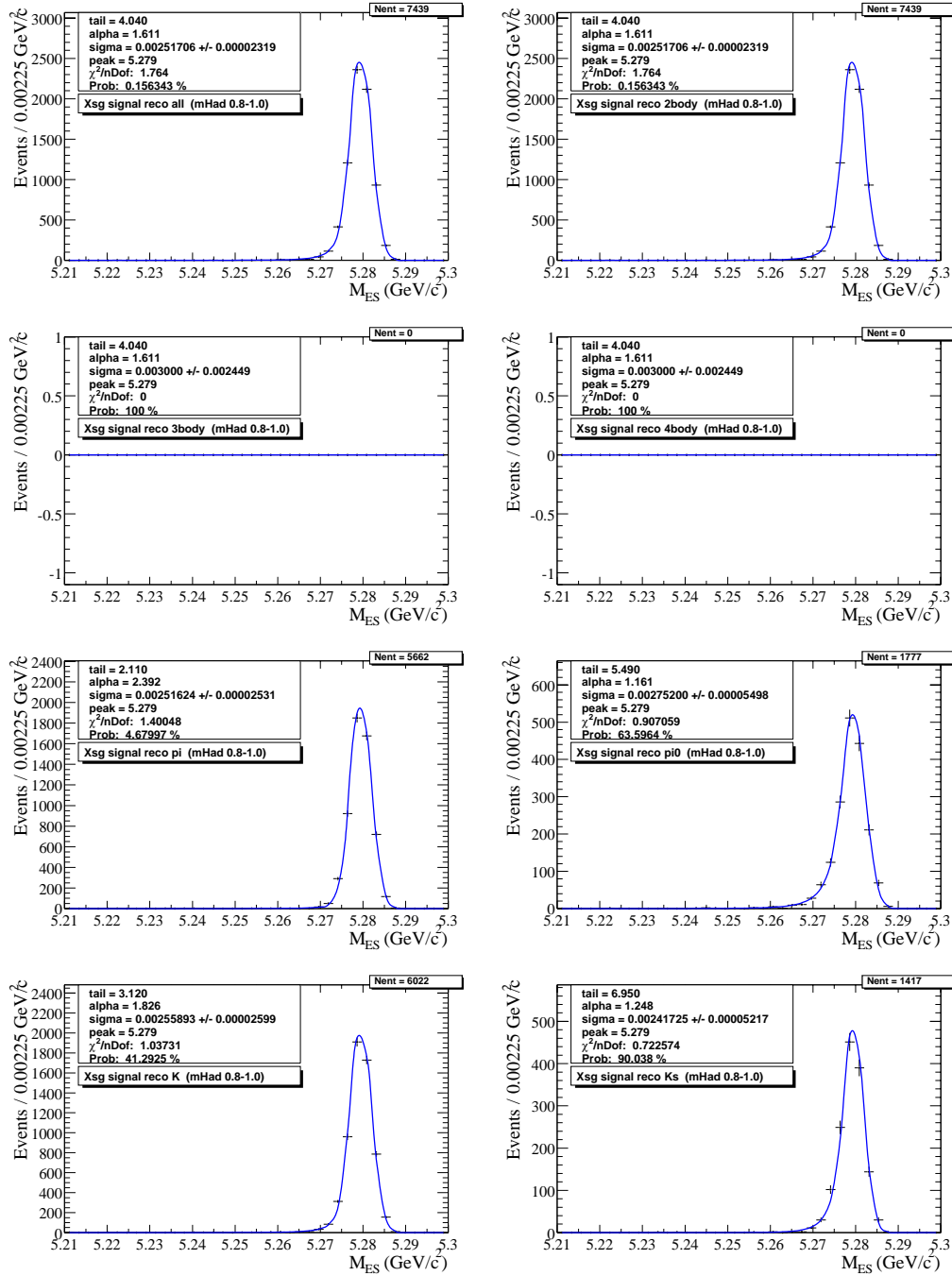


Figure D.2: MC signal fits for  $M_{Had} = 0.8-1.0 \text{ GeV}/c^2$ .

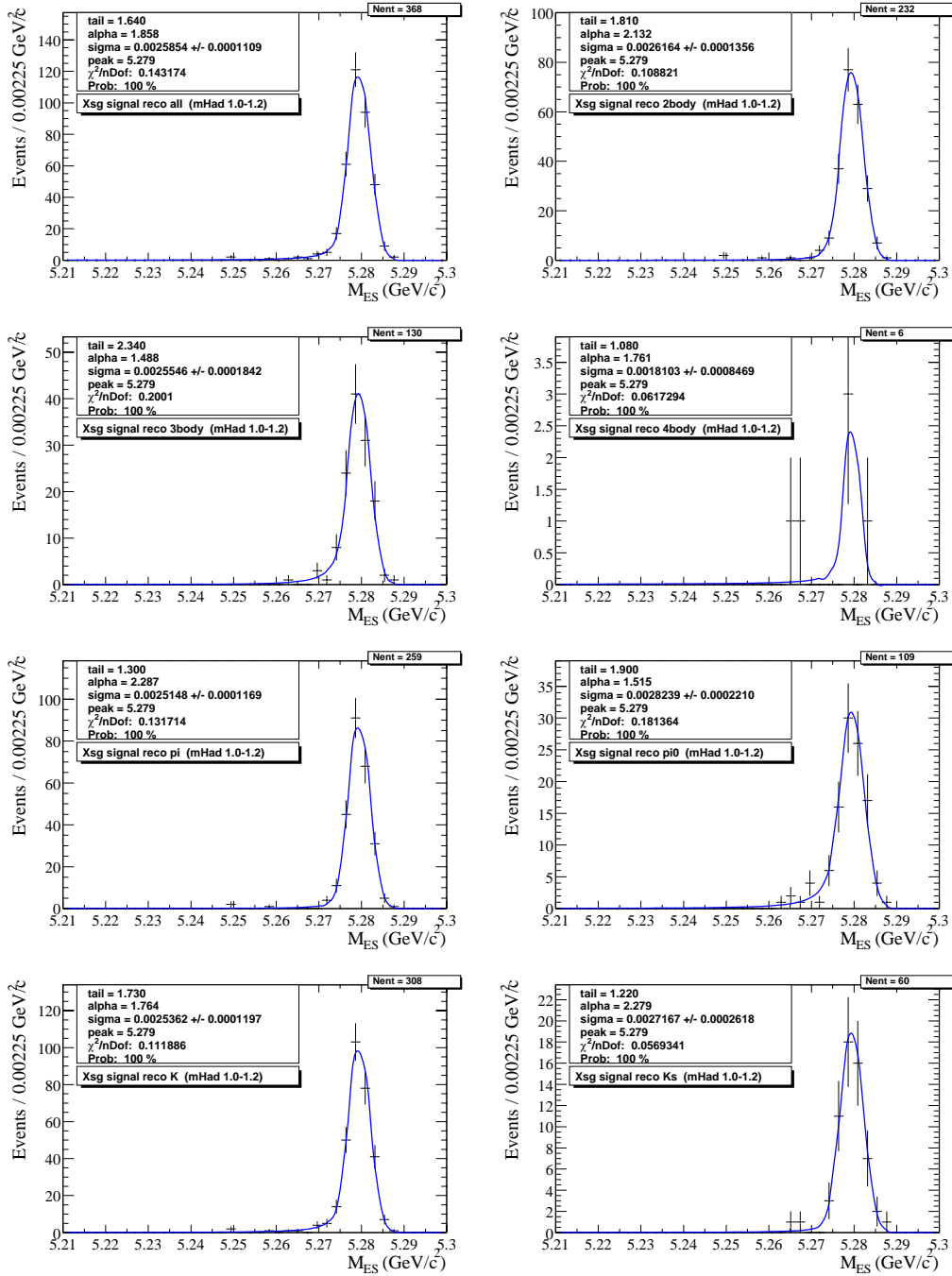


Figure D.3: MC signal fits for  $M_{Had} = 1.0-1.2 \text{ GeV}/c^2$ .

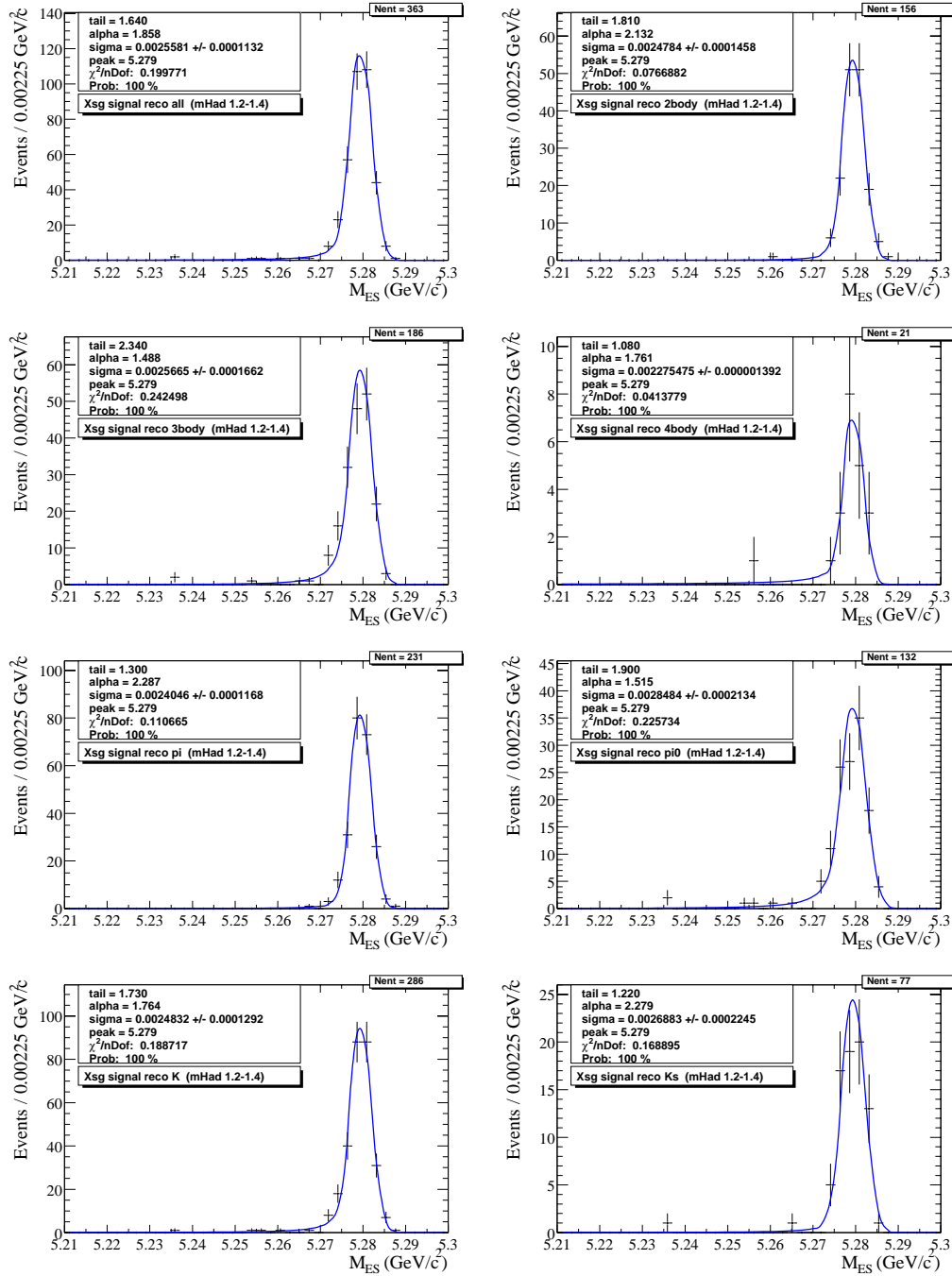


Figure D.4: MC signal fits for  $M_{Had} = 1.2-1.4 \text{ GeV}/c^2$ .

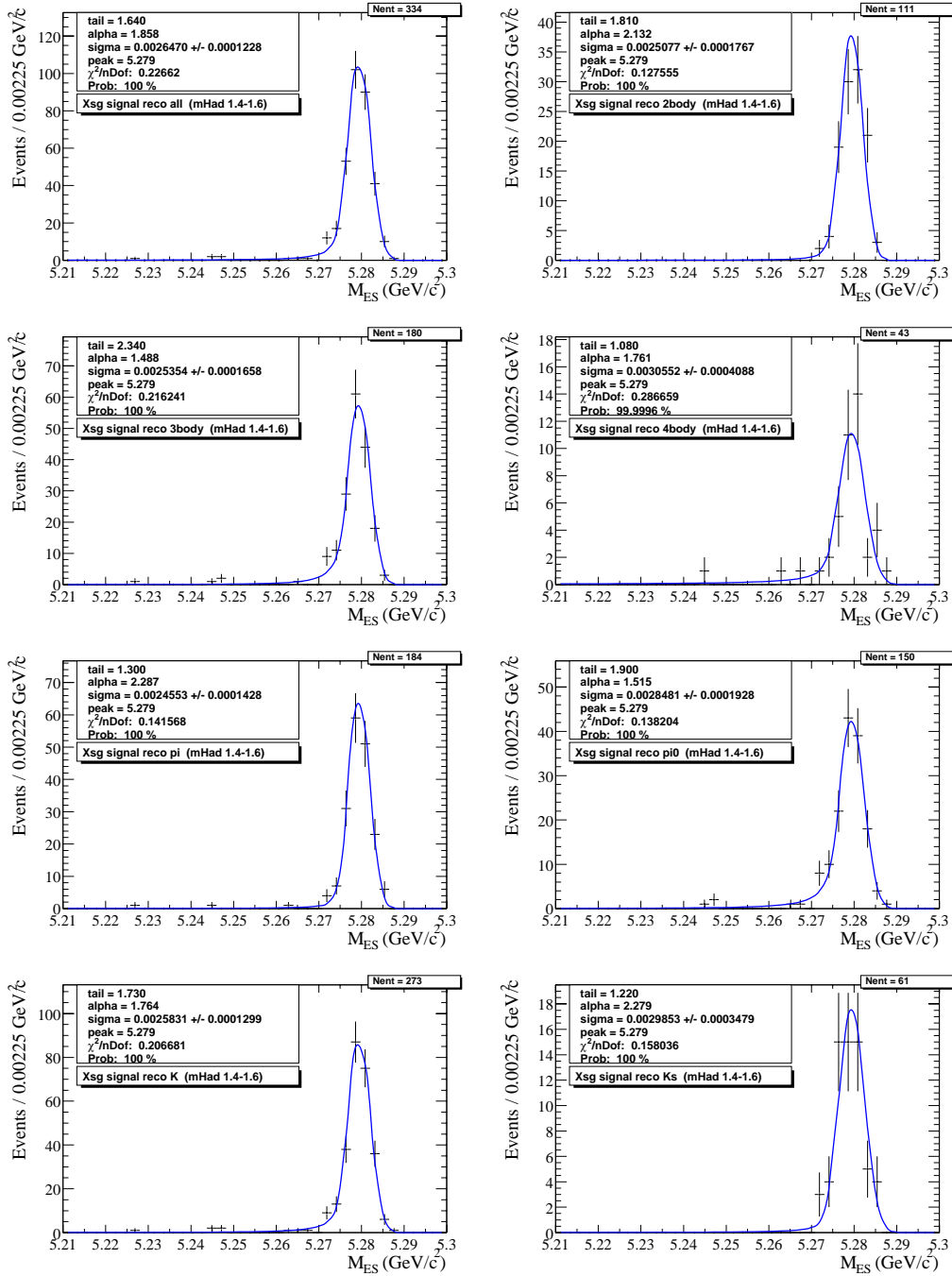


Figure D.5: MC signal fits for  $M_{Had} = 1.4-1.6 \text{ GeV}/c^2$ .

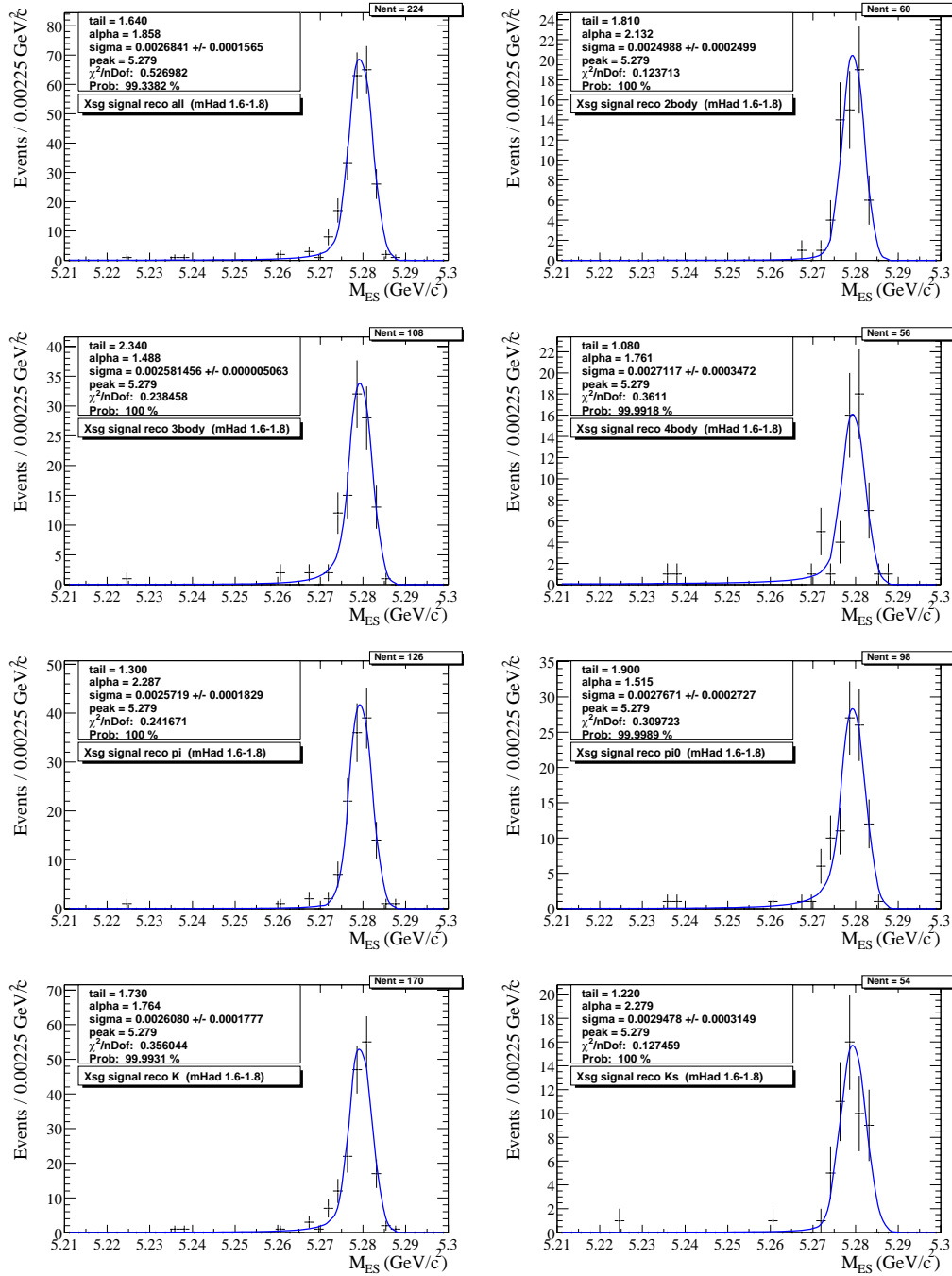


Figure D.6: MC signal fits for  $M_{Had} = 1.6-1.8 \text{ GeV}/c^2$ .

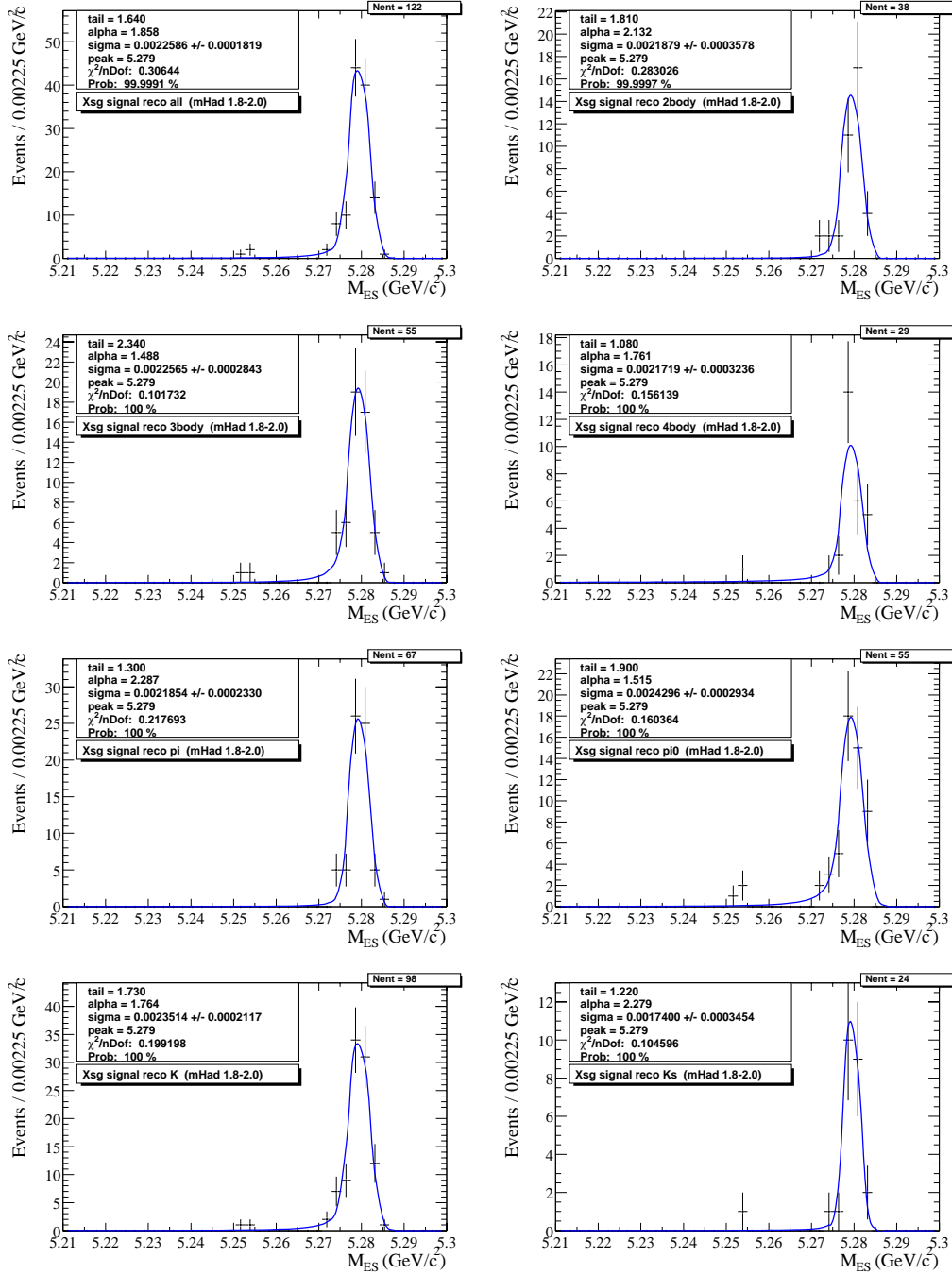


Figure D.7: MC signal fits for  $M_{Had} = 1.8-2.0$  GeV/ $c^2$ .

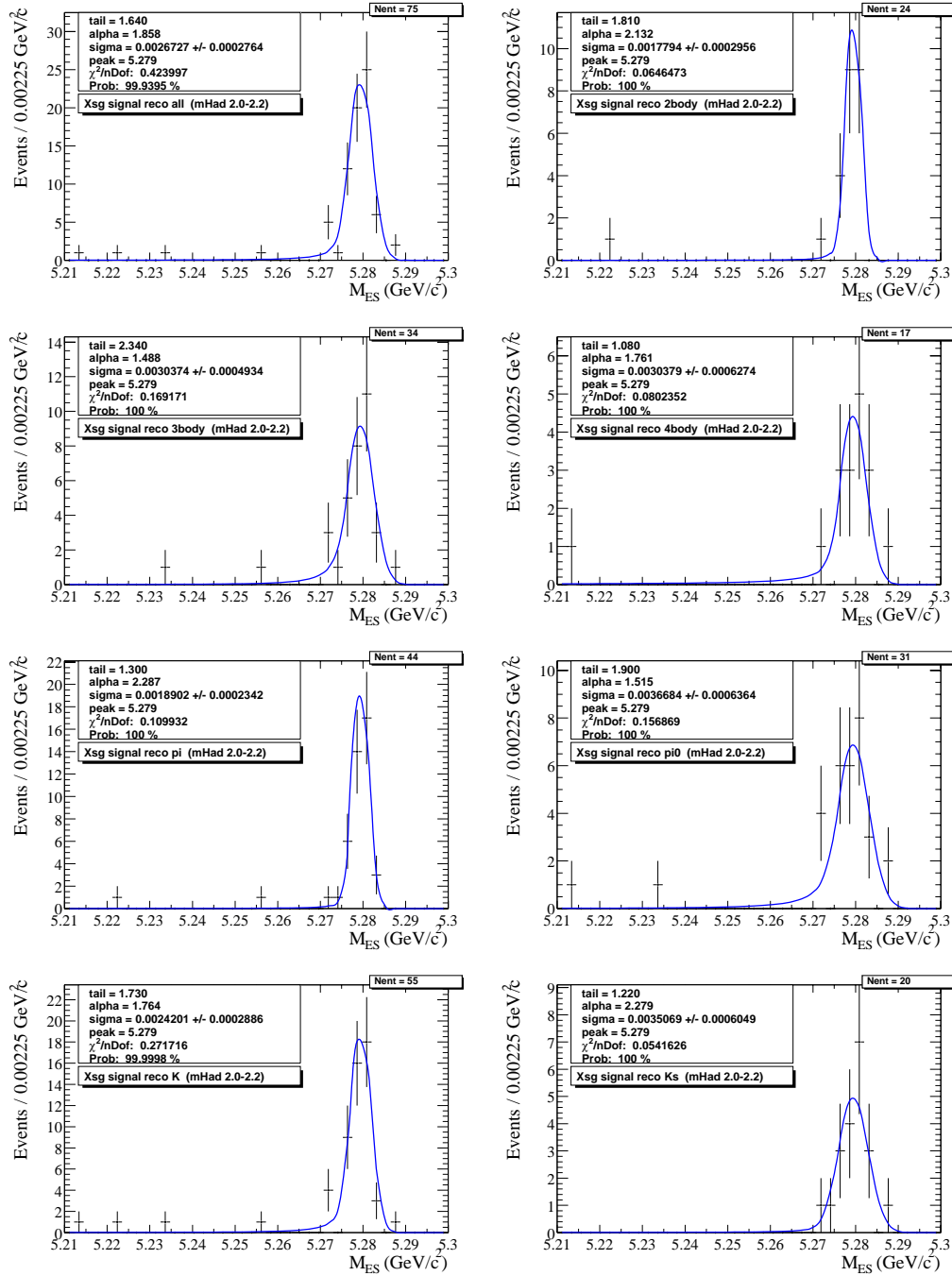


Figure D.8: MC signal fits for  $M_{Had} = 2.0-2.2 \text{ GeV}/c^2$ .

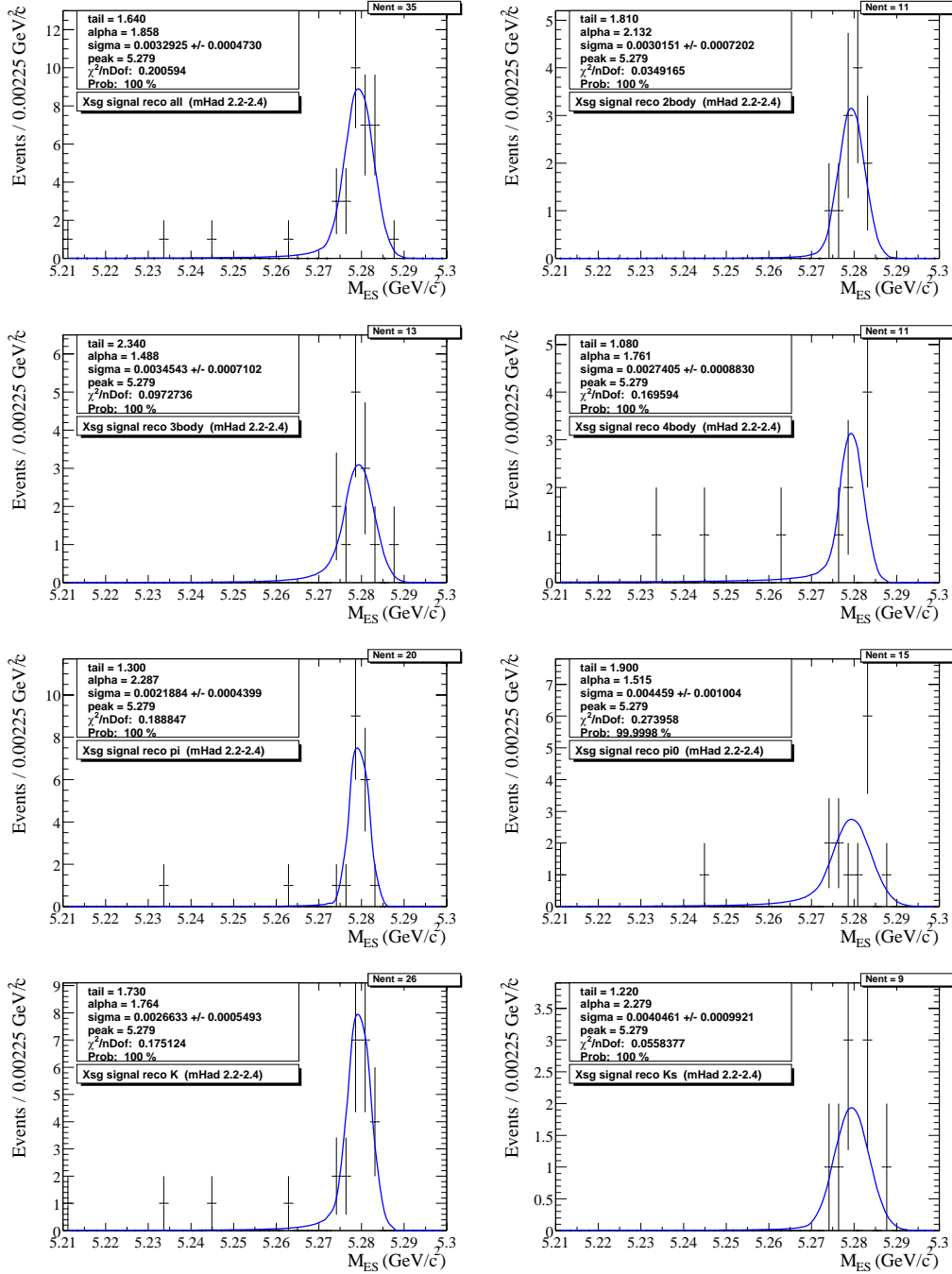


Figure D.9: MC signal fits for  $M_{Had} = 2.2-2.4 \text{ GeV}/c^2$ .

## D.2 Cross-Feed Monte Carlo Fits

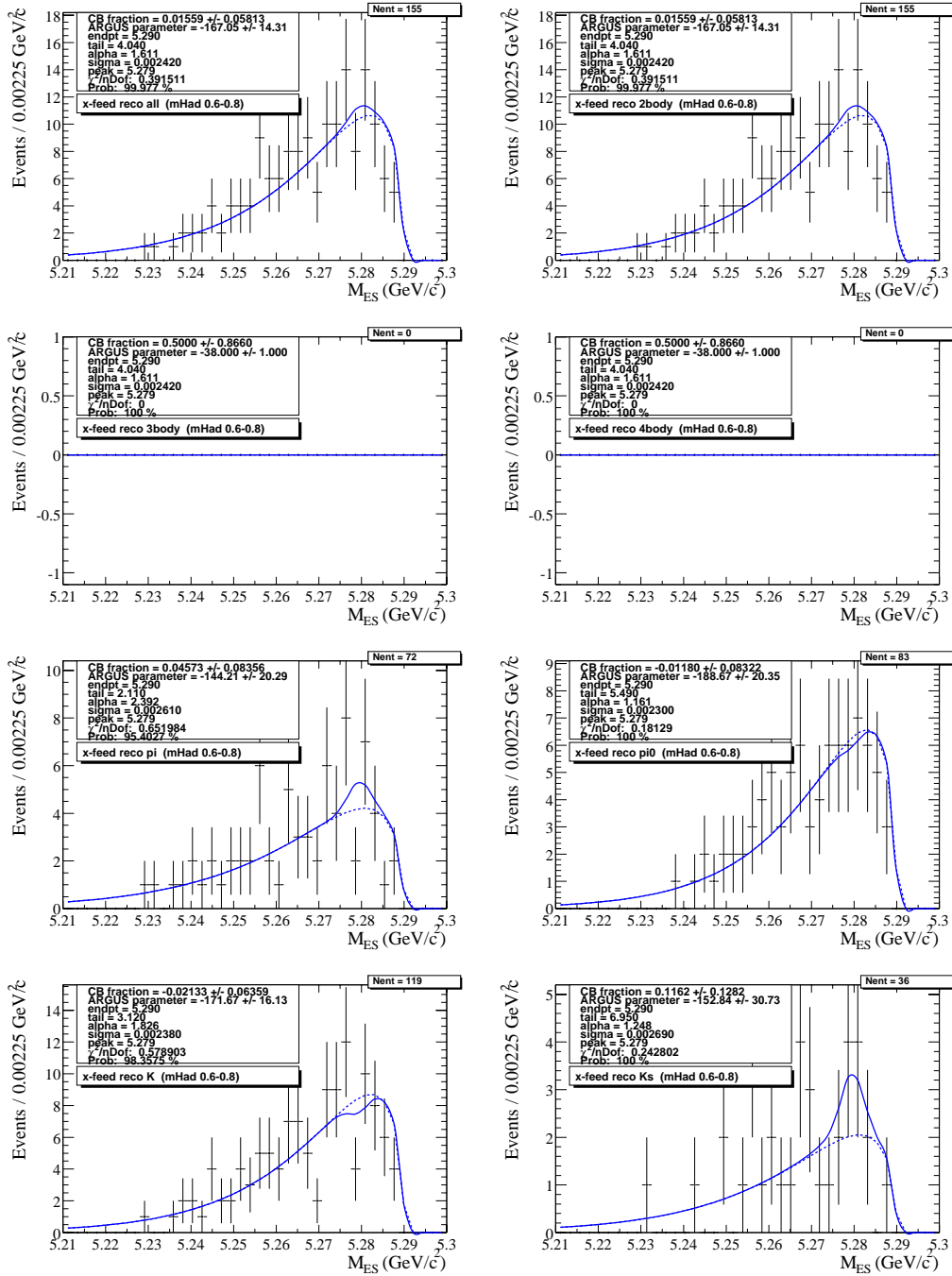


Figure D.10: MC cross-feed fits for  $M_{Had} = 0.6-0.8 \text{ GeV}/c^2$ .

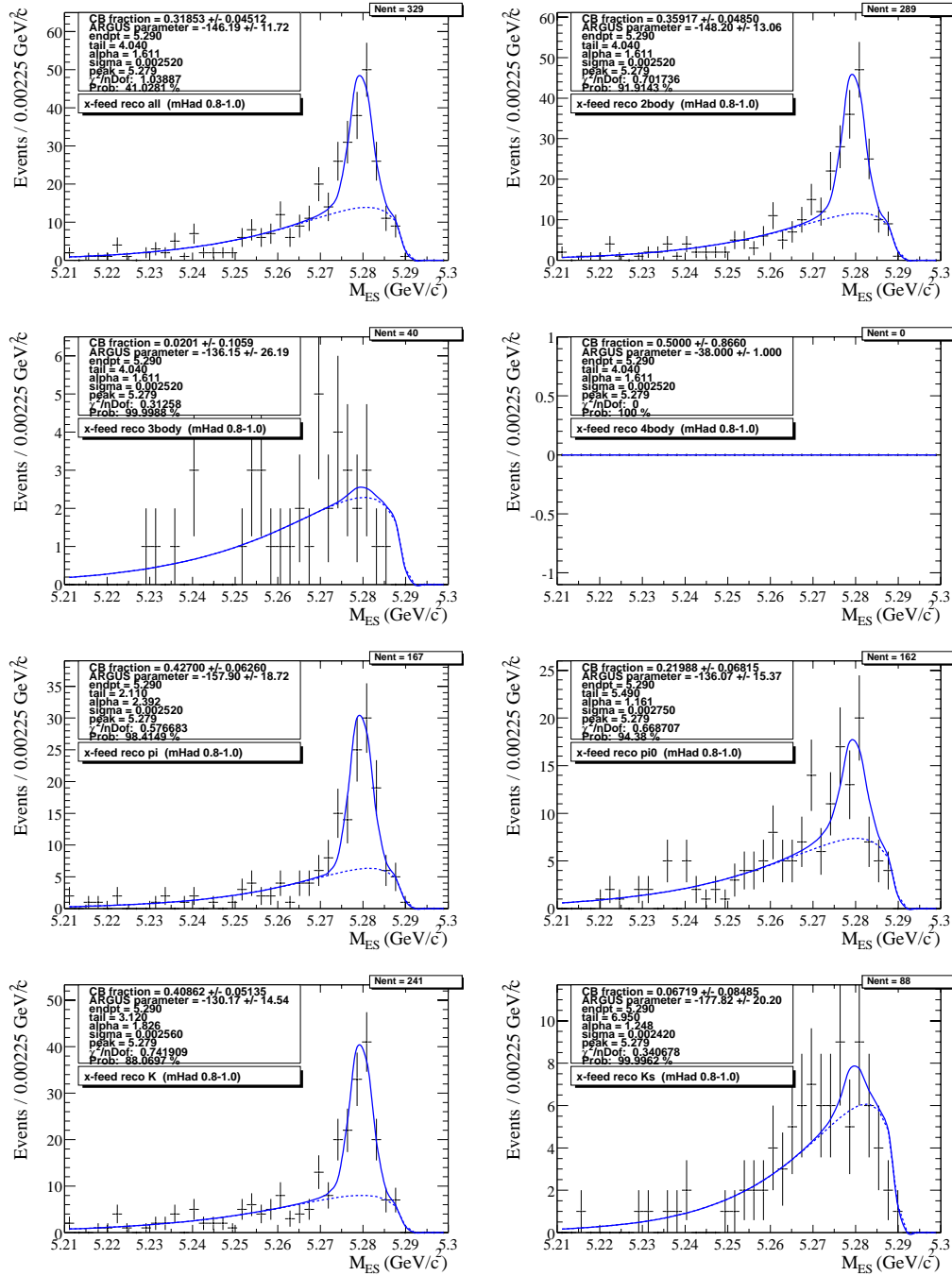


Figure D.11: MC cross-feed fits for  $M_{Had} = 0.8-1.0$   $\text{GeV}/c^2$ .

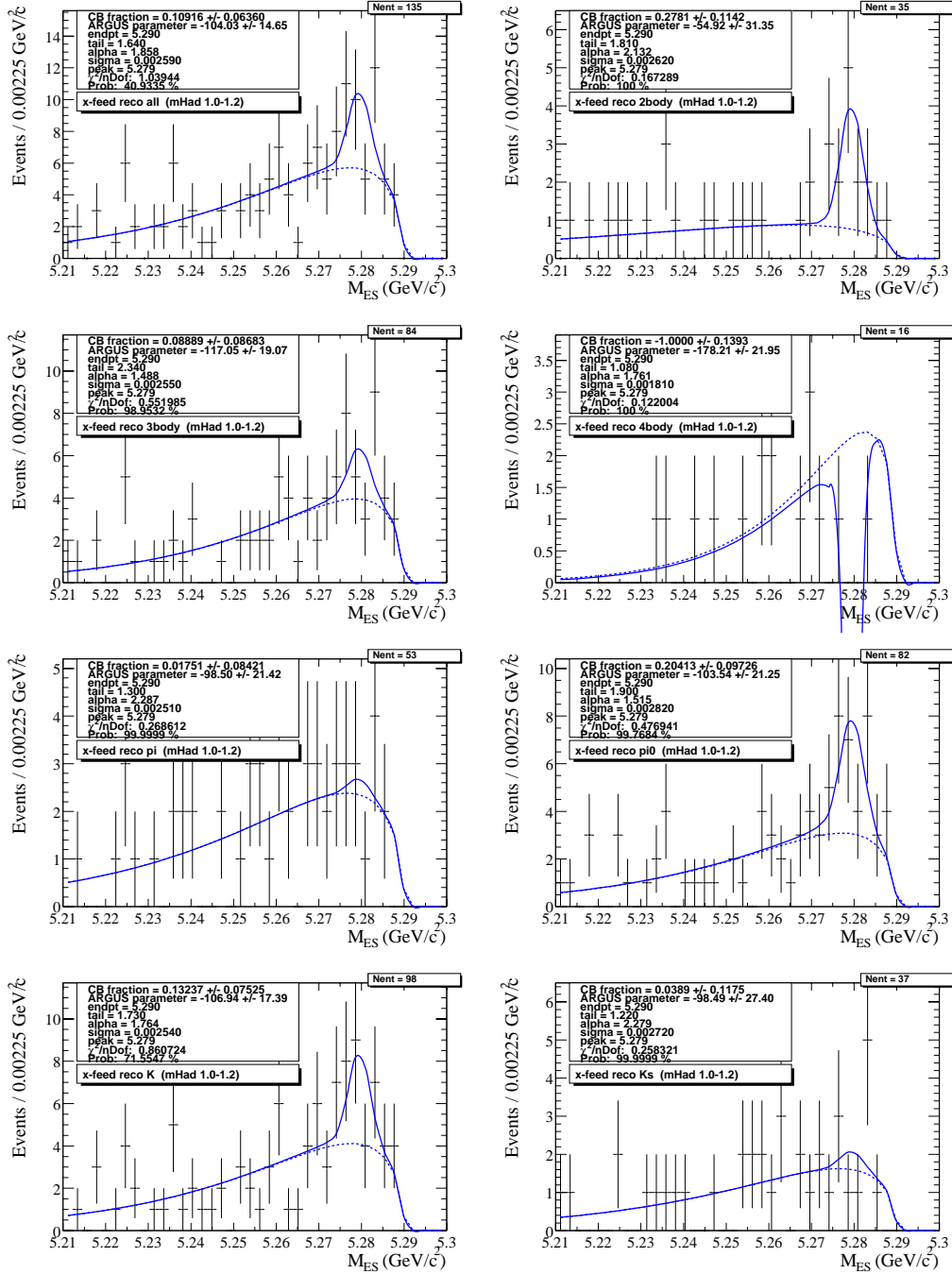


Figure D.12: MC cross-feed fits for  $M_{Had} = 1.0-1.2 \text{ GeV}/c^2$ .

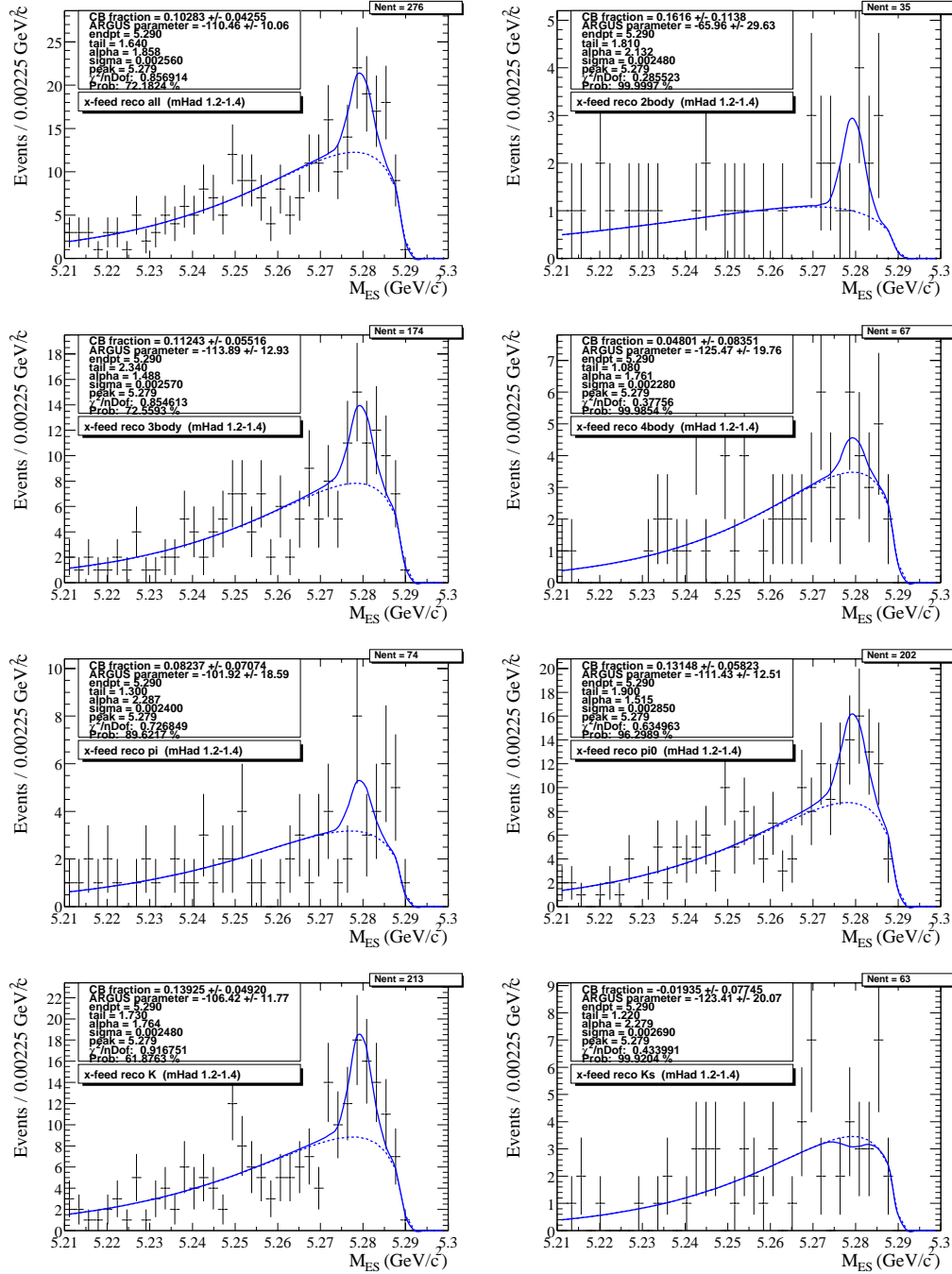


Figure D.13: MC cross-feed fits for  $M_{Had} = 1.2-1.4 \text{ GeV}/c^2$ .

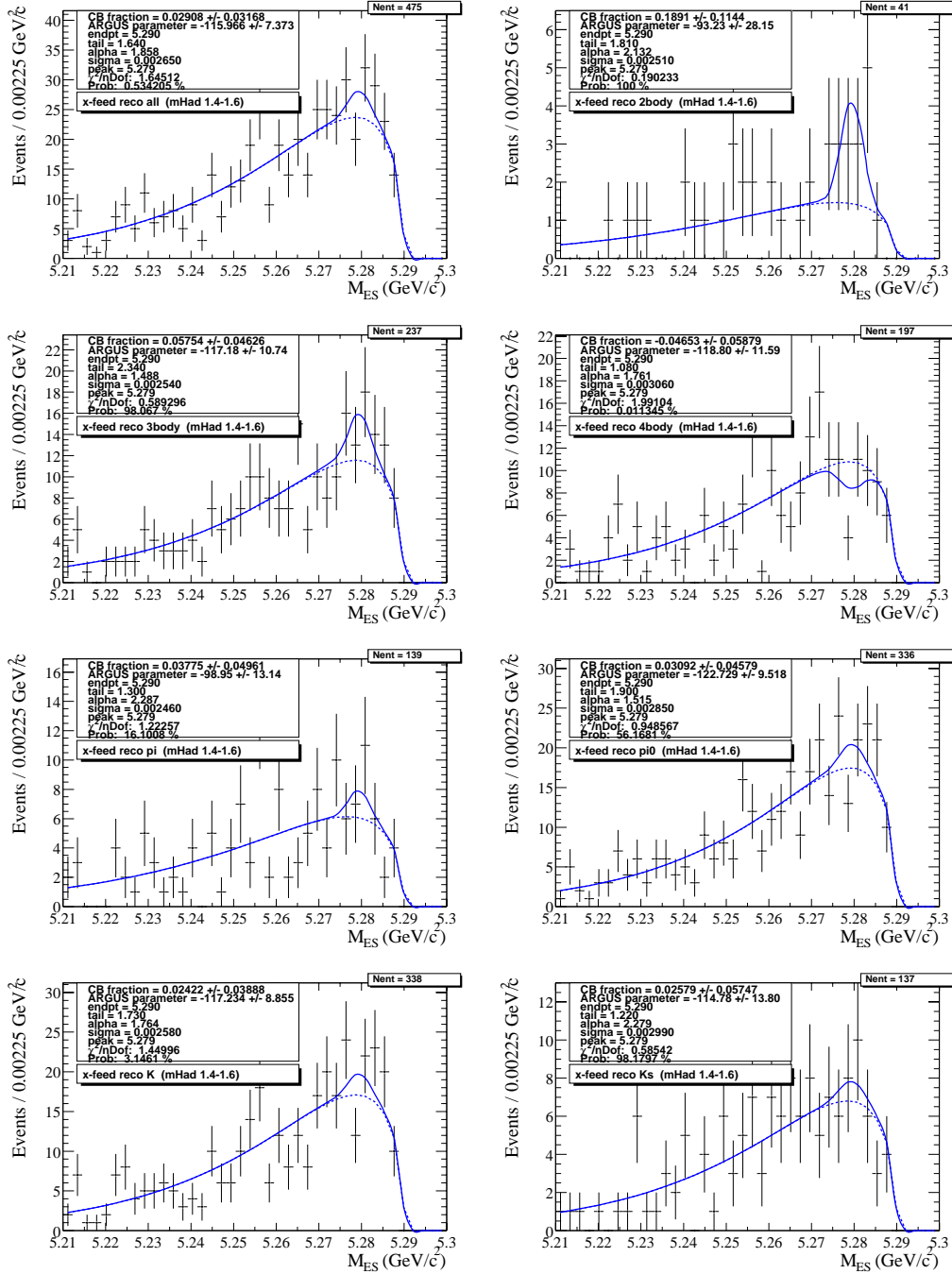


Figure D.14: MC cross-feed fits for  $M_{Had} = 1.4-1.6 \text{ GeV}/c^2$ .

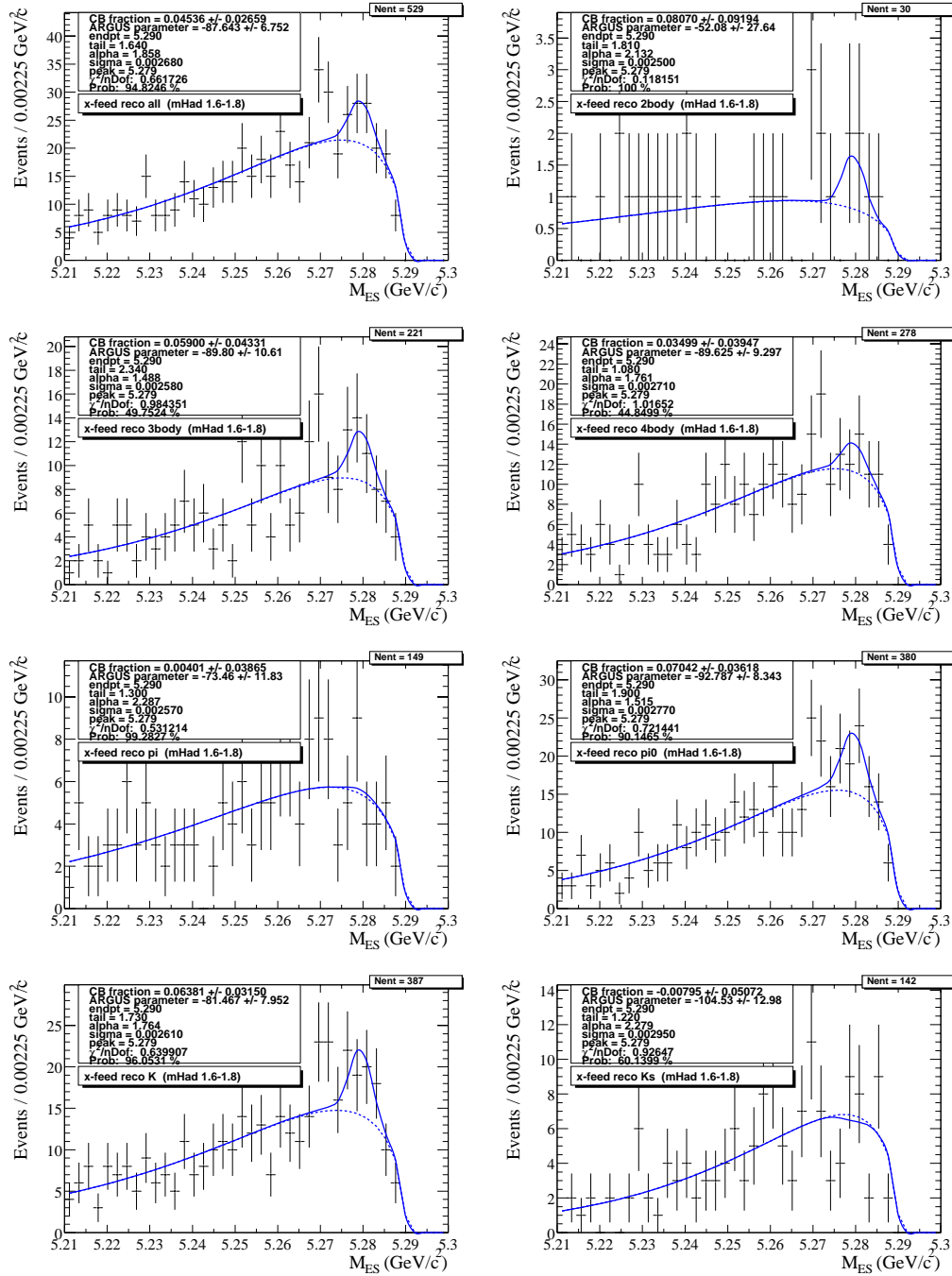


Figure D.15: MC cross-feed fits for  $M_{Had} = 1.6-1.8 \text{ GeV}/c^2$ .

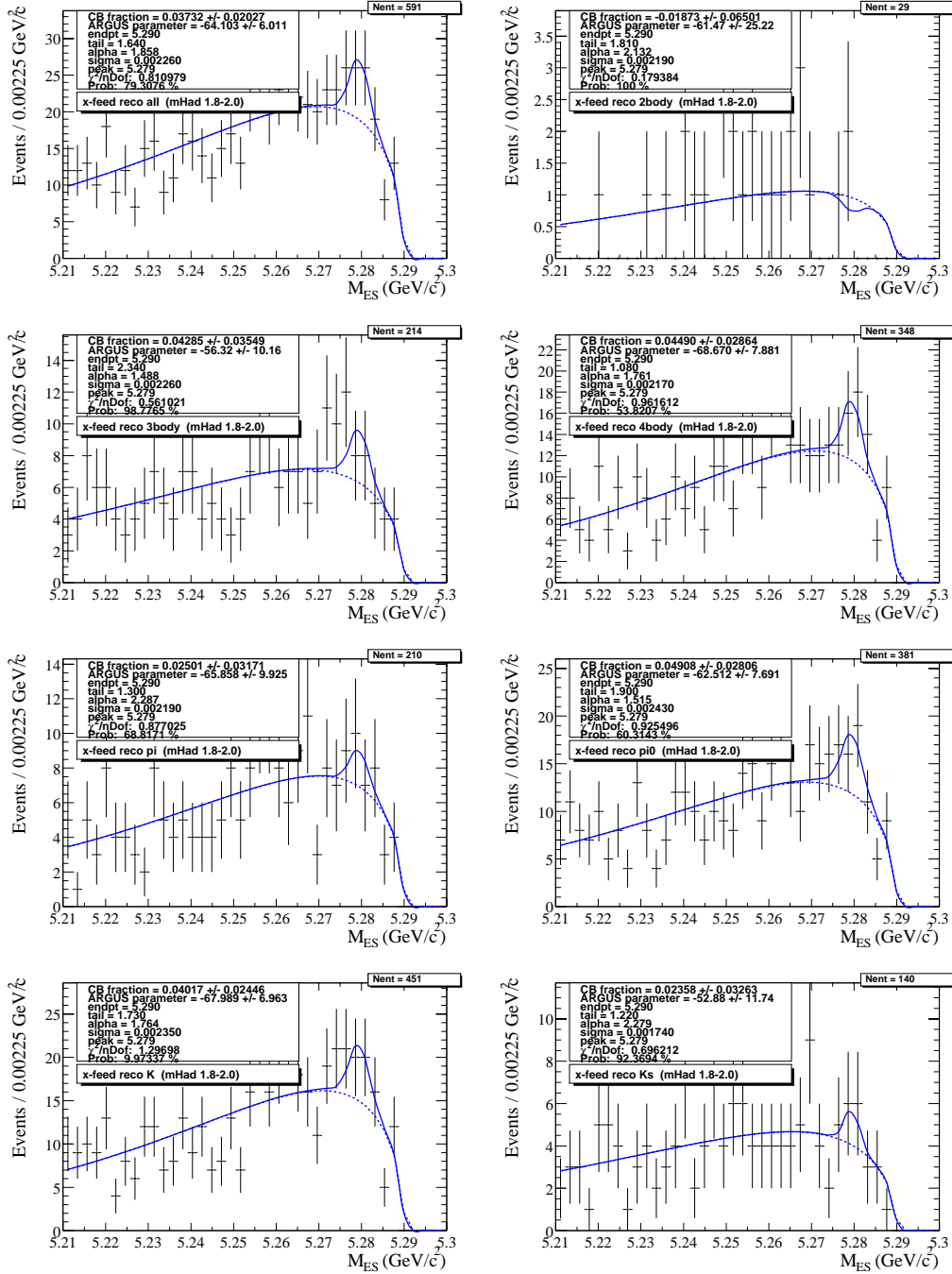


Figure D.16: MC cross-feed fits for  $M_{Had} = 1.8-2.0 \text{ GeV}/c^2$ .

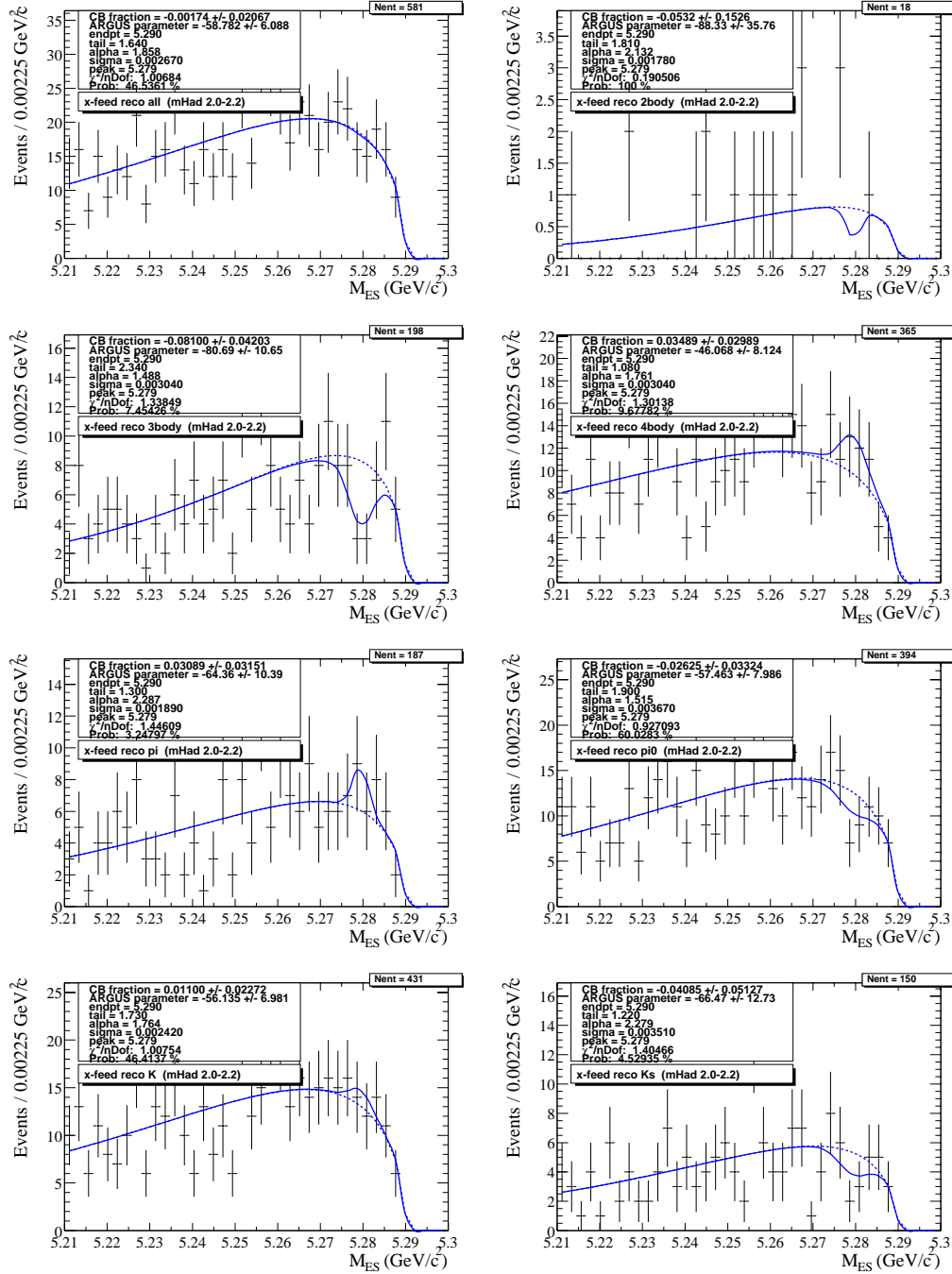


Figure D.17: MC cross-feed fits for  $M_{Had} = 2.0-2.2 \text{ GeV}/c^2$ .

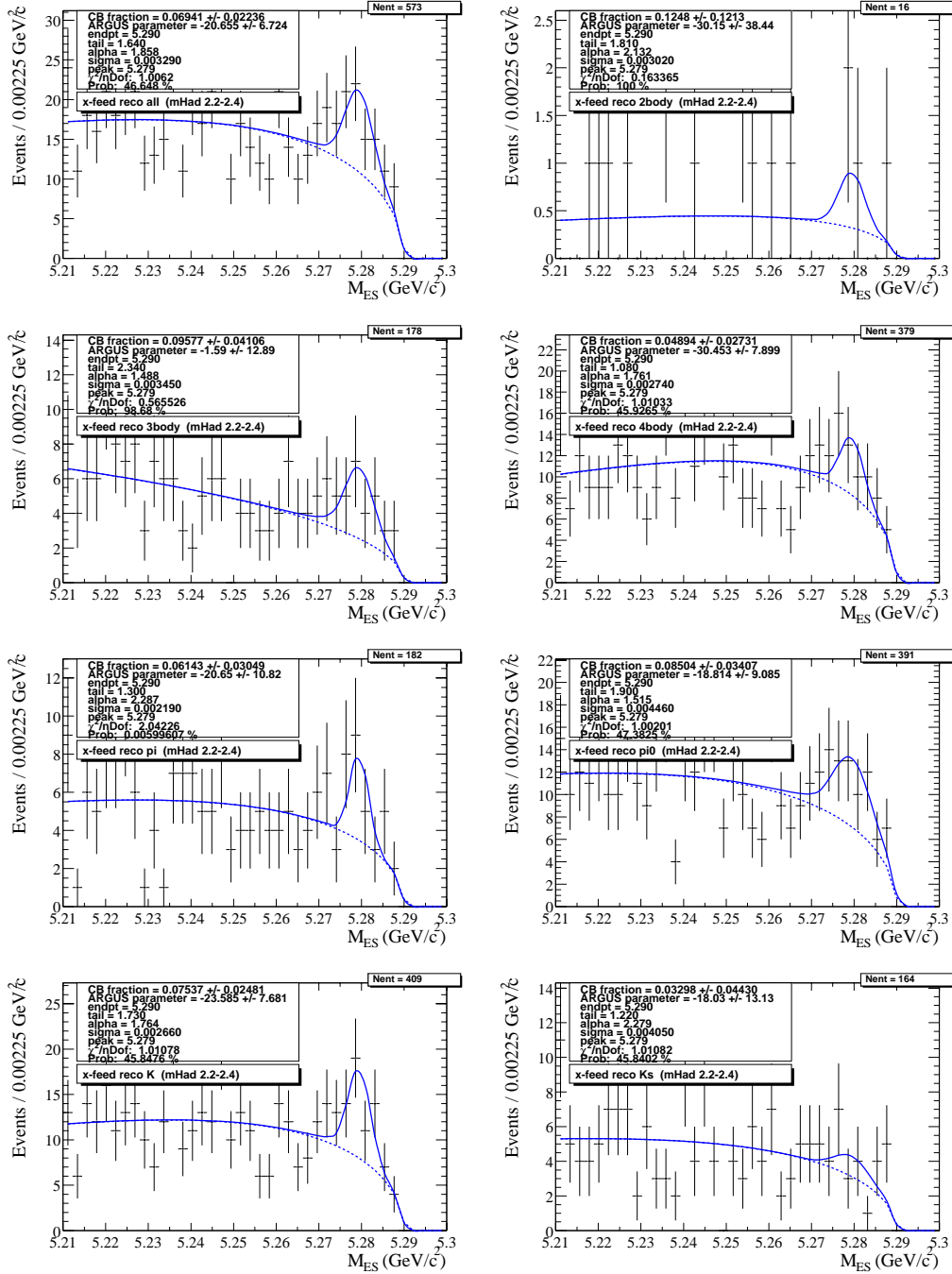


Figure D.18: MC cross-feed fits for  $M_{Had} = 2.2-2.4 \text{ GeV}/c^2$ .

### D.3 $B\bar{B}$ + Continuum Monte Carlo Fits

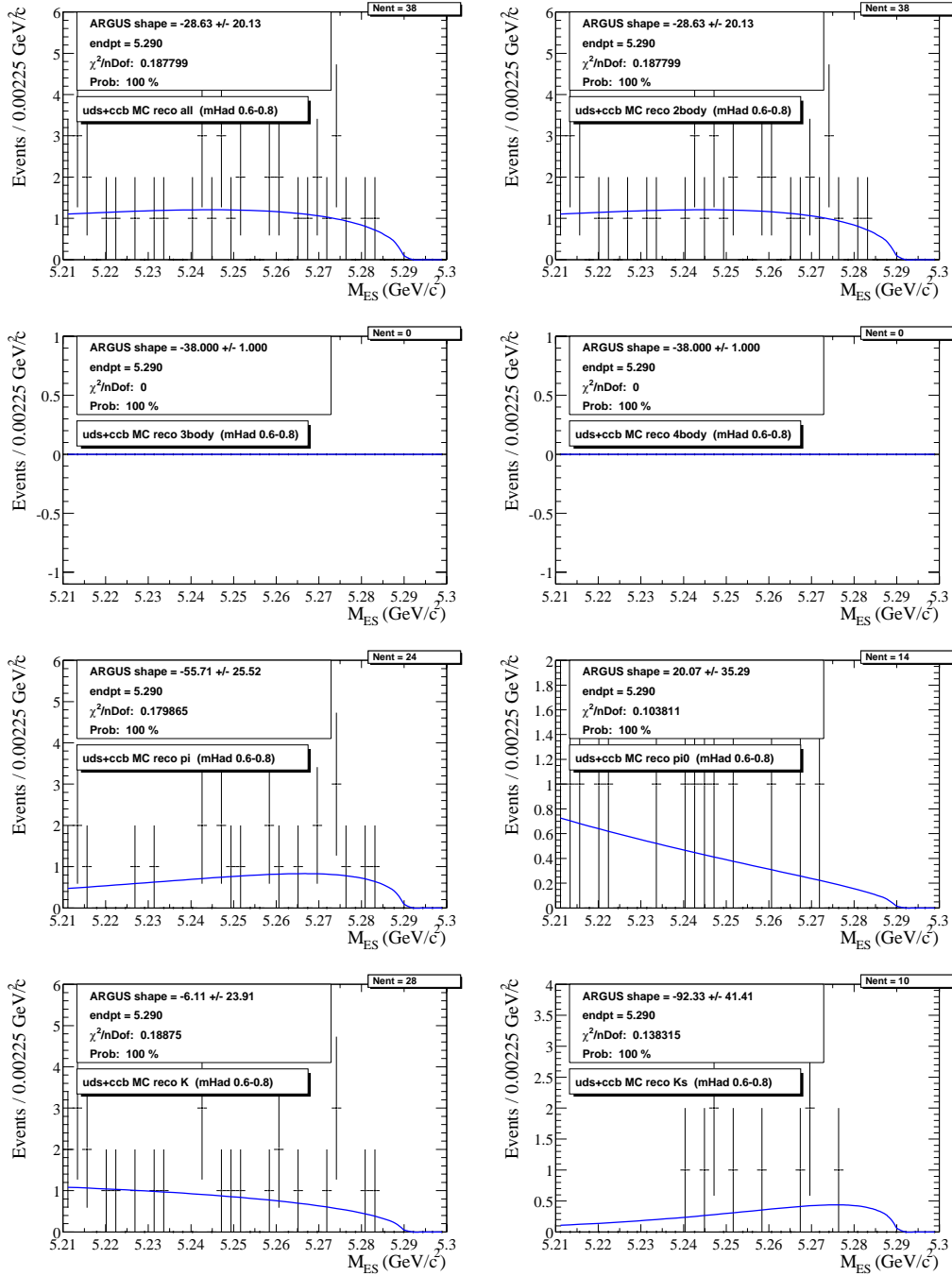


Figure D.19:  $B\bar{B}^+$  continuum fits for  $M_{Had} = 0.6-0.8 \text{ GeV}/c^2$ .

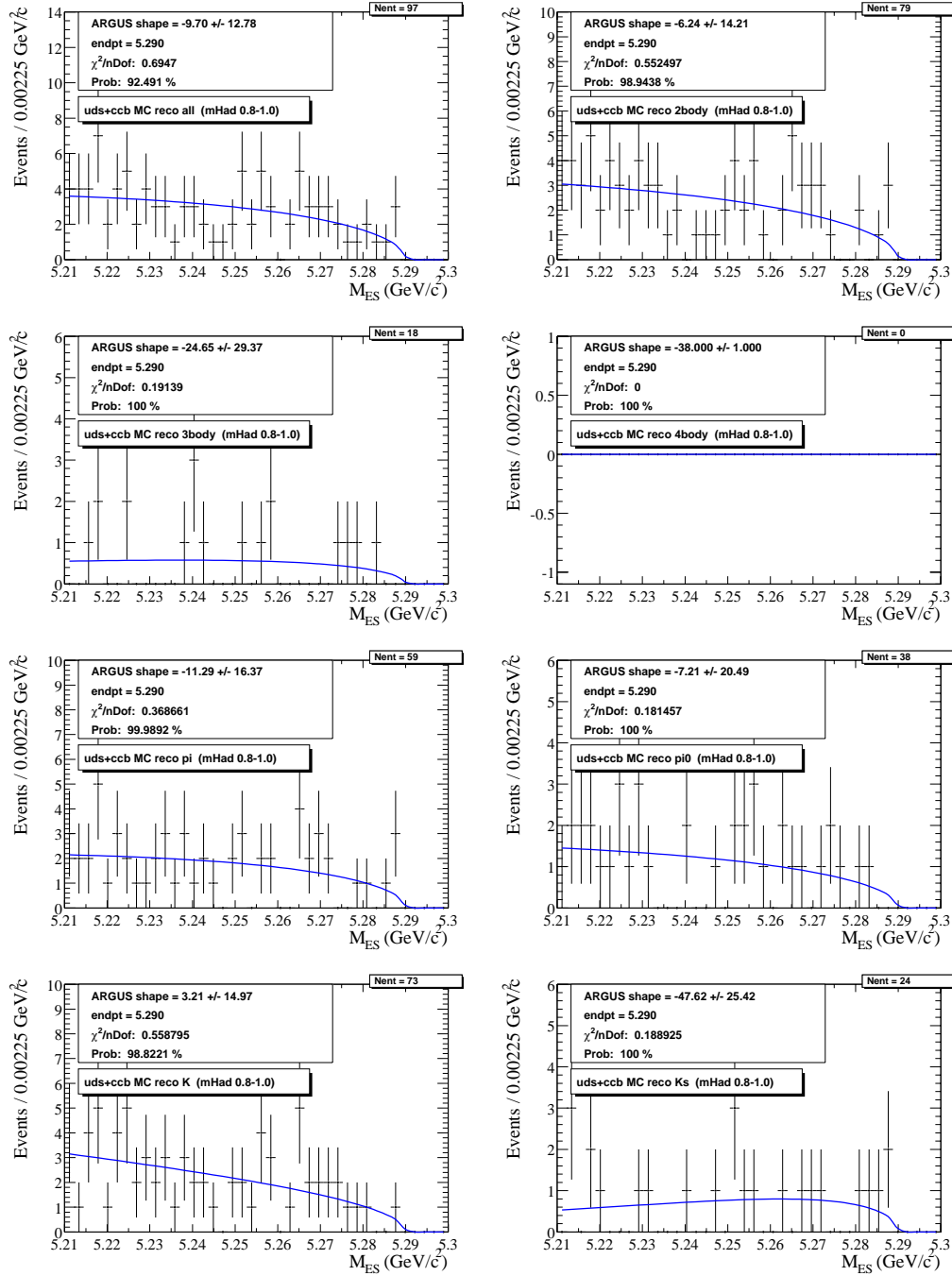


Figure D.20:  $B\bar{B}+$  continuum fits for  $M_{Had} = 0.8-1.0 \text{ GeV}/c^2$ .

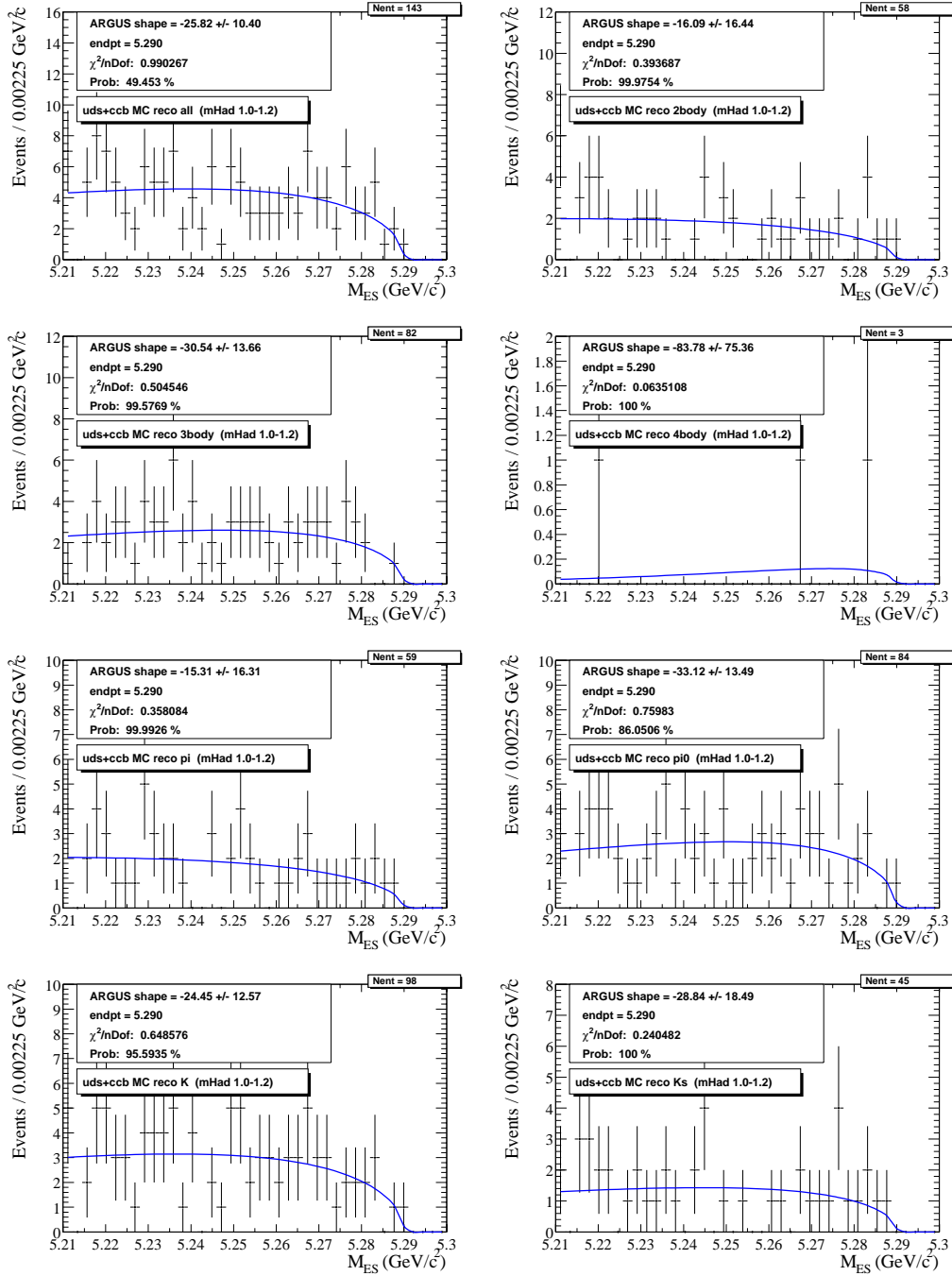


Figure D.21:  $B\bar{B}+$  continuum fits for  $M_{Had} = 1.0-1.2 \text{ GeV}/c^2$ .

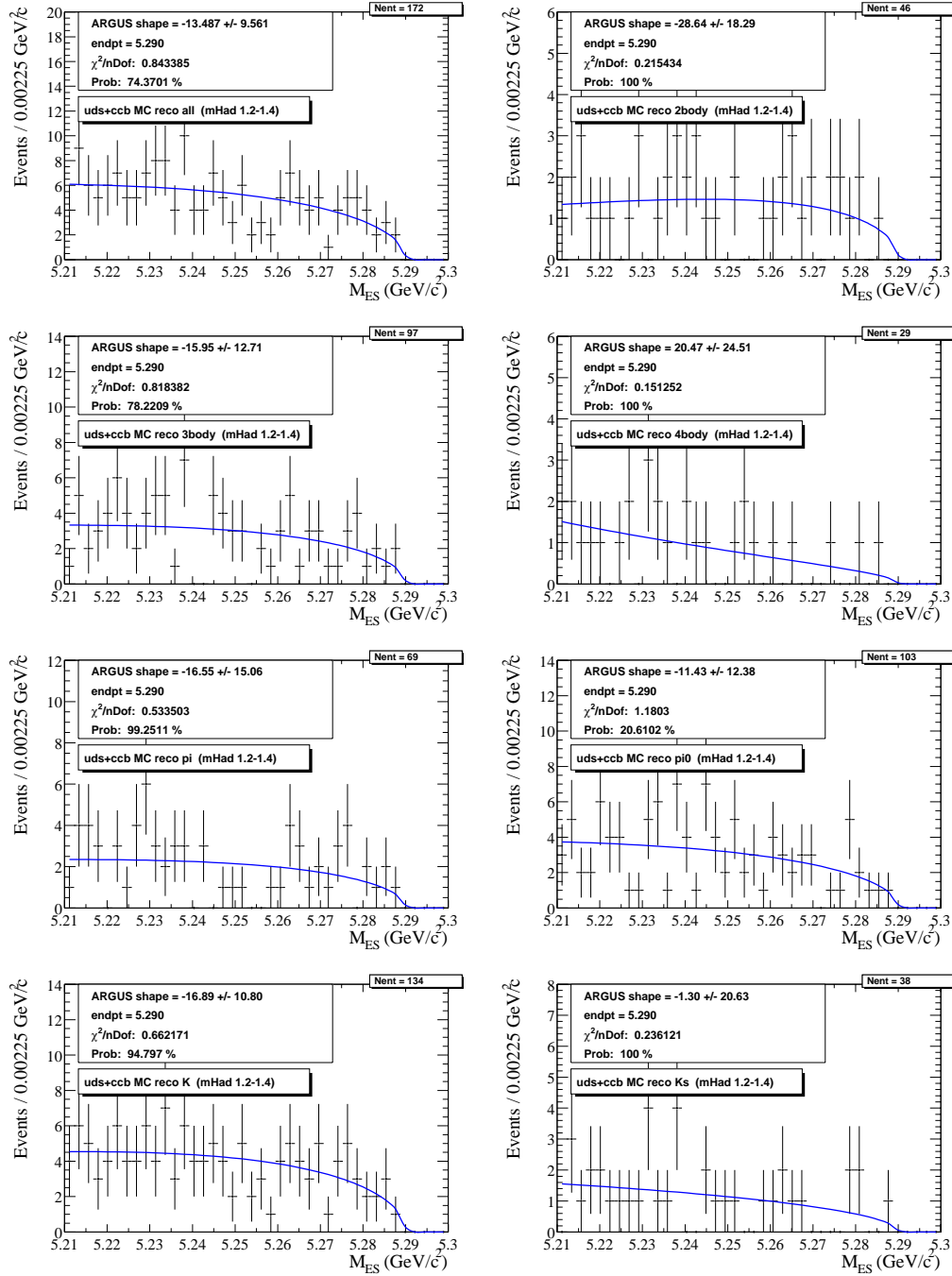


Figure D.22:  $B\bar{B}^+$  continuum fits for  $M_{Had} = 1.2-1.4 \text{ GeV}/c^2$ .

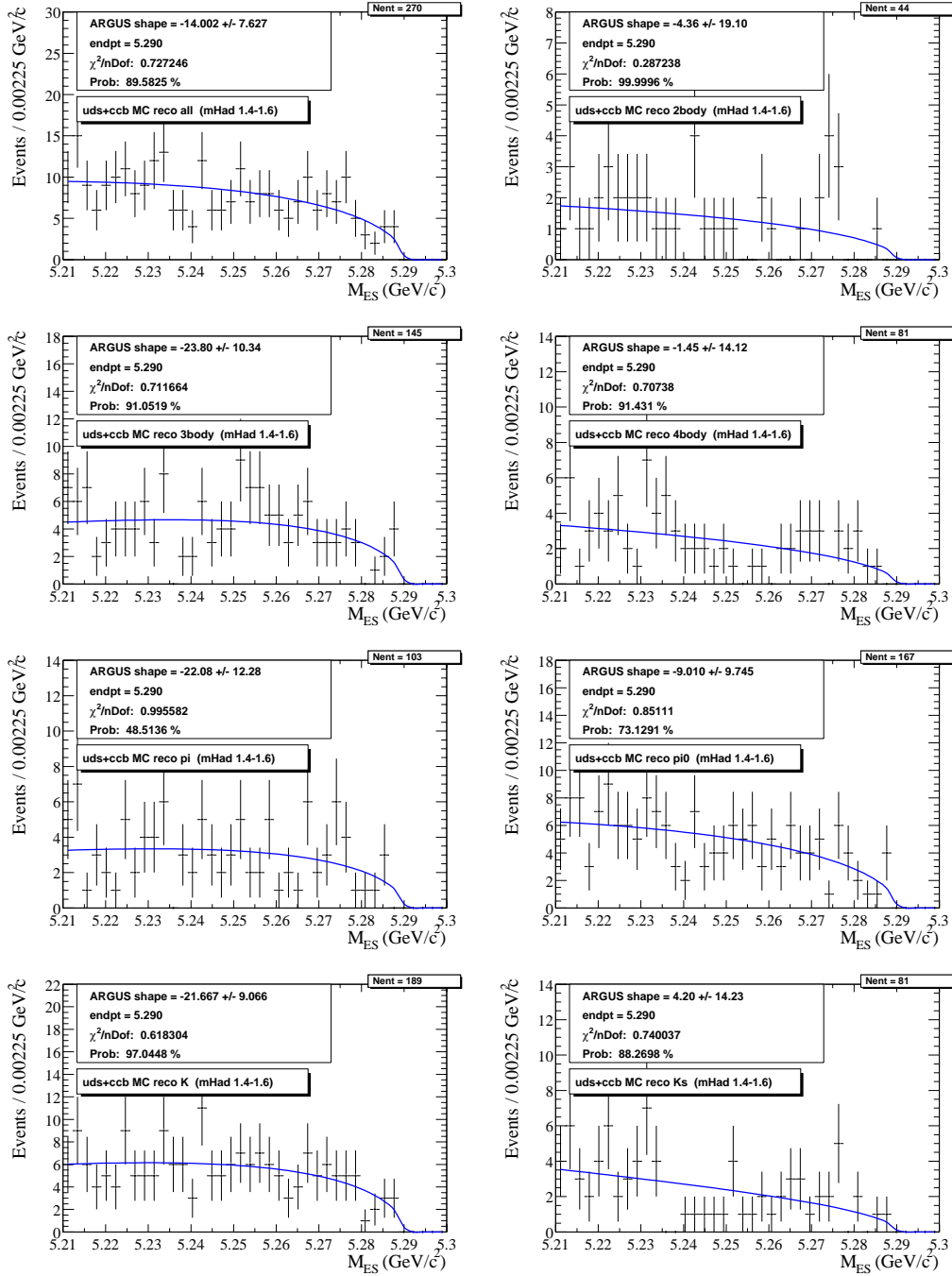


Figure D.23:  $B\bar{B}+$  continuum fits for  $M_{Had} = 1.4-1.6 \text{ GeV}/c^2$ .

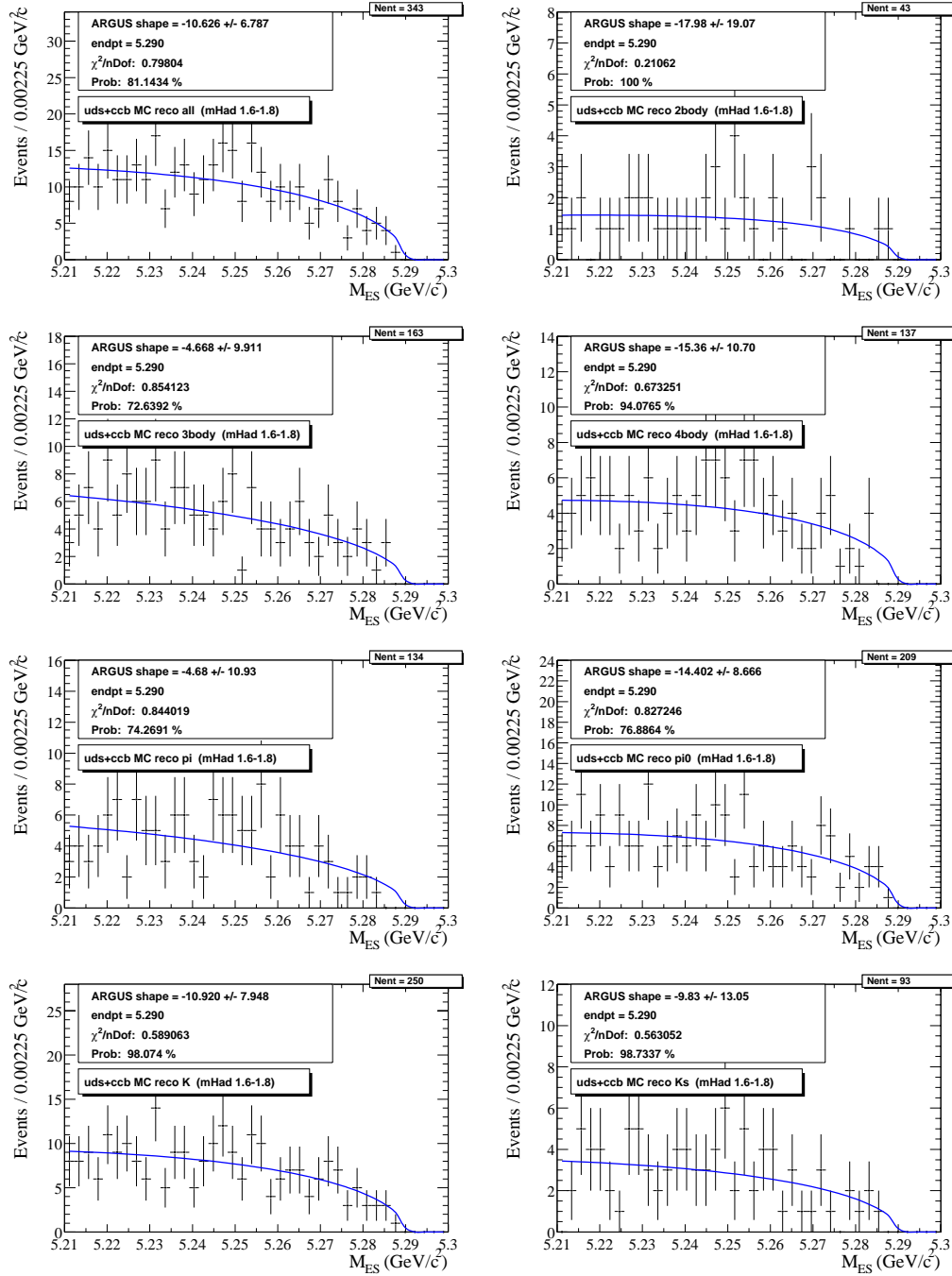


Figure D.24:  $B\bar{B}+$  continuum fits for  $M_{Had} = 1.6-1.8 \text{ GeV}/c^2$ .

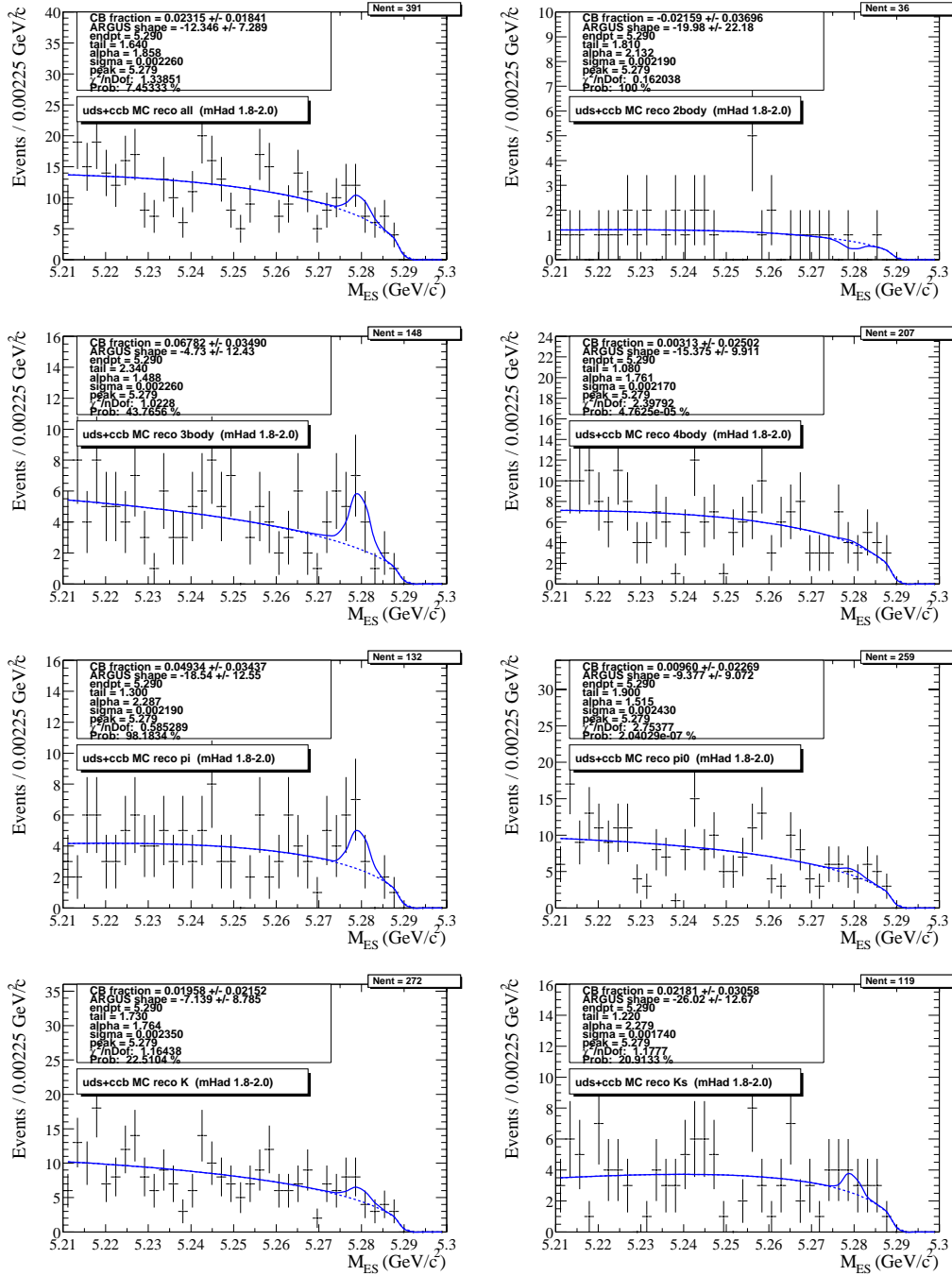


Figure D.25:  $B\bar{B}$ + continuum fits for  $M_{Had} = 1.8-2.0 \text{ GeV}/c^2$ .

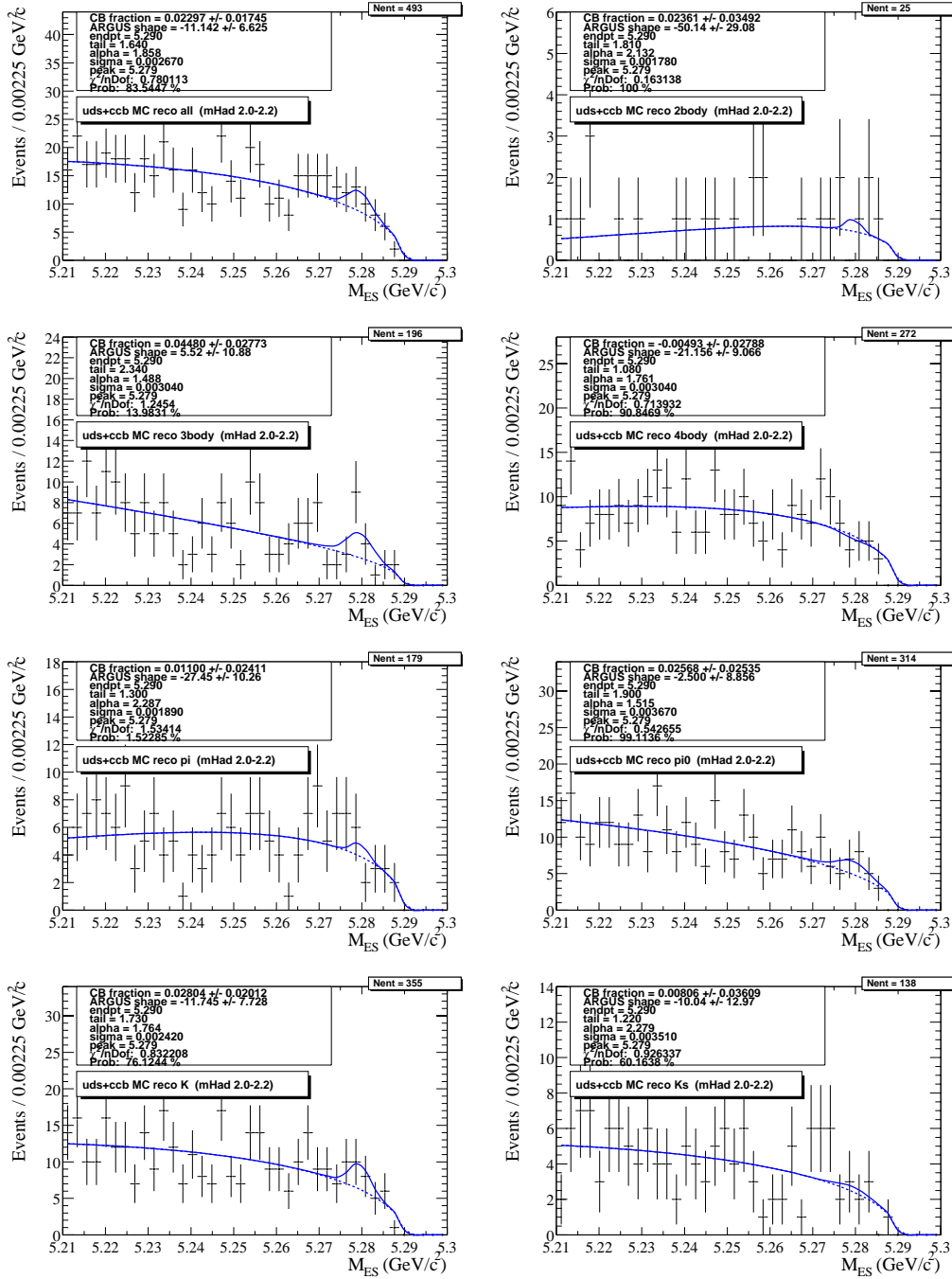


Figure D.26:  $B\bar{B}+$  continuum fits for  $M_{Had} = 2.0-2.2$  GeV/c<sup>2</sup>.

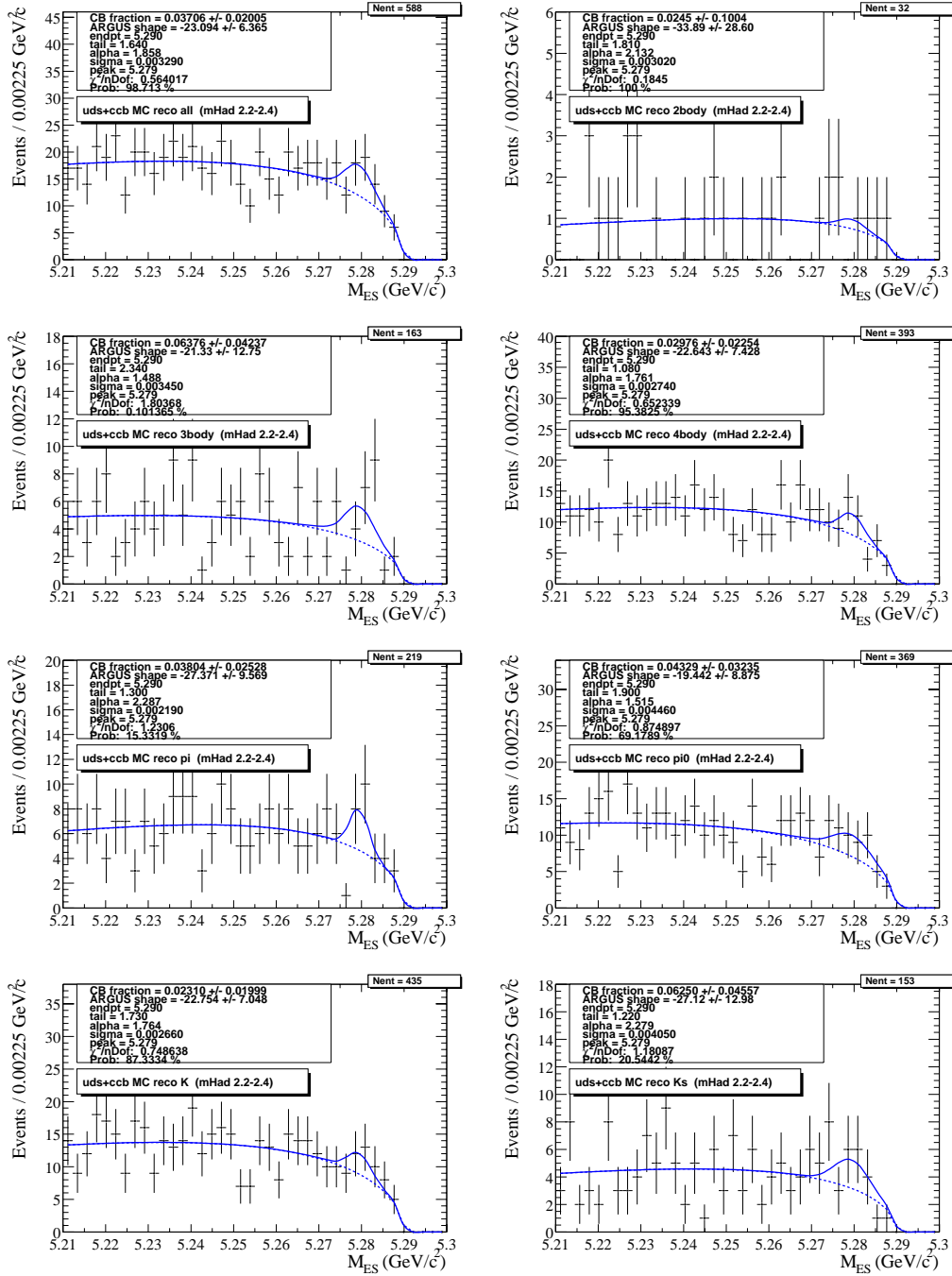


Figure D.27:  $B\bar{B}+$  continuum fits for  $M_{Had} = 2.2-2.4 \text{ GeV}/c^2$ .

## D.4 $B\bar{B}$ Monte Carlo Fits

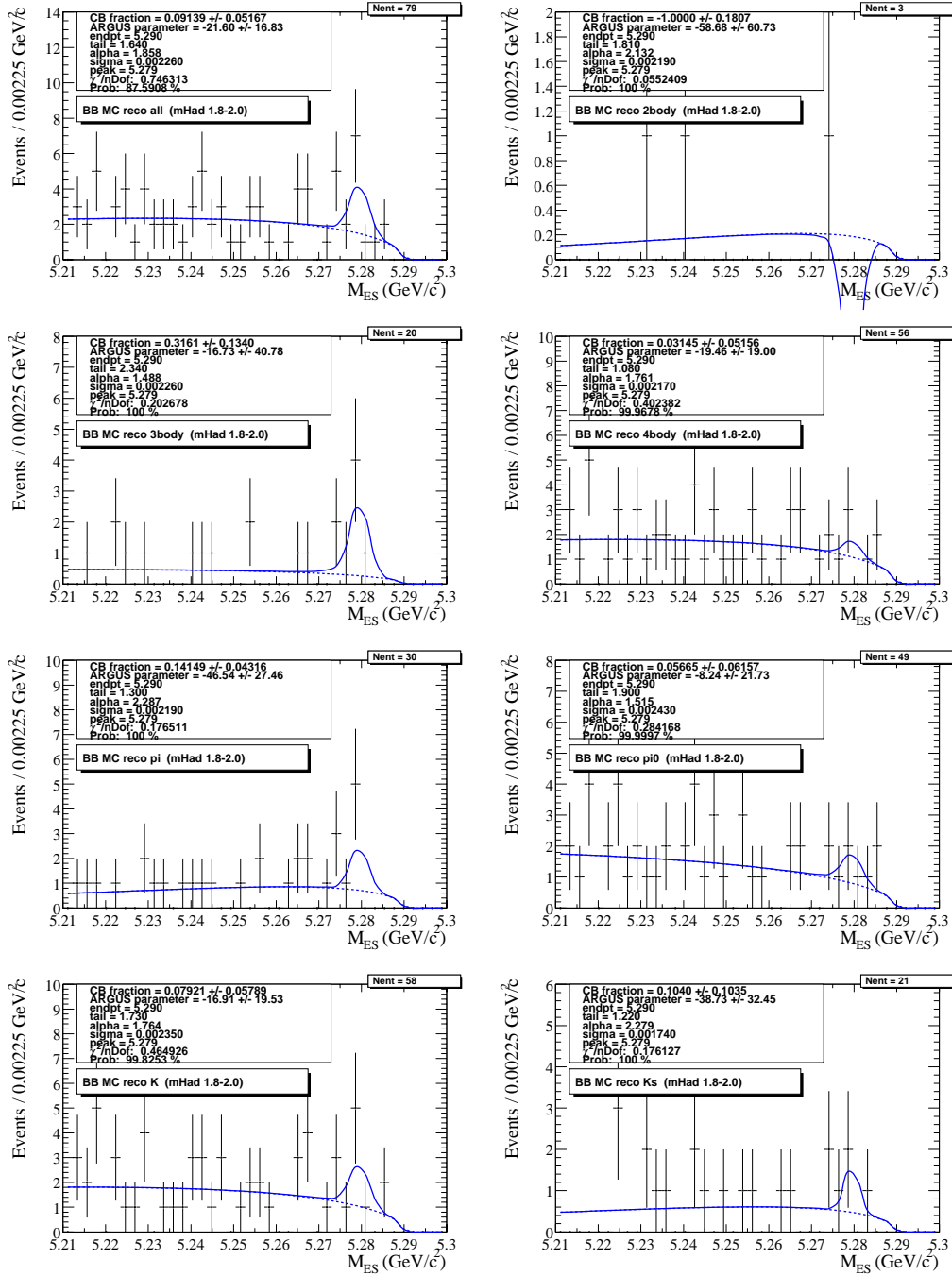


Figure D.28:  $B\bar{B}$  fits for  $M_{Had} = 1.8-2.0 \text{ GeV}/c^2$ .

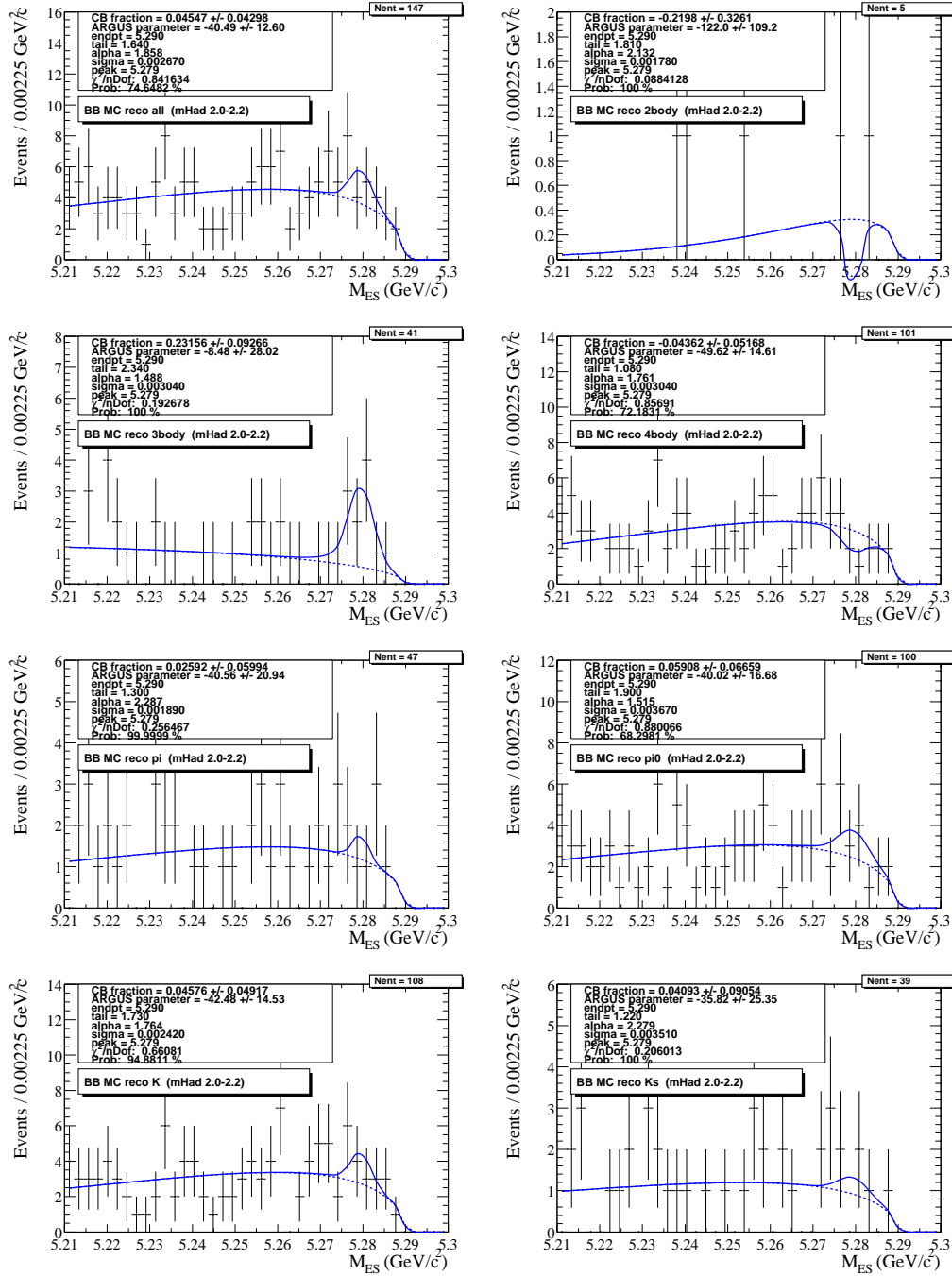


Figure D.29:  $B\bar{B}$  fits for  $M_{Had} = 2.0-2.2 \text{ GeV}/c^2$ .

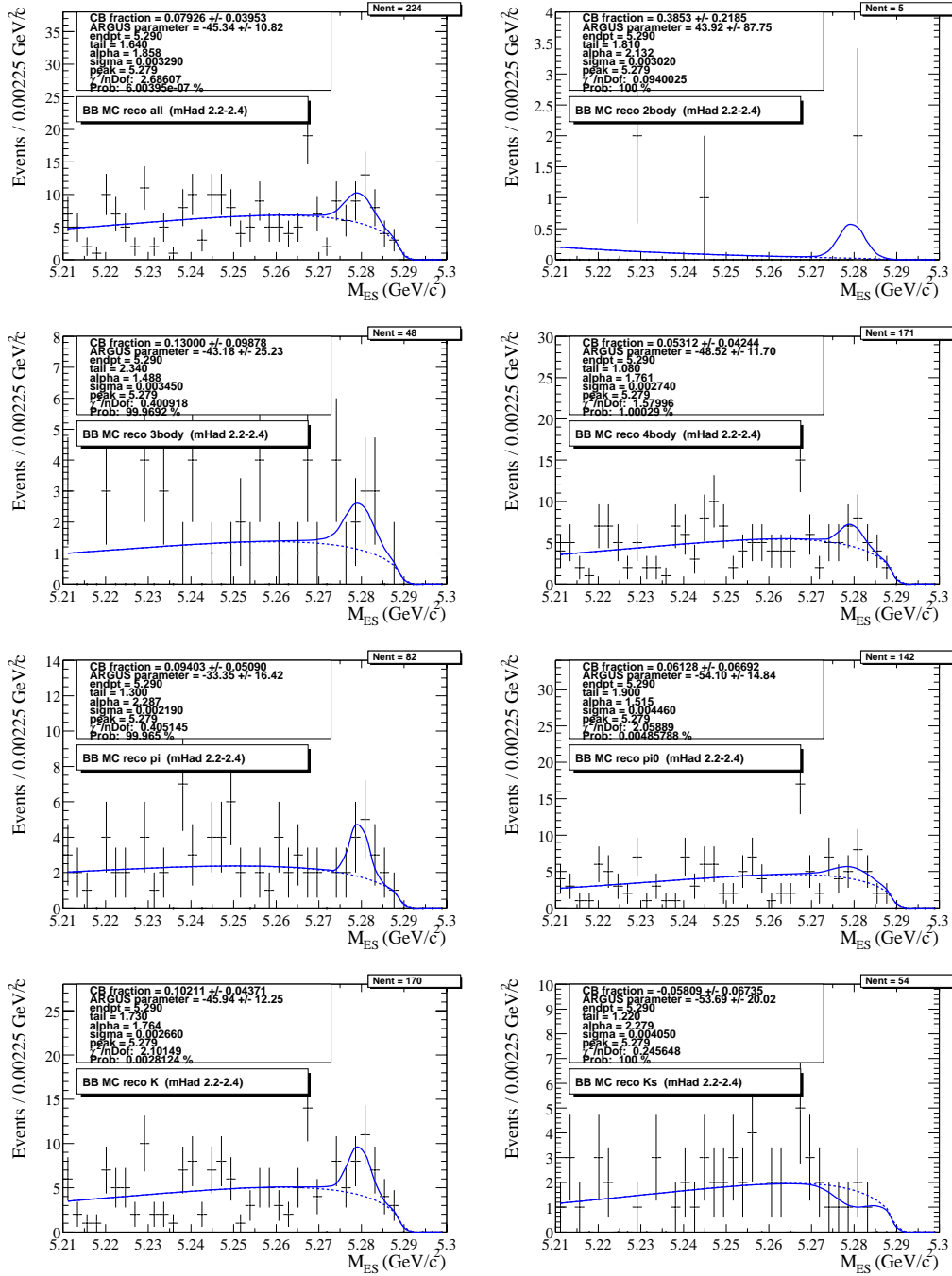


Figure D.30:  $B\bar{B}$  fits for  $M_{Had} = 2.0-2.2 \text{ GeV}/c^2$ .

## D.5 Data Fits

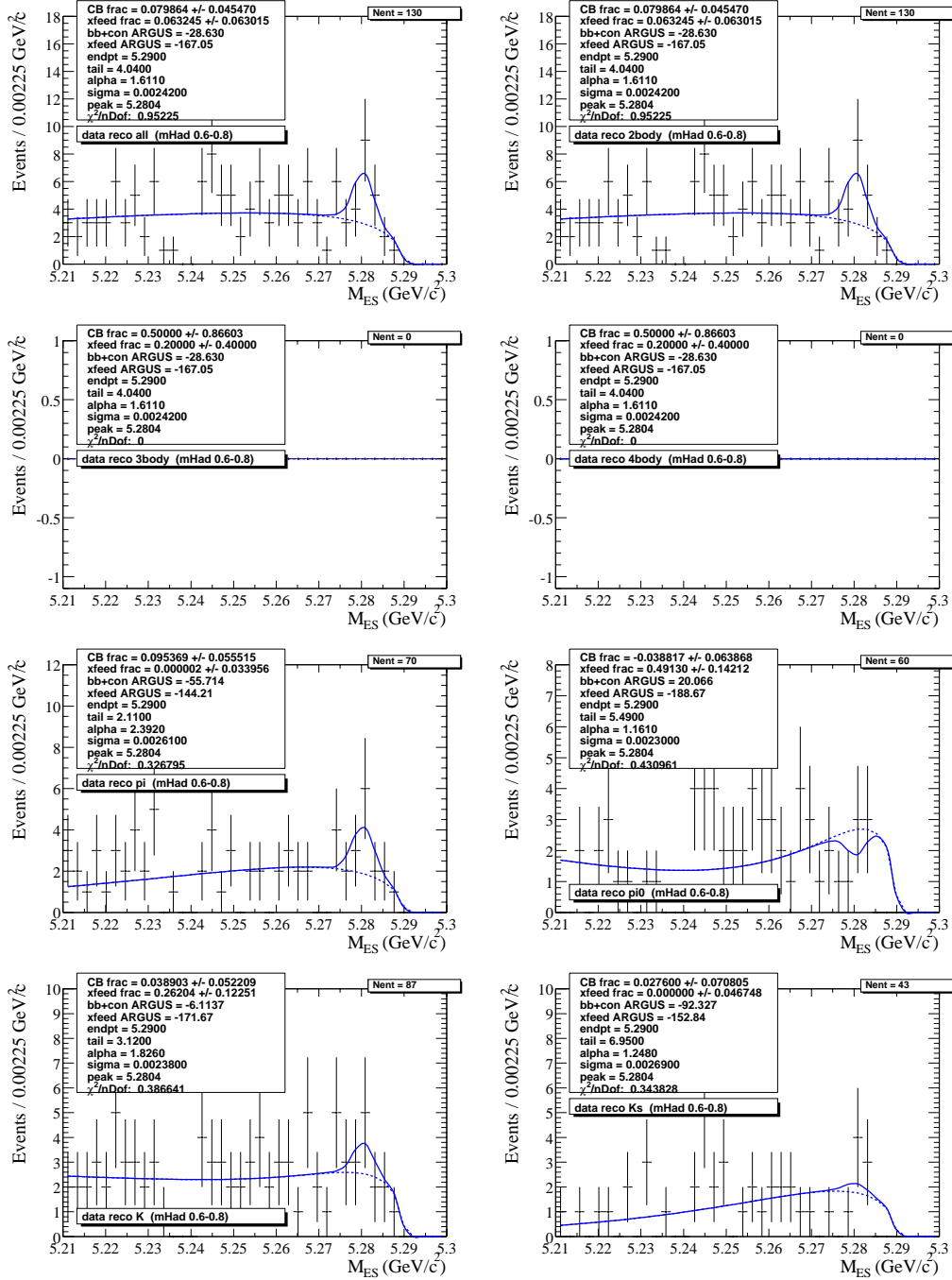


Figure D.31: Data fits for  $M_{Had} = 0.6-0.8 \text{ GeV}/c^2$ .

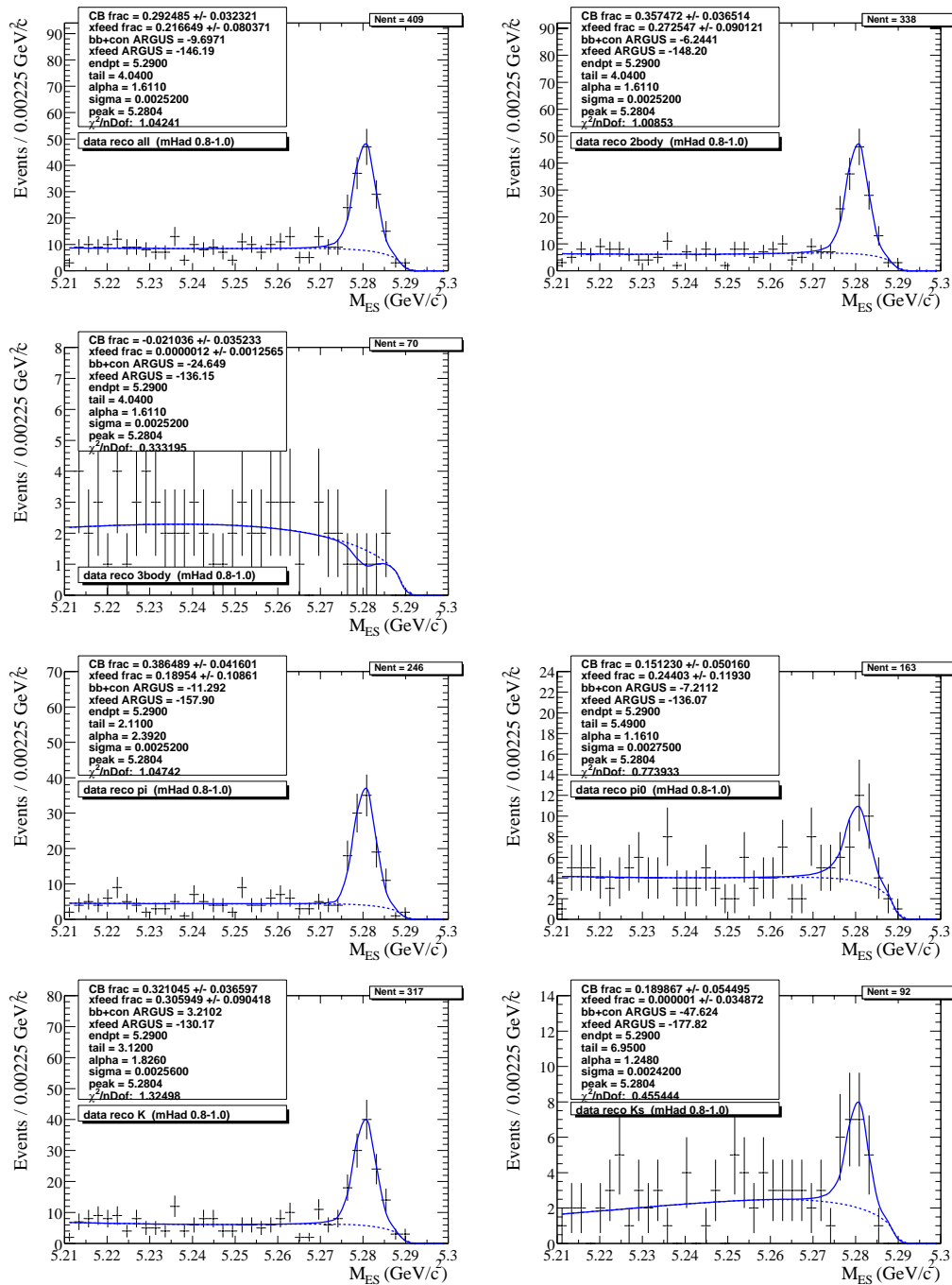


Figure D.32: Data fits for  $M_{Had} = 0.8-1.0 \text{ GeV}/c^2$ .

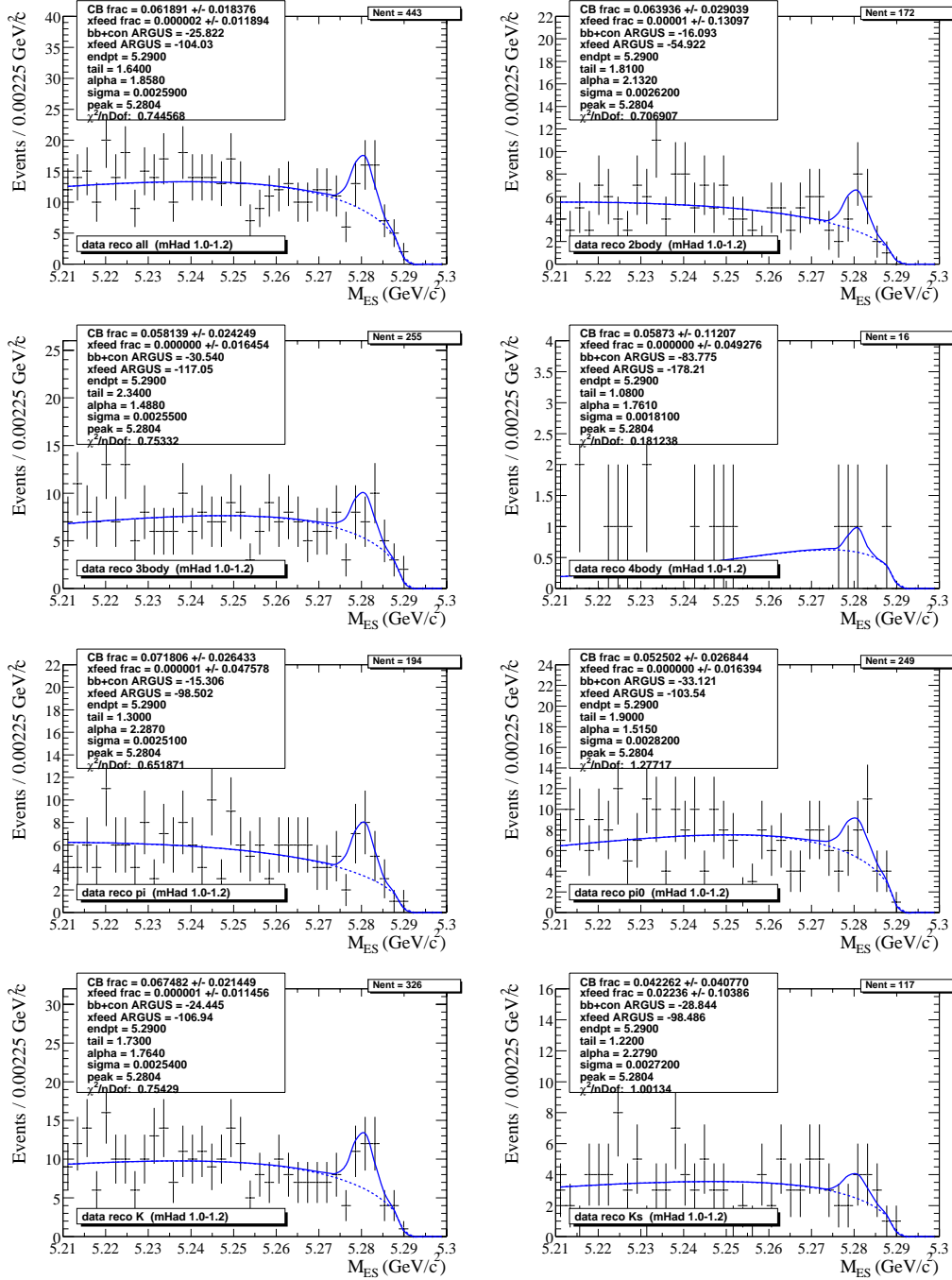


Figure D.33: Data fits for  $M_{Had} = 1.0-1.2 \text{ GeV}/c^2$ .

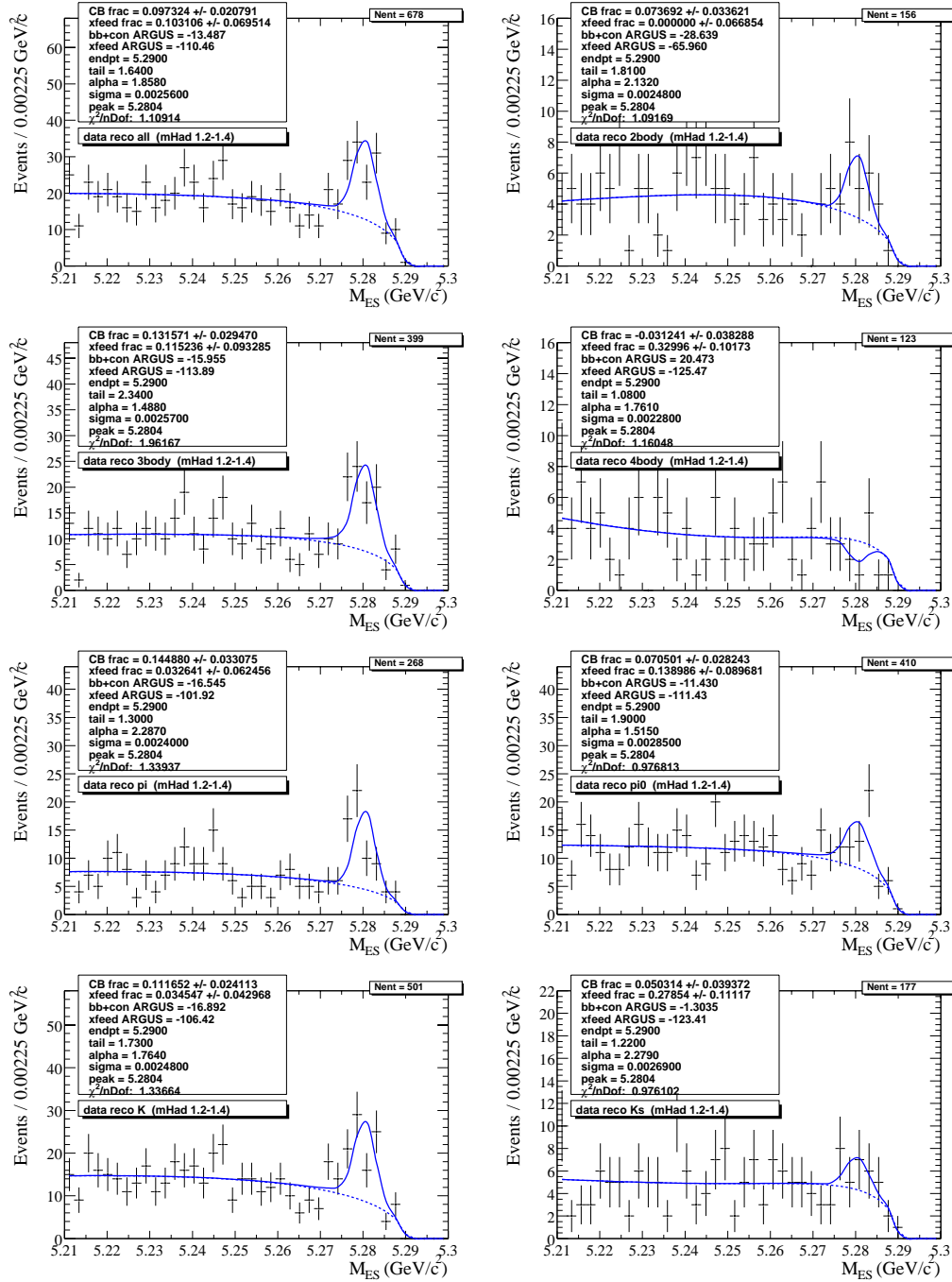


Figure D.34: Data fits for  $M_{Had} = 1.2-1.4 \text{ GeV}/c^2$ .

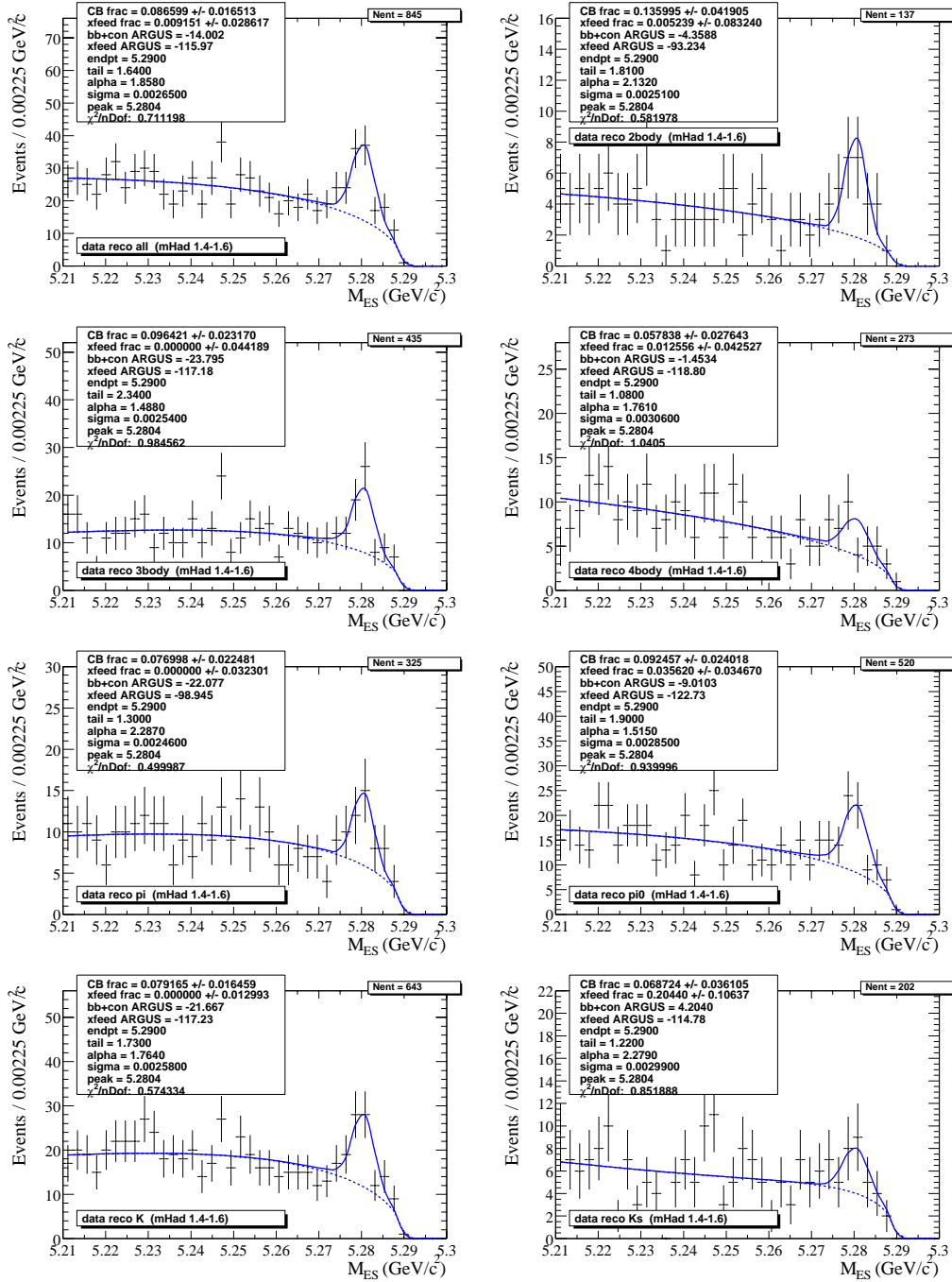


Figure D.35: Data fits for  $M_{Had} = 1.4-1.6 \text{ GeV}/c^2$ .

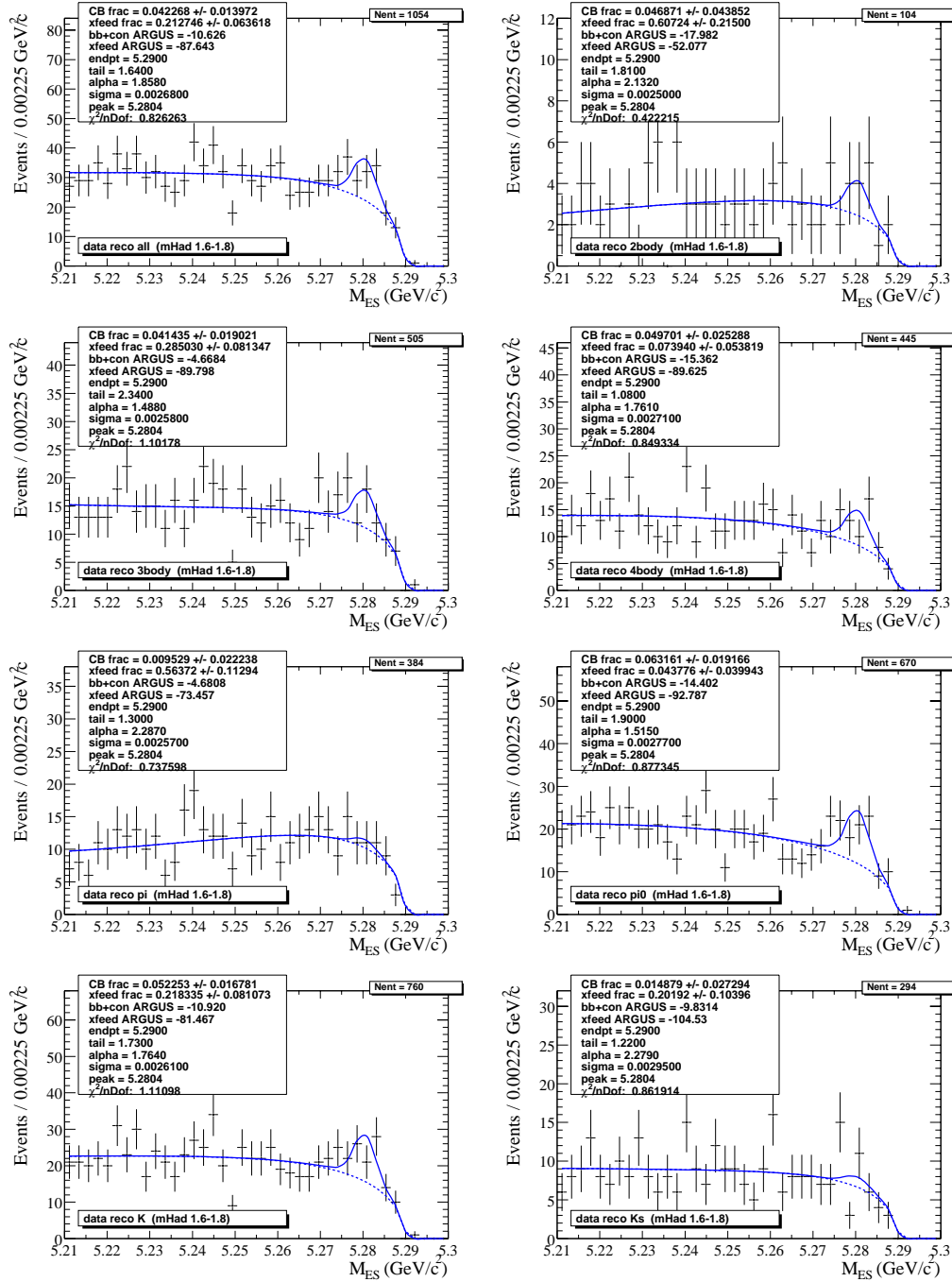


Figure D.36: Data fits for  $M_{Had} = 1.6-1.8 \text{ GeV}/c^2$ .

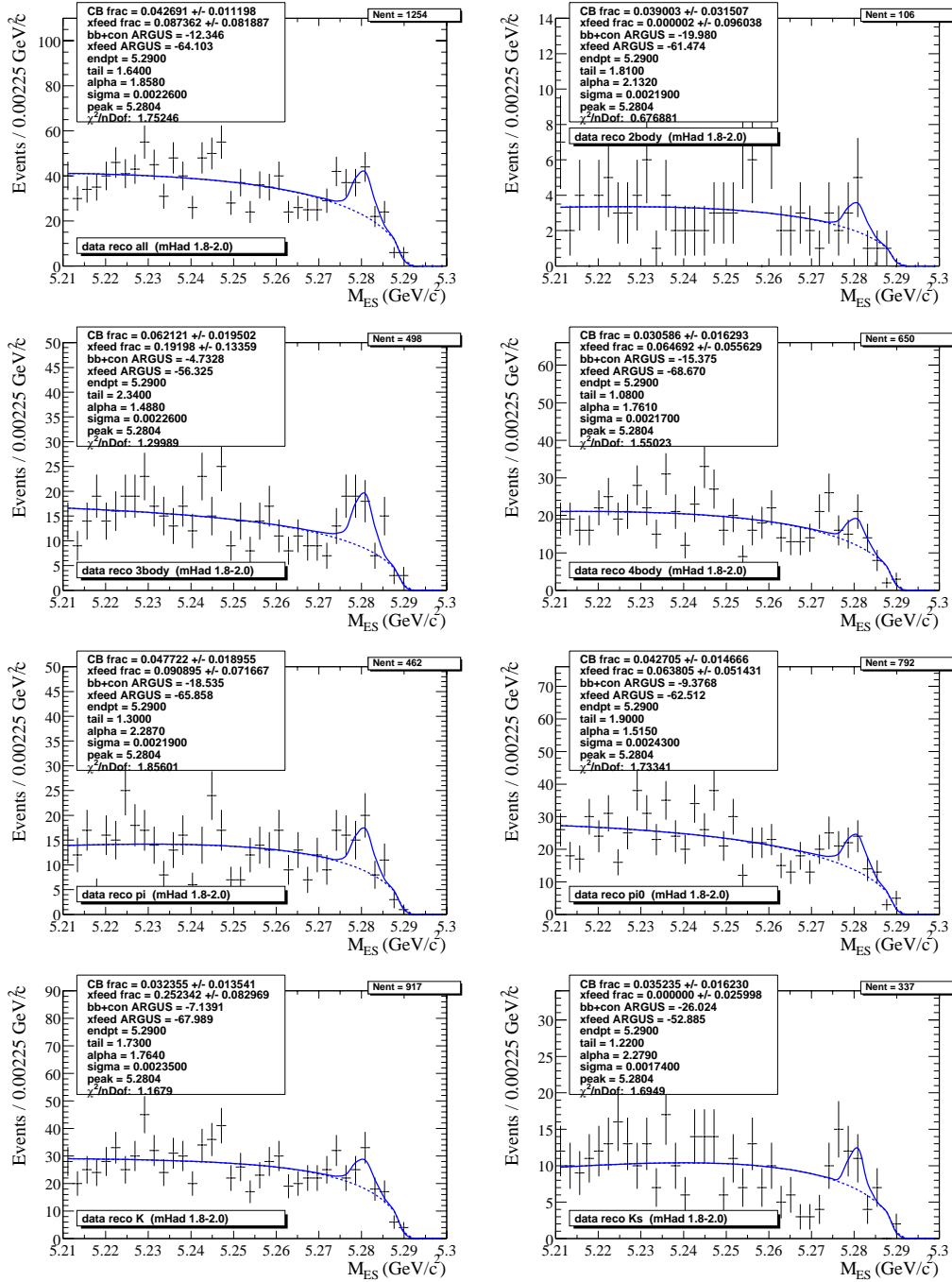


Figure D.37: Data fits for  $M_{Had} = 1.8-2.0$  GeV/c<sup>2</sup>.

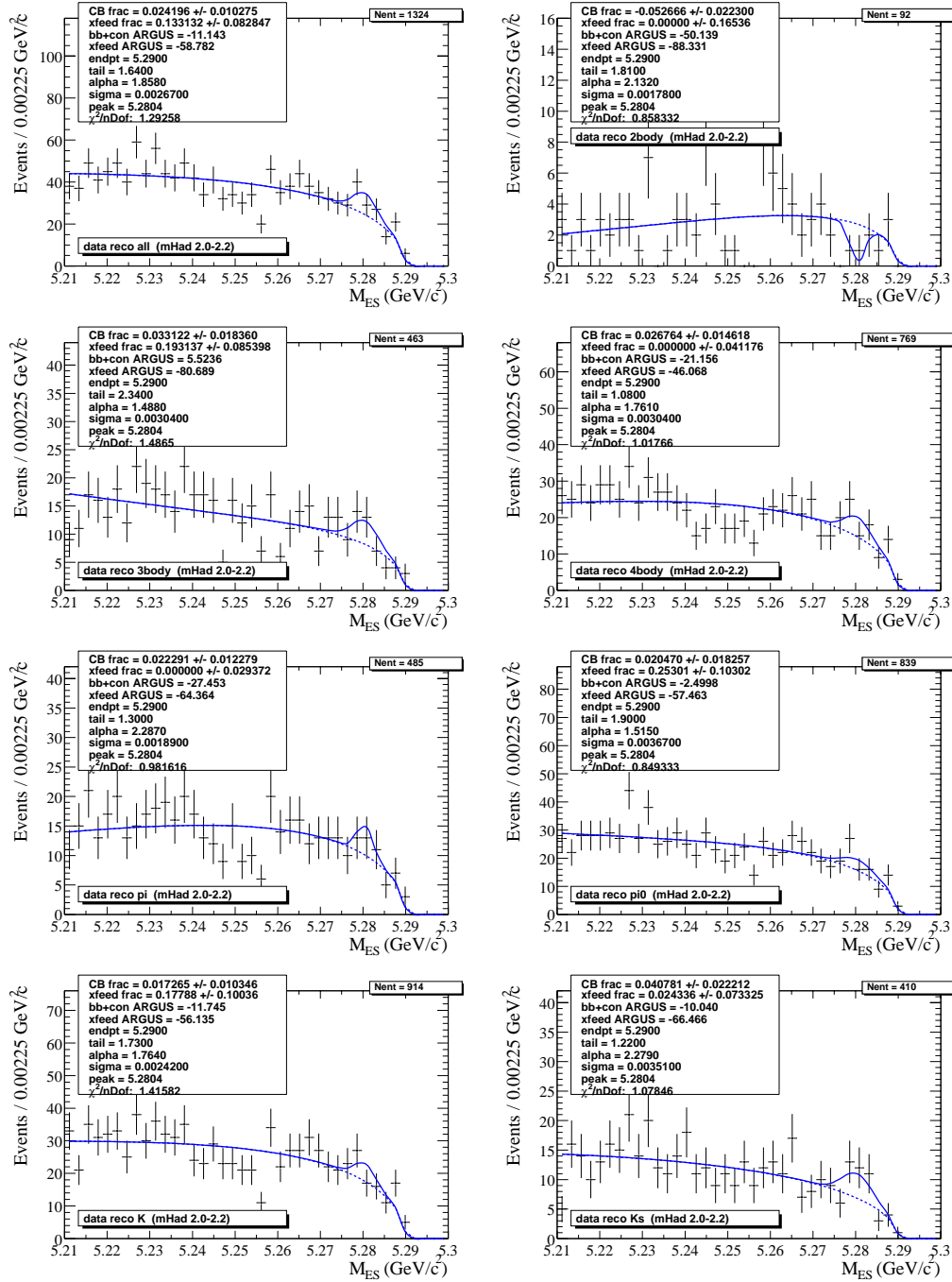


Figure D.38: Data fits for  $M_{Had} = 2.0-2.2 \text{ GeV}/c^2$ .

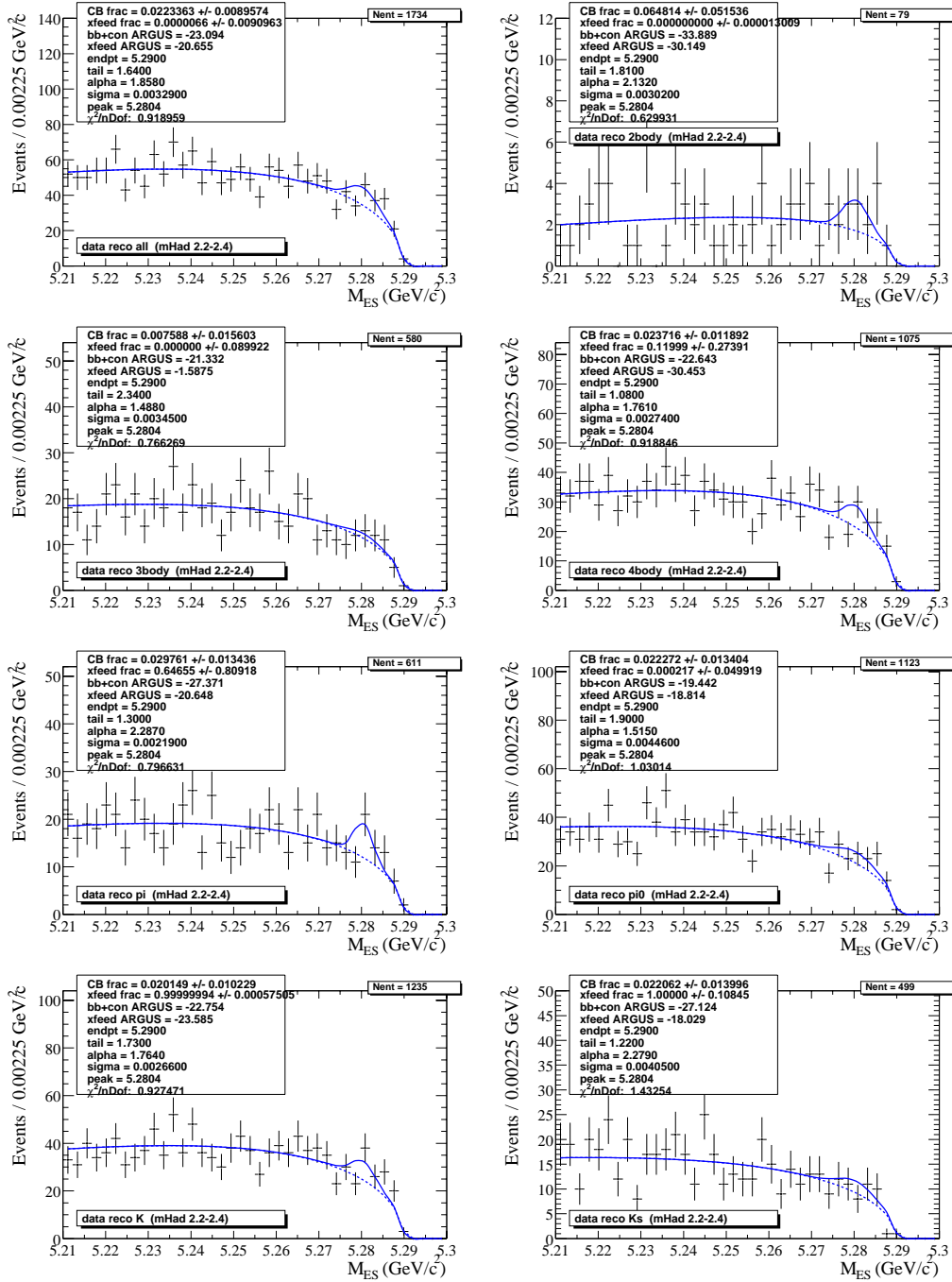


Figure D.39: Data fits for  $M_{Had} = 2.2-2.4 \text{ GeV}/c^2$ .

# Bibliography

- [1] BaBar, P. F. Harrison and H. R. Quinn, editors, *The BaBar Physics Book: Physics at an asymmetric B factory*, 1998, SLAC-R-504.
- [2] J. L. Hewett and J. D. Wells, Phys. Rev. **D55**, 5549 (1997), hep-ph/9610323.
- [3] K. G. Chetyrkin, M. Misiak, and M. Muenz, Phys. Lett. **B400**, 206 (1997), hep-ph/9612313.
- [4] P. Gambino and M. Misiak, Nucl. Phys. **B611**, 338 (2001), hep-ph/0104034.
- [5] A. L. Kagan and M. Neubert, Eur. Phys. J. **C7**, 5 (1999), hep-ph/9805303.
- [6] M. Neubert, Phys. Rev. **D49**, 4623 (1994), hep-ph/9312311.
- [7] M. Neubert, Phys. Lett. **B513**, 88 (2001), hep-ph/0104280.
- [8] CLEO, M. S. Alam *et al.*, Phys. Rev. Lett. **74**, 2885 (1995).
- [9] CLEO, S. Chen *et al.*, Phys. Rev. Lett. **87**, 251807 (2001), hep-ex/0108032.
- [10] ALEPH, R. Barate *et al.*, Phys. Lett. **B429**, 169 (1998).
- [11] Belle, K. Abe *et al.*, Phys. Lett. **B511**, 151 (2001), hep-ex/0103042.
- [12] CLEO, T. E. Coan *et al.*, Phys. Rev. Lett. **84**, 5283 (2000), hep-ex/9912057.
- [13] Belle, Y. Ushiroda, (2001), hep-ex/0104045.
- [14] BABAR, B. Aubert *et al.*, Phys. Rev. Lett. **88**, 101805 (2002), hep-ex/0110065.
- [15] M. Beneke, T. Feldmann, and D. Seidel, Nucl. Phys. **B612**, 25 (2001), hep-ph/0106067.
- [16] Belle, S. Nishida *et al.*, (2002), hep-ex/0205025.

- [17] S. Veseli and M. G. Olsson, Phys. Lett. **B367**, 309 (1996), hep-ph/9508255.
- [18] T. Sjostrand *et al.*, Comput. Phys. Commun. **135**, 238 (2001), hep-ph/0010017.
- [19] BABAR, B. Aubert *et al.*, Nucl. Instrum. Meth. **A479**, 1 (2002), hep-ex/0105044.
- [20] G. Mancinelli and S. Spanier, BaBar Analysis Document **116**.
- [21] R. Brun, F. Bruyant, M. Maire, A. McPherson, and P. Zancarini, CERN-DD/EE/84-1.
- [22] T. Colberg, BaBar Analysis Document **196**.
- [23] H. Tanaka, BaBar Analysis Document **33**.
- [24] N. A. W. Group, BaBar Analysis Document **20**.
- [25] C. Hearty, BaBar Analysis Document **134**.
- [26] E. Varnes, BaBar Analysis Document **157**.
- [27] M. Bona, <http://babar-hn.slac.stanford.edu:5090/HyperNews/get/physAnal/1042.html>
- [28] D. L. et al., BaBar Analysis Document **220**.
- [29] D. L. et al., BaBar Analysis Document - Summary **255**.
- [30] A. Ali and C. Greub, Phys. Lett. **B361**, 146 (1995), hep-ph/9506374.